

1 2 3 4 5 6 7 8 9 10 11 12



(NASA-CR-190348) DESIGN
CONSIDERATIONS OF NATURAL LAMINAR
FLOW AIRFOILS FOR MEDIUM-SPEED
REGIONAL AIRCRAFT Progress Report,
1 Aug. 1983 - 31 Mar. 1984 (Kansas
Univ. Center for Research) 264 p

N92-70907

Unclass

Z9/02 0091386

THE UNIVERSITY OF KANSAS CENTER FOR RESEARCH, INC.

2291 Irving Hill Drive-Campus West

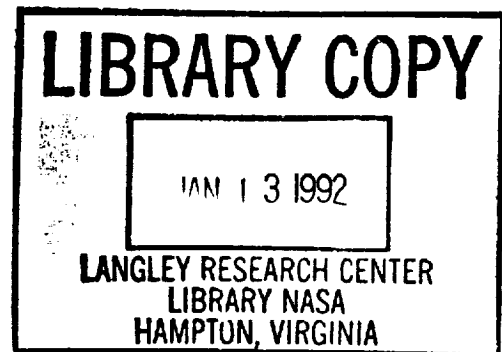
Lawrence, Kansas 66045

01386

Progress Report
under
NASA Grant NAG 1-345

DESIGN CONSIDERATIONS
OF NATURAL LAMINAR FLOW AIRFOILS
FOR MEDIUM-SPEED REGIONAL AIRCRAFT

KU-FRL-6131-1



Paul Vijgen, Project Manager
Ken Williams, Graduate Research Assistant
Bob Williams, Research Assistant

Jan Roskam, Principal Investigator

Flight Research Laboratory
University of Kansas Center for Research, Inc.
Lawrence, Kansas 66045

October 1984

TABLE OF CONTENTS

	<u>Page</u>
<u>ABSTRACT</u>	vi
<u>LIST OF FIGURES</u>	viii
<u>LIST OF TABLES</u>	xx
<u>LIST OF SYMBOLS</u>	xxi
<u>INTRODUCTION</u>	1
1.0 <u>CHARACTERISTICS OF REGIONAL AIRCRAFT</u>	4
1.1 INTRODUCTION.....	4
1.2 DEFINITION OF REGIONAL AIRCRAFT RELATIVE TO EXISTING CLASSES OF AIRCRAFT.....	4
2.0 <u>EXISTING NLF AIRFOILS</u>	4
2.1 INTRODUCTION.....	8
2.2 NLF AIRFOILS FOR LOWER M_{des} AND Re	8
2.3 NACA AND NASA NATURAL LAMINAR FLOW AIRFOILS.....	10
2.4 NLF AIRFOILS FOR $M_{des} \approx 0.60$ AND $Re > 20 \times 10^6$	11
3.0 <u>AIRFOIL DESIGN AND MODIFICATION METHODS</u>	13
3.1 INTRODUCTION.....	13
3.2 OVERVIEW OF DESIGN METHODS FOR AIRFOILS.....	13
3.3 DESIGN METHODS AVAILABLE.....	15
3.3.1 <u>Eppler Design Code</u>	15
3.3.2 <u>BGK and TRANSEP Design Codes</u>	17
3.4 STREAMLINE-CURVATURE METHOD.....	17
3.4.1 <u>Introduction</u>	17
3.4.2 <u>Airfoil Modification Procedure</u>	19

TABLE OF CONTENTS (continued)

	<u>Page</u>
3.4.3 <u>Modification fo the Original Streamline Curvature Method</u>	19
3.4.4 <u>Application of Streamline-Curvature Method</u>	20
3.4.5 <u>Disadvantages of the Streamline-Curvature Method</u>	21
3.4.6 <u>Advantages of the Streamline-Curvature Method</u>	22
4.0 <u>AIRFOIL ANALYSIS CODES USED</u>	23
4.1 INTRODUCTION.....	23
4.2 EPPLER CODE.....	23
4.2.1 <u>Introduction</u>	23
4.2.2 <u>Program Capabilities: Analysis Mode</u>	23
4.2.3 <u>Boundary-Layer Calculations</u>	24
4.2.4 <u>Transition Criteria in Eppler Code</u>	24
4.2.5 <u>Calculation of Section Coefficients</u>	25
4.2.6 <u>Flapping Routine</u>	26
4.2.7 <u>Advantages and Disadvantages of Eppler Code</u>	26
4.3 NORTH CAROLINA STATE CODE.....	27
4.3.1 <u>Introduction</u>	27
4.3.2 <u>Program Capabilities</u>	27
4.3.3 <u>Transition Criteria</u>	29
4.3.4 <u>Boundary-Layer Calculations</u>	29
4.3.5 <u>Limitations of the North Carolina State Code</u>	30
4.4 TRANSEP CODE.....	31
4.4.1 <u>Introduction</u>	31
4.4.2 <u>Characteristics of the TRANSEP Analysis Code</u>	32

TABLE OF CONTENTS (continued)

	<u>Page</u>
4.4.2.1 Inviscid Potential Flow.....	32
4.4.2.2 Boundary-Layer Theory.....	32
4.4.3 <u>Problems in Operating TRANSEP</u>	34
4.4.3.1 Airfoils with Thin Leading Edge.....	34
4.4.3.2 $M = 0.60$ and Above.....	34
4.4.4 <u>Choice of Grid Size and Convergence</u> <u>Parameters</u>	35
4.4.5 <u>Comparison of TRANSEP and NCS Codes</u>	36
4.5 SUMMARY OF AIRFOIL ANALYSIS CODES.....	37
5.0 <u>FACTORS AFFECTING CHOICE OF TARGET PRESSURE DISTRIBUTION</u>	38
5.1 INTRODUCTION.....	38
5.2 TRANSITION MECHANISMS.....	39
5.2.1 <u>Tollmien-Schlichting Disturbances</u>	39
5.2.2 <u>Crossflow Disturbances</u>	40
5.2.3 <u>Taylor-Goertler Vortices</u>	40
5.2.4 <u>Attachment-Line Contamination</u>	40
5.3 INTERACTION BETWEEN C-F AND T-S DISTURBANCES.....	41
5.4 PRESSURE RECOVERY.....	42
5.5 SAMPLE NLF TARGET PRESSURE DISTRIBUTION.....	44
6.0 <u>DEVELOPMENT AND ANALYSIS OF K.U. AIRFOILS</u>	45
6.1 INTRODUCTION.....	45
6.2 CHOICE OF AIRFOIL TO BE MODIFIED.....	45
6.3 MS(1)-0317 PRESSURE DISTRIBUTION AND INITIAL TARGET PRESSURE DISTRIBUTION.....	46
6.4 PRESENTATION AND ANALYSIS OF K.U. AIRFOILS.....	47
6.4.1 <u>Introduction</u>	47

TABLE OF CONTENTS (continued)

	<u>Page</u>
6.4.2 <u>Airfoil 26A</u>	47
6.4.2.1 Development.....	47
6.4.2.2 Incompressible Characteristics (from Eppler Code).....	48
6.4.2.3 Subcritical Characteristics (NCS Code).....	49
6.4.2.4 SALLY Boundary-Layer Stability Analysis for Airfoil 26A.....	52
6.4.3 <u>Airfoil 32</u>	56
6.4.3.1 Development.....	56
6.4.3.2 Incompressible Low-Speed Characteristics.....	56
6.4.3.3 Subcritical Characteristics (NCS).....	57
6.4.3.4 Compressible Characteristics of Airfoil 32...	57
6.4.4 <u>Airfoil 35</u>	59
6.4.4.1 Development.....	59
6.4.4.2 Low-Speed Characteristics (Eppler).....	60
6.4.4.3 Subcritical Characteristics (NCS).....	60
6.4.4.4 Compressible Characteristics of Airfoil 35...	61
6.4.5 <u>Airfoil 37</u>	62
6.4.5.1 Development.....	62
6.4.5.2 Low-Speed Characteristics (Eppler).....	62
6.4.6 <u>Airfoil 40</u>	63
6.4.6.1 Development.....	63
6.4.6.2 Low-Speed Characteristics (Eppler).....	63

TABLE OF CONTENTS (continued)

	<u>Page</u>
6.4.6.3 Subcritical Characteristics (NCS).....	64
6.4.6.4 Compressible Characteristics of Airfoil 40...	65
6.5 COMPARISON OF K.U. AIRFOILS WITH NLF(1)-0414F AND DERIVATIVE	66
6.5.1 <u>Comparison of NLF(1)-0414F with Derivative</u>	66
6.5.2 <u>Comparison with K.U. Airfoils</u>	68
6.5.2.1 Incompressible Characteristics.....	68
6.5.2.2 Compressible Characteristics (M = 0.6).....	70
7.0 <u>FLAPPING OF AIRFOILS</u>	72
7.1 INTRODUCTION.....	72
7.2 EFFECTS OF A PLAIN FLAP ON AIRFOIL PERFORMANCE.....	72
7.3 APPLICATION OF FLAP TO K.U. AIRFOILS.....	74
7.3.1 <u>Application of Flap during Cruise</u>	74
7.3.2 <u>Application of Flap at Low Speeds</u>	75
8.0 <u>CONCLUSIONS AND RECOMMENDATIONS</u>	77
8.1 CONCLUSIONS.....	77
8.2 RECOMMENDATIONS.....	82
9.0 <u>REFERENCES</u>	85
APPENDIX I: <u>COORDINATES OF K.U. NLF AIRFOILS</u>	232

ABSTRACT

This report documents the work in the area of Natural Laminar Flow over regional aircraft at the University of Kansas FLight Research Lab from August 1, 1983, until March 31, 1984, performed under NASA Grant NAG 1-345.

Five advanced, medium-speed natural laminar flow airfoils, intended for application in medium-speed ($M = 0.6$) regional aircraft, have been developed using a modified streamline-curvature method. An evaluation of the codes used in this development (Eppler, NCState, and TRANSEP) is also presented.

The pressure distribution of these K.U. airfoils is subcritical in the design condition. In view of crossflow considerations, both flat and favorable mid-chord pressure gradients were examined. The pressure recovery is concave.

Thickness of the airfoils is approximately $0.17c$. Length of the laminar run is $0.55 - 0.58c$ on both surfaces in cruise ($c_{\ell_{des}} = 0.3 - 0.5$), as well as for c_{ℓ} up to 0.8 to 1.0 at incompressible speeds. $c_{d_{min}}$ is near 40 counts in cruise for airfoils developed first in this report. Application of a $0.2c$ trailing-edge cruise/climb flap reduces c_m by 40% at $c_{\ell_{des}}$ and can widen the low-drag bucket from $c_{\ell} = 0.2$ to $c_{\ell} = 1.2$, thereby providing low drag also to the initial climb phase of regional aircraft and low cruise c_{ℓ} values. The Eppler-predicted $c_{\ell_{max}}$'s are comparable to the predicted value for NASA NLF(1)-0414F. A comparison of the five K.U. NLF airfoils with NASA MS(1)-0317 and NASA NLF(1)-0414F airfoils concludes this report. Coordinates of the developed airfoils are included in the Appendix.

The airfoils developed will be used in an NLF wing design study in the second phase of this study of application of NLF over medium-speed regional aircraft under this grant.

LIST OF FIGURES

	<u>Page</u>
Figure 1.1	Short-haul Aircraft Market Study. 89
Figure 1.2	Lockheed's Proposed 30 PAX Short-haul Aircraft. 89
Figure 1.3	Estimated DOC for 30 PAX Short-haul Aircraft for Both 100 and 600 NM Ranges. 90
Figure 1.4	Mission Profiles for 30 PAX Short-haul Aircraft. 90
Figure 1.5	Three-View of the 3-Surface Configuration . . . 91
Figure 1.6	Relationship Between Wing Loading and Mach Number for Existing Aircraft. 92
Figure 1.7	Relationship Between Cruise Lift Coefficient and Mach Number for Existing Aircraft 92
Figure 2.1	Representative Cruise Mach and Reynolds Numbers for Several Airplane Classes. 93
Figure 2.2	Wortmann FX 60-157 Airfoil. 93
Figure 2.3	NLF(1)-0416 Airfoil Contour 96
Figure 2.4	NACA 66 ₂ -015 Pressure Distribution. 97
Figure 2.5	NACA 66 ₂ -015 Drag Polars and Pitching Moment Curves. 98
Figure 2.6	NACA 67 ₁ -015 Contour and Pressure Distribution. 99
Figure 2.7	NACA 67 ₁ -215 Drag Polar and Moment Curve. . . . 100
Figure 2.8	NASA NLF(1)-0414 Airfoil Contour and Pressure Distribution. 101
Figure 2.9	Aerodynamic Characteristics of NLF(1)-0414F and Derivative as Calculated by the Eppler Code Using Natural Transition 102
Figure 2.10	Supercritical Pressure Distribution for Design Case of Boeing NLF Airfoil. 103
Figure 2.11	Subcritical Pressure Distribution for Design Case of Vought-ATC NLF Airfoil. 104

LIST OF FIGURES (continued)

		<u>Page</u>
Figure 5.4	Effect of Mid-chord Upper Surface Pressure Gradient, Sweep Angle and Reynolds Number on Transition.	120
Figure 5.5	Effect of Lower Surface Pressure Gradient, Reynolds Number and Sweep Angle on Extent of Laminar Flow.	121
Figure 5.6	Illustration of the Effect of Recovery Velocity Distribution on Development of Turbulent Boundary Layer for Low Chord Reynolds Number.	122
Figure 5.7	Characteristics of Typical NLF Pressure Distribution for Unswept and Moderately Swept Wings.	123
Figure 6.1	MS(1)-0317 Pressure Distribution as Calculated by the NCS Code	124
Figure 6.2	Locations of Transition and Turbulent Separation on the MS(1)-0317 as Calculated by the Eppler Code	124
Figure 6.3	MS(1)-0317 Pressure Distribution and First Target Pressure Distribution	125
Figure 6.4	Comparison of MS(1)-0317 and 26A Pressure Distributions and Contours	126
Figure 6.5	Comparison of MS(1)-0317 and 26A Curvature Distributions.	126
Figure 6.6	Aerodynamic Characteristics of 26A and MS(1)-0317 as Calculated by the Eppler Code Using Natural Transition	127
Figure 6.7	Aerodynamic Characteristics of 26A and MS(1)-0317 as Calculated by the Eppler Code Using the Laminar Separation Criterion	128
Figure 6.8	Aerodynamic Characteristics of 26A and MS(1)-0317 as Calculated by the Eppler Code with Transition Fixed at 5-percent Chord . . .	129
Figure 6.9	Transition and Turbulent Separation Locations for 26A and MS(1)-0317 as Calculated by the Eppler Code Using Natural Transition.	130

LIST OF FIGURES (continued)

		<u>Page</u>
Figure 6.10	Transition and Turbulent Separation Locations for 26A and MS(1)-0317 as Calculated by the Eppler Code Using the Laminar Separation Criterion.	131
Figure 6.11	Effect of Reynolds Number on the Aerodynamic Characteristics of 26A as Calculated by the Eppler Code Using Natural Transition.	132
Figure 6.12	Effect of Reynolds Number on the Aerodynamic Characteristics of 26A as Calculated by the Eppler Code Using the Laminar Separation Criterion.	133
Figure 6.13	Comparison of NCS-predicted Characteristics at M=0.2 and Incompressible Eppler Predictions for 26A Using Natural Transition	134
Figure 6.14	Comparison of NCS-predicted Characteristics at M=0.2 and Incompressible Eppler Predictions for 26A Using the Laminar Separation Criterion.	135
Figure 6.15	Transition and Turbulent Separation Locations for 26A as Calculated by the NCS Code at M=0.2 and by the Incompressible Eppler Code Using Natural Transition.	136
Figure 6.16	Transition and Turbulent Separation Locations for 26A as Calculated by the NCS Code at M=0.2 and by the Incompressible Eppler Code Using the Laminar Separation Criterion.	137
Figure 6.17	Effect of Trailing-edge Thickness on the Aerodynamic Characteristics of 26 as Calculated by the NCS Code at M=0.2 Using Natural Transition.	138
Figure 6.18	Effect of Trailing-edge Thickness on the Aerodynamic Characteristics of 26 as Calculated by the NCS Code at M=0.2 Using the Laminar Separation Criterion	139
Figure 6.19	Effect of Reynolds Number on the Aerodynamic Characteristics of 26B as Calculated by the NCS Code at M=0.2 Using the Laminar Separation Criterion.	139

LIST OF FIGURES (continued)

		<u>Page</u>
Figure 3.1	KU-Airfoil 8019 Designed by Using Eppler Design Mode.	105
Figure 3.2	Airfoil Design and Modification Procedure Used at KU	106
Figure 3.3	Method to Recover Trailing-Edge Location After Integration.	107
Figure 3.4	Example of Modified Streamline Curvature Method Used to Obtain Airfoil 26A.	108
Figure 3.5	Methods to Eliminate Leading-edge Spikes in Pressure Distributions	109
Figure 4.1	Airfoil Contour Resulting From Eppler Flapping Routine	110
Figure 4.2	Low-speed Characteristics of MS(1)-0317. Comparison Between Eppler Code Prediction and Wind-tunnel Data	111
Figure 4.3	Comparison of Wind-tunnel Data to NCS Calculations Using Natural Transition.	112
Figure 4.4	Comparison of Aerodynamic Characteristics of Airfoil 26A by Eppler and NCS Codes	113
Figure 4.5	Comparison of Viscid and Inviscid Pressure Distributions Calculated by the NCS Code Using Natural Transition	114
Figure 4.6	Comparison of Convergence Parameter in Transep Code	115
Figure 4.7	Pressure Distribution Comparison for Transep and NCS at $M = 0.60$	116
Figure 4.8	Pressure Distribution Comparison for Transep and NCS at $M = 0.60$	116
Figure 5.1	Explanation of Origin of Crossflow on a Swept Wing	117
Figure 5.2	Forward Chord Pressure Distribution Optimized for Different Schlichting Conditions	118
Figure 5.3	Effect of Initial Upper Surface Pressure Gradient, Sweep Angle and Reynolds Number on Transition.	119

LIST OF FIGURES (continued)

	<u>Page</u>
Figure 6.20 Effect of Mach Number on the Aerodynamic Characteristics of 26A as Predicted by the NCS Code Using the Laminar Separation Criterion.	140
Figure 6.21 Effect of Mach Number on the Pressure Distribution of 26A as Predicted by the NCS Code Using Natural Transition.	140
Figure 6.22 Effect of Mach Number on the Aerodynamic Characteristics of 26A as Predicted by the NCS Code Using Natural Transition.	141
Figure 6.23 Aerodynamic Characteristics of 26A and MS(1)-0317 as Predicted by the NCS Code Using Natural Transition.	141
Figure 6.24 Aerodynamic Characteristics of 26A and MS(1)-0317 as Predicted by the NCS Code Using the Laminar Separation Criterion.	142
Figure 6.25 Procedure to Determine T.S. Disturbance Growth.	143
Figure 6.26 Amplification Factor n , Upper Surface Airfoil 26A $c_1 = 0.28$, $Re = 8.9 \times 10^6$, $M = 0.60$	144
Figure 6.27 Amplification Factor n , Lower Surface Airfoil 26A $c_1 = 0.28$, $Re = 8.9 \times 10^6$, $M = 0.60$	145
Figure 6.28 Amplification Factor n , Upper Surface Airfoil 26A $c_1 = 0.45$, $Re = 8.9 \times 10^6$, $M = 0.60$	146
Figure 6.29 Amplification Factor n , Lower Surface Airfoil 26A $c_1 = 0.45$, $Re = 8.9 \times 10^6$, $M = 0.60$	147
Figure 6.30 Amplification Factor n , Upper Surface Airfoil 26A $c_1 = 0.46$, $Re = 8.9 \times 10^6$, $M = 0.60$	148
Figure 6.31 Amplification Factor n , Lower Surface Airfoil 26A $c_1 = 0.46$, $Re = 8.9 \times 10^6$, $M = 0.60$	149
Figure 6.32 Frequency Dependence of n_{max} for Airfoil 26A.	150
Figure 6.33 Airfoil 26 Pressure Distribution and Target Pressure Distribution for Airfoil 32.	151

LIST OF FIGURES (continued)

		<u>Page</u>
Figure 6.34	Airfoils 26 and 32.	151
Figure 6.35	Curvature Distributions of Airfoils 26 & 32.	152
Figure 6.36	Pressure Distributions of Airfoils 26 & 32 as Calculated by the NCS Code Using Natural Transition.	152
Figure 6.37	Aerodynamic Characteristics of 32 and MS(1)-0317 as Calculated by the Eppler Code Natural Transition.	153
Figure 6.38	Aerodynamic Characteristics of 32 and MS(1)-0317 as Calculated by the Eppler Code Laminar Separation.	154
Figure 6.39	Aerodynamic Characteristics of 32 and MS(1)-0317 as Calculated by the Eppler Code Transition Fixed at .05c.	155
Figure 6.40	Effect of Reynolds Number on the Aerodynamic Characteristics of 32 as Predicted by the Eppler Code. Natural Transition.	156
Figure 6.41	Effect of Reynolds Number on the Aerodynamic Characteristics of 32 as Predicted by the Eppler Code. Laminar Separation.	157
Figure 6.42	Effect of Reynolds Number on the Aerodynamic Characteristics of 32 as Predicted by the Eppler Code. Transition Fixed at .05c.	158
Figure 6.43	Effect of Trailing-edge Thickness on the Aerodynamic Characteristics of Airfoil 32 as Predicted by the Eppler Code. Natural Transition.	159
Figure 6.44	Effect of Trailing-edge Thickness on the Aerodynamic Characteristics of Airfoil 32 as Predicted by the Eppler Code. Laminar Separation.	160
Figure 6.45	Aerodynamic Characteristics of Airfoil 32 as Predicted by the NCS Code. Natural Transition.	161
Figure 6.46	Aerodynamic Characteristics of Airfoil 32 as Predicted by the NCS Code. Laminar Separation.	161

LIST OF FIGURES (continued)

		<u>Page</u>
Figure 6.47	Pressure Distribution for Airfoil 32 as Calculated by the NCS Code Using Natural Transition.	162
Figure 6.48	Calculated Pressure Distributions Airfoil 32; TRANSEP Code (Medium Grid).	163
Figure 6.49	Critical Flow Condition Airfoil 32, M = 0.60 TRANSEP Code (Medium Grid)	164
Figure 6.50	Pressure Distribution Design Condition Airfoil 32 TRANSEP Code (Medium Grid)	164
Figure 6.51	Pressure Distributions for Several Mach Numbers TRANSEP Code (Medium Grid).	165
Figure 6.52	Drag Rise Estimate Airfoil 32 TRANSEP (Medium Grid)	165
Figure 6.53	Airfoil 32 Pressure Distribution and Target Pressure Distribution.	166
Figure 6.54	Curvature Distributions of Airfoils 32 & 35	166
Figure 6.55	Comparison of Airfoils 32 and 35 Pressure Distributions	167
Figure 6.56	Airfoil 32 and 35 Contours.	167
Figure 6.57	Comparison of MS(1)-0317 and 35 Contours.	168
Figure 6.58	Aerodynamic Characteristics of 35 and MS(1)-0317 as Calculated by the Eppler Code Using Natural Transition.	169
Figure 6.59	Aerodynamic Characteristics of 35 and MS(1)-0317 as Calculated by the Eppler Code Using Laminar Separation.	170
Figure 6.60	Aerodynamic Characteristics of 35 and MS(1)-0317 as Calculated by the Eppler Code Using Fixed Transition at 5-percent Chord on Both Surfaces.	171
Figure 6.61	Effect of Reynolds Number on the Aerodynamic Characteristics of 35 as Predicted by the Eppler Code. Natural Transition.	172

LIST OF FIGURES (continued)

	<u>Page</u>
Figure 6.62 Effect of Reynolds Number on the Aerodynamic Characteristics of 35 as Predicted by the Eppler Code. Laminar Separation.	173
Figure 6.63 Effect of Reynolds Number on the Aerodynamic Characteristics of 35 as Predicted by the Eppler Code. Transition Fixed at .05c	174
Figure 6.64 Aerodynamic Characteristics of 35 and MS(1)-0317 as Calculated by NCS Code Using Natural Transition.	175
Figure 6.65 Aerodynamic Characteristics of 35 and MS(1)-0317 as Calculated by NCS Code Using Laminar Separation.	176
Figure 6.66 Pressure Distributions Airfoil 35 for Different α	177
Figure 6.67 Pressure Distributions Airfoil 35 for Increasing Mach Number TRANSEP Code (Fine Grid)	178
Figure 6.68 Drag Rise Estimate Airfoil 35 TRANSEP (Fine Grid)	178
Figure 6.69 Airfoil 35 Pressure Distribution, Target Pressure Distribution, and Resulting Pressure Distribution for Airfoil 37.	179
Figure 6.70 Airfoils 35 and 37.	179
Figure 6.71 Curvature Distributions of Airfoils 35 and 37.	180
Figure 6.72 Airfoils 37 and MS(1)-0317.	180
Figure 6.73 Aerodynamic Characteristics of 37 and MS(1)-0317 as Calculated by the Eppler Code Using Natural Transition	181
Figure 6.74 Aerodynamic Characteristics of 37 and MS(1)-0317 as Calculated by the Eppler Code Using the Laminar Separation Criterion.	182
Figure 6.75 Aerodynamic Characteristics of 37 and MS(1)-0317 as Calculated by the Eppler Code Using Fixed Transition at 5-percent Chord on Both Surfaces.	183

LIST OF FIGURES (continued)

		<u>Page</u>
Figure 6.76	Airfoils 37, 40, and MS(1)-0317.	184
Figure 6.77	Curvature Distributions of 37 and 40	185
Figure 6.78	Aerodynamic Characteristics of 40 and MS(1)-0317 as Calculated by the Eppler Code Using Natural Transition.	186
Figure 6.79	Aerodynamic Characteristics of 40 and MS(1)-0317 as Calculated by the Eppler Code Using the Laminar Separation Criterion.	187
Figure 6.80	Aerodynamic Characteristics of 40 and MS(1)-0317 as Calculated by the Eppler Code With Transition Fixed at 5-percent Chord.	188
Figure 6.81	Effect of Reynolds Number on the Aerodynamic Characteristics of 40 as Predicted by the Eppler Code Using Natural Transition	189
Figure 6.82	Effect of Reynolds Number on the Aerodynamic Characteristics of 40 as Calculated by the Eppler Code Using the Laminar Separation Criterion.	190
Figure 6.83	Effect of Reynolds Number on the Aerodynamic Characteristics of 40 as Calculated by the Eppler Code with Transition Fixed at 5-percent Chord.	191
Figure 6.84	Aerodynamic Characteristics of Airfoil 40 as Predicted by the NCS Code. Natural Transition	192
Figure 6.85	Aerodynamic Characteristics of Airfoil 40 as Predicted by the NCS Code. Laminar Separation	192
Figure 6.86	Design Pressure Distribution Airfoil 40. NCS Predicted Transition at Begin Pressure Recovery	193
Figure 6.87	Aerodynamic Characteristics of Airfoil as Predicted by the NCS Code.	194
Figure 6.88	Pressure Distributions of Airfoil 40 for Different α	195

LIST OF FIGURES (continued)

		<u>Page</u>
Figure 6.89	Pressure Distributions of Airfoil 40 for Increasing Mach Number TRANSEP Code (Fine Grid)	196
Figure 6.90	Drag Rise Estimate Airfoil 40 TRANSEP (Fine Grid) and NLR Method.	196
Figure 6.91	Supersonic Pocket and Strong Shock Wave Over Airfoil 40 at $M = 0.70$	197
Figure 6.92	Airfoils NLF(1)-0414F and Derivative.	198
Figure 6.93	Aerodynamic Characteristics of NLF(1)-0414F and Derivative as Calculated by the NCS Code Using Natural Transition	198
Figure 6.94	Aerodynamic Characteristics of NLF(1)-0414F and Derivative as Calculated by the Eppler Code Using Natural Transition	199
Figure 6.95	Aerodynamic Characteristics of NLF(1)-0414F and Derivative as Calculated by the Eppler Code Using the Laminar Separation Criterion	200
Figure 6.96	Aerodynamic Characteristics of NLF(1)-0414F and Derivative as Calculated by the Eppler Code with Transition Fixed at 5-percent Chord	201
Figure 6.97	Location of Turbulent Separation for NLF(1)-0414F and Derivative as Calculated by the Eppler Code.	202
Figure 6.98	Aerodynamic Characteristics of NLF(1)-0414F and Derivative as Predicted by the NCS Code Using Natural Transition.	204
Figure 7.1	.20c Cruise/Climb Flap Incorporated Into .30c Fowler Flap.	205
Figure 7.2	Calculated Inviscid Pressure Distributions of Airfoil 32 with Deflection of a 20% Chord Cruise/Climb Flap	206
Figure 7.3	Inviscid Pressure Distributions of Airfoil 32 with $\delta_F = -5$ deg	208
Figure 7.4	Inviscid Pressure Distributions of Airfoil 32 with $\delta_F = 10$ deg	209

LIST OF FIGURES (continued)

		<u>Page</u>
Figure 7.5	Inviscid Pressure Distributions of Airfoil 35 with Deflection of a 20% Chord Cruise/Climb Flap.	210
Figure 7.6	Inviscid Pressure Distribution of Airfoil 35 with $\delta_F = -5$ deg	212
Figure 7.7	Inviscid Pressure Distributions of Airfoil 35 with $\delta_F = 10$ deg	213
Figure 7.8	Calculated Inviscid Pressure Distributions of Airfoil 40 with Deflection of a 20% Cruise/Climb Flap	214
Figure 7.9	Inviscid Pressure Distribution of Airfoil 40 with $\delta_F = -5$ deg	216
Figure 7.10	Inviscid Pressure Distribution of Airfoil 40 with $\delta_F = 10$ deg	217
Figure 7.11	Calculated Aerodynamic Characteristics of Airfoil 32 (For Laminar Separation, Natural Transition, and Fixed Transition Criteria) with $\delta_F = -5, 0$, and 10 Deg	218
Figure 7.12	Calculated Aerodynamic Characteristics of Airfoil 35 (For Laminar Separation, Natural Transition, and Fixed Transition Criteria) with $\delta_F = -5, 0$, and 10 Deg	221
Figure 7.13	Calculated Aerodynamic Characteristics of Airfoil 40 (For Laminar Separation, Natural Transition, and Fixed Transition Criteria) with $\delta_F = -5, 0$, and 10 Deg	224
Figure 7.14a	Effect of Flap Deflection on Aerodynamic Characteristics of Airfoil 40 as Predicted by the NCS Code	227
Figure 7.14b	Effect of Flap Deflection on the Pressure Distribution of Airfoil 40 as Predicted by the NCS Code.	228
Figure 7.15	The Change in Predicted Point of Turbulent Separation with Changes in Both Angle of Attack and Flap Deflection Angle for Airfoil 32.	229

LIST OF FIGURES (concluded)

	<u>Page</u>
Figure 7.16 The Change in Predicted Point of Turbulent Separation with Changes in Both Angle of Attack and Flap Deflection Angle for Airfoil 35.	230
Figure 7.17 The Change in Predicted Point of Turbulent Separation with Changes in Both Angle of Attack and Flap Deflection Angle for Airfoil 40.	231

LIST OF TABLES

<u>Number</u>	<u>Title</u>	<u>Page</u>
1.1	Design Characteristics of Regional Aircraft.....	6
3.1	Sample Input and Output for KU-Eppler Design 8019.....	16
6.1	Cruise Flight Condition.....	46
6.2	SALLY Analysis Airfoil 26A.....	53
6.3	Summary Low-Drag Bucket of Studied Airfoils.....	71
6.4	c_{l_α} Comparison of Studied Airfoils.....	71

LIST OF SYMBOLS

<u>Symbol</u>	<u>Definition</u>	<u>Units</u>
A	aspect ratio	-
b	span	ft.
c	chord	ft.
C-F	crossflow	-
c_d	airfoil drag coefficient	-
c_{d_f}	friction drag coefficient	-
$c_{d_{wave}}$	airfoil wave drag coefficient	-
c_l	airfoil lift coefficient	-
$c_{l_{max}}$	maximum airfoil lift coefficient	-
C_L	airplane lift coefficient	-
$c_m, c_{m_{1/4}}$	airfoil pitching moment coefficient about 1/4 chord	-
c_p	pressure coefficient	-
c_p^*	critical pressure coefficient	-
DOC	direct operating cost	\$/seat n.mi.
FRL	Flight Research Laboratory at K.U.	-
H_{21}	Shape factor: δ_2/δ_1	-
H_{32}	Shape factor: δ_3/δ_2	-
IMSL	International Mathematical and Statistical Libraries	-
K.U.	University of Kansas, Lawrence	-
l.e.	leading edge	-
M	Mach number	-
mgc	mean geometric chord	-
n	amplification factor in linear boundary-layer theory	-

LIST OF SYMBOLS (continued)

<u>Symbol</u>	<u>Definition</u>	<u>Units</u>
p	pressure	psf
Re, R	Reynolds number based on chord length	-
Re_{δ_2}	Reynolds number based on local velocity and displacement thickness, δ_2	-
s	arc length	ft.
S	area	ft. ²
T	thrust	lbs.
T-S	Tollmien-Schlichting	-
t/c	airfoil thickness ratio	-
U, V	free-stream velocity	ft./sec.
v	local velocity	ft./sec.
W	weight	lbs.
α	angle of attack	deg.
δ_f	flap deflection	deg.
Λ	sweep angle	deg.
λ	taper ratio	deg.
δ_1/c	boundary-layer displacement thickness/chord	-
$\delta_2/c, \theta$	boundary-layer momentum thickness/chord	-
δ_3/c	boundary-layer energy thickness/chord	-
ω	relaxation factor (in finite difference method)	-

LIST OF SYMBOLS (continued)

SUBSCRIPTS:

<u>Subscript</u>	<u>Definition</u>	<u>Units</u>
a.c.	aerodynamic center	-
c	chord	ft.
cr	cruise condition	-
des	design condition	-
t.e.	trailing-edge	-
∞	free-stream condition	-

INTRODUCTION

JUSTIFICATION

This report documents the work performed under NASA grant NAG 1-345, at the University of Kansas Flight Research Lab from August 1, 1983 until March 31, 1984 in the area of Natural Laminar Flow for regional aircraft. Although the contract year for this NASA grant formally started on March 1, 1983, the work performed up to August 1, 1983 is not reported in this paper. The effort during these five months was concentrated in a wing-weight trade-off analysis using a method developed at KU-FRL (Reference 1). Also, the geometry package for generating input data for a three-dimensional potential-flow program (Hess Code, see Reference 2) was made operational on the mainframe computer system at K.U.

The wing-weight analysis will be included and reported in an NLF performance pay-off study to be started in June 1984.

The Hess-paneling procedure will be used to prepare input for the Hess code in an investigation into the possibility of laminarizing parts of the fuselage of a regional aircraft. Parallel to these two efforts, an NLF wing-design study was started also in June 1984.

This report documents the development and computational analysis of several medium-speed Natural Laminar Flow (NLF) airfoils designed for a cruise Mach number of 0.60. The development of medium-speed NLF airfoils represents the first step towards the design of NLF wings for medium-speed regional aircraft. The overall objective of this NLF study as of March 1, 1983 is the geometrical definition of a family of wings most likely to procure an efficient, cost-effective regional aircraft.

The airfoils developed in this report, among others, will be applied in this NLF wing design study. Since firm data on boundary-layer stability for laminar flow wings for regional aircraft are lacking, the original objective has been modified to also include an NLF performance payoff study and an NLF fuselage feasibility study mentioned above.

INTRODUCTION TO REPORT LAYOUT

First, an introduction to the desired aerodynamic characteristics of future regional aircraft is presented to provide a design objective for a three-dimensional NLF wing design study and an airfoil development study. After an overview of existing NLF airfoils in Chapter 2, the airfoil modification procedure method used in this study is presented in Chapter 3. This discussion of the streamline-curvature method is followed in Chapter 4 by a critical assessment of the computational codes used to predict the potential-flow and boundary-layer development around the airfoils. An assessment is required because of two characteristics of the current study. First, off-design flight conditions for medium-speed airfoils can extend into the region where supercritical flow is present around the airfoil. Hence, a code must be used that models this type of mixed flow appropriately. Second and of greater importance is the accurate modeling of the transition from the laminar boundary layer to a turbulent one. Chapter 5 then presents some considerations underlying the establishment of a target pressure distribution for a medium-speed NLF airfoil. Based upon computational and experimental data found in literature, typical pressure gradients for characteristic chordwise airfoil parts are given.

The medium-speed NASA MS(1)-0317 airfoil was used as starting point for the streamline-curvature modification procedure, and several NLF airfoils were developed. Chapter 6 summarizes this development and analyzes the characteristics of these basic airfoils. A comparison is made with the MS(1)-0317 airfoil. Also, a comparison of calculated characteristics of the NASA NLF(1)-0414F and a KU-FRL modification of this airfoil is made. Chapter 7 explores the effect of incorporating a small trailing-edge flap (i.e., a cruise/climb flap) into the basic airfoils developed at K.U. It is found that cruise section pitching moment can be reduced and that the low-drag "bucket" can be shifted to lower and higher c_{ℓ} -values with negative and positive flap deflections respectively.

Chapter 8 summarizes the reported design effort and brings forward suggestions for further research based upon the results obtained in this report.

ACKNOWLEDGEMENTS

Finally, we want to express our gratitude to Mr. Lou Williams, Dr. Bruce Holmes and Dr. Kees van Dam, all at NASA Langley Research Center, for their helpful monitoring and advising. We thank Mr. Cliff Obara (Langley Research Center) for performing the SALLY boundary-layer stability calculations discussed in Chapter 6.

1.0 NOMENCLATURE AND CHARACTERISTICS OF REGIONAL AIRCRAFT

1.1 INTRODUCTION

This chapter provides an introduction to the concept of regional aircraft. In this report, regional aircraft are defined to be aircraft which cruise at a Mach number of 0.5-0.7 and carry 20-60 passengers. By defining the desired characteristics of these aircraft one can formulate aerodynamic objectives for the wings of these aircraft which in turn provide two-dimensional (airfoil) design objectives to aid the establishment of a target pressure distribution (see Chapters 5 and 6).

1.2 DEFINITION OF REGIONAL AIRCRAFT RELATIVE TO EXISTING CLASSES OF AIRCRAFT

Figure 1.1 compares the relative positions of recent and established short-haul passenger aircraft based on their cruise Mach numbers. It can be seen that, apart from the commercially unsuccessful VFW-614, no designs are located in the Mach number range between 0.5 and 0.65. Figure 1.1 also indicates that for $M_{\text{cruise}} > 0.5$ no aircraft offers a passenger capacity between 20 and 75. Recognizing this gap in the present short-haul market, the term regional aircraft is introduced to define the aircraft category covering a cruise Mach number range from 0.5 to 0.7 and a passenger capacity of 20-60.

1.3 CHOICE OF FLIGHT CONDITIONS

Numerous studies of domestic airline and commuter operations (done by NASA, FAA, and private industry) project a post-1985 need for aircraft which carry 20-60 passengers on stage lengths less

than 500 n.mi. A 1980 Lockheed study (Reference 3) found that relatively high cruise speeds ($M=0.6$ to 0.7) can be cost-effective in fulfilling this role. Lockheed designed an aircraft (Figure 1.2) with a range of 600 n.mi. to allow fly-throughs for short hauls (average range is 100 n.mi.). Figure 1.3 shows the direct-operating costs of the proposed 30-passenger short-haul aircraft as a function of cruise Mach number and stage length. At the design range (600 n.mi.), cruise at $M=0.6$ provides a payoff in DOC relative to lower cruise speeds due to a significant reduction in block time. Figure 1.4 shows the mission profiles for the two ranges.

Another benefit of specifying a higher Mach number is found in improved available climb potential in comparison to existing $M_{des} < 0.5$ commuter aircraft. The increase in climb speed enables a quick climb to a less turbulent atmosphere, improving the ride-quality of the aircraft.

A comparative design investigation was done at the University of Kansas in 1982 (Reference 4) to determine whether the use of an unconventional configuration could achieve the mission requirements more effectively than the baseline design presented in the Lockheed report. The configurations featured the use of NLF airfoils (NASA NLF(1)-0416, see Section 2.2), propfans, and composite structures. A tail-aft, a canard, and a three-surface configuration were analyzed and compared. Of these configurations, the three-surface configuration (see Figure 1.5) outperformed the other two configurations. Therefore, the wing of this aircraft was chosen as a starting point for this project. The design flight condition is given in Table 1.1.

Table 1.1 Design Characteristics of Regional Aircraft

Number of passengers	30
Design range 600 n.mi. (1111.2 km)	
Cruise altitude	28,000 ft.
Cruise Mach number	0.60
Cruise lift coefficient	0.38
Mean geometric chord (mgc)	4.7 ft. (1.43 m)
Reynolds number in cruise based on mgc 8.6×10^6 (8.9×10^6 was used in calculations)	
Climb lift coefficient	approximately 1.0
Planform area 284 sq. ft. (26.4 m ²)	
Aspect ratio 14	
Weight (half-loaded)	18,800 lbs. (8530 kg)

This K.U. design is characterized by a relatively high wing loading. Figure 1.6 (Reference 5) shows the maximum wing loading to those of existing aircraft. For comparison, note the wing loading of the Boeing B737-200 is approximately 125 psf. In order to improve the inherent ride-quality, without applying a system for ride-quality augmentation (Reference 6), to a level which will satisfy 90% of the passengers, it is necessary that the wing loading be greater than 60 psf. Closely related to the wing loading is the lift cruise coefficient C_L . Figure 1.7 shows the overall airplane lift coefficient to vary between 0.3 and 0.55 for existing aircraft.

Another classification with respect to the Mach number can be made based upon the attainability of natural laminar flow over the wing. Research in recent years (Reference 7), as well as in the early fifties (Reference 8), has indicated that a laminar boundary layer can be maintained over a substantial portion of the wing area for Mach numbers as high as 0.6 when a favorable pressure gradient is present. When the Mach number is increased above 0.60, thereby introducing wing sweep, it will eventually become necessary to apply an active form of boundary-layer control to maintain a laminar boundary layer. Decisive is the interference between crossflow (C-F) and Tollmien-Schlichting (T-S) waves. In summary it can be said that in the indicated Mach number range (0.5 - 0.7) a transition will probably occur between a natural laminar flow (NLF) to an actively controlled laminar flow (LFC) wing.

2.0 EXISTING NLF AIRFOILS

2.1 INTRODUCTION

This chapter provides an overview of existing airfoils which provide appreciable amounts of natural laminar flow in their design condition. This summary is included as a reference point for later analyses in this report.

From the desired aerodynamic characteristics of the proposed regional aircraft in Chapter 1, more specific characteristics for two-dimensional NLF airfoils may be inferred. Two similarity parameters are of great importance to airplane aerodynamics:

- a. Reynolds number
- b. Mach number

The Reynolds number characterizes the development of the laminar boundary layer, the location and type of the transition region, and the turbulent boundary-layer growth over an airfoil at a particular Mach number and pressure distribution. The compressibility effects are represented by the freestream Mach number, and are significant for $M > 0.40$.

The chord Reynolds numbers for the wing of the regional aircraft discussed in Chapter 1.0 range from about 4 to 17 million. The design Mach number is 0.60. To obtain high wing loading, the cruise c_l will be on the order of 0.4 to 0.6. In order to combine a high aspect ratio wing with a high M_{des} it might be necessary to introduce supercritical NLF airfoils for regional aircraft at a higher cruise Mach number ($M_{cruise} = 0.7$). In view of the importance of these cruise Reynolds and

Mach numbers, the overview of existing NLF airfoils will be split up with respect to the magnitude of the M_{des} and Reynolds numbers.

2.2 NLF AIRFOILS FOR LOWER M_{des} AND Re_c

Natural laminar flow airfoils have been designed and successfully tested specifically for incompressible flight conditions ($M_{des} < 0.40$) and $Re < 5.10$. These airfoils have been incorporated in sailplanes and single piston-engined G.A. aircraft (see Figure 2.1). Airfoils designed for sailplanes are given by Wortmann (Reference 9), Eppler (Reference 10) and Van Ingen/Boermans (Reference 11). Figure 2.2 shows a typical Wortmann airfoil and its measured characteristics. Somers designed an NLF airfoil for G.A. application (Reference 12) using the Eppler airfoil design procedure (see Section 3.2). Figure 2.3 gives aerodynamic characteristics of this airfoil NLF(1)-0416. This airfoil achieves approximately 30% laminar flow on the upper surface and 60% on the lower surface in the cruise condition ($c_l = 0.4$). The modest amount of NLF over the upper surface leads to an airfoil with overall acceptable characteristics for G.A. applications. An increase of the laminar run by pushing the point of minimum pressure aft, generally results in a more typical NLF-type airfoil shape (i.e., point of maximum airfoil thickness is located further aft and the leading-edge radius is smaller), which generally compromises $c_{l_{max}}$ to gain a lower $c_{d_{min}}$.

2.3 NACA AND NASA NATURAL LAMINAR FLOW AIRFOILS

In the late 1930's, NACA developed the well-known 6-series airfoils, using Theodorsen's method (Reference 13). Figure 2.4 shows the calculated pressure distribution for airfoil NACA 66₂-015 (a symmetric section, Reference 13). Two characteristics of this pressure distribution are apparent. First, there is a relatively flat favorable upper-surface pressure gradient approximately to 0.60c. The flatness of this pressure gradient implies that this airfoil is near the end of its drag bucket, as can be seen in Figure 2.5. Second, the pressure recovery is linear. The amount of aft-chord loading is very small, which results in a near-zero pitching moment.

NACA 6-series airfoils were incorporated in World War II high speed fighters and later in high speed G.A. aircraft. However, conventional manufacturing and operational techniques (i.e. presence of rivets, surface waviness) prohibited attainment of significant laminar flow.

Nevertheless, flight tests in the late 1940's of a smoothed Bell P63A King Cobra indicated achievement of a laminar boundary layer over 60% of the wing chord for $M=0.60$ and above (Reference 8).

A 70% NLF airfoil was also developed by NACA (Reference 13): airfoil NACA 67₁-215. Figure 2.6 shows the (uncambered) velocity distribution. Figure 2.7 shows its sectional aerodynamic characteristics. Observe $c_{d_{min}} = 0.0034$ ($Re = 6.0 \times 10^6$) and a low $c_{l_{max}}$. Also, a dramatic decrease in $c_{l_{max}}$ occurs if the boundary-layer transition is fixed near the leading edge (NACA Standard Roughness Method).

Recently (1982-1984), Viken and Pfenninger (at NASA Langley) successfully designed an airfoil (NASA NLF(1)-0414F see Figure 2.8) which obtained very low drag and a respectable $c_{l_{\max}}$ (Reference 14). This airfoil also has a favorable pressure gradient to .70c. However, the pressure recovery differs favorably from that of the NACA 67₁-215 airfoil. Figure 2.9 shows characteristics as determined by the Eppler code at FRL, of the NLF(1)-0414F airfoil.

2.4 NLF AIRFOILS FOR $M_{\text{des}} > 0.6$ AND $Re_c > 20 \times 10^6$

Motivated by soaring fuel prices (Reference 15) and experimental evidence which indicated the feasibility of achieving natural laminar flow wings at high Mach and Reynolds numbers (Reference 8), NASA initiated NLF research within the framework of its Aircraft Energy Efficiency program (ACEE). (This initiative has resulted in theoretical and experimental work by NASA and private industry concerning laminar flow in the higher Mach range [$M > 0.7$]).

Figure 2.10 (Reference 16) shows a supercritical NLF airfoil arrived at by Boeing. In 1980 an NLF-airfoil, developed by NASA Langley and NASA Dryden, was testflown on a gloved F-111 (Reference 17). These test results were used to make an initial assessment of the interaction of crossflow and T-S type disturbances in the boundary layer (to be discussed in more detail in Chapter 5). These airfoils are typically designed for 45-50% NLF on the lower and 65-70% over the upper airfoil surface, and have slightly favorable mid-chord pressure gradients on the upper surface.

Mask (Reference 18) designed a subcritical airfoil to obtain 80% NLF on the upper surface for a Reynolds number of 40 million. The design incorporated a blowing jet (active diffusion control jet) to prevent boundary-layer separation in off-design performance. Figure 2.11 shows the design pressure distribution and the shape of this airfoil. Note the presence of flat "transition instability ramps" to promote transition before the Stratford recovery region. Wind-tunnel testing at full-scale Reynolds numbers (but at reduced Mach numbers) validated the establishment of the laminar run in the design Reynolds number condition.

3.0 AIRFOIL DESIGN AND MODIFICATION METHODS

3.1 INTRODUCTION

This chapter gives an overview of design methods for airfoils available at KU-FRL. In Section 3.3, the streamline-curvature method used in this report to develop NLF airfoils is discussed.

3.2 OVERVIEW OF DESIGN METHODS FOR AIRFOILS

The objective of an airfoil design effort is to arrive at an airfoil that exhibits specific desired characteristics. There are two approaches that can be used to arrive at these desired characteristics: direct-design and inverse-design methods.

Direct-Design Methods

The direct-design approach is a method of direct modification of the airfoil contour. The characteristics of the resulting airfoil are determined by experimental or numerical analysis of potential-flow and boundary-layer development. Comparison of the actual performance to the desired performance might indicate the necessity for another modification. This empirical direct-design methodology was used extensively until the early 1950's. The NACA 5-series (1935) and other early designs were all obtained in this fashion. Recently, the NASA NLF(1)-0414 F was also derived in this manner (see 2.3).

Successful application of this method requires extensive experience to determine how modifications to the airfoil contour will affect the airfoil performance. Also, the speed of this process is not great,

particularly when there is not a satisfactory starting point. However, once this experience has been gained, the method is very lucid.

In an attempt to increase the speed of this "French-curve style," numerical procedures have been developed by several authors (e.g., Reference 19). In these procedures, parts of the airfoil are represented by a mathematical series. The terms of this series may then be perturbed and the resulting changed airfoil analyzed.

Direct-Inverse Methods

Another approach is the direct-inverse method. Historically, the exact conformal mapping techniques in the Joukowski and von Kármán-Trefftz transformations can be classified as direct-inverse methods (i.e., the design process is regulated by the choice of one or more parameters which result in a specific airfoil shape). The direct-inverse method consists of two steps. In the first step, the desired airfoil characteristics are translated into a target pressure distribution. It must be realized that this transformation is, again, entirely based upon the experience accumulated in performing direct analyses of airfoils. Second, an inverse-design method derives the airfoil coordinates using this target distribution.

Although based upon different mathematical approaches, inverse-design methods have in common the need for a numerical algorithm and the choice of parameters that control the numerical process. Choice of these parameters also requires experience.

3.3 DESIGN METHODS AVAILABLE

Four airfoil design methods were available to the KU-FRL at the beginning of the contract year. The Eppler design code, the TRANSEP and BGK codes and the streamline-curvature method. These methods were assessed briefly before it was decided to use the streamline-curvature method (see Section 3.3).

3.3.1 Eppler Design Code

Eppler (References 20, 21) developed a very fast and elegant algorithm to design lower Reynolds number airfoils neglecting compressibility effects. The method is based upon the specification of the velocity distribution both in the expansion zone as well as the recovery zone. The expansion region (over which a laminar boundary layer is expected) is controlled by specifying angles of attack at which a particular segment shows a flat velocity ratio. In this sense the progression of transition over the upper surface towards the leading edge with increasing angle of attack can be controlled. The steepness, concavity and extent of the pressure recovery can also be controlled. Figure 3.1a shows an airfoil arrived using the method in ref 21. Table 3.1 summarizes the input parameters used to obtain this airfoil. The velocity distributions in Figure 3.1b indicate that the favorable gradient on the upper surface extends to only $0.2c$. Further refinement of this airfoil has not been continued at the FRL. One man-month was needed to learn the design mode of the Eppler code and to arrive at the design shown. This method is a powerful design tool for subcritical laminar-flow airfoil design.

re 100 0 0. ##### 0. 0. 0. 0. 0.

16

3.3.2 BGK and TRANSEP Design Codes

The airfoil design codes by Bauer, Garabedian and Korn (BGK) (Reference 22) and by Carlson (TRANSEP code, Reference 23) are both suitable for the transonic airflow regime. The BGK code solves the inverse-design problem in the hodograph plane. Control over the design process is provided by a set of logarithmic terms involving the location of singularities inside the airfoil contour. The TRANSEP code utilizes the (full) inviscid potential-flow equations in a stretched Cartesian grid system in contrast to the conformal hodographic mapping in the BGK code. In the present TRANSEP version, it is necessary to specify the first 5 to 10% chord of the airfoil. The target pressure distribution determines the actual shape of the airfoil. A problem inherent to direct-inverse methods is that physically impossible airfoils (i.e., negative thicknesses in the trailing-edge region) or open-ended airfoils may be output by such methods.

The rather straightforward simplicity of empirical direct-design methods and the time-effectiveness of numerical inverse-design methods can be combined to a certain extent to form a third category of design methods. Optimization methods, which utilize gradient or feasible direction approaches, and the streamline-curvature method fall in this class.

3.4 STREAMLINE-CURVATURE METHOD

3.4.1 Introduction

A modified streamline-curvature method for recontouring existing airfoils has been implemented on the mainframe computer (Honeywell

series 60; level 66) at KU. The original method of Barger and Brooks (see Reference 24) relates a desired increment in local velocity to an increment in the local curvature of the airfoil:

$$\Delta(d^2z/dx^2) = C(d^2z/dx^2)\Delta U/U$$

$$C \approx 10(1-M_\infty^2)$$

where: U is the local potential flow velocity

d^2z/dx^2 is the original local curvature

C is an empirical constant (usually a function of M , as indicated above, or local curvature) which may be adjusted to speed convergence towards the target pressure distribution. Usually, only one adjustment is required. The new airfoil is obtained by integrating the new curvature using initial boundary conditions dz/dx and z/c at the point where this new curvature distribution starts to deviate from the original curvature distribution. The upper and lower surfaces are separately integrated from their respective points of deviation to the trailing edge. Since the trailing-edge location will be different, the ordinates are linearly adjusted to recover the original trailing edge location without changing the curvature.

The achievability of any particular pressure distribution is not guaranteed, but results are usually significantly closer to the target distribution than the starting airfoil, provided the leading-edge region (to about 2% chord) does not require modification.

3.4.2 Airfoil Modification Procedure

The present airfoil modification procedure is outlined below and in Figure 3.2.

1. Obtain original pressure distribution and curvature distribution from the North Carolina State code.
2. Compare with target pressure distribution. If pressure distribution is desirable, then analyze off-design conditions (using Eppler, NCS or TRANSEP).
3. If pressure distribution is undesirable, then recontour the airfoil using the modified streamline-curvature method of Section 3.3.3 discussed below.
4. Set trailing-edge location and thickness by adding a line segment to the upper and/or lower surface ordinates (see Figure 3.3). The segments are constructed to produce the desired trailing-edge location and thickness without changing the ordinates at the "points of rotation" (which are usually near the leading edge). Smooth the region near the points of rotation if required. Usually, smoothing is unnecessary.
5. Return to step one.

3.4.3 Modification to the Original Streamline Curvature Method

The original streamline-curvature method (Reference 24) did not change the curvature when the old curvature was near zero (e.g., on aft upper surface of the MS(1)-0317; see Figure 3.4). Also, it pushed the curvature towards zero when attempting to reduce velocity regardless of the sign (+ or -) of the old curvature (see Figure 3.4). As a result,

the original streamline-curvature method was unable to obtain a concave pressure recovery on the upper surface of the MS(1)-0317 because it could not generate positive curvature on the aft upper surface. To enable the method to correctly change the curvature of the aft-chord region, the proportionality of the new curvature to the old was replaced by an increment to the old curvature. The modified streamline-curvature method is:

Upper surface:

$$\Delta(d^2x/dx^2) = C(d^2z/dx^2)\Delta U/U \quad \text{for } d^2z/dx^2 < -0.5$$

$$\Delta(d^2z/dx^2) = C(-0.5)\Delta U/U \quad \text{for } d^2z/dx^2 > -0.5$$

Lower surface:

$$\Delta(d^2z/dx^2) = C(0.5)\Delta U/U \quad \text{for } d^2z/dx^2 < -0.5$$

$$\Delta(d^2z/dx^2) = C(d^2z/dx^2)\Delta U/U \quad \text{for } d^2z/dx^2 > -0.5$$

This modified method was able to generate positive curvature and thereby obtain a concave pressure recovery on the aft upper surface of airfoil 26 (see Figure 3.5).

3.4.4 Application of Streamline-Curvature Method

An example of an airfoil modification is shown in Figure 3.5. Small modifications ($\Delta C_p < \sim .05$) may be achieved fairly accurately with only one or two iterations. Large modifications may require 5 or more iterations. For this reason, the inexpensive inviscid pressure distribution from the North Carolina State code (run time approx. 0.5 min. on Honeywell 60/66) is used if many intermediate runs of the streamline-

curvature method are anticipated. For small modifications, the more accurate viscous pressure distribution (run time approx. 2.4 min.) is used. One iteration of the modification procedure described above requires about 15 minutes once the target pressure distribution has been created.

3.4.5 Disadvantages of the Streamline-Curvature Method

The modified streamline-curvature method has produced satisfactory results at the FRL as long as the magnitude of the curvature is less than about 30. Near the leading edge, however, the curvature is generally much greater and changing too rapidly to allow accurate integration. Also, the assumptions made in arriving at the streamline-curvature method are invalid near the leading edge (see Reference 24). Therefore, the streamline-curvature method cannot be used to modify the leading edge of an airfoil. Modifications to the leading edge are made by "splicing" the scaled leading edge of an existing airfoil with a desired fore-chord pressure distribution to the original airfoil. If a kink occurs, it is smoothed out with an IMSL smoothing subroutine (see Reference 25). Another method of modifying the leading edge was used successfully. Instead of inputting the actual desired target distribution, a low-pressure spike was input near the leading edge. These trial-and-error procedures were successfully used to eliminate lower surface spikes (see Figure 3.4).

Another potential disadvantage of the streamline-curvature method is that there is no guarantee of producing a physically realizable airfoil (i.e., the upper and lower surfaces may cross). This did not prove to be a problem with the airfoils modified at the FRL.

3.4.6 Advantages of the Streamline-Curvature Method

The streamline-curvature method possesses several advantages over other airfoil design methods (see Section 3.2 for an overview of design methods). First, it is very simple to program and very inexpensive to use (the cost of an iteration is essentially the cost of obtaining the pressure distribution by the NCS code). Second, the user has a physical grasp on what the method does (because a curvature increase is equivalent to a velocity increase). Third, the method is applicable to a wide range of flight conditions including supercritical flows with shock waves (see Reference 16). However, in this case a code capable of analyzing a supercritical flow field must be used.

4.0 AIRFOIL ANALYSIS CODES USED

4.1 INTRODUCTION

This chapter presents an introduction and a discussion of the computer programs used in this study to determine the potential-flow and boundary-layer development about airfoils. The Eppler analysis code, the North Carolina State code and the TRANSEP code are discussed.

4.2 EPPLER CODE

4.2.1 Introduction

The Eppler code (see Reference 21) is a two-dimensional incompressible flow code which may be used either in an analysis or design mode. The analysis mode uses a panel method to calculate the potential flow about an airfoil. Boundary-layer characteristics are calculated, but no interaction with the potential-flow field is included in the version used at the KU-FRL. The design mode (see Section 3.2) uses a conformal mapping method to design airfoils with prescribed velocity-distribution characteristics.

4.2.2 Program Capabilities: Analysis Mode

The potential-flow airfoil analysis method uses curved panels with distributed surface vorticities. The geometry of the panels is determined by a spline fit of the airfoil coordinates, with the end points of the panels being the input airfoil coordinates themselves. The program also features a flapping routine, which will be discussed below.

An integral method is used for the analysis of the boundary layer. The displacement, momentum, and energy thicknesses of the boundary layer are calculated. These factors are then used to predict boundary-layer transition, short or long bubble formation, turbulent separation, and viscous drag.

4.2.3 Boundary-Layer Calculations

The laminar boundary layer is calculated under the assumption of Hartree boundary-layer profiles (Reference 26). The turbulent boundary layer is calculated using the slightly modified empirical expressions of Weighardt, Ludwig-Tillmann, and Rotta (Reference 27). Turbulent separation is assumed to occur when $H_{32} = 1.46$.

4.2.4 Transition Criteria in Eppler Code

The Eppler code utilizes three transition criteria: 1) natural transition, 2) transition at the point of laminar separation, and 3) fixed transition. It is thought that the transition location in flight will occur somewhere between the predictions of natural transition and laminar separation depending on the shape of the pressure distribution. Natural transition is assumed to occur if:

$$\ln R_{\theta} > 18.4H_{32} - 21.74 - 0.36r$$

where

R_θ = momentum thickness Reynolds number

H_{32} = shape factor

r = roughness factor (0 for smooth wings with no freestream turbulence); see Reference 21

The Eppler code predicts laminar separation when $H_{32} = 1.51509$. If the code predicts laminar separation, it checks to whether a long or short bubble has been formed based on the behavior of the shape factor H_{32} . The code does not model the bubbles. It gives a warning if a long bubble is predicted, and switches to a turbulent boundary layer calculation.

4.2.5 Calculation of Section Coefficients

The Eppler code uses the Squire-Young formula to obtain the drag coefficient. If turbulent separation of the boundary layer is predicted, an empirically determined penalty is added to the drag coefficient. The viscous effect on lift and pitching moment is empirically modeled as follows. The potential-flow zero-lift angle is calculated. From this point, the lift-curve slope is assumed to be equal to 2π (i.e. the potential-flow thickness effect is assumed to be cancelled by the viscous effect of the boundary layer). The lift coefficient is empirically decreased if turbulent separation is predicted. In this manner, the Eppler code will generate a lift curve which appears realistic for trailing-edge stalling airfoils.

4.2.6 Flapping Routine

The shape of an airfoil analyzed by the panel method can be altered to represent the deflection of a plain flap. Since panel methods tend to be very sensitive to surface discontinuities, an arc is smoothed-in between the flap and the forward portion of the airfoil (see Figure 4.1). The code allows the user to select the hinge-point location, flap deflection (positive or negative), and flap size.

4.2.7 Advantages and Disadvantages of Eppler Code

Figure 4.2 compares wind-tunnel and calculated aerodynamic coefficients for the MS(1)-0317 airfoil (Reference 28). It shows that the greatest discrepancy is in the prediction of the pitching-moment coefficient. The Eppler code over-predicts the pitching moment coefficient by about 30 percent in the $c_{l_{\text{design}}}$ -range. This occurs because the code is non-iterative, i.e., there is no interaction between the potential-flow field and the boundary layer. As a result, the method does not predict the decambering effect caused by the relatively thick turbulent boundary layer over the aft-chord region. The lift-curve slope is underpredicted. Evidently, the potential-flow thickness effect is greater than the viscous effect and so the lift-curve slope is actually greater than 2π for the MS(1)-0317. Eppler also underpredicts $c_{l_{\text{max}}}$ and over-predicts c_d slightly in this case.

The Eppler code is easy to operate and relatively inexpensive to use. (A complete airfoil drag polar can be calculated for about \$10.00; run-time on Honeywell 60/66 is approximately 2.3 min.) The code is

applicable for a wide range of Reynolds numbers. It has been successfully applied at Reynolds numbers from 2.0×10^4 to 1.0×10^8 (see Reference 29).

The Eppler code used at FRL is not valid for compressible flow ($M_\infty > 0.4$). However, versions of the Eppler code presently at NASA Langley incorporate a viscous correction, a compressibility correction, and have the capability of analyzing unslotted Fowler type flaps.

4.3 NORTH CAROLINA STATE CODE

4.3.1 Introduction

The North Carolina State (NCS) computer code was obtained by K.U. in 1975 via North Carolina State via a NASA-Langley/Lockheed-Georgia contract. (See Reference 30 for the original NASA/Lockheed report). The code predicts compressible aerodynamic characteristics of two-dimensional sections at subcritical Mach numbers. It also includes weak viscous interaction by adding the boundary-layer displacement thickness to the original airfoil and recalculating the pressure distribution. (The NCS code iterates four times.) The original NASA/Lockheed program could analyze multi-element airfoils, but the North Carolina State version analyzes single airfoils only.

4.3.2 Program Capabilities

The program calculates the subsonic potential flow about an airfoil which is modeled by a closed polygon with distributed vorticity. Compressibility is modeled by the Kármán-Tsien relation. Next, the

integral boundary layer characteristics (e.g. displacement thickness, momentum thickness) corresponding to the calculated pressure distribution are determined. The displacement thickness of the boundary layer is then added to the original airfoil and the pressure distribution of this "equivalent" airfoil is calculated. The code performs this iteration four times in the viscid mode. It then calculates lift, drag, and pitching moment coefficients by integrating the pressure and skin-friction forces which act on the airfoil. The Squire-Young drag prediction is also calculated at K.U. using boundary layer information provided by the program. The compressible Squire-Young formula (in the absence of shock waves) is (see References 31 and 32):

$$c_d = 2 \frac{\rho_{te}}{\rho_{\infty}} \frac{\theta}{c} \left(\frac{U_{te}}{U_{\infty}} \right) \frac{5 + H_{12,te}^*}{2}$$

where $H_{12}^* = H_{12}$ for $H_{12} < 2.5$
 $H_{12}^* = 2.5$ for $H_{12} > 2.5$

c_d is the drag coefficient of one surface

ρ is density

θ is the momentum thickness of the boundary layer

H_{12} is a shape factor

subscripts:

te indicates trailing-edge value

The formula is applied separately to the upper and lower surfaces. The upper and lower surface drag coefficients are then added. The Squire-Young method provides more reasonable drag prediction than the integrated drag prediction of the original code.

4.3.3 Transition Criteria

Three criteria may be used to determine the location of boundary-layer transition from laminar to turbulent flow: free transition (Granville correlation), transition at the indicated point of laminar separation (this option was added to the NCS code at KU), or fixed transition. Flight-test results for a propeller-driven aircraft (King Cobra) with smooth wings flying at chord Reynolds numbers between ten and fifteen million (Reference 8) indicate that the laminar separation criterion provides the most accurate location of transition in flight (see 4.2.4). Wind-tunnel measurements correlate more closely with the natural transition criterion. The actual location of transition in flight will be located somewhere between the values predicted by these two criteria. At any rate, the natural transition criterion is conservative for smooth wings. For a rough wing (characterized by rivets, steps, gaps, insect remains, ice), fixed transition near the leading edge is most realistic.

4.3.4 Boundary-Layer Calculations

The laminar boundary layer is calculated using the basic approach of Cohen and Reshotko. Natural transition is predicted using the Granville correlation. The code indicates short or long hubble

formation at the point of laminar separation by an empirical correlation which contains the inviscid velocity gradient and the momentum-thickness Reynolds number of the boundary-layer. Reattachment of the turbulent boundary layer is assumed in either case so results are not valid if long bubble formation is indicated.

Two turbulent boundary-layer calculation methods are included in the program. The first is an approximate method developed by Goradia along the lines of the Truckenbrodt boundary-layer equations which is used in the initial iterative calculations. The second and more accurate model reflects the methods of Nash and is used to portray the boundary layer in the final viscous solution. Separation of the turbulent boundary layer is predicted using the Nash separation parameter (Reference 33).

4.3.5 Limitations of the North Carolina State Code

Figure 4.3 compares wind-tunnel and calculated coefficients for the NACA 66-418 (see Reference 13) and the NLF-0416 (Reference 12) airfoils. Results are fairly accurate (within a 10% deviation range) as long as separation does not occur before about 95% chord. The predicted drag coefficients of the NACA 66-418 airfoil are too low when more separation is predicted. Also, the lift coefficients are too high. Highly separated flows require some form of separation modeling to obtain reliable results. The empirical method used in the Eppler code (see Section 4.2) for reducing the lift coefficient when turbulent separation is predicted was found to improve results as shown in Figure 4.3, but the code underpredicts the amount of separation if more than

about five per cent separation is present. As a result, the modification will not yield a $c_{l_{\max}}$ prediction as realistic as that of the Eppler code (see Figure 4.4).

The North Carolina State code will not accurately analyze supercritical cases (there is no shock-wave modeling).

One run costs \$7-10 (approx. 2.4 min. run time on Honeywell 60/66) or \$2-3 (approx. 0.5 min. run time) in the inviscid (non-iterative) mode. Figure 4.5 compares the viscous and inviscid pressure distributions for airfoil 40 (see Chapter 6).

4.4 TRANSEP CODE

4.4.1 Introduction

The TRANSEP code (Reference 23) provides a method for analyzing the highly separated flow about an airfoil in low-speed high-lift flight conditions. This code is an extension of the direct/inverse TRANDES code. The TRANDES code provides a design and analysis method for airfoils in transonic flow conditions including only the effects of weak viscous interaction (References 34, 35 and 36). The design method of TRANDES has been discussed briefly in Section 3.2. Of paramount importance to the current NLF effort is the addition of a laminar boundary layer and a transition model to the original TRANDES code.

4.4.2 Characteristics of the TRANSEP Analysis Code

4.4.2.1 Inviscid Potential Flow

The TRANSEP analysis code is a transonic code that employs a finite-difference solution to the full inviscid perturbation potential-flow equation for an airfoil in a stretched Cartesian coordinate system exposed to a uniform flowfield. The coordinate stretching is such, that the infinite physical plane is mapped to a finite (orthogonal) computational space.

The code iterates to a preset level of accuracy (imposed on the circulation around the airfoil) through a specific number of refinements of the Cartesian grid. The obtained difference equations are solved by column relaxation, which is done on successively finer grids to speed convergence. First, the equations are solved on the very coarse grid (13x7). This solution is then interpolated and used as an initial condition for the solution on the coarse grid (25x13). This procedure may be repeated twice to obtain solutions on the medium grid (49x25) and also fine grid (97x49). The fine grid has 130 points on the airfoil. However, as indicated in Reference 32, the medium grid will yield accurate results for subcritical cases (i.e., no local supersonic flow is present).

4.4.2.2 Boundary-Layer Theory

The TRANSEP code includes a laminar/turbulent boundary-layer analysis. The laminar boundary layer is calculated using a compressible integral Thwaites method, based upon a version developed by Grumman Aerospace Corporation. The transition point is determined from a

Granville-type correlation based on the pressure-gradient history and the difference between the local momentum-thickness Reynolds number Re_θ and its value at the laminar instability point. When laminar separation is predicted (predicted by Thwaites method), the local Re_θ is compared to an empirical correlation in order to determine whether the laminar bubble is long or short.

If the bubble is short its length is assumed to be one horizontal grid width and the turbulent-flow computation is initiated at the next grid point. When a long bubble is found a warning message is printed. The turbulent boundary layer is computed using the well-known Nash-MacDonald method (Reference 32). In this integral method, separation of the turbulent boundary layer is assumed when

$$-\frac{\theta}{U} \frac{dU}{ds} > 0.0040$$

The displacement effect of the boundary layer is included for weak interaction. When separation is predicted forward of $0.95c$, this weak interaction becomes inadequate and it becomes necessary to model the strongly interacting separated zone. Extensive turbulent separation is modeled in TRANSEP by assuming a constant pressure level over the separated part of the airfoil. This massive separation model does not produce reasonable results at Mach numbers higher than 0.30. The restriction to lower Mach numbers means that this code cannot be used to evaluate the effect of trailing-edge separation on the pressure distribution and the location of a shock in medium and high-speed conditions. The massive separation model is valid only for low-speed high-lifting conditions.

4.4.3 Problems in Operating TRANSEP

A brief discussion of problems encountered in operating TRANSEP is presented for both low-speed application as well as application in the Mach range for design conditions and higher speeds.

4.4.3.1. Airfoils with Thin Leading Edge

NLF airfoils showing a considerable amount of laminar flow are characterized by a relatively small l.e. radius. Due to the fact that TRANSEP uses a fixed orthogonal grid to obtain a finite-difference solution, the actual number of grid points near and on this thin leading edge is relatively small. The development of the (laminar) boundary layer and the possible presence of laminar separation in high-lift conditions depends very much on the growth over the initial part of the airfoil. Carlson and others are currently trying to adjust the grid embedding around the leading edge to improve high-lift predictions for airfoils with small l.e. radii. TRANSEP prediction of the high-lift behavior of the NACA 65-213 airfoil is poor (Reference 34). Since the airfoils presented in Chapter 6 have comparable l.e. radii TRANSEP has not been used to evaluate $c_{l_{\max}}$ for the airfoils described in this report.

4.4.3.2 **M = 0.60 and Above**

As mentioned already in Section 4.2.2 the massive separation model is only realistic for $M < 0.3$. It has also been found that the empirical boundary-layer correction (controlled by input parameter ITEUPC) which is provided in case of extensive trailing-edge separation

leads to a significant decrease in predicted c_l at the design Mach number. The predicted point of turbulent separation moves forward when this correction is used. Also, separation is predicted in the design case when no separation is expected. Therefore, all TRANSEP applications in this report have been run with ITEUPC=0.

If a shockwave is predicted, two facts must be considered. First, the estimation of shockwave drag is uncertain in that only the relative increase in wavedrag is correctly predicted. The simple correction suggested in Reference 34 to adjust the absolute value of $c_{d_{wave}}$ is probably not correct. Second, shockwave/boundary layer interaction is not modeled, apart from the strong local pressure rise through the shock. In this report the simple empirical criterion of $M_{shock} < 1.30$ for no shock-induced separation is applied.

4.4.4 Choice of Grid Size and Convergence Parameter

Unless stronger shockwaves ($M_{shock} > 1.30$) are present, the c_p -distribution (and c_l and $c_{m_{.25c}}$) is hardly affected by using the medium grid instead of the fine grid (see 4.4.2.1). However, prediction of friction drag c_{d_f} is strongly affected by the choice of the grid. Therefore, for each different airfoil for subcritical conditions a comparison must be made between medium and fine grid. Choice of grid size affects the total computing time for each run.

Two convergence criteria must be set by the user in the application of TRANSEP. First, for strong supercritical conditions control parameters (ω and EPPS) must be adjusted to ensure numerical stability. For subcritical cases the default values were used. In supercritical conditions $\omega = 1.4$ and EPPS = 1.0 were used to obtain

stability. Second, a convergence control value CONV must be assigned that will stop the iterative solution procedure. TRANSEP stops the iterations when the maximum change in the perturbation potential is less than CONV. Figure 4.6 compares the influence of reducing the value of CONV from its default value of 1.0×10^{-5} to 1.0×10^{-4} for $M=0.70$. This change reduces run times by more than 60%. It can be seen that $CONV=1.0 \times 10^{-4}$ predicts coefficients c_l , c_{d_f} and $c_{m,25c}$ sufficiently accurate for the purpose of this study.

Run time on Honeywell 60/66 for one subcritical condition is about 2.5 min (\$8.50 run cost). For a supercritical condition with fine grid and reduced relaxation typical run time is 3.5 min.

4.4.5 Comparison of TRANSEP and NCS Codes

Figure 4.7 and 4.8 compare pressure distributions predicted by TRANSEP and NCS code (see 4.3). Although c_l is not in exact agreement (particular c_l 's must be found by trial-and-error in both codes) some interesting conclusions can be inferred from these graphs. Figure 4.7 shows the critical condition ($c_p = c_p^*$); NCS predicts the minimum pressure 0.05c ahead of TRANSEP. This forwardly prediction is typical of subcritical codes. For the subcritical condition, Figure 4.8 shows a similar trend, resulting in a steeper initial gradient. From Figure 4.7 it can be observed that $c_{p_{T,E}}$ is 0.06 lower in comparison to TRANSEP. Moreover, TRANSEP predicts upper surface separation at $x=0.96c$, in contrast to NCS, which predicts no separation.

Also, in comparing results, it has been found that TRANSEP typically predicts viscous drag to be 5 counts (0.0005) under the (Squire-Young) prediction by NCS (see Figure 4.0). Figure 4.7

illustrates that in this condition the grid size of TRANSEP is too coarse for a realistic c_{df} . The TRANSEP code calculates into the wake up to $x=8c$; this explains the continuation of the curve further than $x/c=1.0$.

4.5 SUMMARY OF AIRFOIL ANALYSIS CODES

According to a division of the possible flow conditions about airfoils in this report, three analysis codes have been used:

- Eppler analysis code to establish incompressible characteristics (in medium and high-lift conditions);
- NCS code to establish the compressible subcritical flow in the design condition;
- TRANSEP code to establish the subcritical flow in the Mach number design range and the development of supercritical flow in off-design conditions.

5.0 FACTORS AFFECTING CHOICE OF TARGET PRESSURE DISTRIBUTION

5.1 INTRODUCTION

Several objectives were identified for the airfoils to be used for a natural laminar flow wing. The primary objective was to develop an airfoil which would have low drag by obtaining natural laminar flow over about 60-percent of both surfaces. Secondary objectives included: 1) the maximum lift coefficient $c_{l_{\max}}$ should be comparable to that of the MS(1)-0317 and should not decrease with transition fixed near the leading edge; 2) the pitching-moment coefficient c_m should not be more negative than -0.10 at the cruise lift coefficient to reduce trim drag (This requirement may not be necessary for three-surface aircraft); and 3) the airfoil should be about 17-percent thick as is the MS(1)-0317.

Airfoil development primarily involves the selection of a desired pressure distribution. Once this is done, the shape can be derived by a design procedure (see Chapter 3). To develop a target pressure distribution, it is necessary to understand the characteristics of boundary layers on wings, including: 1) the transition mechanisms which act on a (swept) wing and the effect the pressure distribution has on these transition mechanisms, 2) the interaction between these transition mechanisms and 3) the effect the two-dimensional pressure distribution has on the development of the turbulent boundary layer.

5.2 TRANSITION MECHANISMS

There are four basic mechanisms which can cause transition on a swept wing. They are: 1) amplification of Tollmien-Schlichting (T-S) disturbances; 2) amplification of crossflow (C-F) disturbances; 3) instability of Taylor-Goertler vortices; and 4) leading-edge attachment line contamination.

5.2.1 Tollmien-Schlichting Disturbances

Tollmien-Schlichting disturbances propagate in a direction nearly parallel to the local freestream direction outside of the boundary layer. In a favorable pressure gradient, the amplification of T-S disturbances is relatively small and of the viscid type. However, in an adverse pressure gradient the boundary-layer profile will develop an inflection point. Amplification of disturbances for a velocity profile which contains an inflection point is primarily of the inviscid type (i.e. the amplification would be expected even in inviscid flow) and is usually greater than the amplification of viscid-type disturbances. Therefore, a favorable pressure gradient will diminish the magnitude of T-S disturbances. In general, (Reference 26) T-S stability depends on the freestream Reynolds number and the frequency of the disturbance. In 6.4.2.4, more attention will be given to the analysis of this type of boundary-layer stability.

5.2.2 Crossflow Disturbances

Crossflow in the wing boundary layer results from the spanwise pressure gradient on a swept wing which is caused by the combination of sweep angle and the chordwise pressure gradient. Figure 5.1 shows how the boundary layer responds to this spanwise pressure gradient which is present on a swept wing. A crossflow velocity profile always contains an inflection point and is therefore inherently unstable. The development of C-F disturbances may be minimized for a particular wing by reducing the magnitude of the mid chord pressure gradient (see Figure 5.2) and the wing sweep angle.

5.2.3 Taylor-Goertler Vortices

Taylor-Goertler vortices can occur in laminar boundary layers over concave surfaces. They are not of concern for natural laminar flow airfoils in this report because these NLF airfoils are convex over the region of anticipated laminar flow.

5.2.4 Attachment-Line Contamination

Leading-edge attachment-line contamination refers to the spanwise spread of turbulence along the wing leading-edge attachment (stagnation) line. The turbulence comes from the turbulent fuselage or nacelle boundary layer and from roughness on the leading edge (e.g. insects, ice). To reduce the chance of attachment-line contamination, the leading edge sweep-back angle should be reduced. Also, the initial

pressure drop should be steep (i.e. the nose radius of the airfoil should be small) to reduce the thickness and growth of the attachment-line boundary layer.

5.3 INTERACTION BETWEEN C-F AND T-S DISTURBANCES

A Boeing/NASA-Langley project (see Reference 17) examined the interaction of T-S and C-F type disturbances using the variable sweep TACT F-111. The aircraft was flown (from Dryden Flight Research Center) with an NLF glove over the wing. The flight tests did show significant amounts of natural laminar flow over the wing glove. Analysis of data obtained from these flight tests has provided a preliminary assessment of T-S/C-F interaction for Mach numbers ranging from 0.80 to 0.85, Chord Reynolds numbers from 23 to 29 million, and sweep angles from 9 to 25 degrees.

Boeing and NASA Langley performed another laminar flow study (see Reference 34) which provided useful information. They analytically researched the effects of pressure gradient, Reynolds number, and sweep angle on predicted boundary-layer transition. The Mach number normal to the leading edge was fixed at 0.78 for all cases which were analyzed. The amplification of disturbances (T-S and C-F) in the boundary layer was calculated at sweep angles of 15, 20, and 25 degrees and Reynolds numbers of 15, 30, and 45 million. The analyses were performed both with and without leading-edge suction so the results are applicable for NLF and laminar flow control wings. Although this study was carried out for higher Reynolds numbers, Mach numbers, and sweep angles than those

focused on in this report, figures 5.3, 5.4, and 5.5 reveal that lower Reynolds numbers and sweep angles tend to increase the laminar run. On the other hand, it is also known that compressibility has a stabilizing effect on the laminar boundary layer. Therefore, although this study can not be directly applied to the design of NLF wings for regional aircraft, it does predict certain trends which are useful. The following trends were found in the above-mentioned studies to be favorable to maintain natural laminar flow on moderate and highly swept wings: 1) a steep favorable mid-chord pressure gradient on the upper surface; 2) a steep initial pressure drop; 3) lower Reynolds numbers; and 4) lower sweep angles. Conversely, on the lower surface a rather flat mid-chord pressure gradient is more favorable, because the C-F disturbances are more critical than the T-S disturbances on the lower surface of highly swept wings.

It can be inferred from these trends that the choice of pressure distribution (see Figure 5.2) in the leading-edge region must negotiate the growth of both C-F and T-S instabilities. More research is needed to minimize C-F and T-S disturbance growth and interaction for NLF wings of regional aircraft.

5.4 PRESSURE RECOVERY

As noted above, the pressure gradient of an NLF airfoil should be slightly favorable up to the desired transition point. After the point of minimum pressure, the pressure gradient becomes unfavorable and the boundary layer soon becomes turbulent. The unfavorable pressure gradient increases the rate of growth of the turbulent boundary layer

thereby increasing drag. Therefore, the design of the pressure recovery is critical to obtain a practical NLF airfoil, particularly when laminar runs of 70% or more are involved.

To recover the most pressure over the least distance, the turbulent boundary layer should be kept on the verge of separation throughout the pressure recovery (Stratford recovery; Reference 35). A genuine Stratford recovery is not suited for G.A. use, however, because the turbulent boundary layer is likely to separate completely at off-design conditions. Nevertheless, a milder concave pressure recovery which resembles a Stratford recovery will delay turbulent separation as compared to a linear pressure recovery typical of the NACA-6 series airfoils (Figure 5.6). The turbulent boundary layer is able to overcome a steeper pressure gradient in the initial recovery area. Towards the end of the recovery region, a smaller adverse pressure gradient is imposed on the boundary layer by a concave recovery in comparison to a linear recovery.

If the pressure recovery is initially very steep, an "instability ramp" may be desirable (particularly at lower Reynolds numbers) to avoid the formation of a laminar short bubble at the beginning of the pressure recovery. The instability ramp is a region which has a neutral or mildly unfavorable pressure gradient prior to the steep concave portion of the pressure recovery, thus promoting transition of the laminar boundary layer (see Reference 18 and 36).

5.5 SAMPLE NLF TARGET PRESSURE DISTRIBUTION

Figure 5.7 illustrates the characteristics of a typical natural laminar flow airfoil pressure distribution. It has a favorable pressure gradient to about 60% chord and a concave pressure recovery. The actual pressure distributions used to derive NLF airfoils in the streamline-curvature method will be presented in Chapter 6 together with the obtained airfoil shapes.

6.0 AIRFOIL DEVELOPMENT AND ANALYSIS

6.1 INTRODUCTION

This chapter describes the development and analysis of medium-speed NLF airfoils at the KU-FRL during 1983-84. The modified streamline-curvature method discussed in Chapter 2 was used to obtain these airfoils. Leading edge modifications were made by "splicing" scaled leading edges of existing airfoils to intermediate airfoils. Estimated aerodynamic characteristics of the airfoils for several flight conditions are also presented and discussed.

6.2 CHOICE OF AIRFOIL TO BE MODIFIED

The NASA MS(1)-0317 airfoil (Figure 6.1 and Reference 28) was chosen to be the first starting point for the modification procedure. The airfoil is a 17-percent thick medium-speed airfoil designed for a cruise lift coefficient of 0.30, a Reynolds number of 14.0×10^6 , and a Mach number of 0.68. This airfoil was chosen in preference to an NACA 6-series airfoil because of its higher $c_{l_{max}}$ and because it was designed to fly at a Mach number comparable to the expected cruise Mach number of new regional aircraft ($M \approx 0.6$). Also, the Eppler code predicts that the MS(1)-3017 will achieve as much as 50% laminar flow on the upper surface for $c_l < 0.1$ and on the lower surface for $c_l > 0.6$ (Figure 6.2). It was hoped that the streamline-curvature method could create an airfoil which would obtain 50-60% laminar flow on both surfaces in the cruise flight condition ($c_l \approx 0.3$ to 0.5). In Chapter 1, the cruise flight condition was chosen to be as follows

Table 6.1 Cruise Flight Condition

$$\begin{aligned}M_{\text{des}} &= 0.60 \\c_{l_{\text{des}}} &= 0.30 \text{ to } 0.50 \\Re &= 8.9 \times 10^6\end{aligned}$$

6.3 MS(1)-0317 PRESSURE DISTRIBUTION AND INITIAL TARGET PRESSURE DISTRIBUTION

Figure 6.3 shows the MS(1)-0317 pressure distribution (as calculated by the NCS code) for the above flight condition. It also shows the initial target pressure distribution. The target pressure distribution has the following characteristics:

1. Both surfaces have a favorable pressure gradient to 50% chord followed by a region of constant pressure which extends to 60% chord.
2. Both surfaces have concave pressure recoveries which are similar in shape to Stratford recoveries, but much milder.
3. The lift coefficient of the target pressure distribution is about the same as that of the MS(1)-0317. Therefore, the camber of the modified airfoil should be about the same as that of the MS(1)-0317.
4. The difference in pressure coefficients of the MS(1)-0317 and the target pressure distributions at any point is less than 0.2.

6.4 PRESENTATION AND ANALYSIS OF K.U. AIRFOILS

6.4.1 Introduction

The estimated aerodynamic characteristics of five medium-speed NLF airfoils will be presented in this section. For each airfoil the development process is briefly discussed. Incompressible characteristics as predicted by the Eppler code, subcritical compressible characteristics as predicted by the NCS code, and supercritical characteristics as predicted by the TRANSEP code are also shown and discussed. The growth of T-S disturbances as calculated by the SALLY code is discussed for airfoil 26A. Airfoil coordinates and nose radii are given in Appendix I.

6.4.2 Airfoil 26A

6.4.2.1. Development

Airfoil 26A (Figure 6.4) was the first modification which closely resembled the target pressure distribution of Figure 6.3. The airfoil is 17.4% thick and has a trailing-edge thickness of .0075c. Figure 6.5 compares the curvature (ds^2_z/dx^2) distribution of airfoil 26A to that of the MS(1)-0317. It also shows the pressure distributions at equal flight conditions.

6.4.2.2. Incompressible Characteristics (from Eppler code)

Comparison of 26A to the MS(1)-0317

Figures 6.6, 6.7, and 6.8 show the aerodynamic characteristics of airfoil 26A as predicted by the Eppler code using the free transition criterion, transition at the point of laminar separation, and transition fixed at five percent chord, respectively. For the free transition criterion (Figure 6.6), the $c_{d_{min}}$ of 48 counts for airfoil 26A is about 12 counts lower than the $c_{d_{min}}$ of the MS(1)-3017. However, Figure 6.7 shows that the drag of airfoil 26A is similar to that of the MS(1)-0317 when the laminar separation criterion is used. The only major improvement is an extension of the low drag "bucket" from $c_l \approx 0.7$ for the MS(1)-0317 to $c_l \approx 0.78$ for airfoil 26A. The large discrepancy between drag polars when these different transition criteria are used indicates that free transition occurs well ahead of the point of laminar separation. Figures 6.9 and 6.10 compare the predicted transition points as a function of c_l . If transition is fixed at 5% chord, the minimum drag coefficient of 26A increases to 93 counts (Figure 6.8).

Another major difference between the airfoils is the Eppler-predicted reduction of $c_{l_{max}}$ from 1.96 to 1.76 when the laminar separation criterion is used. The reduction of $c_{l_{max}}$ for 26A implies that the predicted point of turbulent separation moves forward faster for 26A than for the MS(1)-0317 (Figures 6.9 and 6.10). Notice that $c_{l_{max}}$ (and therefore the point of turbulent separation) of 26A is unaffected by fixing transition in this Eppler prediction.

Reynolds Number Effect

Figures 6.11 and 6.12 show the effect of Reynolds number on the predicted aerodynamic characteristics of 26A. As expected, drag is usually higher and $c_{l_{\max}}$ is lower at lower Reynolds numbers. Since the turbulent boundary layer is thicker at lower Reynolds numbers, it is more prone to separate (thereby reducing the Eppler-predicted $c_{l_{\max}}$) at lower Reynolds numbers. The location of free transition as predicted by the Eppler code is also affected by Reynolds number. As the Reynolds number increases, the thinner boundary layer becomes more sensitive to small disturbances. Therefore, the free transition point tends to move forward as the Reynolds number increases. As a result, the predicted drag using the free transition criteria may actually increase with an increase in Reynolds number (Figure 6.11). The predicted point of laminar separation is primarily determined by the pressure distribution and is not significantly affected by Reynolds number, unless Re is very small.

6.4.2.3. Subcritical Characteristics (NCS Code)

Comparison of Eppler and NCS Predictions

Figures 6.13 and 6.14 show the characteristics of airfoil 26A at $M = 0.2$ as predicted by the NCS code using the free transition criterion. The incompressible Eppler predictions are also shown in these figures. The NCS-predicted lift curve slope is higher than the Eppler-predicted value of $2\pi/\text{rad}$. The NCS- and Eppler-predicted drag

polars are noticeably different in comparison. The Eppler code tends to overpredict drag outside the low-drag bucket. NCS predicts a free transition $c_{d_{min}}$ of 40 counts. This is eight counts less than the Eppler prediction and is caused by differences in transition prediction. Figures 6.15 and 6.16 compare the predicted locations of free transition according to both codes. The NCS code predicts a wider drag bucket than the Eppler code when the laminar separation criterion is used (Figures 6.14 and 6.16). Notice the over-prediction of pitching moment by the Eppler code (see Section 4.2.7).

Effect of Finite Trailing-Edge Thickness

Three versions of airfoil 26A were examined: airfoil 26A with a trailing-edge thickness of $0.0075c$, 26B with a trailing-edge thickness of $0.00375c$ and 26C with a zero-thickness trailing edge. A nonzero trailing-edge thickness is necessary to make an economical flap structure possible. Also a nonzero trailing edge thickness should increase $c_{l_{max}}$ by delaying separation, since the pressure recovery may extend beyond the airfoil into the wake. Unfortunately, a large trailing-edge thickness also leads to substantial base (pressure) drag. These effects must be studied to determine the optimum trailing-edge thickness for practical applications.

Figures 6.17 and 6.18 show the NCS-predicted characteristics of the three versions of airfoil 26 at $M = 0.2$. The characteristics of these three versions are nearly identical. As expected, the lift curves of the thinner trailing-edge airfoils become nonlinear before the lift curves of the thicker trailing-edge airfoils bend over. This implies that $c_{l_{max}}$ will probably be greater for the thicker trailing-edge

airfoils. The difference in drag is virtually unnoticeable (less than two counts). However, the Squire-Young drag prediction method (Section 4.3.2) does not account for the effect of trailing-edge thickness, so the drag prediction does not include base drag. Experimental data (see Reference 37) indicate typical drag increments on the order of one to five counts for blunt trailing edge. No numerical methods are presently available to predict base and separation drag.

Effect of Reynolds and Mach Numbers (NCS code)

Figure 6.19 shows the effect of Reynolds number on airfoil 26B as predicted by the NCS code using the laminar separation criterion. Results are similar to the Eppler results discussed above.

Figure 6.20 shows the NCS-predicted effect of Mach number on airfoil 26A when the laminar separation criterion is used. Figure 6.21 shows the effect of Mach number on the pressure distribution and the predicted point of laminar separation for airfoil 26A. Figure 6.22 shows the effect of compressibility when the free transition criterion is used. The free transition point moves aft at Mach 0.6. Figure 6.21 shows that the mid chord gradient becomes less unfavorable. As expected, lift curve slope and pitching moment increase with Mach number.

Comparison of 26A to the MS(1)-0317

Figures 6.23 and 6.24 compare the cruise characteristics of the MS(1)-0317 and 26A with use of the free transition and laminar separation criteria, respectively. Both drag and pitching moment

coefficients of airfoil 26A are lower in magnitude than those of the MS(1)-0317. In the cruise range c_d is eight to ten counts lower.

6.4.2.4. SALLY Boundary-Layer Stability Analysis for Airfoil 26A

In order to assess the implication of a slightly favorable and also slightly adverse mid-chord pressure gradient on the development of T.S. waves, a SALLY stability analysis was performed for airfoil 26A by Mr. Cliff Obara at NASA Langley Research Center. The discussion of this analysis will be divided into two parts. First, the numerical procedure to arrive at the T-S. wave development will be summarized. Next, the specific results for airfoil 26A will be presented and commented on.

Description of Numerical Process

Figure 6.25 shows the calculation steps in this analysis. Most important input to the SALLY code (References 37 and 38) are the boundary-layer velocity profiles along the laminar run. These detailed data are provided by a two-dimensional differential Cebeci boundary-layer code (Reference 39). The pressure distribution over the airfoil, which is an input to the Cebeci code, has been calculated by MCARF (Multi-Component-Airfoil-Code), a NASA Langley update of the original Lockheed-Goradia code (Reference 30). By examining only the wave propagation in a streamwise direction, the three-dimensional SALLY code can be used to study two-dimensional T-S. amplifications. The SALLY code solves the Orr-Sommerfeld eigenvalue problem (see Reference 26) for different disturbance frequencies, which are to be imposed by the user. For each frequency SALLY indicates the growth of an amplifica-

tion factor $n = \ln A/A_0$; i.e., the logarithmic ratio of the amplitude A of a sinusoidal wave with this frequency at a particular chord station to the neutral amplitude A_0 of this wave.

Analysis

Two aspects are of primary interest in this analysis:

- a. The maximum amplification factor n_{\max} as a function of the wave frequencies will give a first insight into the achievability of NLF in flight for above-stated conditions.
- b. N_{\max} and the relative growth of n indicate the relative importance of different favorable and slightly adverse pressure gradients in the conditions presented in the table.

Three conditions of airfoil 26A have been analyzed: see Table 6.2.

Table 6.2 SALLY Analysis Airfoil 26A

Condition	c_l	M	Re	Figure
I	-.28	0.60	8.9×10^6	6.26-6.27 (design condition)
II	0.45	0.60	8.9×10^6	6.28-6.29
III	0.46	0.60	8.9×10^6	6.30-6.31

Condition I is represented in Figures 6.26 and 6.27. Over the upper surface n_{\max} is almost 10 for $f = 1000$ Hz at $x/c = 0.58$ (i.e., the location of laminar separation predicted by MCARF). Note the rapid growth of n after $x/c = 0.15$. The characteristics are similar for the lower surface in this design condition, n_{\max} occurring for $f = 4000$ Hz. Increasing the pressure gradient on the upper surface

to a (slightly) adverse gradient in condition II (Figure 6.28) leads to $n_{\max} = 14.89$ for $f = 4500$ Hz. Also a steep growth for almost all frequencies immediately after the local pressure peak at $x/c = 0.10$ must be noted. As expected, the rate of growth is reduced in the flat pressure zone after $x/c = 0.3$. Except for $f = 6000$ Hz, note the absence of stable regions in this condition, in contrast to the design condition. The effect of a favorable initial and mid-chord pressure gradient (see Figure 5.7) is evident by comparing Figure 6.27 and Figure 6.29. Note in Figure 6.29 the congruence of stable wave regions and local increase in the negative pressure gradient (compare with the design philosophy indicated in Reference 14).

Increasing c_l to 0.46 (condition III) makes these observations even more pronounced. Now $n_{\max} = 15.4$ for $f = 4500$ Hz (Figures 6.30 and 6.31).

Figure 6.32 summarizes the growth of T.S. waves for airfoil 26A. The most amplifying frequency is found in the region of 3500-5000 Hz. However, in the design case of all-favorable pressure gradients, amplification is greatest for disturbances in the 4500-6000 Hz range.

Conclusions

The correlation of the value of n_{\max} with the location of transition is empirical. The exactness of the predicted n-factors must be argued when high amplification rates are reached. The assumption of linearity and a sinusoidal disturbance character in the derivation of the Orr-Sommerfeld problem is no longer valid above a certain wave amplification. However, it has been found (References 40, 41, and recently References 42 and 43) that application of this linear stability

theory can give an indication of the location of transition of the laminar boundary layer by correlating experimentally found transition locations with the calculated local amplification factor n_{trans} . The amplification at transition depends primarily on the level of turbulence of the air encountering the airfoil. For wind-tunnel correlation, $n_{trans} = 10$, typically (References 40 and 41). For free flight conditions (in absence of significant sound levels) n_{trans} appears to be 15 and even higher (References 42 and 43).

Given this empirical correlation, it can be inferred from Figures 6.28 and 6.30 that in the presence of these moderate adverse pressure gradients, free flight transition will not occur before the onset of the steep pressure rise; i.e., the transition is of a laminar separation type. Also note that the prediction of transition at laminar separation by MCARF is consistent with the indicated level of n_{max} . In general, one has to be aware of the specific computational order (Figure 6.25), since the length of the laminar run indicated by CEBECI determines ultimately the maximum value of n to be reached by SALLY. It is required to assume transition to occur at the beginning of the recovery pressure rise in these stability considerations.

6.4.3 Airfoil 32

6.4.3.1 Development

A new target distribution (see Figure 6.33) was created in an attempt to further extend the low-drag bucket as predicted when the laminar separation criterion is applied. The target distribution is similar to airfoil 26's pressure distribution in shape, but the lift coefficient has been increased, and therefore the new airfoil should be more cambered. Airfoil 32 was the next airfoil to be analyzed. It is 17.0% thick. Figure 6.34 compares the contours of this airfoil and 26A. Note the reduction in nose radius (see Appendix I). Figures 6.35 and 6.36 compare the curvatures and resulting design pressure distributions of airfoils 26A and 32.

6.4.3.2 Incompressible Low-Speed Characteristics

Figures 6.37, 6.38, and 6.39 compare the aerodynamic characteristics of airfoil 32 to those of the MS(1)-0317 as calculated by the Eppler code. Airfoil 32's $c_{d_{min}}$ is higher than that of airfoil 26A (see Figure 6.6), but it is still nine counts less than $c_{d_{min}}$ of the MS(1)-0317 (using the natural transition criterion). A large extension of the drag bucket (from $c_l \approx 0.78$ for 26A to $c_l \approx 1.0$ for 32) is predicted by the Eppler code with use of laminar separation as the transition criterion (Figures 6.7 and 6.36). The $c_{l_{max}}$ as predicted by the Eppler code is 1.76, compared to 1.90 for airfoil MS(1)-0317. Figures 6.40, 6.41, and 6.42 show the effect of Reynolds number on the aerodynamic characteristics of airfoil 32. Figures 6.43 and 6.44

show the Eppler-predicted effect of a finite trailing-edge thickness on the aerodynamic characteristics of airfoil 32. The large change in c_m is unexpected.

6.4.3.3 Subcritical Characteristics (NCS)

Figures 6.45 and 6.46 compare the cruise performance of airfoil 32 and the MS(1)-0317 using the free transition and laminar separation criteria, respectively. The minimum drag coefficient is 12 counts lower, and it occurs at a higher lift coefficient ($c_l = 0.50$) for airfoil 32. The pitching moment coefficient of airfoil 32 is slightly more negative than that of the MS(1)-0317. Figure 6.47 shows the location of predicted transition and the favorable mid chord pressure gradient in the design condition.

6.4.3.4 Compressible Characteristics of Airfoil 32

This section presents some sub- and supercritical characteristics of airfoil 32 as determined by TRANSEP. Results are given for constant Mach number and constant angle of attack.

Constant Mach Number $M = 0.60$

Figure 6.48 gives the pressure distributions for several angles of attack. Flow over the upper surface becomes critical for $c_l = 0.78$ (see Figure 6.49). Figure 6.48 indicates that up to $c_l \approx 0.6$ the upper-surface pressure gradient is favorable. The adverse pressure gradient up to $c_l = 0.8$ is modest; i.e., laminar flow is likely to be available also for maneuvering at $M = 0.60$.

A comparison was given between NCS and TRANSEP in 4.4.4 (Figure 4.7). Due to the less steep gradient predicted by a subcritical NCS code, care should be taken in calculation of crossflow stability for compressible conditions when a subcritical code is used. Note that only the initial part of the upper-surface pressure recovery grows slightly steeper as α increases (Figure 6.50). The recovery after 0.70c is equal to that of the design condition.

Increasing Mach Number

Figure 6.51 presents estimated pressure distributions at $\alpha = -0.9^\circ$ for increasing Mach number. The flow is near critical for $M = 0.65$. Due to the compressibility of air, c_{ℓ} is fairly high at the highest indicated Mach number; i.e., to be expected only at a pull-up maneuver outside the cruise envelope.

A pronounced shock is apparent for $M = 0.70$. The local Mach number just ahead of this shock, M_{shock} is predicted to be 1.27. According to the criterion mentioned in 4.4.3.2, we conclude that no shock-induced separation occurs. In contrast, for $M = 0.75$, $M_{\text{shock}} = 1.52$: the boundary layer will separate.

Figure 6.52 shows friction and wave drag as a function of M . Referring to the uncertainty of $c_{d_{\text{wave}}}$ by TRANSEP (see 4.4.3.2), no attempt was made to correct the predicted $c_{d_{\text{wave}}}$ values. Clearly, the divergence Mach number lies between $M = 0.65$ and 0.70 .

6.4.4 Airfoil 35

6.4.4.1 Development

A new target distribution was created in an attempt to extend the low-drag bucket to even higher lift coefficients (see Figure 6.53). Also, the target pressure distribution for the upper surface was rounded in an attempt to increase $c_{l_{\max}}$. It was expected that the rounding of the pressure distribution would also result in a gradual forward movement of transition (see discussion of Eppler design mode in Section 3.2). Also, the suction spike at the leading edge might be delayed, thereby relieving danger of leading-edge bubble. This time, however, the integration subroutine (or possibly the "rotation" which is used to recover the original trailing edge location; see Section 3.3.2) in the streamline-curvature method did not correctly modify the upper surface near the leading edge. A local kink in the curvature (Figure 6.54) and pressure distribution (Figure 6.55) of airfoil 35 are apparent. Nevertheless, this 17.1% thick airfoil was analyzed to see what effect the local acceleration (similar to the local accelerations used by Viken in Reference 14) would have on its aerodynamic characteristics.

Figure 6.56 compares the airfoil shape of 35 with the previous airfoil 32. Figure 6.57 shows the new airfoil and the MS(1)-0317 contour.

6.4.4.2 Low-Speed Characteristics (Eppler)

Figures 6.58, 6.59, and 6.60 compare the low-speed characteristics of airfoil 35 and the MS(1)-0317. Although $c_{d_{min}}$ of airfoil 35 is the highest of the modifications analyzed (only five counts less than that of the MS(1)-0317 at $c_l = 0.3$), this low drag is maintained through a wider range of lift coefficients (from about 0.2 to 0.5) than the other modifications which were analyzed (assuming natural transition). When laminar separation is used as the transition criterion, the predicted minimum drag of airfoil 35 is again very similar to that of the MS(1)-037. The maximum lift coefficient (1.78) of airfoil 35 is only slightly higher than that of airfoil 32. A small decrease in $c_{l_{max}}$ is found (from 1.78 to 1.74) by fixing transition at 5% chord (Figure 6.60). Comparison of Figures 6.58 and 6.59 shows that in the natural transition case a pronounced drag bucket is present; i.e., the transition location predicted by Eppler is relatively close to the point of laminar separation. Figures 6.61, 6.62, and 6.63 show the Eppler-predicted effect of Reynolds number on airfoil 35.

6.4.4.3 Subcritical Characteristics (NCS)

Figures 6.64 and 6.65 compare airfoil 35 to the MS(1)-0317 in cruise condition using free transition and laminar separation. A result of the upper surface kink near the leading edge of the airfoil is an increase in the critical lift coefficient at $M = 0.6$. Airfoil 35 has the highest critical lift coefficient of the airfoils developed at K.U. ($c_{l_c} \approx 0.8$ at $M = 0.6$). At $c_l = 0.50$, c_d is 11 counts lower than that of the MS(1)-0317 airfoil.

6.4.4.4 Compressible Characteristics of Airfoil 35

Subcritical and critical characteristics of airfoil 35 have been estimated by the TRANSEP code.

M = 0.60 Characteristics

Figure 6.66 shows c_p distributions for $c_l = 0.47$ and $c_l = 0.788$ (critical condition). Note the clear movement of the minimum pressure point to $x/c = 0.4$ for $\alpha = 1.1^\circ$, which reduces the laminar run on the upper surface.

Increasing Mach Number

Figure 6.67 gives the estimated characteristics of increasing M for $\alpha = 1.1^\circ$. At $M = 0.7$ a stronger shock is present for this airfoil than for airfoil 32; $M_{\text{shock}} = 1.40$ indicates separation according to 4.4.3.2. Accordingly, Figure 6.68 indicates that the drag divergence starts shortly after $M = 0.65$.

6.4.5 Airfoil 37

6.4.5.1 Development

The next modification was an attempt to create an airfoil that would have a low-drag bucket using the natural transition criterion which resembled the drag bucket obtained with use of the laminar separation as the transition criterion. To achieve this, the upper surface must retain a favorable pressure gradient even at higher lift coefficients. Figure 6.69 shows the pressure distribution used for modification ($M = 0.2$, $\alpha = 2.7$ deg.). The target pressure distribution has a favorable gradient to 50% chord, a region of constant pressure to 60% chord, and a concave pressure recovery. Figures 6.60 and 6.71 compare airfoil 35 and the 19%-thick airfoil that was obtained (airfoil 37). Figure 6.72 shows the high camber and thickness of this airfoil in comparison to the MS(1)-0317 airfoil.

6.4.5.2 Low-Speed Characteristics (Eppler)

Figures 6.73, 6.74, and 6.75 compare the low-speed characteristics of airfoil 37 and the MS(1)-0317. The $c_{d_{min}}$ of airfoil 37 is 18 counts less than $c_{d_{min}}$ of the MS(1)-0317. Also, the low-drag range using natural transition is as wide (from $c_l \approx 0.4$ to $c_l \approx 1.0$) and almost as deep as the drag bucket predicted when laminar separation is used as the transition criterion. Unfortunately, the low-drag bucket does not include low lift coefficients. This occurs because the large amount of camber in airfoil 37 requires that the angle of attack be low ($\alpha \approx -3$ deg) to obtain low lift coefficients. As a result, a pressure spike occurs on the lower surface leading edge, resulting in lower

surface transition near the leading edge. However, a negative (upward) flap deflection could translate the low-drag bucket to lower lift coefficients if desired (see chapter 7 for application of this concept). The value of $c_{l_{\max}}$ of this airfoil as predicted by the Eppler code is higher than that of the MS(1)-0317 $c_{l_{\max}} \approx 1.9$). Since this airfoil is substantially thicker than desired for $M = 0.6$ cruise flight, only its incompressible characteristics were examined in this study.

6.4.6 Airfoil 40

6.4.6.1 Development

A thinner ($\approx 17\%$) airfoil was desired to avoid the formation of shock waves at the design condition ($M = 0.6$), so airfoil 37 was scaled down and a new lower surface leading edge was spliced on to obtain airfoil 40 (see Figure 6.76). Airfoil 40 is 17.1% thick. The curvature distribution is shown in Figure 6.77.

6.4.6.2 Low-Speed Characteristics (Eppler)

Figures 6.78, 6.79, and 6.80 compare the incompressible aerodynamic characteristics of airfoil 40 and the MS(1)-0317. The low drag range of airfoil 40 extends from $c_d \approx 0.3$ to $c_d \approx 0.85$. The difference between the predicted drag coefficients using natural transition and laminar separation is small (eight to 14 counts throughout the low drag range). The minimum drag coefficient (as predicted by Eppler) using natural transition is about 16 counts less than that of the MS(1)-0317. The maximum lift coefficient has dropped to about 1.8. The Eppler code predicted the formation of a long bubble on the lower

surface for lift coefficients less than about 0.3. This occurred because of the small nose radius (see Appendix I) and the large amount of camber of airfoil 40. The predicted long bubble formation may preclude the use of airfoil 40 without further modification of the lower surface. Figures 6.81, 6.82, and 6.83 show the effect of reducing Re to 4.0×10^6 .

6.4.6.3 Subcritical Characteristics (NCS)

Figures 6.84 and 6.85 compare the cruise characteristics of airfoil 40 and the MS(1)-0317. Again, only subcritical data are given by the NCS code. The NCS code predicts long bubble formation on the lower surface for lift coefficients less than about 0.3. The long bubble formation occurs due to the steeply adverse pressure gradient on the lower surface at low angles of attack. The amount of camber and the pitching moment of airfoil 40 are the largest of any airfoils developed at K.U. $c_{d_{min}}$ is 43 counts for $c_l = 0.5$, which is 10 counts below the value for MS(1)-0317 at the same c_l . The shape of the drag polars in both figures is similar, indicating that natural transition occurs at the point of laminar separation for $c_l = 0.50$ (see Figure 6.86).

Figure 6.87 shows the effect of fixing transition at 5% chord on the performance of airfoil 40. Lift and pitching moment are both decreased in magnitude when transition is fixed. Also, the lift curve slope is decreased. Fixing transition on the upper surface affects performance much more than fixing transition on the lower surface.

6.4.6.4 Compressible Characteristics of Airfoil 40

M = 0.6 Characteristics

Figure 6.88 shows pressure distributions for several angles of attack at $M = 0.60$. Note that for $\alpha = -1.5^\circ$ (above indicated at the design condition) the flow over the upper surface is just critical.

At $\alpha = 0^\circ$, $M_{\text{local}} < 1.05$.

Increasing Mach Number

Figure 6.89 presents the pressure distribution as determined by TRANSEP for $\alpha = -1.5^\circ$ and increasing Mach number. As can be inferred from the high amount of camber of this airfoil, the flow will become supercritical and shocks will arise shortly after $M_{\text{des}} = 0 = .60$. At $M = 0.65$, a mild shock is present and $M_{\text{shock}} = 1.24$ indicates no shock-induced separation. At $M = 0.70$, however, an extensive supersonic flow field is terminated by a strong shock ($M_{\text{shock}} = 1.56$) and separation will occur.

Figure 6.90 indicates the estimated drag rise. In order to evaluate to a first degree the uncertainty in $c_{d_{\text{wave}}}$ as predicted by TRANSEP (see 4.4.3.2), Figure 6.90 also indicates the results of a method applied at NLR in the Netherlands. The wave drag of a shock is determined by directly integrating the entropy production along the shock wave:

$$c_{d_{\text{wave}}} = \frac{(1 + 0.20M_\infty^2)^3}{0.28M_\infty^2} \int_0^{y_s/c} (1 + 0.20M_n^2)^{-3} M_n \left(\frac{\Delta S}{c_v}\right) d\left(\frac{y}{c}\right)$$

where: $\frac{y_s}{c}$: height of shock above crest

$$\frac{\Delta S}{c_v} = \ln\left(\frac{7M_n^2 - 1}{6}\right) - 1.4 \ln\left(\frac{6M_n^2}{M_n^2 + 5}\right)$$

(Entropy production according to Oswatitsch)

$M_n\left(\frac{y_s}{c}\right)$: Mach number just ahead of the shock

Using the output of TRANSEP, $c_{d_{wave}}$ can absolutely be estimated using a Simpson integration procedure. Figure 6.90 shows that for $M = 0.65$ the TRANSEP prediction is close to the above prediction. For $M = 0.70$ the above procedure fails also due to the numerical representation over three grid widths of the strong shock in TRANSEP. A generally accepted estimation of $c_{d_{wave}}$ can be found using the Garabedian code (Reference 22). However, this approach has not been pursued in this report.

Finally, Figure 6.91 gives a pictorial representation of the extent of the supersonic pocket and shock wave of airfoil 40 for $M = 0.70$, determined by TRANSEP.

6.5 COMPARISON OF K.U. AIRFOILS WITH NLF(1)-0414F AND DERIVATIVE

6.5.1 Comparison of NLF(1)-0414F with Derivative

In section 2.3 airfoil NASA NLF(1)-0414F (DESB165, Reference 14) was introduced. Figure 6.92 shows a derivative of this airfoil, which was obtained by linearly scaling to 17% thickness (which is the average thickness of K.U. airfoils). Figure 6.93 compares c_p -distributions of both airfoils at $M = 0.60$ (NCS estimate). Figures 6.94, 6.95, and 6.96 present a comparison of the original and scaled airfoil in the incompressible speed range (Eppler estimate). Scaling up

implies an increase in camber, resulting in a shift upwards of the low-drag bucket (Figure 6.92). Also, this drag bucket is wider, and $c_{d_{min}}$ is predicted to be six counts above $c_{d_{min}}$ of the original airfoil.

Scaling also leads to an increased steepness of the pressure recovery. Figure 6.94 shows that a sudden dramatic increase in drag occurs for $c_\ell \approx 0.7$ for the natural transition criterion. Accordingly, the Eppler code predicts a dip in the c_ℓ and c_m curves. Figure 6.95 (laminar separation transition criterion) shows this separation behavior explicitly. The dip in the c_ℓ curve originates from the empirical lift reduction in the Eppler code when separation is present (see Section 4.2.5). Also the width of the already wide low-drag bucket is increased up to $c_\ell = 1.0$ for the scaled airfoil. Notice that $c_{d_{min}} = 25$ counts. $c_{\ell_{max}}$ increases from 1.8 for the original airfoil to 2.0 for the scaled airfoil using natural transition. The larger $c_{\ell_{max}}$ value is a result of the delay in forward movement of the separation region, once separation has jumped to $0.85c$ (see remark above). Fixing transition at 5% does not lead to a depreciation of $c_{\ell_{max}}$ (compare Figures 6.94 and 6.96). Figure 6.97 illustrates the separation behavior for both airfoils.

Figure 6.98 shows the compressible characteristics of both airfoils. These NCS data include boundary-layer iterations: at $c_\ell = 0.50$ the derivative airfoil shows trailing-edge separation. Minimum drag increases from 32 counts (at $c_\ell = 0.45$) to 36 counts for the derivative airfoil. Also the width of the drag bucket is smaller, indicating forward movement of transition. Both airfoils show a

considerably lower drag (10-15 counts) than airfoil NASA MS(1)-0317. Figure 6.98 also shows that c_m of the derivative airfoil greatly increases.

6.5.2 Comparison with K.U. Airfoils

A comparison of the NLF(1)-0414F, its derivative, and the airfoils discussed in this report is justified in view of soon-to-be-published wind-tunnel data for the NLF(1)-0414F airfoil. The following comparison will be based completely upon the calculated characteristics of these airfoils.

6.5.2.1 Incompressible Characteristics

Shape of Drag Bucket

Using the natural transition criterion, the shape of the drag bucket of NLF(1)-0414F (Figure 6.94) resembles that of airfoil 26A (Figure 6.6). Airfoil 35 (Figure 6.58) shows a more squared low-drag bucket. This trend towards compliance with the shape of the bucket for the laminar separation criterion (which indicates that the location of free transition occurs close to that of laminar separation) is also apparent for airfoil 37 (Figure 6.73) and airfoil 40 (Figure 6.78). The $c_{d_{min}}$ of NLF(1)-0414F is eight counts less than that of airfoil 40 (Figure 6.78). Using the laminar separation criterion, the difference in $c_{d_{min}}$ increases to 12 counts (Figures 6.79 and 6.95). Comparison of the scaled NLF(1)-0414F airfoil with the K.U. airfoils shows that $c_{d_{min}}$ in the natural transition case is more comparable.

Generally in this comparison, it is concluded that $c_{d_{min}}$ of the NASA NLF(1)-0414F airfoil is substantially less than that of the K.U. airfoils. However, the shape of the drag bucket is very different when the criteria of natural transition or transition at laminar separation are applied. The narrow bucket as found in Figure 6.94 is confirmed in yet-unpublished NASA-Langley wind-tunnel experiments. By comparison, the K.U. airfoils show a considerable amount of NLF in early climb, while the NLF(1)-0414F needs a trailing-edge flap to shift the drag bucket to climb c_l values.

$c_{l_{max}}$

$c_{l_{max}}$ of the K.U. airfoils is comparable to the prediction for NLF(1)-0414F: $c_{l_{max}} \approx 1.8$. However, the estimated stalling behavior is less docile for the NLF(1)-0414F airfoil. Comparison of the leading-edge radii (see Appendix I) indicates that $c_{l_{max}}$ of the K.U. airfoils might be restricted by a more severe bursting of the leading-edge bubble.

Pitching Moment c_m

Due to the reduced amount of aft loading of NLF(1)-0414F (compare Figures 2.8 and 6.4), c_m is less than that of the K.U. airfoils. The scaled derivative produces a c_m that approaches that of the K.U. airfoils.

6.5.2.2 Compressible Characteristics ($M = 0.6$)

The characteristics at $M = 0.6$ are most important for a medium-speed airfoil.

Drag Bucket and Minimum Drag

Table 6.3 gives a summary of the depth and width of the low-drag bucket of the K.U. airfoils and the NASA NLF(1)-0414F airfoils. The NLF(1)-0414F shows $c_{d_{min}} = 32$ counts at $c_\ell = 0.5$ in a fairly narrow drag bucket (see Figure 6.98). The scaled version shows a sharp bucket, $c_{d_{min}} = 36$ counts at $c_\ell = .45$. By contrast, airfoil 26A (Figure 6.23, $c_{d_{min}} = 40$ counts), airfoil 32 (Figure 6.45, $c_{d_{min}} = 42$ counts), and airfoil 35 (Figure 6.64, $c_{d_{min}} = 43$ counts) all show a wider low-drag bucket.

$$c_{\ell_\alpha}$$

c_{ℓ_α} , an inverse proportional factor for gust sensitivity, of the K.U. airfoils is near the value of the MS(1)-0317 value (see Table 6.4). This table shows that NLF(1)-0414F has a smaller c_{ℓ_α} . c_{ℓ_α} of the derivative is close to the K.U. airfoils, for $c_\ell < 0.5$.

$$c_m$$

Pitching moment behavior is not much influenced by an increase of Mach number to 0.60.

Table 6.3 Summary Low-Drag Bucket of Studied Airfoils

Natural Transition Criterion
 $Re = 8.9 \times 10^6$, $M = 0.6$

Airfoil	$c_{d_{min}}$ (counts)	$(c_l)c_{d_{min}}$	Figure
KU 26A	40	.20 - .45	6.23
KU 32	42	.35 - .60	6.45
KU 35	43	.40 - .60	6.64
KU 40	44	.45 - .65	6.84
NASA NLF(1)-0414F	32	.45 - .55	6.98
KU-scaled version	36	.40 - .50	6.98

Table 6.4 c_{l_α} Comparison of Studied Airfoils

$Re = 8.9 \times 10^6$, $M = 0.6$

MS(1)-0317	.157	degr^{-1}
K.U. 26A	.157	
K.U. 32	.157	
K.U. 35	.153	
K.U. 40	.153	
NLF(1)-0414F	.132	
NLF(1)-0414F derivative	.146	for $c_l < .5$
	.107	for $c_l > .5$

7.0 FLAPPING OF AIRFOILS

7.1 INTRODUCTION

This chapter examines the benefits of deflecting a small plain flap during climb or cruise. Figure 7.1 shows how a .20c cruise/climb flap might be incorporated into a .30c high-lift Fowler flap. The sign convention for flap deflection is also shown in Figure 7.1. A positive (downward) flap deflection will affect airfoil performance by:

1) increasing the section lift and maximum lift coefficients; 2) increasing the section pitching moment coefficient negatively; and 3) shifting the low drag-range (of NLF airfoils) to higher lift coefficients. A flap deflection will also change the critical Mach number and therefore may be used to control the development of shock waves. This aspect of flapping airfoils has not been studied at the KU-FRL. The most beneficial application of a cruise/climb flap discussed in this chapter is that of shifting the low-drag range of an airfoil to higher lift coefficients during climb or to lower lift coefficients during cruise.

7.2 EFFECTS OF A PLAIN FLAP ON AIRFOIL PERFORMANCE

A plain trailing-edge flap changes the airfoil geometry in two ways. First, it adds (or subtracts) camber to the airfoil, with the greatest amount of change occurring at the hinge point. It also increases (or decreases) the apparent angle of attack based on the "new" chordline of the "new" airfoil. The effect of the change in camber is an increase (or decrease) in the aft-loading of the airfoil and also an apparent drooping of the airfoil nose relative to the "new" chordline.

These two changes combine to increase the circulation about the airfoil. However, since the airfoil nose is dropped relative to the new chordline the stagnation point does not travel as far aft on the lower surface as it would were the angle of attack of the unflapped airfoil increased to obtain the same lift coefficient. Therefore, leading-edge peaks and the extent of trailing-edge separation are less severe at equally high lift coefficients for a positive flapped airfoil than for an unflapped airfoil.

Figures 7.2-7.4, 7.5-7.7, and 7.8-7.10 show the effect of flap deflections on the Eppler-predicted inviscid pressure distributions of airfoils 32, 35, 40. A positive (downward) flap deflection increases the lift positively and the pitching moment negatively. Also note that a positive flap deflection induces a pressure peak on the upper surface and suppresses the formation of one on the lower surface. As a result of the peak formation on the upper surface, the stall angle of attack of the airfoil is reduced although the maximum lift coefficient is increased due to the added camber. A negative flap deflection decreases the lift and increases the pitching-moment coefficient positively. Also, a negative flap deflection tends to suppress upper surface leading-edge pressure peaks at higher angles of attack, in contrast to positive flap deflections.

Another major effect of a positive flap deflection is the shifting of the low-drag bucket to higher lift coefficients. This occurs because lift from an increase in angle of attack may be replaced by lift from an increase in aft camber. This allows the airfoil to achieve the same lift at lower angles of attack, resulting in the restoration of a favorable pressure gradient for c_l values previously outside the low-

drag bucket. The drag bucket will be shifted to higher lift coefficients but is also shifted to lower angles of attack (relative to the unflapped chordline) due to the induced pressure peaks on the upper surface.

7.3 APPLICATION OF FLAP TO K.U. AIRFOILS

A simple, twenty percent chord, trailing-edge flap has been incorporated into airfoils 32, 35, and 40. The Eppler code (see ch. 4) was used to analyze the effect of flap deflections on the potential flow (i.e. pressure distribution, lift- and pitching-moment coefficients) and the boundary-layer development (i.e. shape factor, transition location, and drag). Since the flap was not intended to be used as a high-lift device, its deflection was limited from -10 to +10 degrees. This choice is arbitrary. However, in view of the flap modelling in the Eppler code, results for larger flap deflections are questionable. The flap was intended to be used during two flight conditions: 1) cruise and 2) during lowspeed (climb/loiter) conditions.

7.3.1 Application of Flap during Cruise

Two effects of the flap may be beneficial during cruise: 1) the reduction of the pitching-moment coefficient and therefore of trim drag; and 2) the shifting of the drag bucket to lower lift coefficients for highly cambered airfoils. Figures 7.11-7.13 show the effects of flap deflection on the lift curves, drag polars, and pitching-moment coefficients of airfoils 32, 35, and 40 respectively. A -10 degree flap deflection does add about .05 to the section pitching-moment

coefficient, but this may not justify the installation of a cruise flap to reduce trim drag. This is especially true for three-surface aircraft which do not have as serious trim problems as conventional configurations. Therefore, only the second mentioned effect of a cruise flap was found to be very beneficial. Figure 7.14 shows the NCS-predicted cruise characteristics of airfoil 40 (the most highly cambered airfoil developed in this study). Notice that at low lift coefficients, the unflapped airfoil drag increases for $c_l < \sim 0.3$ due to transition on the lower surface. By negatively flapping the airfoil, transition on the lower surface is delayed to lower lift coefficients ($c_l < \sim 0.2$). As a result, the low drag range is shifted to lower lift coefficients. Also, the long bubble which was predicted for the unflapped airfoil does not appear for the flapped airfoil.

7.3.2 Application of Flap at Low Speeds

At low speeds, higher lift coefficients are required. Since climb to cruise altitude uses a significant portion of short-haul block fuel, obtaining low drag at high lift coefficients ($c_l > 1.0$) is desirable for short-haul aircraft. This may be achieved with NLF airfoils by positively deflecting a flap during climb. Figures 7.11-7.13 show the Eppler predictions of the effect of flap deflection on the aerodynamic characteristics of the NLF airfoils developed at KU. Notice that although the drag bucket may be shifted to a higher c_l range, the pitching-moment coefficient is also increased negatively. However, it must be kept in mind that the Eppler code does not model viscous

effects. These effects are very strong over the aft portion of an airfoil, so the predicted increments to the lift and pitching moment coefficients are too large.

If the drag polars for flap deflections between -5 and 10 degrees are super-imposed, an "overall flapped drag polar" extending from $c_{\ell}=0.0$ to $c_{\ell}=1.2$ (for airfoil 40) may be realized. If a control system were connected to the flap, it would be possible to fly through the "overall flapped drag polar" in an optimal manner. That is, to fly at a flap setting that would not only result in NLF at the desired lift coefficient but also in the smallest pitching-moment coefficient (trim drag) possible at that c_{ℓ} -value. To achieve this, the control system would initiate the lowest positive flap deflection to obtain the lowest trim drag possible within the drag bucket. As confidence is gained in fly-by-wire systems, the likelihood of such a system being installed in a regional aircraft is increasing.

Figures 7.15, 7.16, and 7.17 show the predicted point of turbulent separation as a function of angle of attack and flap deflection for airfoils 32, 35, and 40 respectively. Notice that for negative flap deflections, the flow over the flapped upper surface suddenly separates. This is the reason for the sudden dip in the lift, drag, and pitching moment curves (Figures 7.11-7.13) for negative flap deflections.

8.0 CONCLUSIONS AND RECOMMENDATIONS

8.1 CONCLUSIONS

1. A modified streamline-curvature method was used to develop five medium-speed Natural Laminar Flow (NLF) airfoils. Effective application of this method requires that the pressure distribution of the starting airfoil be not too different from the target distribution. Problems in the high curvature leading-edge region were encountered.
2. The following design objectives and constraints for NLF airfoils for regional aircraft were observed:
 - $M_{des} = 0.60$.
 - $c_{l_{des}}$ preferably larger than 0.40.
 - Length of laminar run is approximately 60% of chord.
 - Obtain a wide low-drag "bucket" to include climb lift coefficients.
 - Airfoil thickness should be of the magnitude of NASA MS(1)-317.
 - No appreciable effect of fixing transition on $c_{l_{max}}$ is allowed.
 - A nonzero trailing-edge thickness is required.
3. The NASA medium-speed MS(1)-0317 airfoil was used as a starting point in this study. This airfoil is predicted to have a fair amount of laminar flow for $c_l < 0.10$. Five medium-speed NLF airfoil shapes have been derived, based upon subcritical design pressure distributions. Comparing the mid-chord and initial

pressure gradients at M_{des} , these airfoils can be divided into two categories.

- a. Airfoils 26A and 32, showing a flat mid-chord and steep initial gradient;
- b. Airfoils 35, 37, and 40, characterized by a shallow initial and mid-chord pressure gradient.

In this context, "a" is most suitable for moderately swept wing applications; "b" is more favorable in the absence of wing sweep. the aft-loaded pressure recovery (preceded by a transition ramp) is concave, in contrast to NACA 6-series airfoils.

4. The Eppler code was used to assess incompressible flapped and unflapped characteristics of resulting airfoils. Subcritical characteristics were determined by the North Carolina State Code. Near critical and supercritical conditions were estimated by the TRANSEP code. Appreciable differences in predictions of pressure distributions and aerodynamic characteristics have been found and commented on. It is concluded that the TRANSEP code is not able to predict $c_{l_{max}}$ of NLF airfoils with a very small leading-edge radius.

5. In assessing the relative drag of the derived airfoils, three operational Mach regions must be discerned:

- a. $M < 0.2$

Airfoils 35, 37, and 40 show the widest low drag bucket in the low-speed region. $c_{d_{min}}$ is around 40 counts for $c_l = 0.3 - 0.80$.

b. $M = 0.60$

Airfoils 26A and 32 show the lowest drag in the cruise regime. The width of the drag bucket (0.2 - 0.4, expressed in c_l - increments) is less wide than in the low speed range. Again, $c_{d_{min}}$ is of the order of 40 counts.

c. $M > 0.60$

Airfoil 32 shows the highest drag divergence Mach number (0.70) of airfoils considered. (Airfoil 26A was not included in this $M > 0.6$ evaluation.) Thickness and high camber of later developed airfoils reduces this Mach number.

6. A SALLY boundary-layer stability analysis for airfoil 26A indicates that the logarithmic amplification factor, n_{max} , does not exceed 10 at the design condition. Also, n_{max} does not exceed 15 when a moderate initial pressure suction peak is followed by a flat mid-chord pressure distribution at higher α 's, indicating that in this case transition will also occur at a laminar separation bubble.

Recent free-flight tests indicate that n_{max} of 15 predicts the actual location of transition fairly accurately. Therefore, it is expected that in flight, airfoil 26A will show transition in the laminar separation bubble, also in the $c_l = 0.45$ condition. The introduction of a more favorable local pressure gradient results in a local stable region of T.S. waves.

7. Application of a small 0.2c plain trailing-edge cruise/climb flap in the basic airfoils shows that

a. A flap deflection upwards (cruise-flap application)

- can reduce the sectional pitching moment by 40% at $c_{l_{des}}$;

- can shift the low-drag bucket down to cruise lifting coefficients $c_\ell = 0.20 - 0.40$.

The flapping angle was restricted to 10° .

- A flap deflection downwards shifts the low-drag bucket to climb lifting coefficients $c_\ell = 1.0 - 1.2$ (climb-flap application). Application of a control system, controlling angle of attack, and the flap deflection can provide a wide low-drag bucket and reduce c_m in an optimum manner.

8. $c_{\ell_{\max}}$ Considerations:

Airfoils showing long runs of laminar flow have a relatively small leading-edge radius, thus compromising $c_{\ell_{\max}}$. Recently, however, in testing the NASA NLF(1)-0414F airfoil it has been found that this compromise is not as detrimental to $c_{\ell_{\max}}$ as was expected.

The Eppler prediction is used to predict $c_{\ell_{\max}}$, which is shown to be a fairly accurate method by comparison to data of the MS(1)-0317 airfoil.

Using this Eppler prediction, it is found that $c_{\ell_{\max}}$ of the airfoils reported in Chapter 6 is $1.75 - 1.80$, whereas for NASA MS(1)-0317, $c_{\ell_{\max}}$ is predicted to be 1.90 . For NASA NLF(1)-0414F, $c_{\ell_{\max}}$ is predicted to be 1.80 .

The effect of fixing transition at 5% has only a very small effect on $c_{\ell_{\max}}$, based on the Eppler code prediction.

9. Comparison with NASA MS(1)-0317:

The airfoils described in this report achieve laminar boundary layers over 55-58% on both surfaces. The minimum drag of 40 counts is achieved over a wide range of c_ℓ values for $M < 0.2$ and is 10 counts less than the estimated MS(1)-0317 values. At cruise

Mach number, the minimum drag is obtained at a higher c_l value and is 5-10 counts below that of the MS(1)-0317 airfoil. The thickness of these airfoils under consideration, combined with a fairly conservative amount of laminar run, does not permit a larger reduction in drag in comparison to the MS(1)-0317 airfoil.

10. Comparison of K.U. airfoils with NASA NLF(1)-0414F and derivative:

a. NLF(1)-0414F

- $c_{d_{min}}$ of the K.U. airfoils at low speed is predicted to be eight counts above the NLF(1)-0414F value. The width of the drag bucket of the higher numbered K.U. airfoils is similar using criteria of natural transition and transition at laminar separation, in contrast to the NASA airfoil. At $M = 0.60$, $c_{d_{min}}$ of airfoil 26A is four counts above the predicted drag of the reference airfoil; also, this low drag is maintained over a wider c_l range.
- $c_{l_{\alpha}}$ is 0.02 degr^{-1} higher for the K.U. airfoils
- c_m is less for the NLF(1)-0414F airfoil, since this 70% airfoil has less aft-loading.
- $c_{l_{max}}$ is predicted to be comparable, viz. 1.8.
- The thickness of NASA NLF(1)-0414F is $0.143c$, whereas the thickness of K.U. airfoils is at least $.17c$.

b. Scaled derivative

A $.17c$ linearly scaled derivative of NASA NLF(1)-0414F airfoil was evaluated.

- Scaling increases $c_{d_{min}}$ at least by four counts, $c_{d_{min}}$ is four counts below $c_{d_{min}}$ of K.U. airfoils. c_m increases substantially when compared to the original airfoil.
- $c_{l_{max}}$ increases to 2.0 by thickening the original airfoil.
- $c_{l_{\alpha}}$ decreases dramatically for $c_l > 0.5$ (Eppler code prediction).

11. In general it is concluded that the development of airfoils in this report serves two purposes:

- Establishment of a class of thick airfoils for medium-speed applications, showing a subcritical design pressure distribution and a concave pressure recovery in contrast to the classic NACA laminar flow airfoils.
- Establishment of the first phase of the definition of a design methodology and actual design of natural laminar flow wings for medium-speed regional aircraft. The airfoils obtained in the first phase, among others, will be used in this wing design study. The knowledge attained in this first phase, as well as the now readily available two-dimensional codes, will facilitate and improve the work under the second phase.

8.2 RECOMMENDATIONS

1. The recommendations of this report coincide to a large extent with a listing of subjects not addressed in this design study of laminar flow airfoils at the KU-FRL. Again, three areas can be discerned:

a. $M < 0.2$ Region

- $c_{l_{max}}$ has been assessed only by using the Eppler code and by comparing with reference airfoils. Estimation of $c_{l_{max}}$

by a code which incorporates a massive separation model and a conformal mapping of the relatively thin leading-edge region of advanced NLF airfoils is required in order to evaluate realistically the compromise between $c_{l_{\max}}$ and $(c_{d_{\min}})_{\text{cruise}}$.

- Structural incorporation and aerodynamic effect of a larger chord high-lift trailing-edge flap should be addressed. Also, the possible integration of an advanced leading-edge Krueger type of flap, or the inclusion of a variable nose shape must be considered to avoid leading-edge stall of advanced NLF airfoils.
- The influence of (heavy) ice accretion over the nose region on $c_{l_{\max}}$ must be determined.
- The incorporation of a climb flap must be studied by detailed aerodynamic analysis of the flap region. Also control aspects of this flap in a practical application must be developed.

b. Design Range ($M = 0.60$)

- The lower-surface nose shape of airfoil 40 needs modification to allow also for an appreciable length of laminar flow over the lower surface at lower c_l 's.
- A parametric analysis should be performed to evaluate the trade-off between the length of the laminar run in the cruise design condition and the steepness and concavity of the pressure recovery in off-design conditions.

Application of trailing-edge suction should be considered, in addition to a trailing-edge flap for control of the recovery in off-design situations.

- This design study should be extended to NLF airfoils which show a flat mid-chord supercritical pressure distribution and are intended for low-sweep applications (i.e., absence of serious crossflow interference).

c. Higher Mach Region ($M > 0.60$)

- The drag rise and shock growth should be estimated by using the Garabedian code up to the point of shock-induced separation.
- Interaction of the shock wave with the turbulent (or laminar) boundary layer should be studied to determine buffet onset.

9.0 REFERENCES

1. Herrera-Vaillard, A.; "Guide to the Use of 'WINGWT,'" KU-FRL-543-4, 1982.
2. Hess, J. L.; "Calculation of Potential Flow about Arbitrary Three-Dimensional Lifting Bodies," Report No. MDC J5679-01, McDonnell Douglas Corp., 1972.
3. Coussens, T. G., and Tullis, R.M.; "Application of Advanced Technologies to Small Short-haul Transport Aircraft," NASA CR-152363, Lockheed California Co., June 1980.
4. Srivatsan, R., et al.: "A Preliminary Design Investigation of Several Unconventional Commuter Configurations," KU-FRL-543-1, University of Kansas Center for Research, Inc., Jan. 1982.
5. Taylor, J. R.; Jane's all the World Aircraft, Edition 1983-1984.
6. Downing, D. R., Hammond, T.A., and Amin, S.P.; "Ride Quality Systems for Commuter Aircraft," The University of Kansas Center for Research, Inc., NASA CR 166118, May 1983.
7. Holmes, B. J., and Obara, C. J.; "Observations and Implications of Natural Laminar Flow on Practical Airplane Surfaces," J. Aircraft, Vol. 24, No. 12, Dec. 1983.
8. Smith, F., and Higton, D. J.; "Flight Test on a King Cobra FZ-440 to Investigate the Practical Requirements for the Achievement of Low Profile Drag Coefficients on a 'Low Drag' Airfoil," British ARC R&M No. 2375, 1950.
9. Althaus, D. and Wortmann, F. X.; Stuttgarter Profilkatalog I, Experimental Results from the Laminar Wind Tunnel of the Institut fuer Aero- und Gasdynamik der Universitaet Stuttgart, Vieweg, Braunschweig, 1981.
10. Eppler, R.; "Some New Airfoils." In: NASA CP2086 (The Science and Technology of Low Speed and Motorless Flight), Part I, 1979.
11. Van Ingen, J. L., Boermans, L. M. M., and Blom, J. J. H. "Low Speed Airfoil Section Research at Delft University of Technology," ICAS-80-10.1, October 1980.
12. Somers, D. M.; "Design and Experimental Results for a Natural-Laminar-Flow Airfoil for General Aviation Applications," NASA TP 1861, June 1981.
13. Abbott, I. H., and Van Doenhoff, A. E.; Theory of Wing Sections, Dover, New York, 1959.

14. Viken, J. K.; Aerodynamic Design Considerations and Theoretical Results for a High Reynolds Number Natural Laminar Flow Airfoil. Master's Thesis, George Washington University, Jan. 1983.
15. Petersen, R. H., and Maddalon, D. V.; "NASA Research on Viscous Drag Reduction," ICAS-82-5.1.4, Seattle 1982.
16. Hanks, G. W., et al.; "Natural Laminar Flow Airfoil Analysis and Trade Studies." NASA CR-159029, Boeing Seattle, May 1979.
17. Hanks, G. W., et al.; "F-111 Natural Laminar Flow Flowe Flight Test Data Analysis and Boundary-layer Stability Analysis." NASA CR-166051, Jan. 1984 (FEDD restricted Jan. 1986).
18. Mask, R. L.; "Low Drag Airfoil Design Utilizing Passive Laminar Flow and Coupled Diffusion Control Technique." Vought ATC R-91100/9cr-71, AD AD90778, Sept. 1980.
19. Szelazek, C. A., et al.; "Upper Surface Modification for $c_{l_{max}}$ improvement of selected NACA-6 series Airfoils," NASA TM-78603, Aug. 1979.
20. Eppler, R., "Direct Calculation of Airfoils from Pressure Distribution." NASA TT F-15,417 (Translated from Ingenieur-Archiv, Vol. 25, No. 1, 1957).
21. Eppler, R., and Somers, D. M.; "A Computer Program for the Design and Analysis of Low-Speed Airfoils." NASA TM-80210, 1980.
22. Bauer, F., Garabedian, P., and Korn, D.; Supercritical Wing Sections III, Lecture Notes in Economics and Mathematical Systems, Springer-Verlag, New York, 1977.
23. Carlson, L. A.; "TRANSEP: A Program for High Lift Separated Flow About Airfoils." NASA CR-3376, Dec. 1980.
24. Barger, R. L., and Brooks, C. W.; "A Streamline Curvature Method for Design of Supercritical and Subcritical Airfoils." NASA-TN-D-7770, Sept. 1974.
25. Anon.; IMSL, International Mathematical and Statistical Library, 7th edition, 1979.
26. Schlichting, H; Boundary-Layer Theory, McGraw Hill Book, Co. 9th ed., 1979.
27. Eppler, R.; "Practical Calculation of Laminar and Turbulent Bled-off Boundary Layers." NASA TM-75328, 1978. (Translated from Ingenieur-Archiv, Vol. 32, 1963).
28. Beasley, P. W., and Mighee, J. R.; "Low-Speed Aerodynamics Characteristics of a 17%-Thick Medium-Speed Airfoil Designed for G.A. Applications," NASA TP 1786, 1980.

29. Eppler, R., and Sommers, D. M.; "Low Speed Airfoil Design and Analysis." Advanced Technology Airfoil Research, Volume I, NASA CP-2045, Part 1, 1979, pp. 73-94.
30. Braden, S. A., Goradia, S. M., Stevens, W.A.; "Mathematical Model for Two-Dimensional Multi-Component Airfoils in Viscous Flow." NASA CR-1843, 1971.
31. Young, A. D. and Wintersbottom, N. E.; "Note on the Effect of Compressibility on the Profile Drag of Aerofoils at Subsonic Mach Numbers in the Absence of Shock Waves." R&M No. 2400 (4667). A.R.C. Technical Report; London, 1950.
32. Nash, J. F.; "Turbulent Boundary-layer Behavior and the Auxiliary Equation," AGARDograph 97.5, 1967.
33. Boeing Commercial Aircraft Company. "Hybrid Laminar Flow Control Study: Final Technical Report," NASA CR-165930, 1982.
34. Stratford, B. S.; "The Prediction of Separation of the Turbulent Boundary Layer," J. Fluid Mech. 5, 1959.
35. Wortman, F. X.; "Progress in the Design of Low Drag Airfoils." In: Boundary-Layer and Flow Control, ed. by Lachmann G.V., Pergamon, London, 1961.
36. Hoerner, S. F.; "Base Drag and Thick Trailing Edges," J. of the Aerodyn. Sciences, Vol. 17, No. 10, Oct. 1950.
37. Srokowski, A. J., and Orzag, S. A.; "Mass Flow Requirements for LFC Wing Design." AIAA paper 77-1222, Aug. 1977.
38. Dagenhart, J. R.; "Amplified Crossflow Disturbances in the Laminar Boundary Layer on Swept Wings with Suction." NASA TP 1902, Nov. 1981.
39. Kaups, K., and Cebeci, T.; "Compressible Laminar Boundary Layers with Suction on Swept and Tapered Wings." J. Aircraft, Vol. 14, No. 7, July 1977.
40. Smith, A. M. D., and Gamborini, N.; "Transition, Pressure Gradient and Stability Theory." Proc. 9th Int. Cong. Appl. Mech., 4,234. Brussels, Belgium. (AD 125559).
41. Van Ingen, J. L.; "A Suggested Semi-empirical Method for the Calculation of the Boundary-layer Transition Region." Delft University of Technology. Report VTH 74, 1956.
42. Rungyan, L. J.; "Amplification Factors at Transition on an Unswept Wing in Free Flight and on a Swept Wing in Wind Tunnel." AIAA paper 79-0267, 1979.
43. Holmes, B. J.; "Flight Investigation of Natural Laminar Flow on the Bellanca Skyrocket II." SAE paper 830717, April 1983.

FIGURES

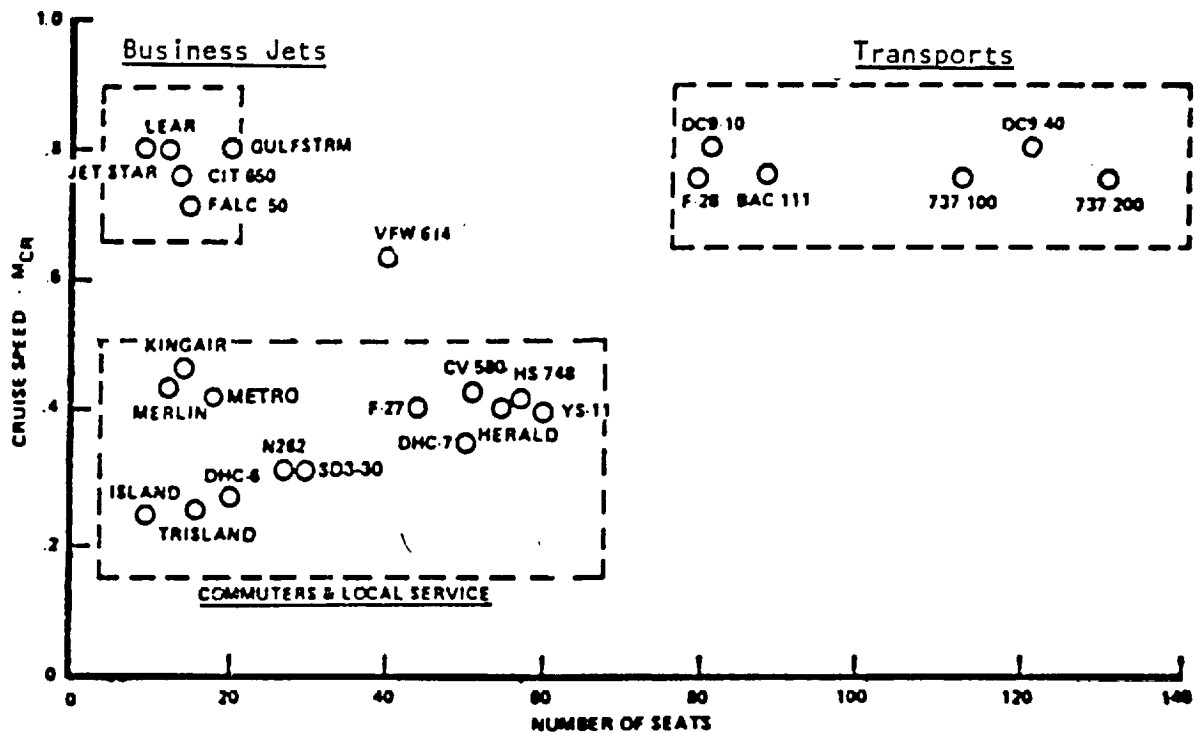


Figure 1.1 Short-haul aircraft market study (ref. 3)

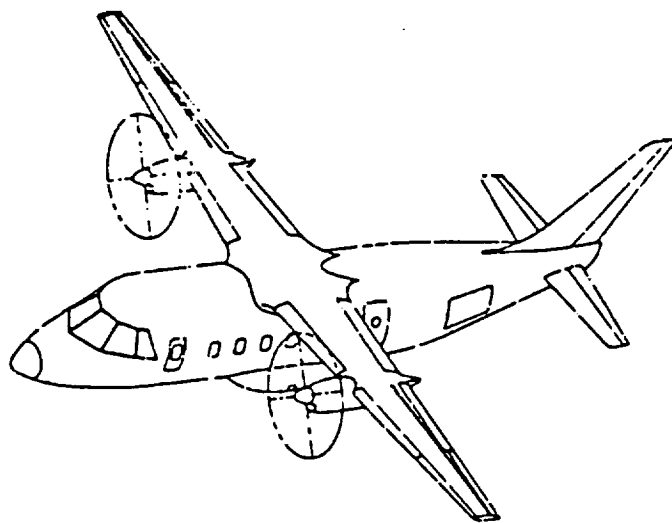


Figure 1.2 Lockheed's proposed 30 PAX short-haul aircraft (ref. 3)

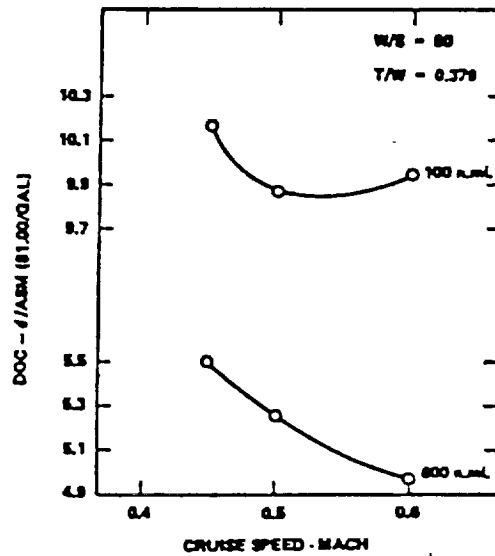


Figure 1.3 Estimated DOC for 30 PAX short-haul aircraft for both 100 and 600 NM ranges (ref. 3)

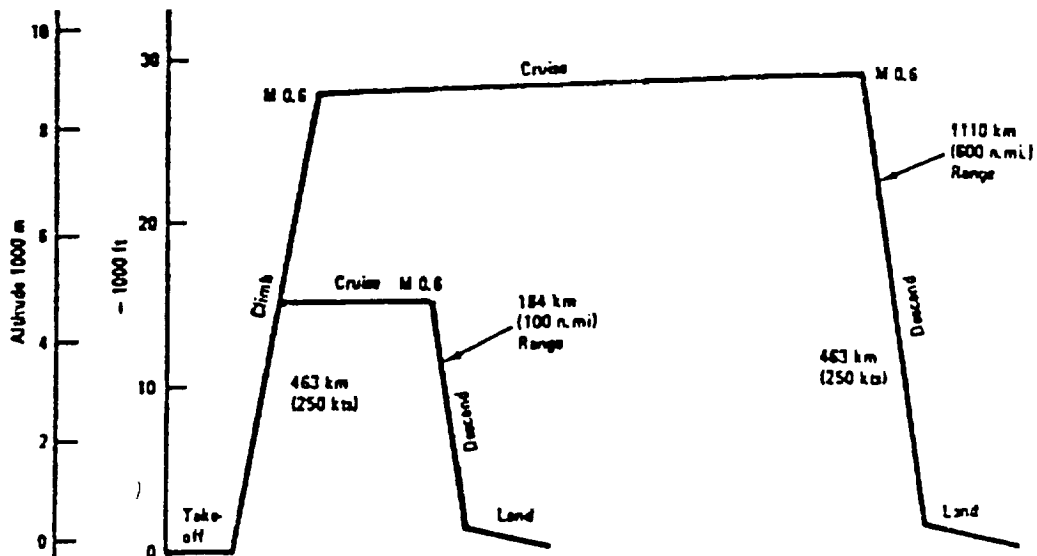


Figure 1.4 Mission profiles for 30 PAX short-haul aircraft (ref. 3)

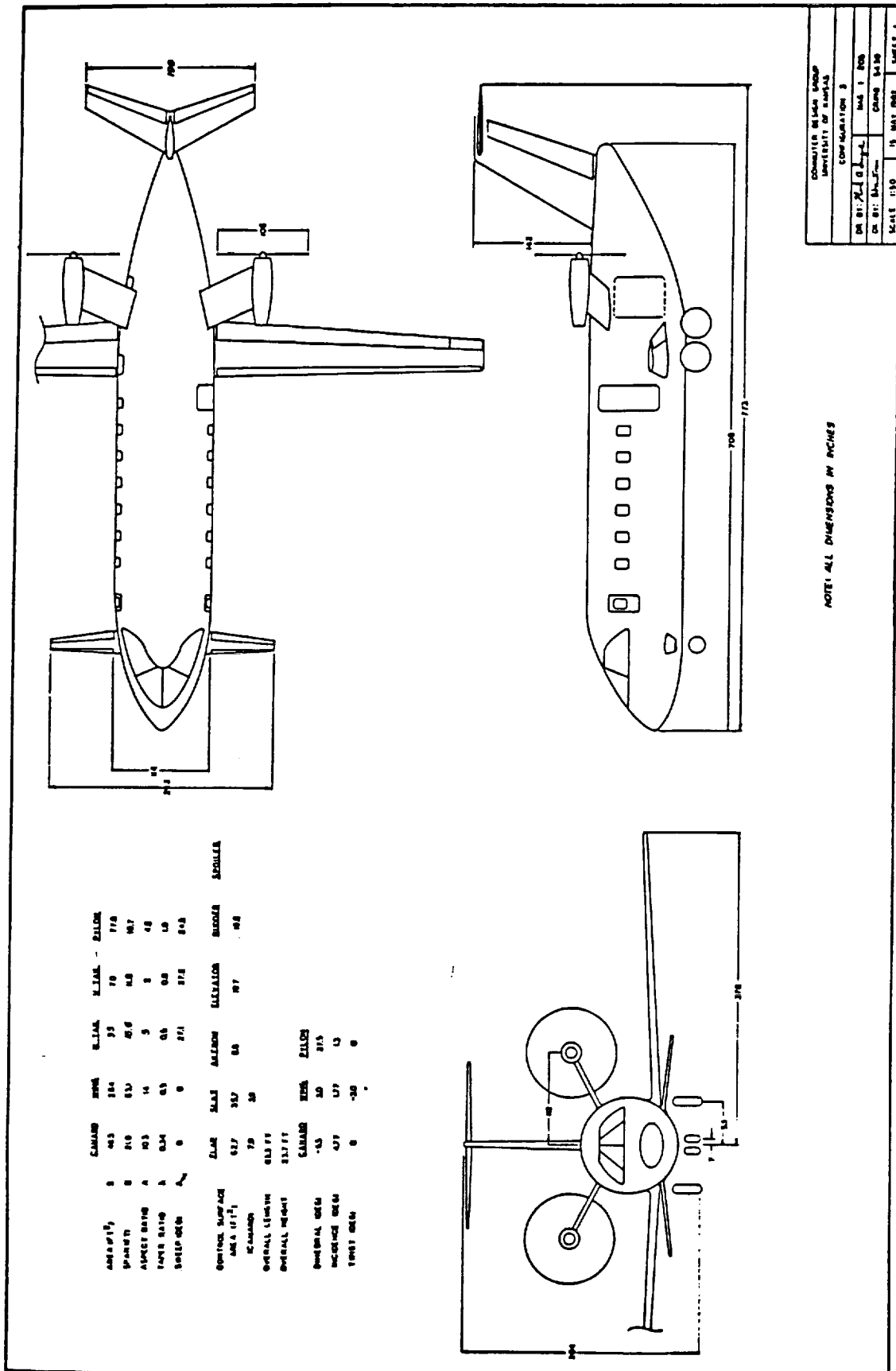


Figure 1.5 Three-View of the 3-Surface Configuration (ref. 4)

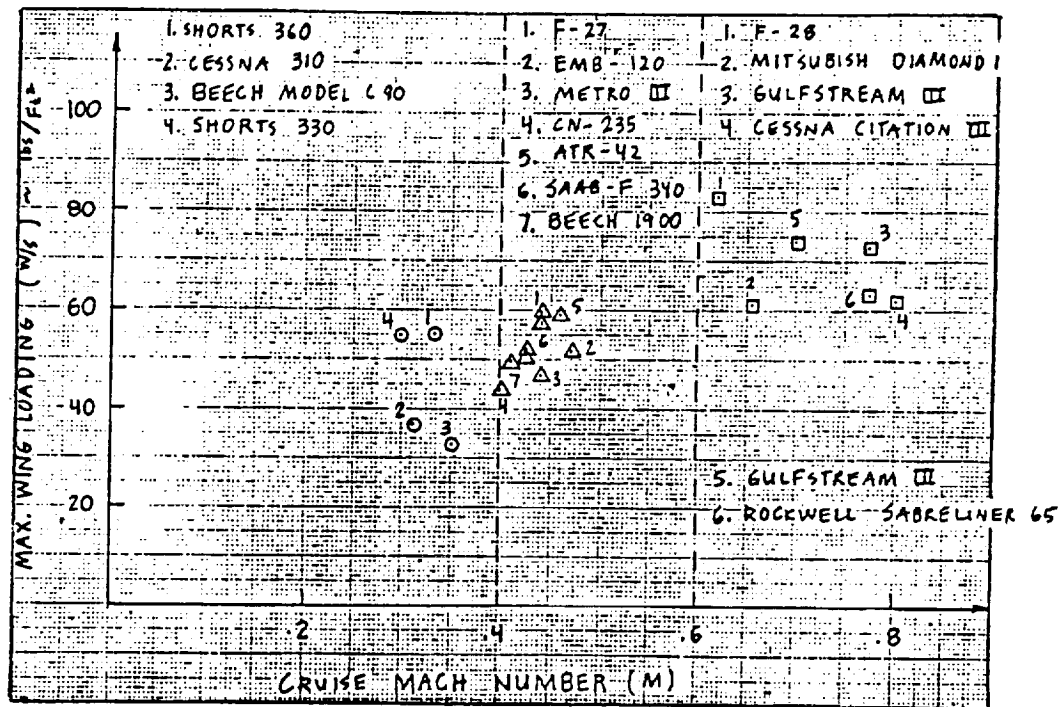


Figure 1.6 Relationship between wing loading and Mach number for existing aircraft

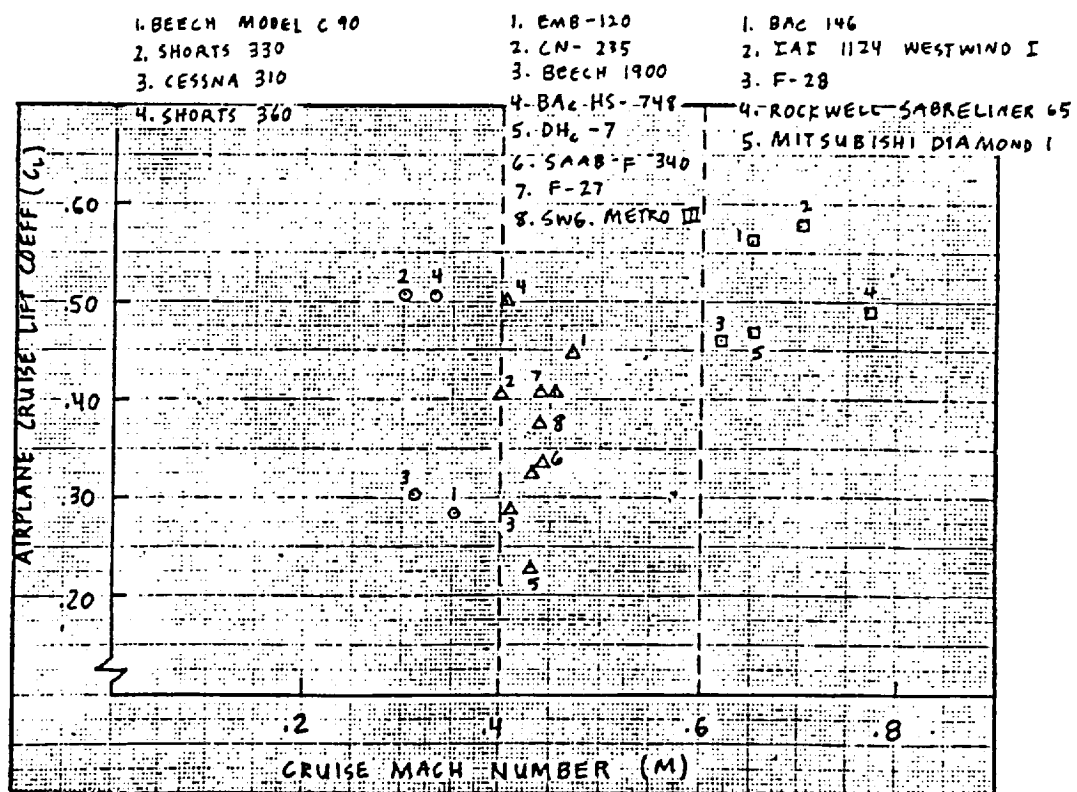


Figure 1.7 Relationship between cruise lift coefficient and Mach number for existing aircraft

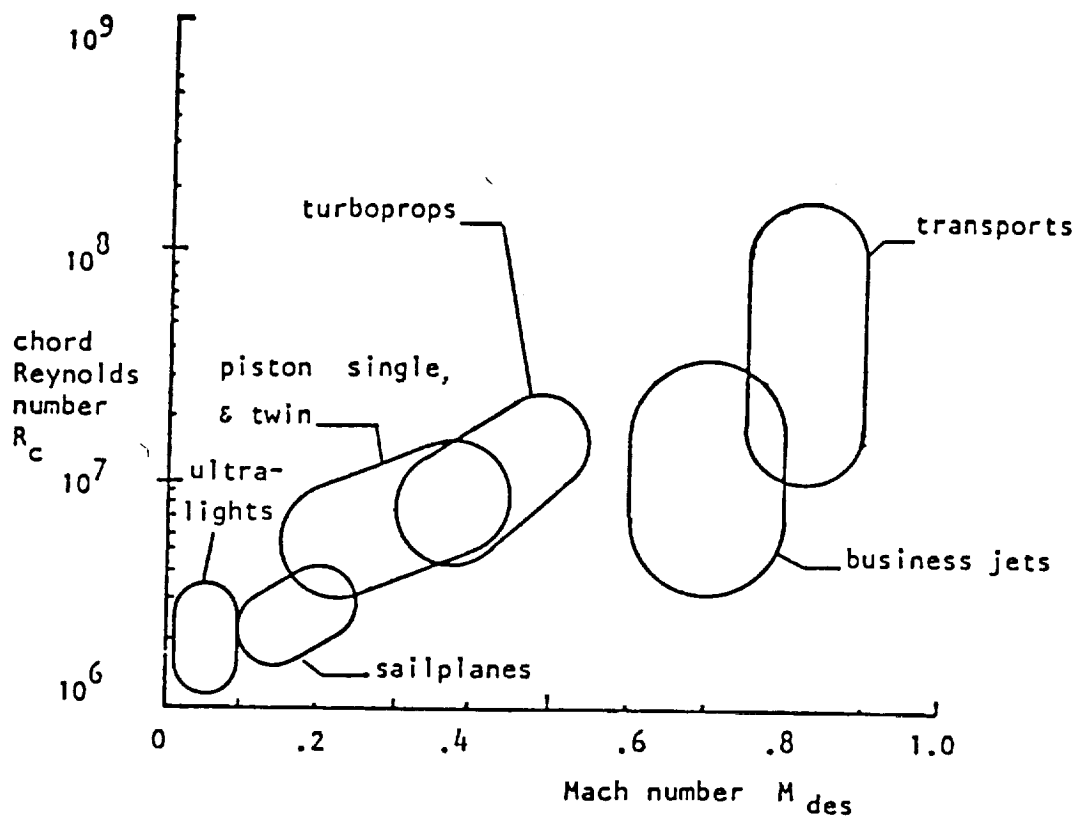


Figure 2.1 Representative cruise Mach and Reynolds numbers for several airplane classes

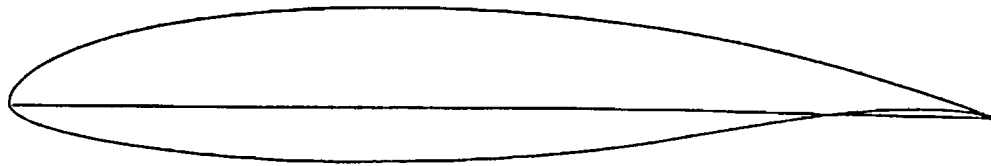
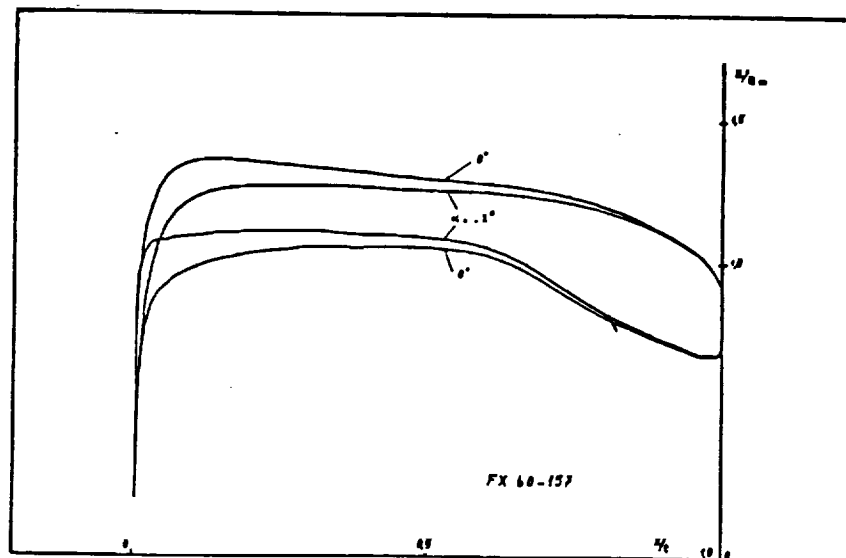
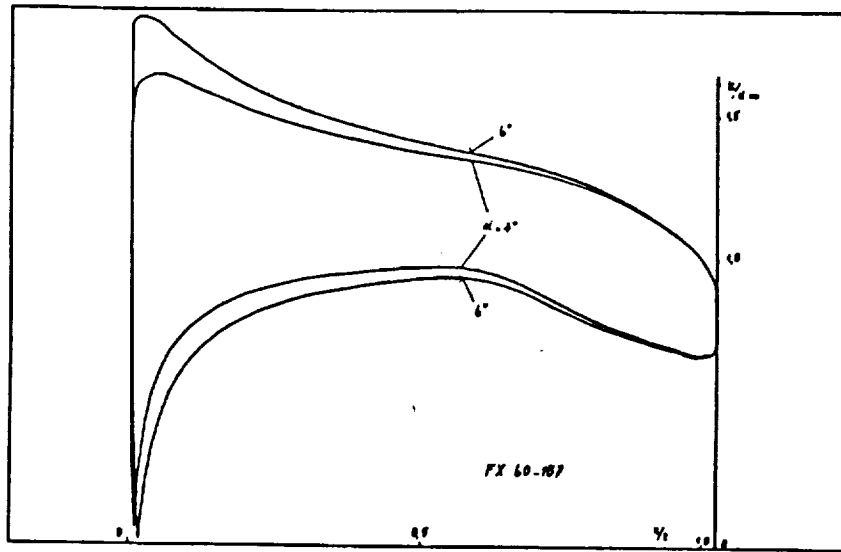
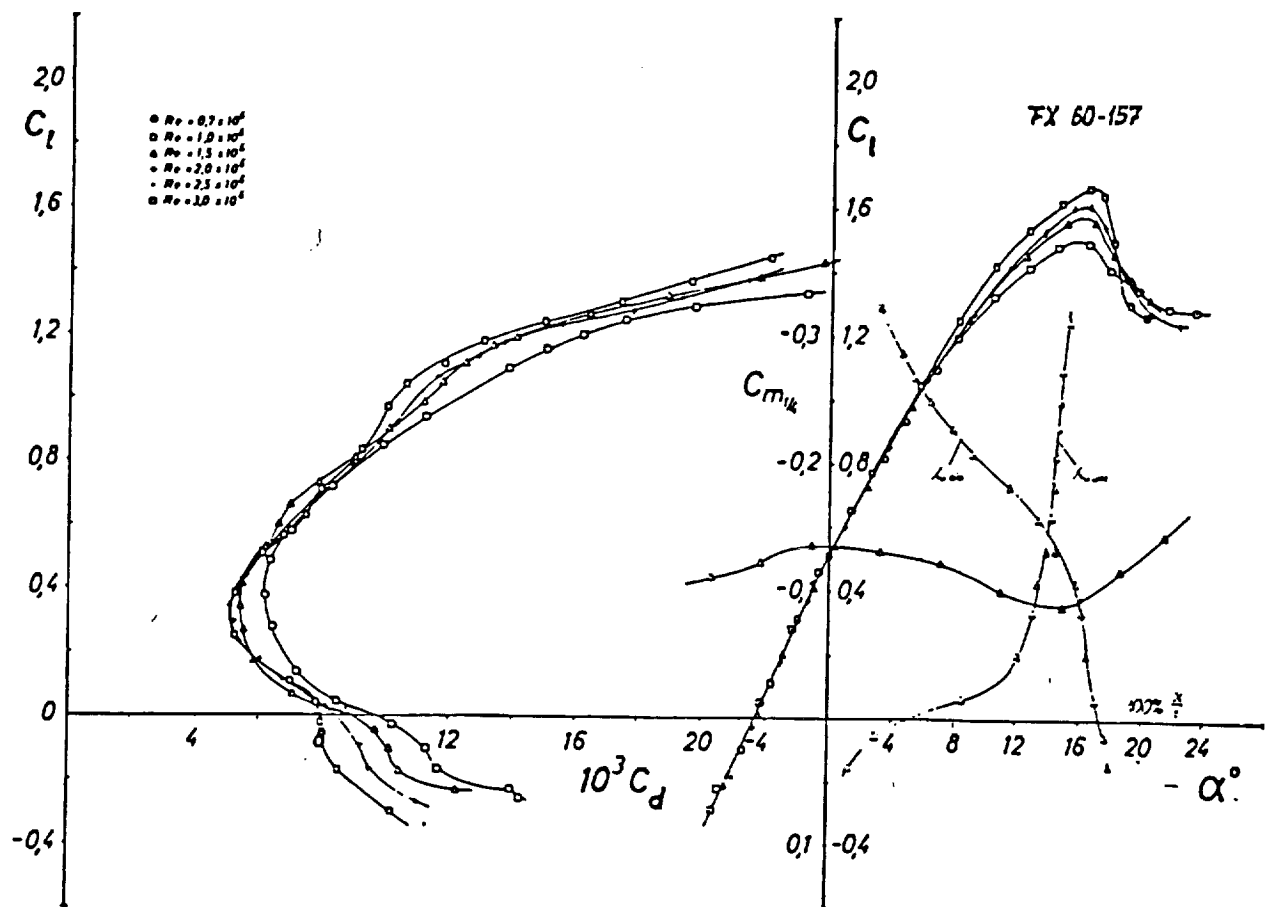


Figure 2.2 a) Wortmann FX 60-157 Airfoil



b) Velocity distributions $\frac{U}{U_{\infty}}$ for several angle-of-attacks (ref. 9)



c) Measured aerodynamic characteristics for Wortmann airfoil with varying Re (ref. 9)

Fig. 2.2 (Concluded)

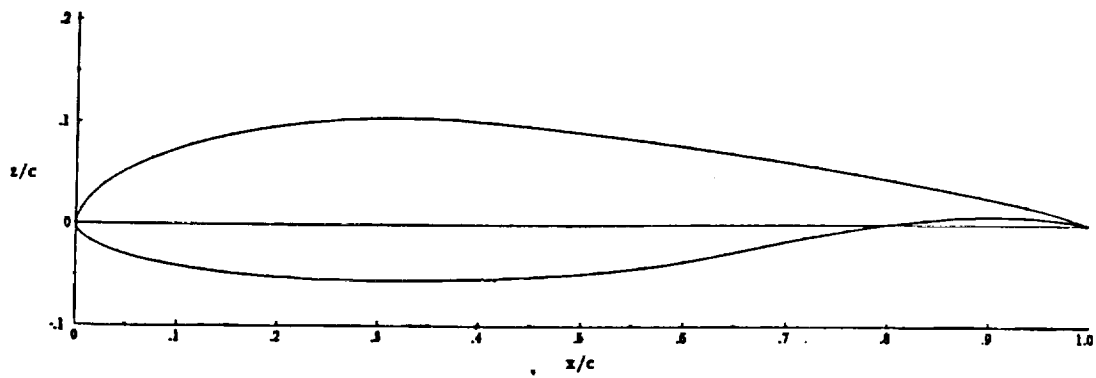
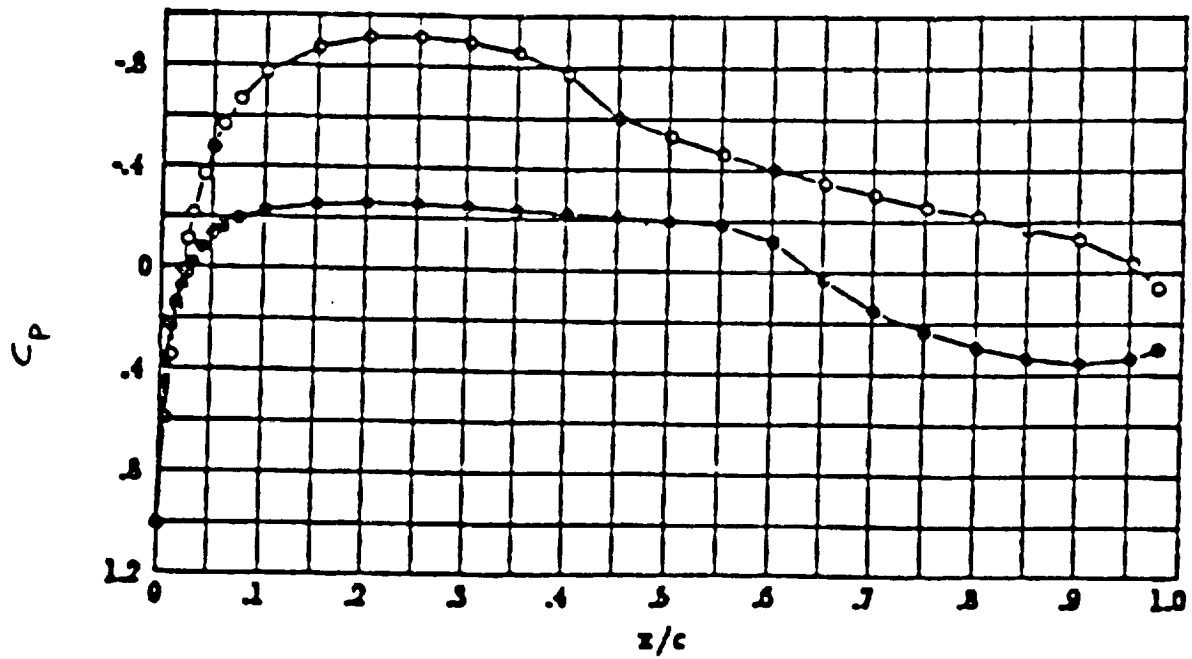


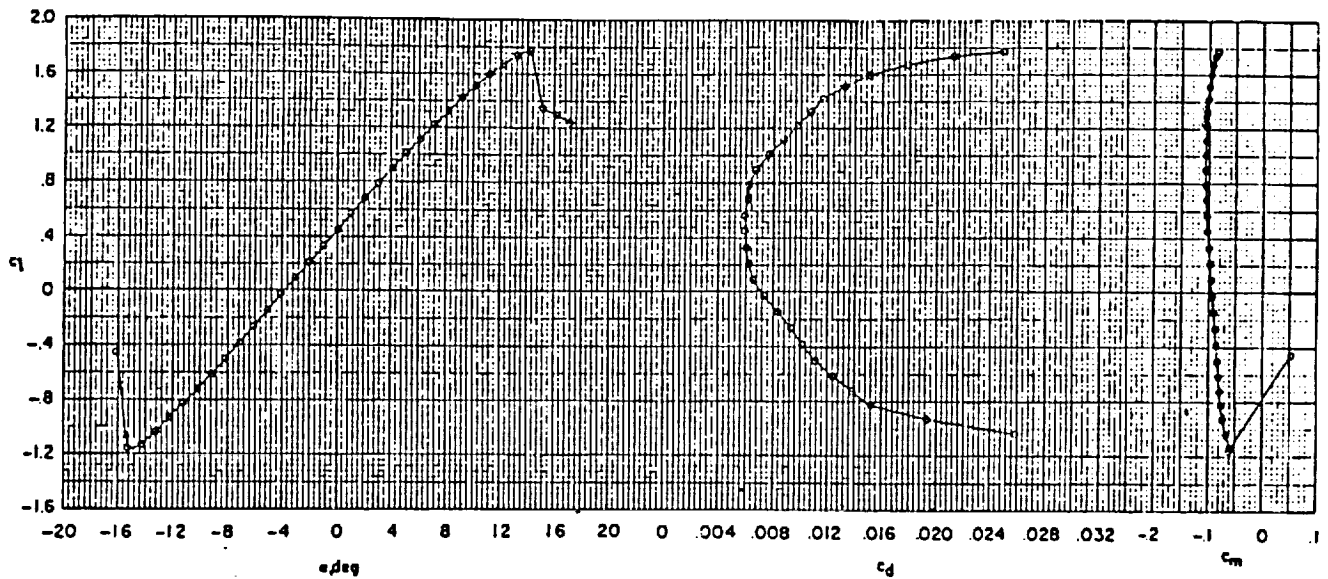
Figure 2.3 a) NLF(1)-0416 airfoil contour



$$\alpha = 0.01^\circ; c_l = 0.447; c_d = 0.0059; c_m = -0.104.$$

$$Re = 4.0 \times 10^6 \quad M = 0.10$$

b) Measured pressure distribution NLF(1)-0416 (ref. 12)



$$R = 4.0 \times 10^6.$$

c) Lift curve, drag polar, and pitching moment curve for NLF(1)-0416 (ref. 12)

Figure 2.3 (Concluded)

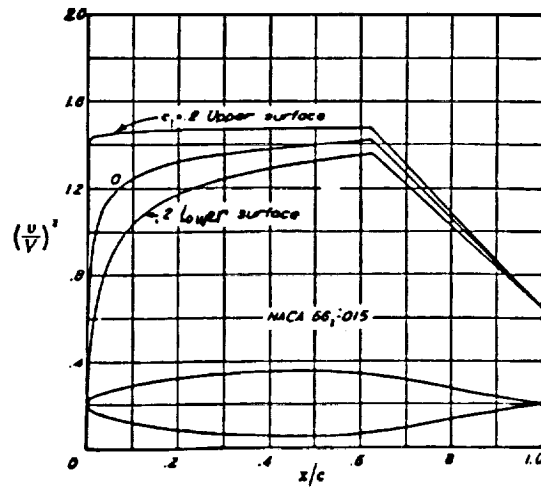


Figure 2.4 NACA 66₂-015 pressure distribution (ref. 13)

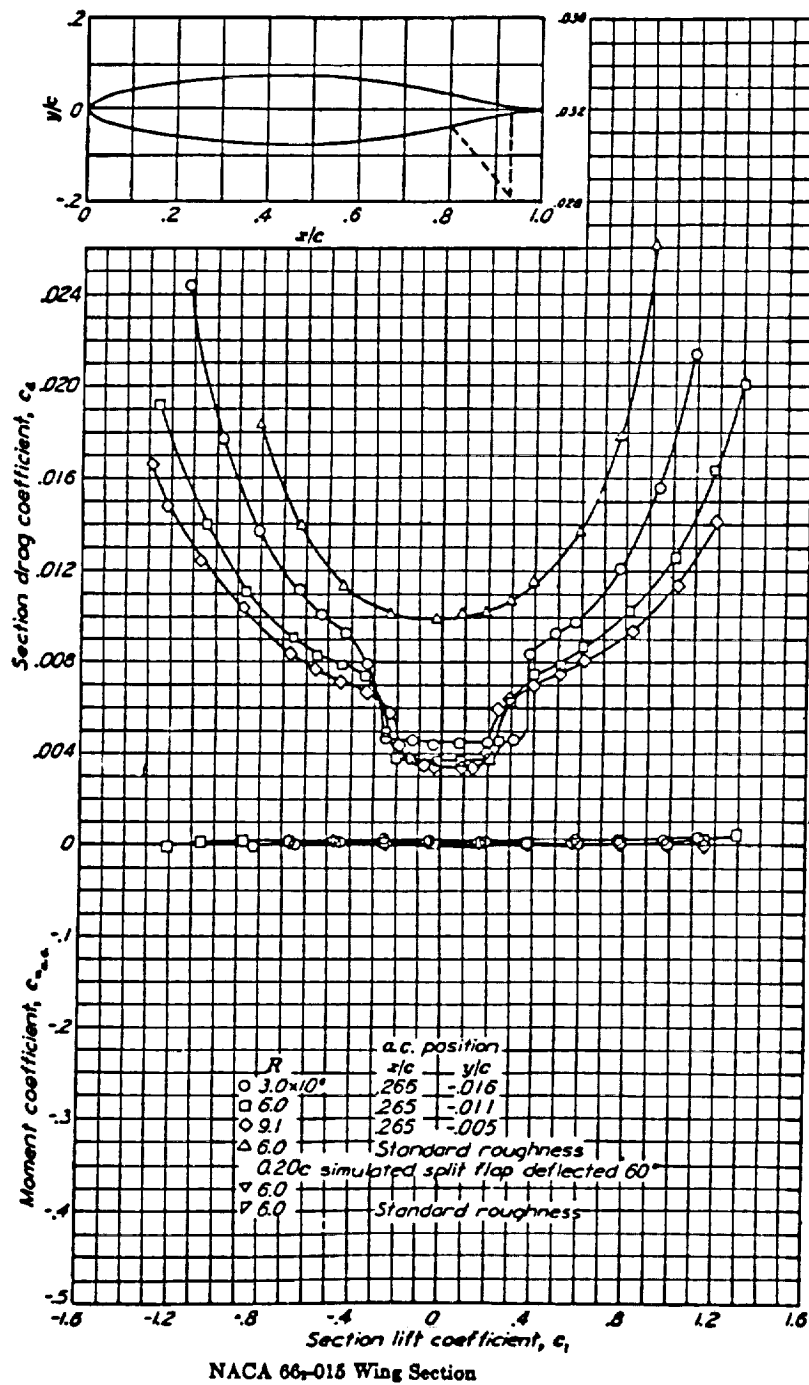


Figure 2.5 NACA 66₂-015 drag polars and pitching moment curves (ref. 13)

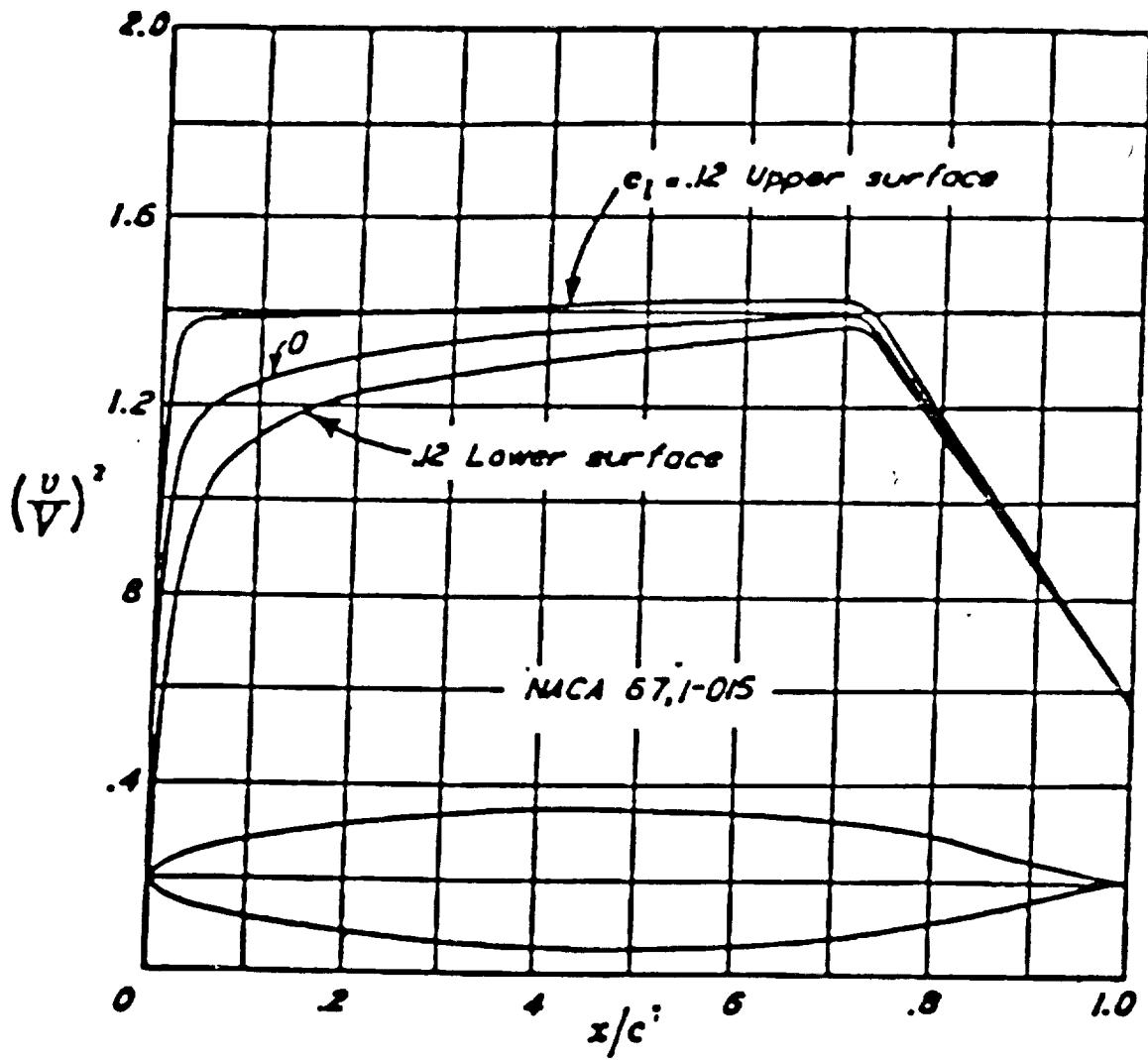


Figure 2.6 NACA 67₁-015 contour and pressure distribution (ref. 13)

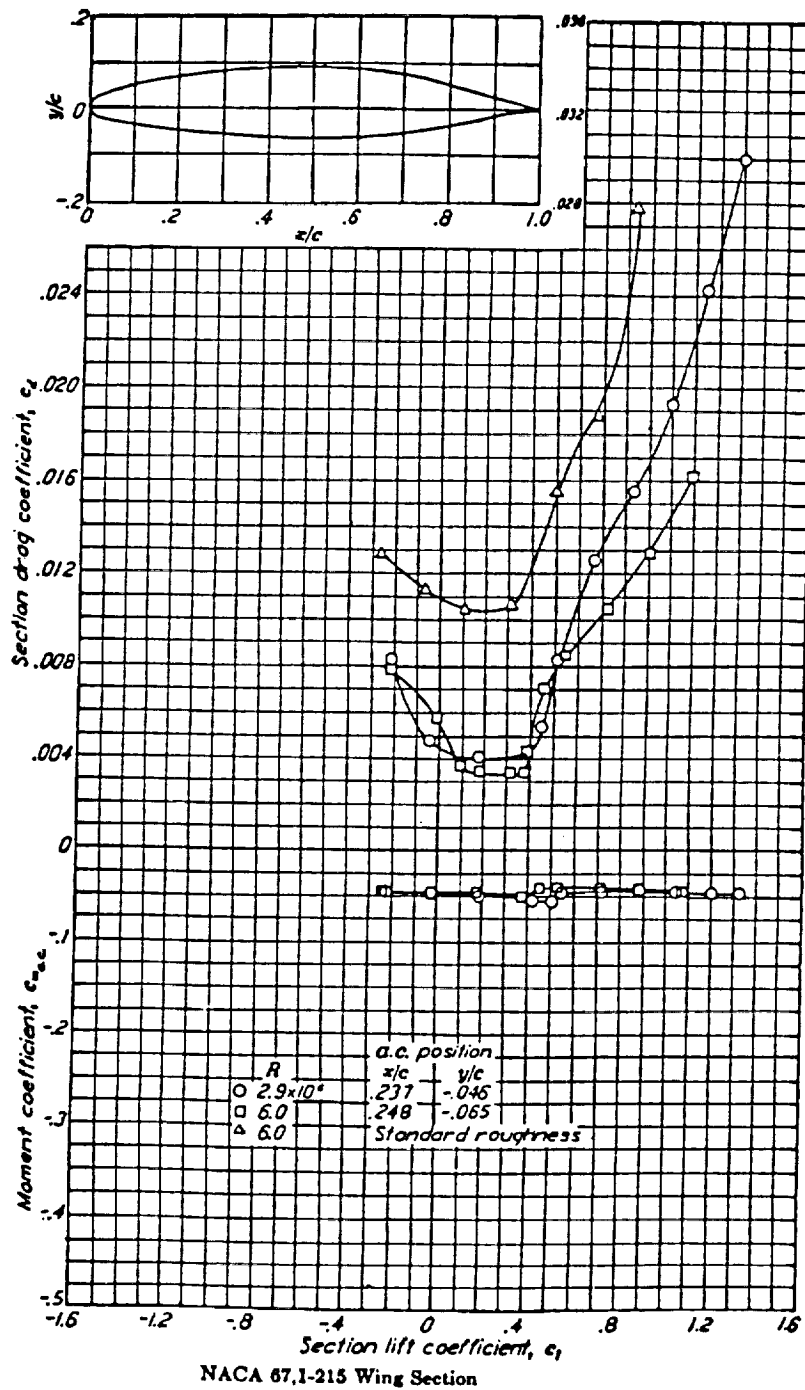
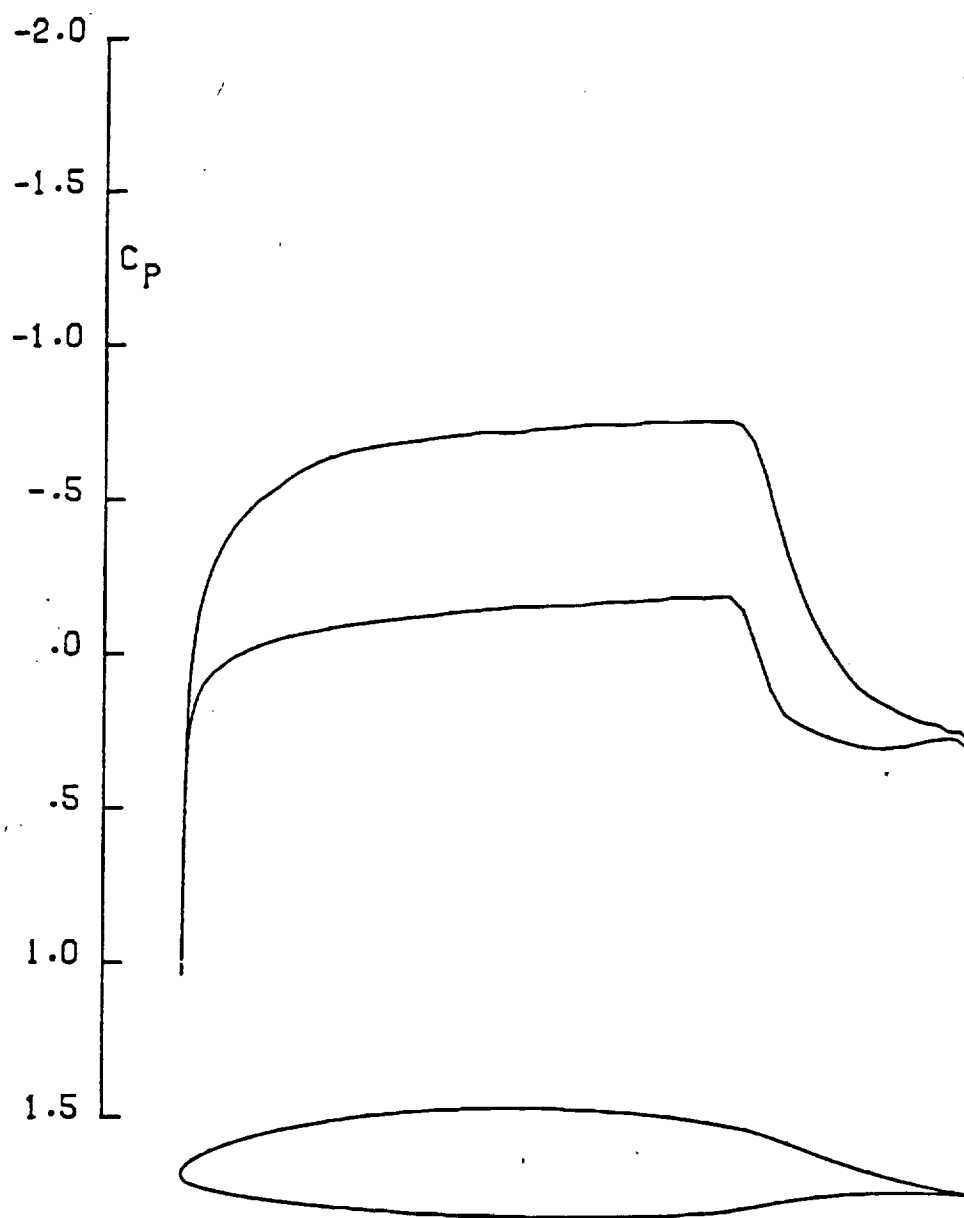


Figure 2.7 NACA 67₁-215 drag polar and moment curve



$$c_l = 0.454; \alpha = -.954; c_m = -.0892$$

$$M = 0.4$$

Figure 2.8 NASA NLF(1)-0414F airfoil contour and pressure distribution
(ref. 14)

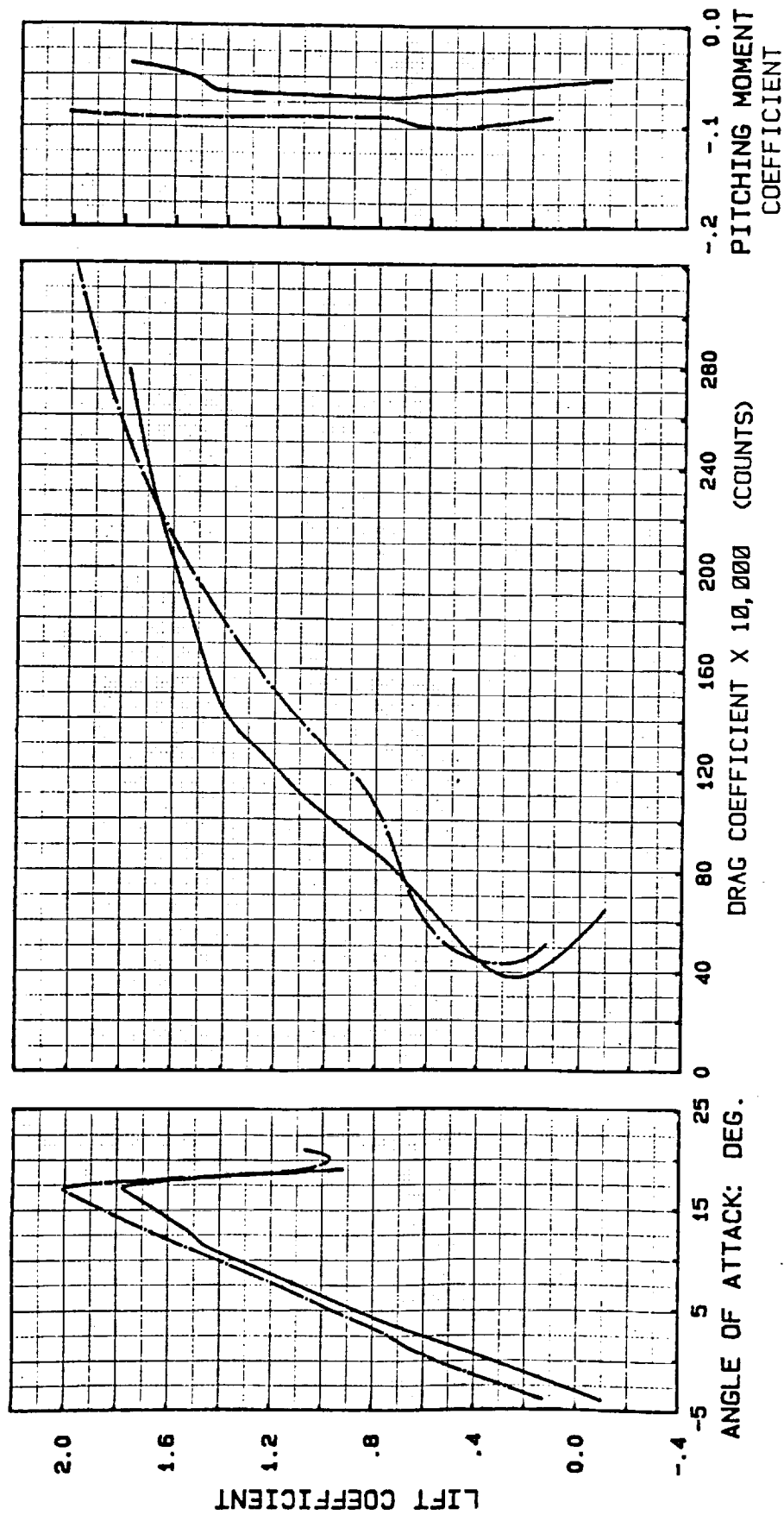


Figure 2.9 Aerodynamic characteristics of NLF(1)-0414F and derivative as calculated by the Eppler code using natural transition.

Re = 8.9×10^6

— NLF(1)-0414F

- - - derivative

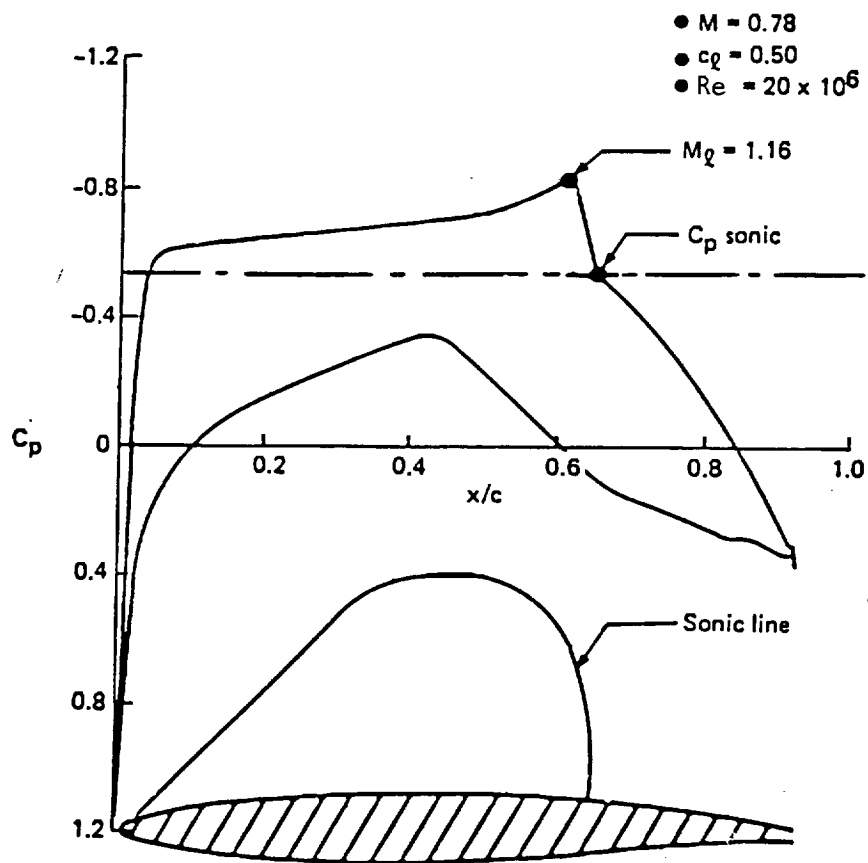


Figure 2.10 Supercritical pressure distribution for design case of Boeing NLF airfoil (ref. 16)

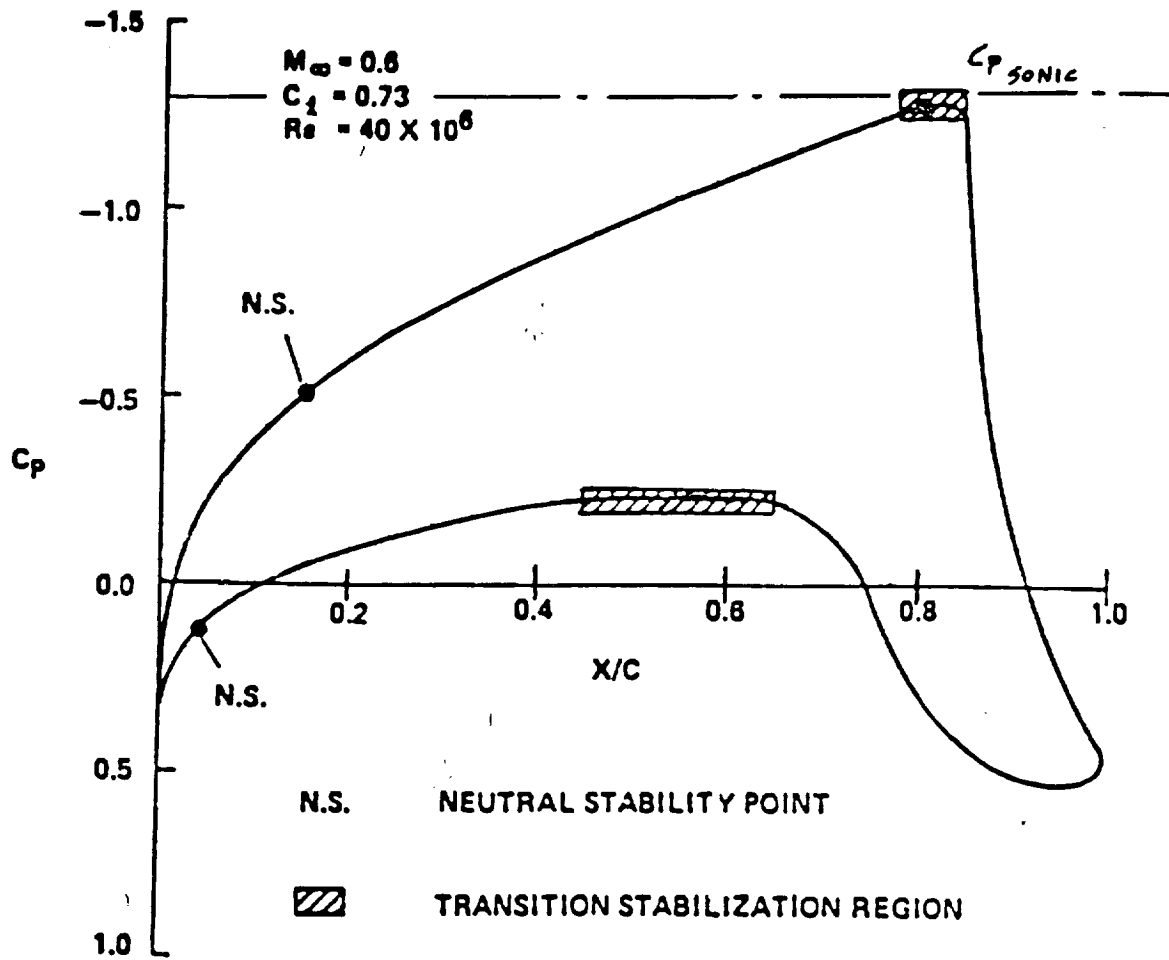
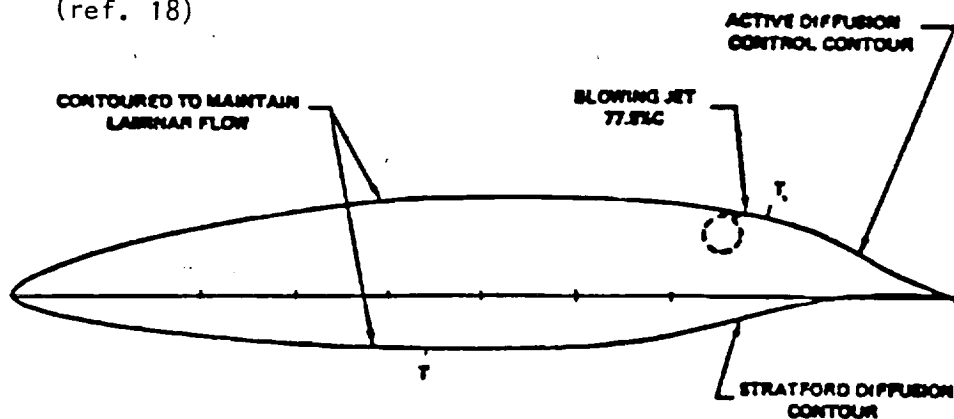


Figure 2.11 a) Subcritical pressure distribution for design case of Vought-ATC NLF airfoil (ref. 18)



b) ATC/Laminar airfoil contour

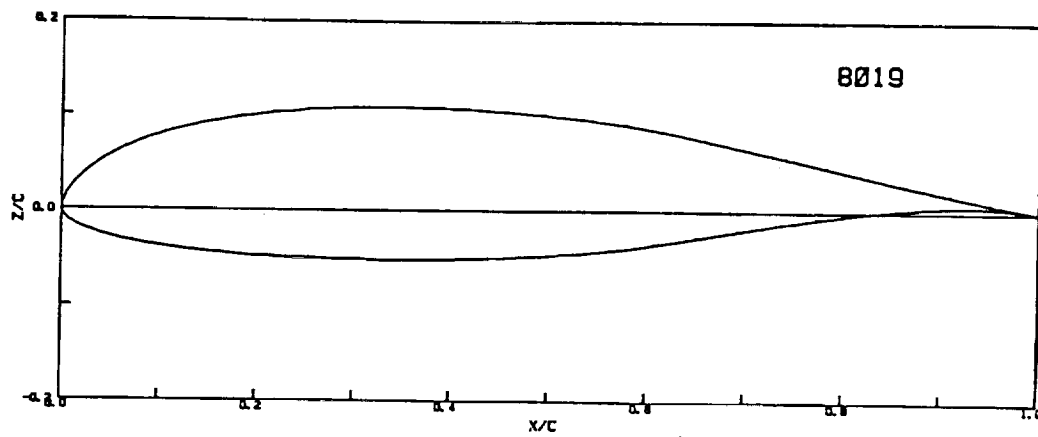
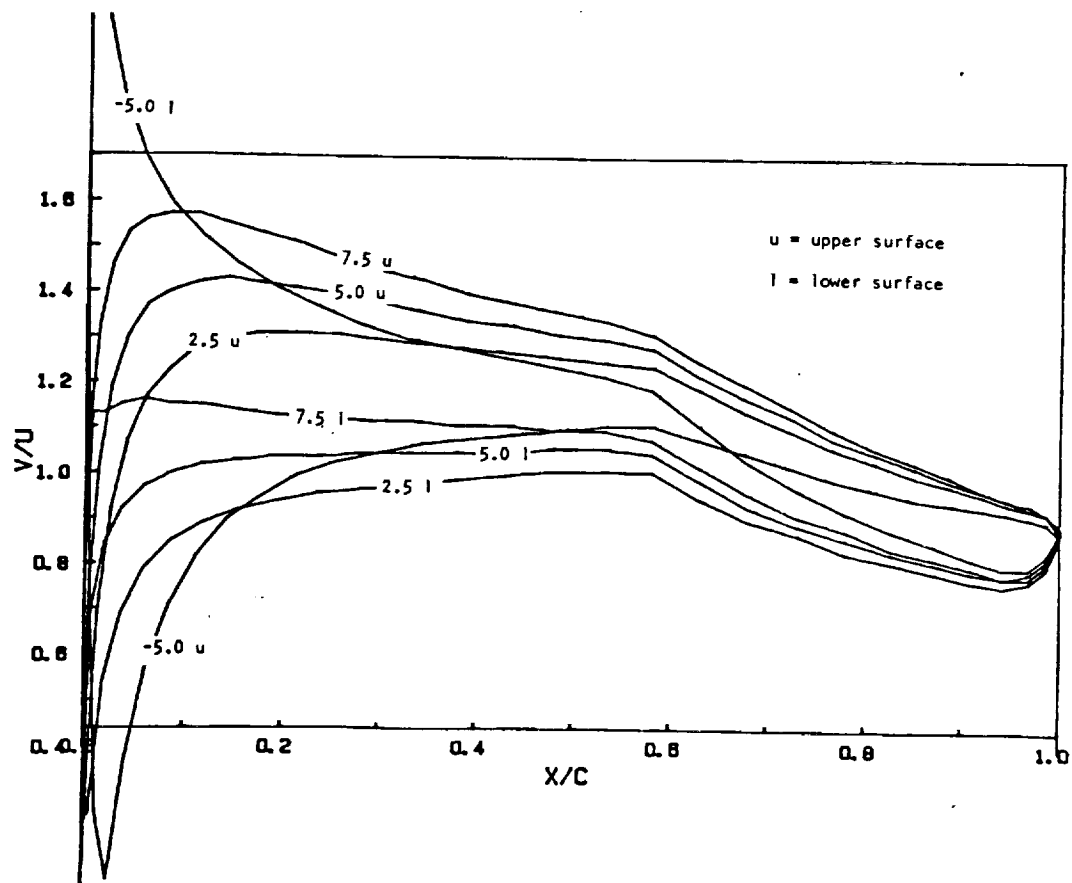


Figure 3.1 a) KU-Airfoil 8019 designed by using Eppler design mode



b) Velocity distributions for KU-8019

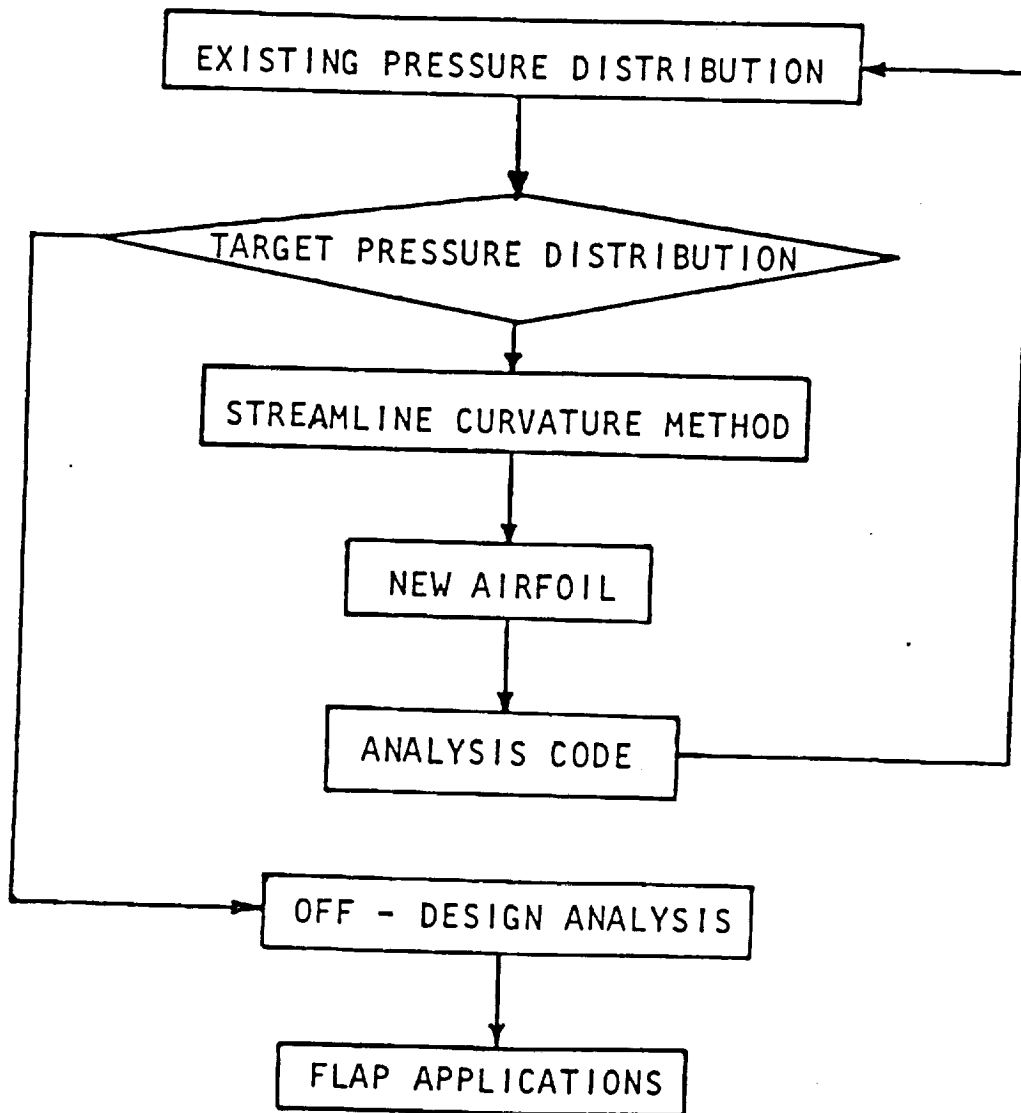


Figure 3.2 Airfoil design and modification procedure used at KU

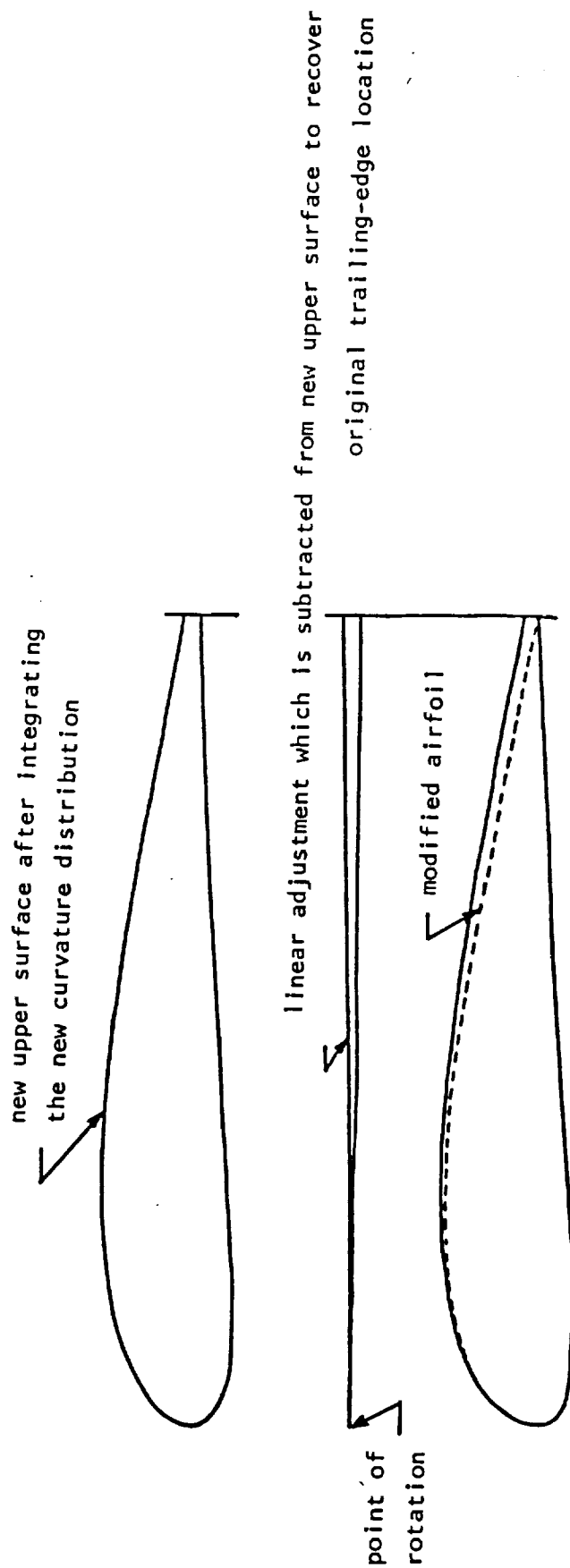


Figure 3.3 Method to recover trailing-edge location after integration.

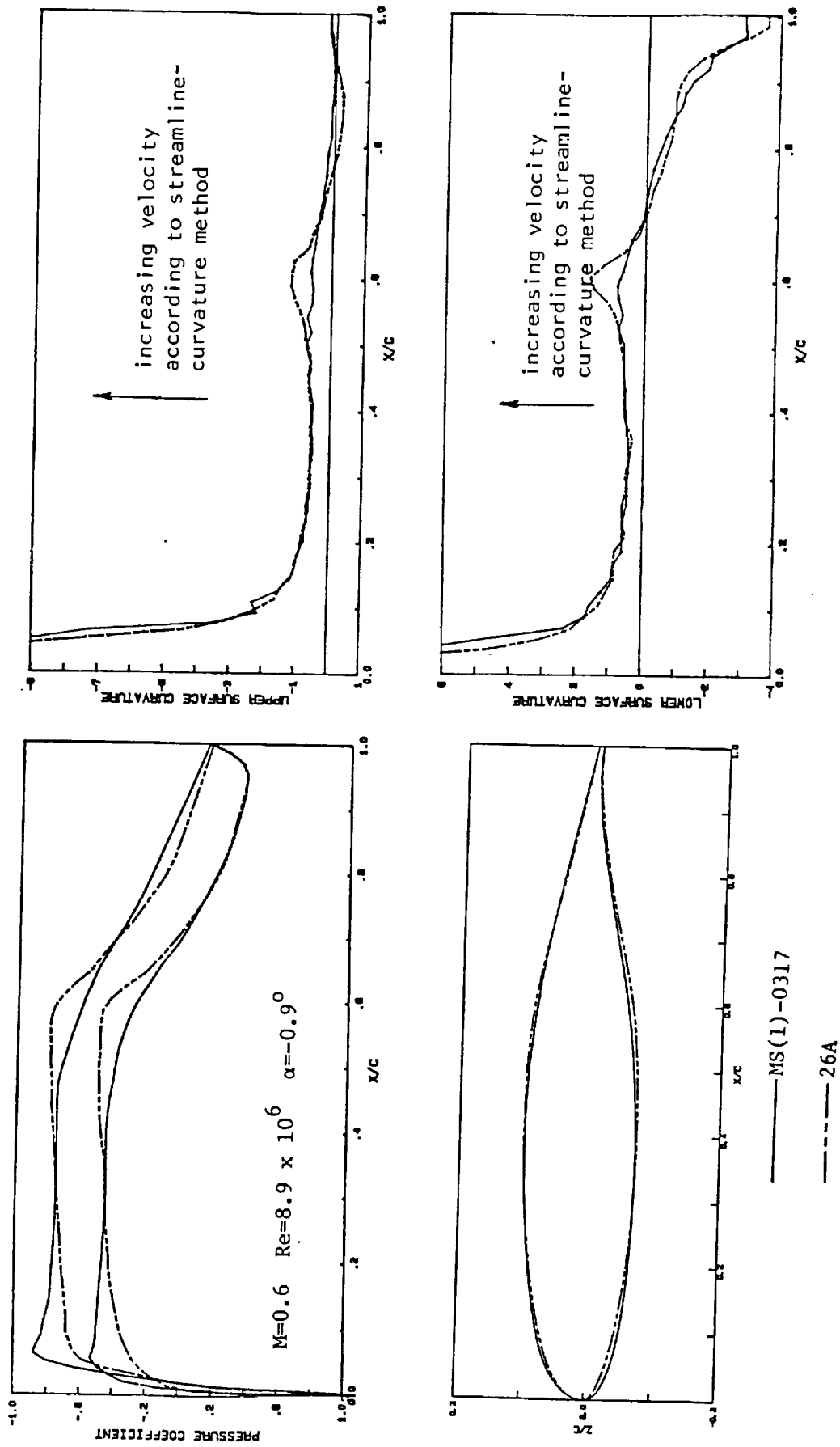
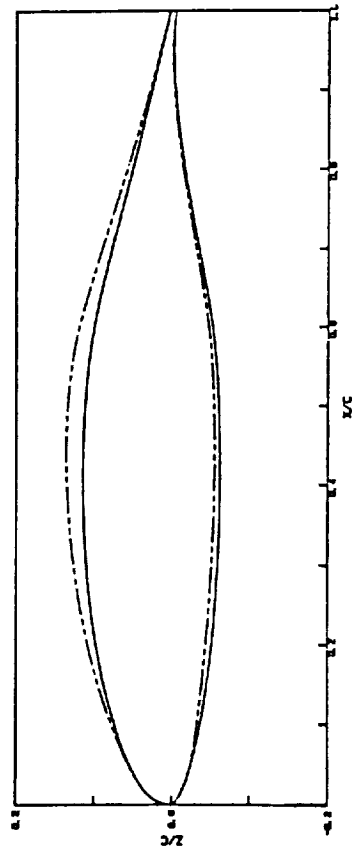
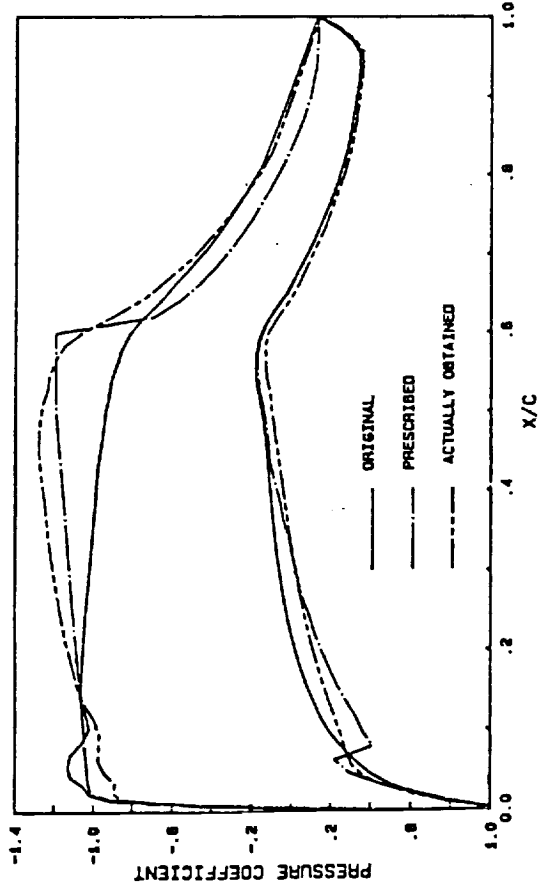
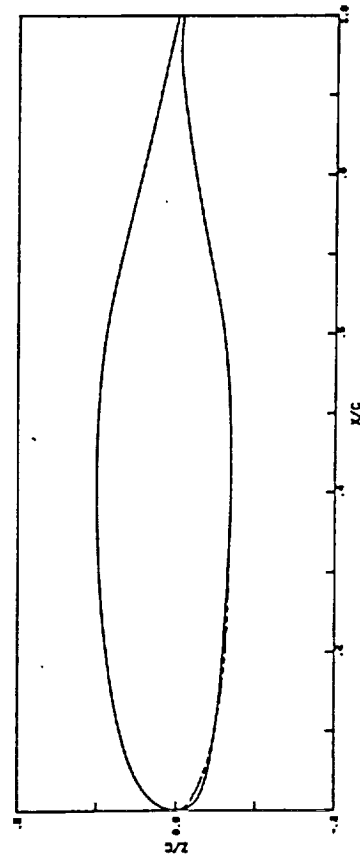
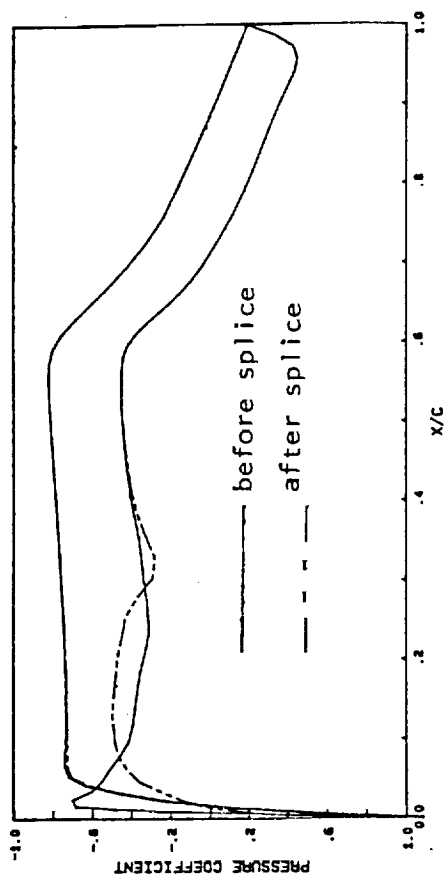


Figure 3.4 Example of modified streamline curvature method used to obtain airfoil 26A.



a) Trial and error method of preventing the formation of a spike on the lower surface; a spike was input for the target pressure distribution.



b) Splicing new leading edge to eliminate spike in lower surface pressure distribution. (NLF-0416 was used here.)

Figure 3.5 Methods to eliminate leading-edge spikes in pressure distributions.

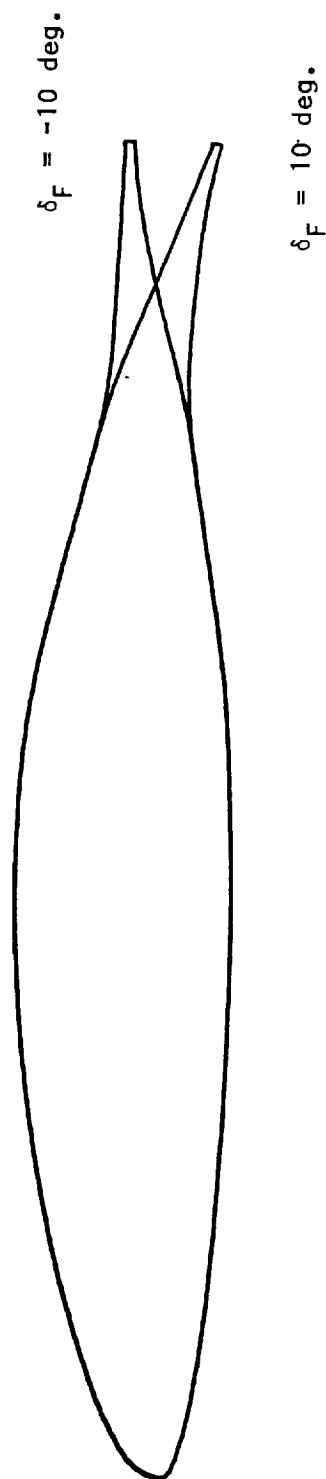


Figure 4.1 Airfoil contour resulting from Eppler flapping routine

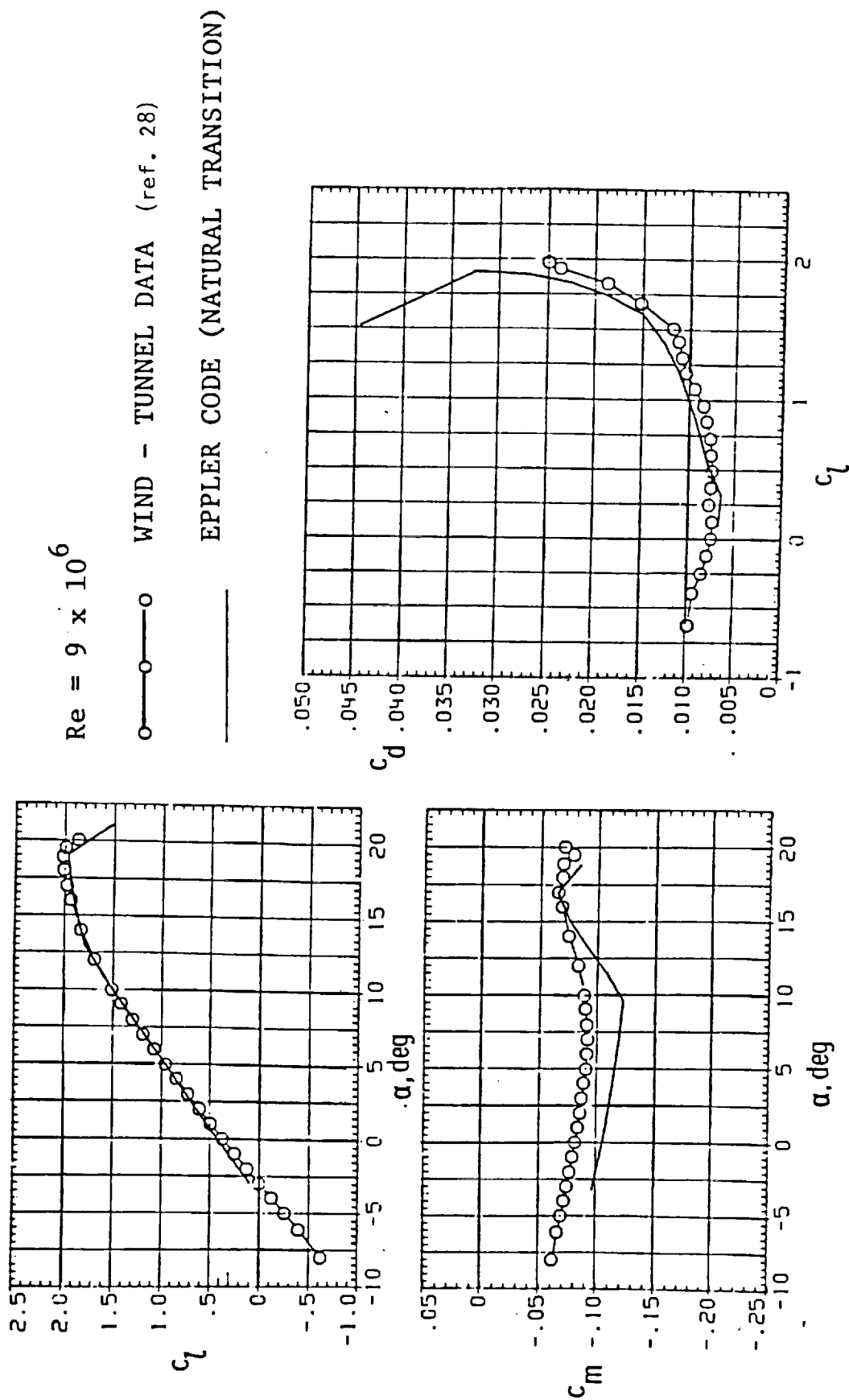


Figure 4.2 Low-speed characteristics of HS(1)-0317. Comparison between Eppler code prediction and wind-tunnel data

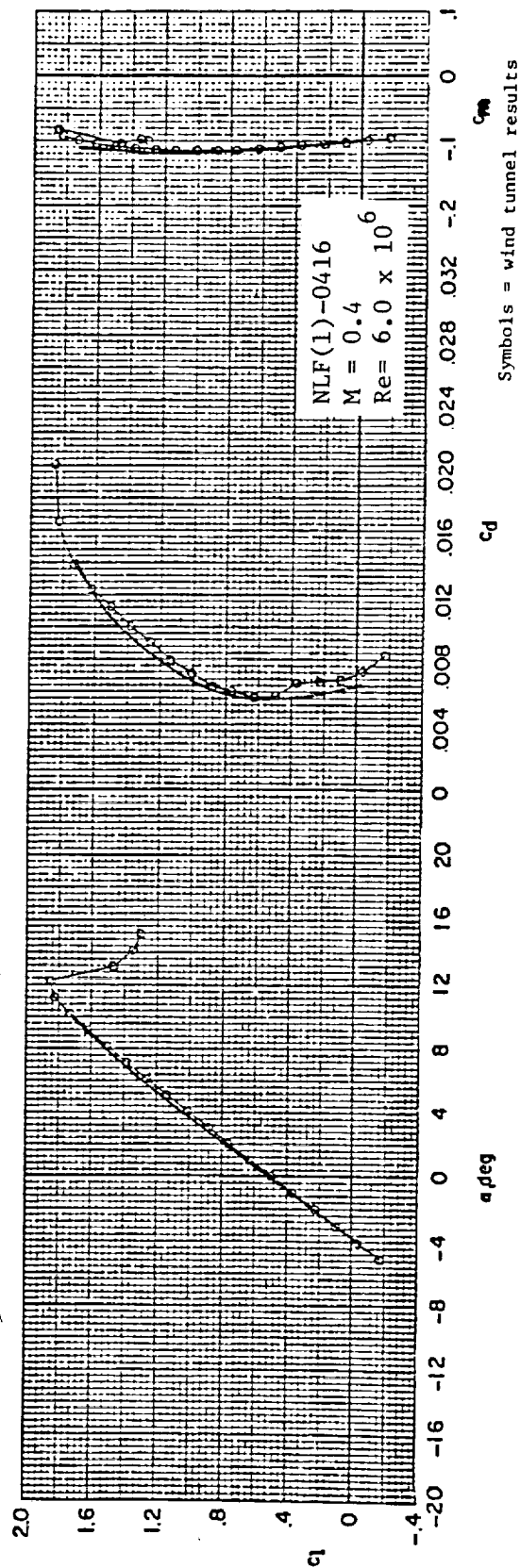
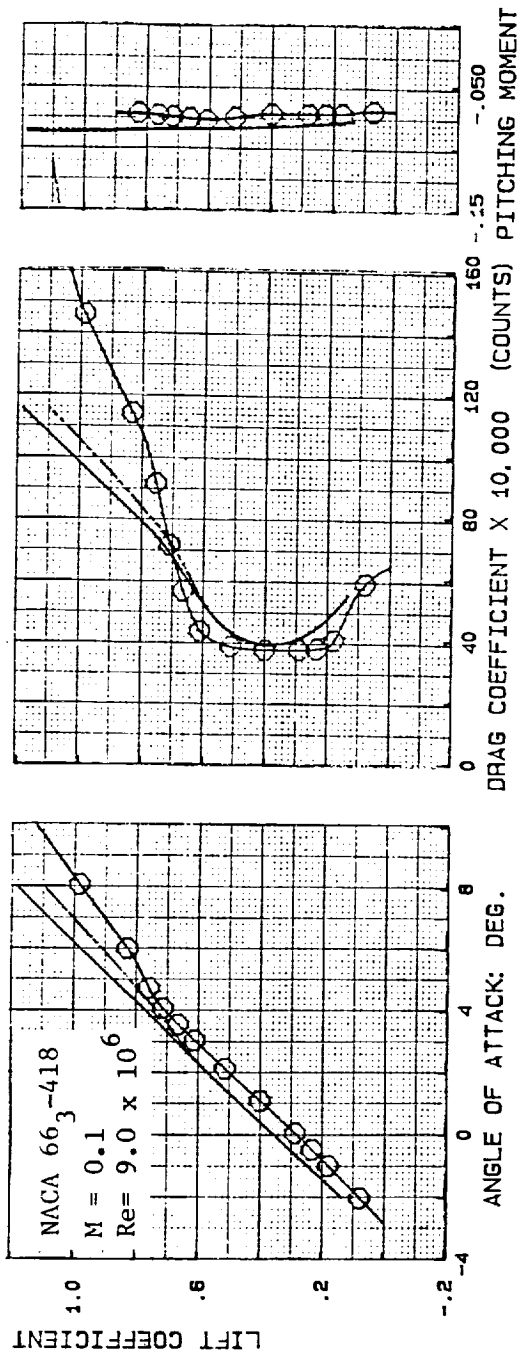


Figure 4.3 Comparison of wind-tunnel data to NCS calculations using natural transition.

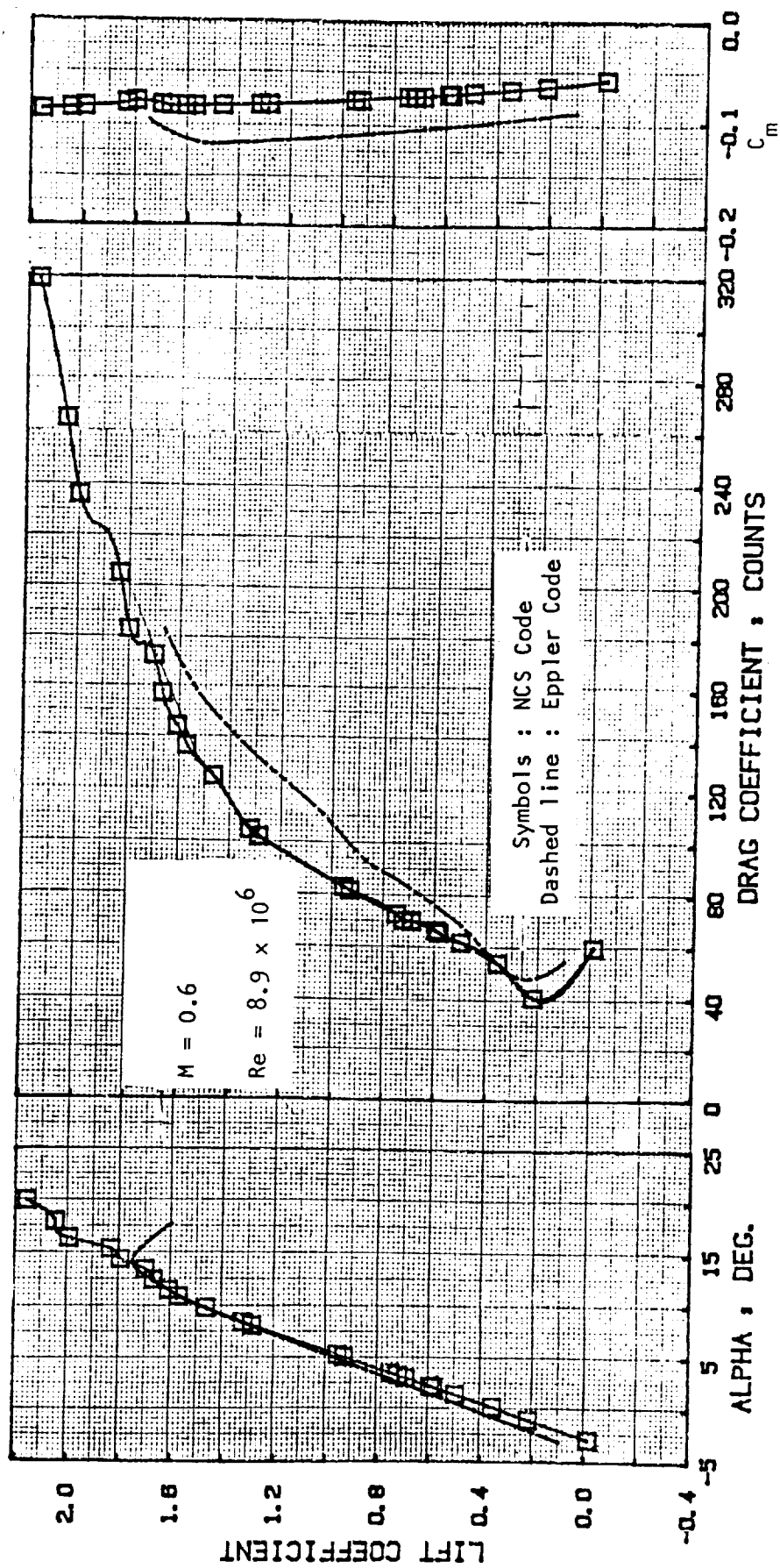


Figure 4.4 Comparison of aerodynamic characteristics of airfoil KU-26 by Eppler and NCS codes.

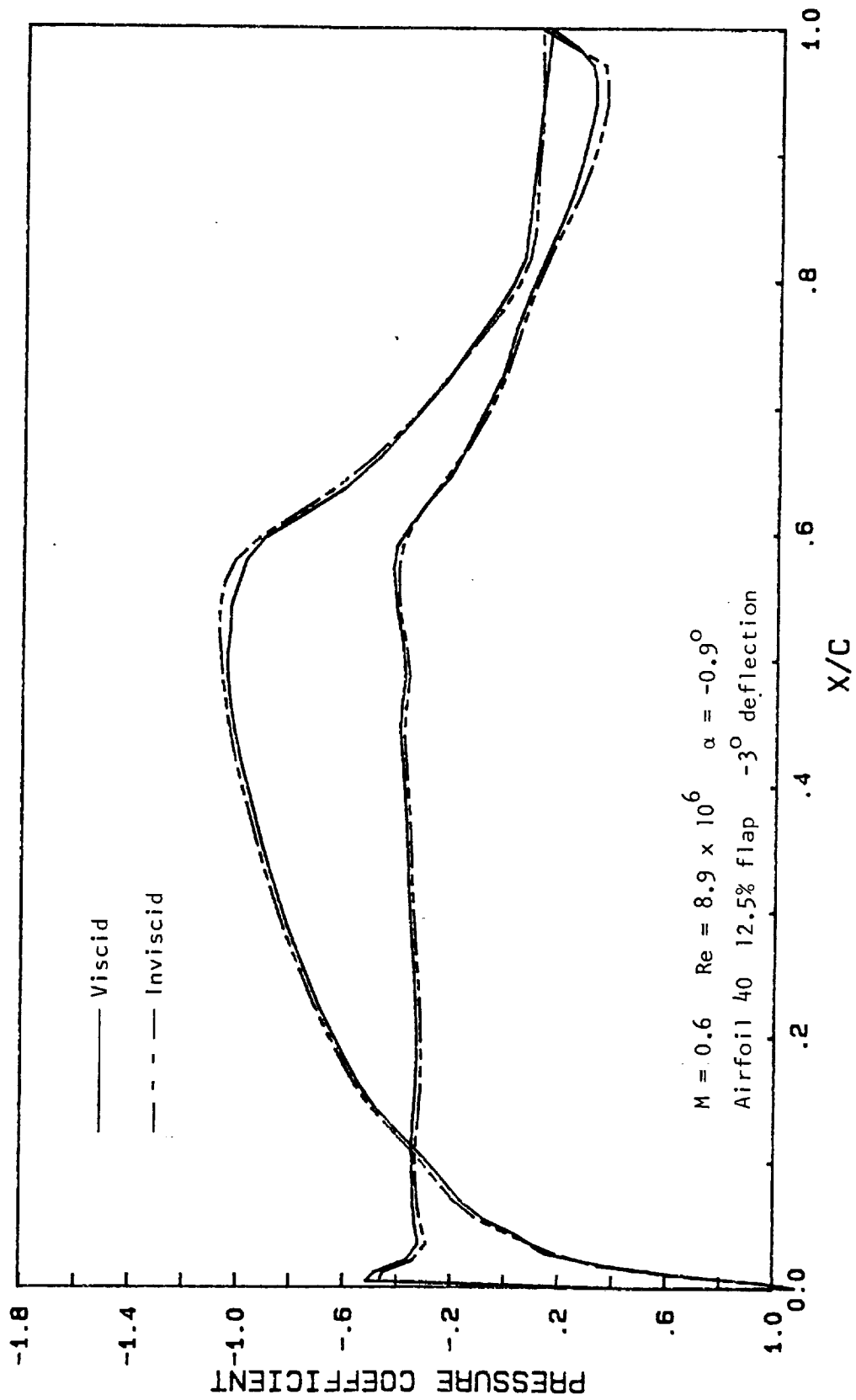


Figure 4.5 Comparison of viscous and inviscid pressure distributions calculated by the NCS code using natural transition.

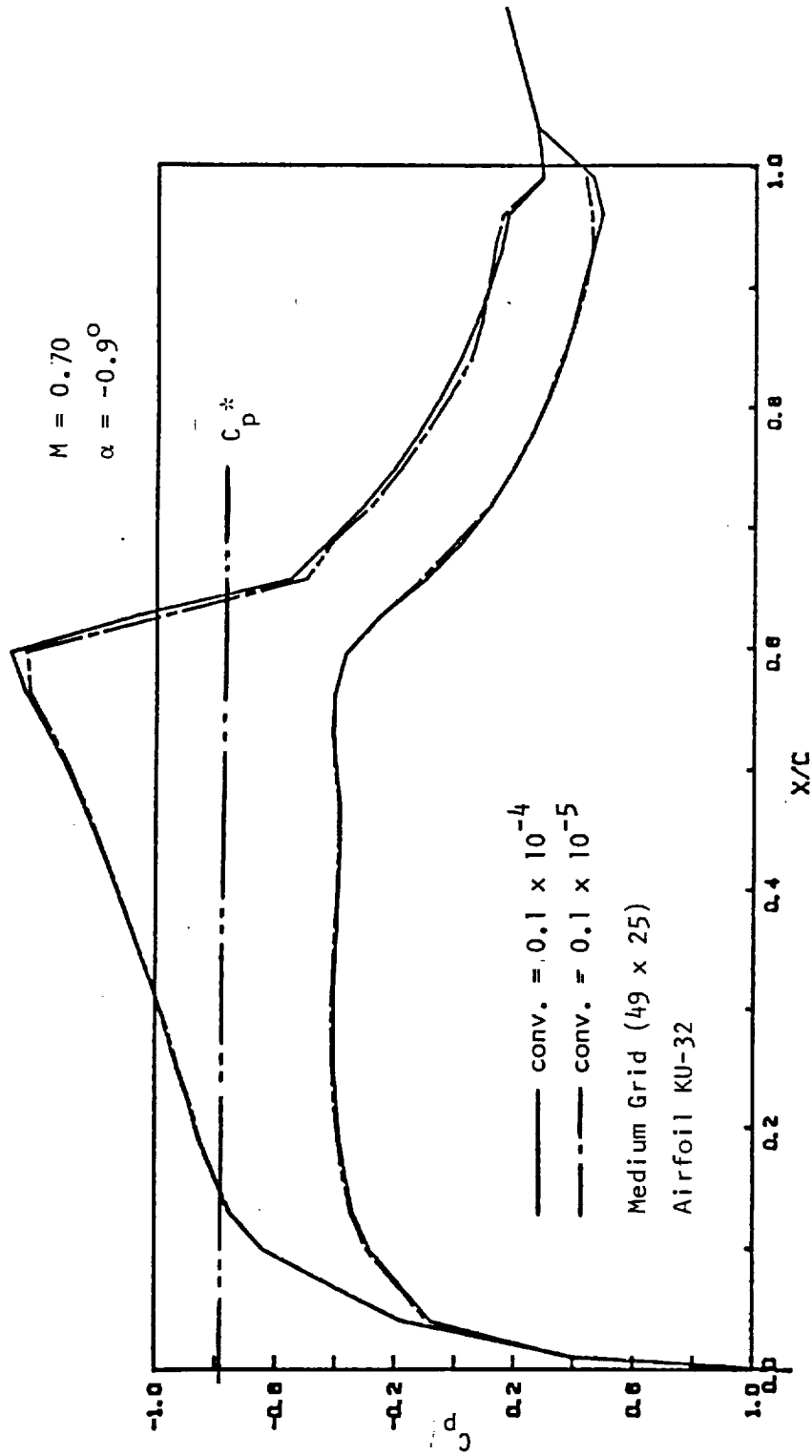


Figure 4.6 Comparison of convergence parameter in Transep code

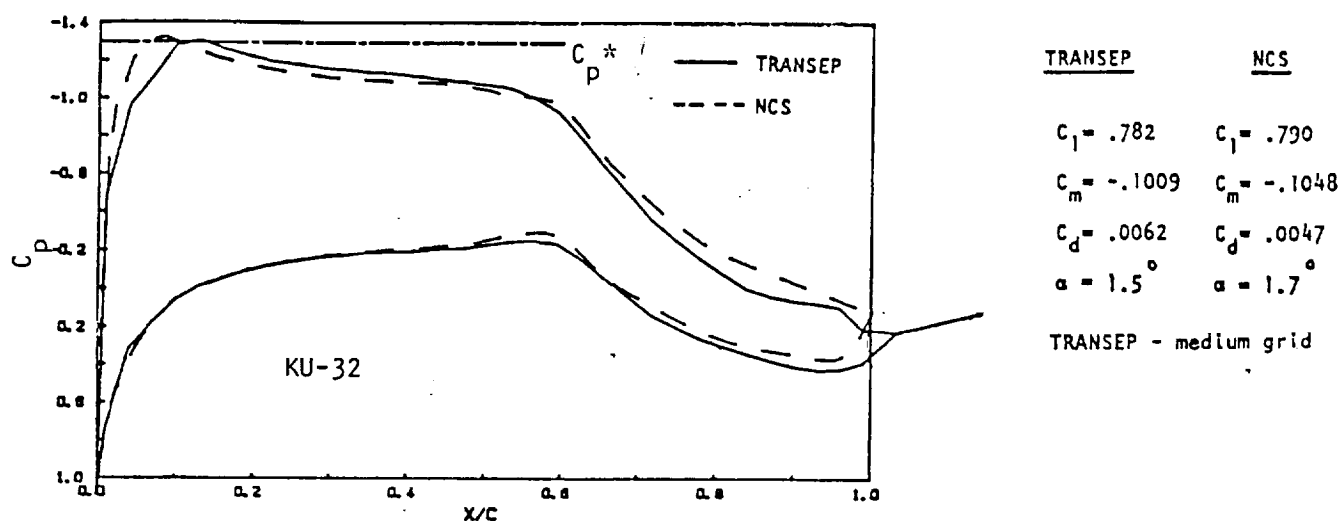


Figure 4.7 Pressure distribution comparison for Transep and NCS at $M = 0.60$

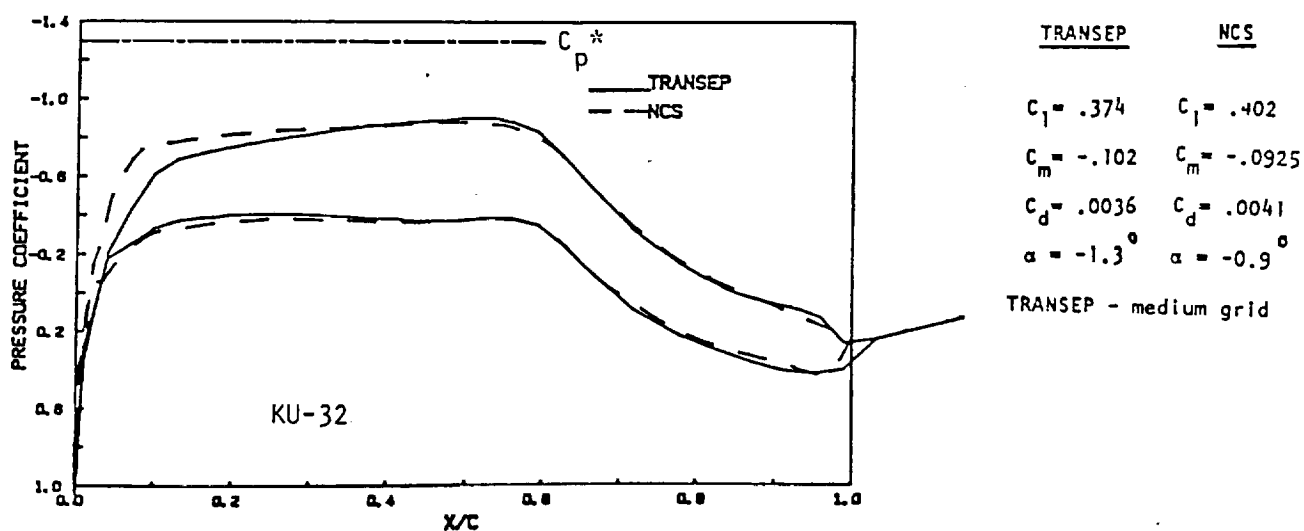


Figure 4.8 Pressure Distribution comparison for Transep and NCS at $M = 0.60$

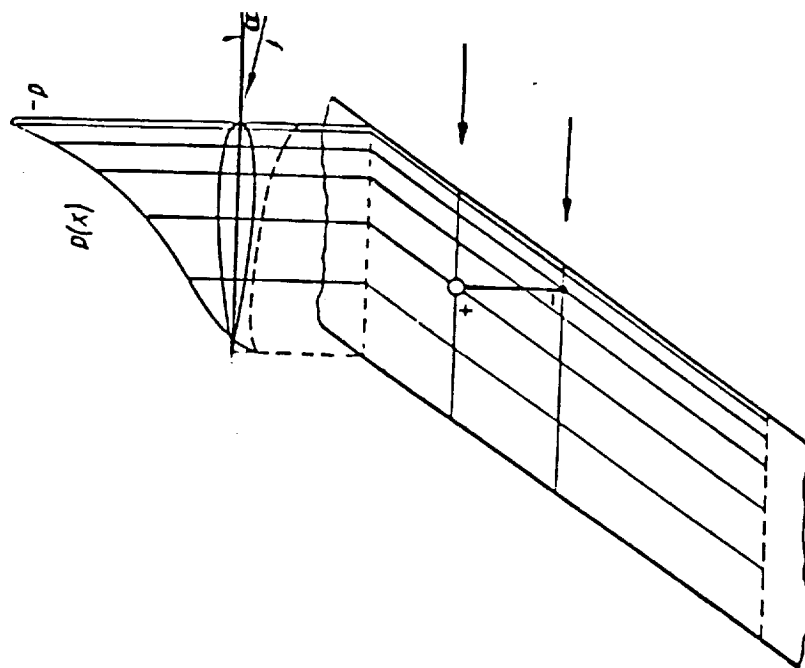
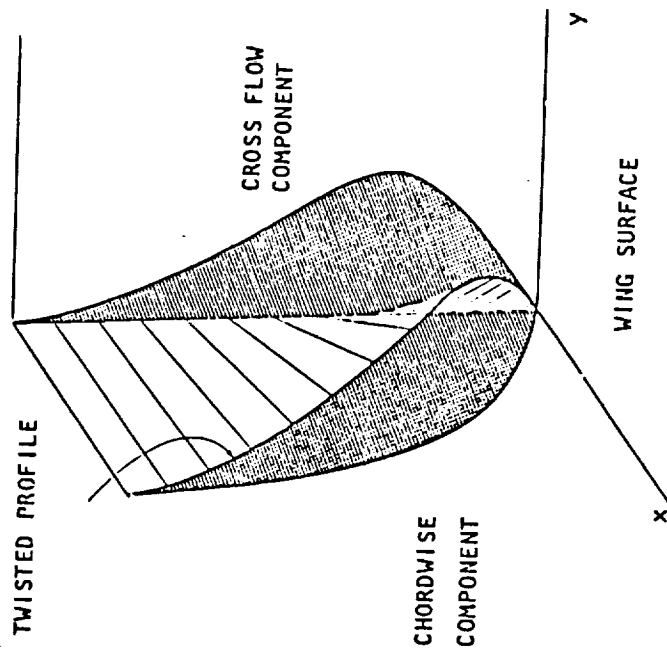


Figure 5.1 a) Explanation of origin of cross-flow on a swept wing



b) Components of boundary-layer velocity profile over a swept wing

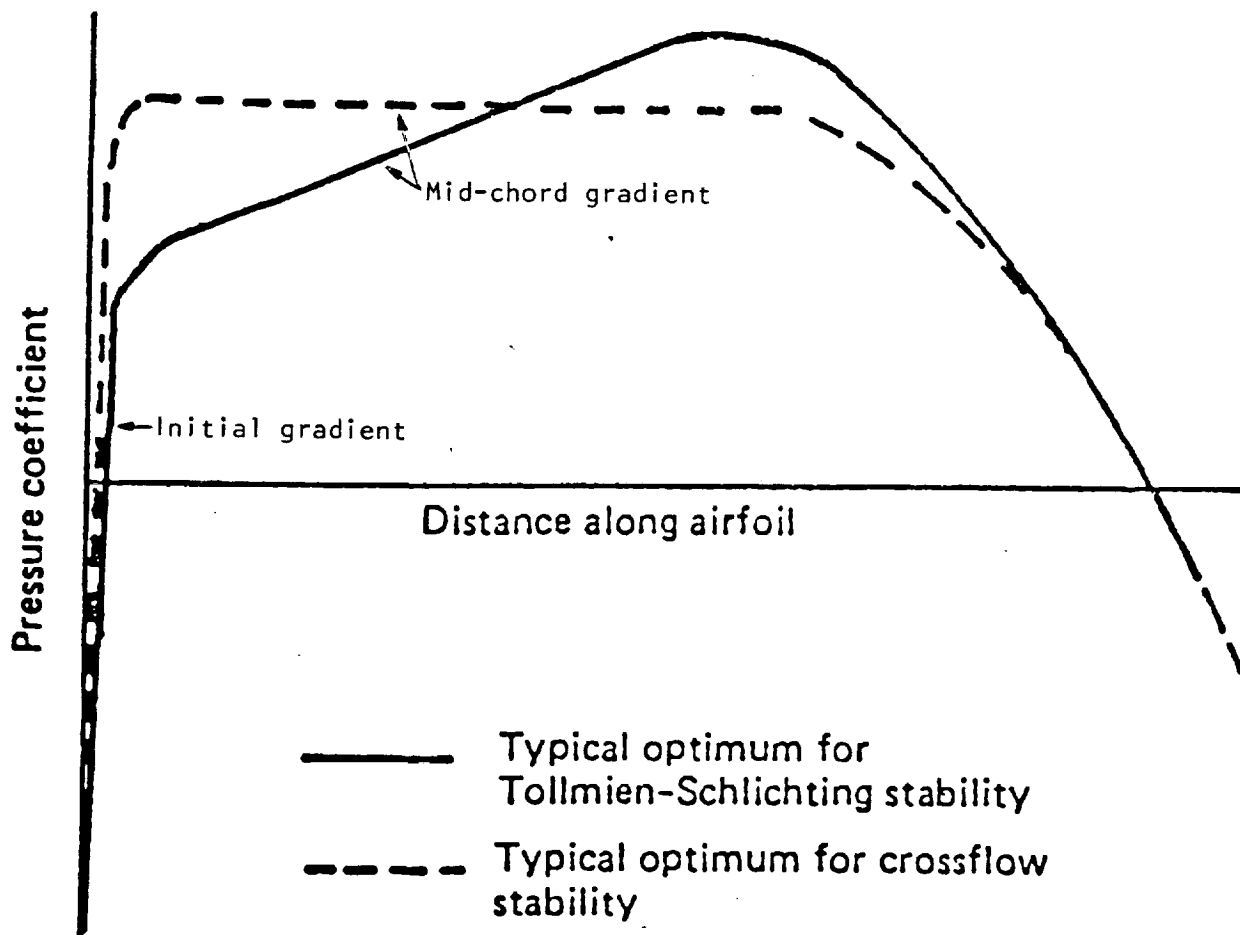
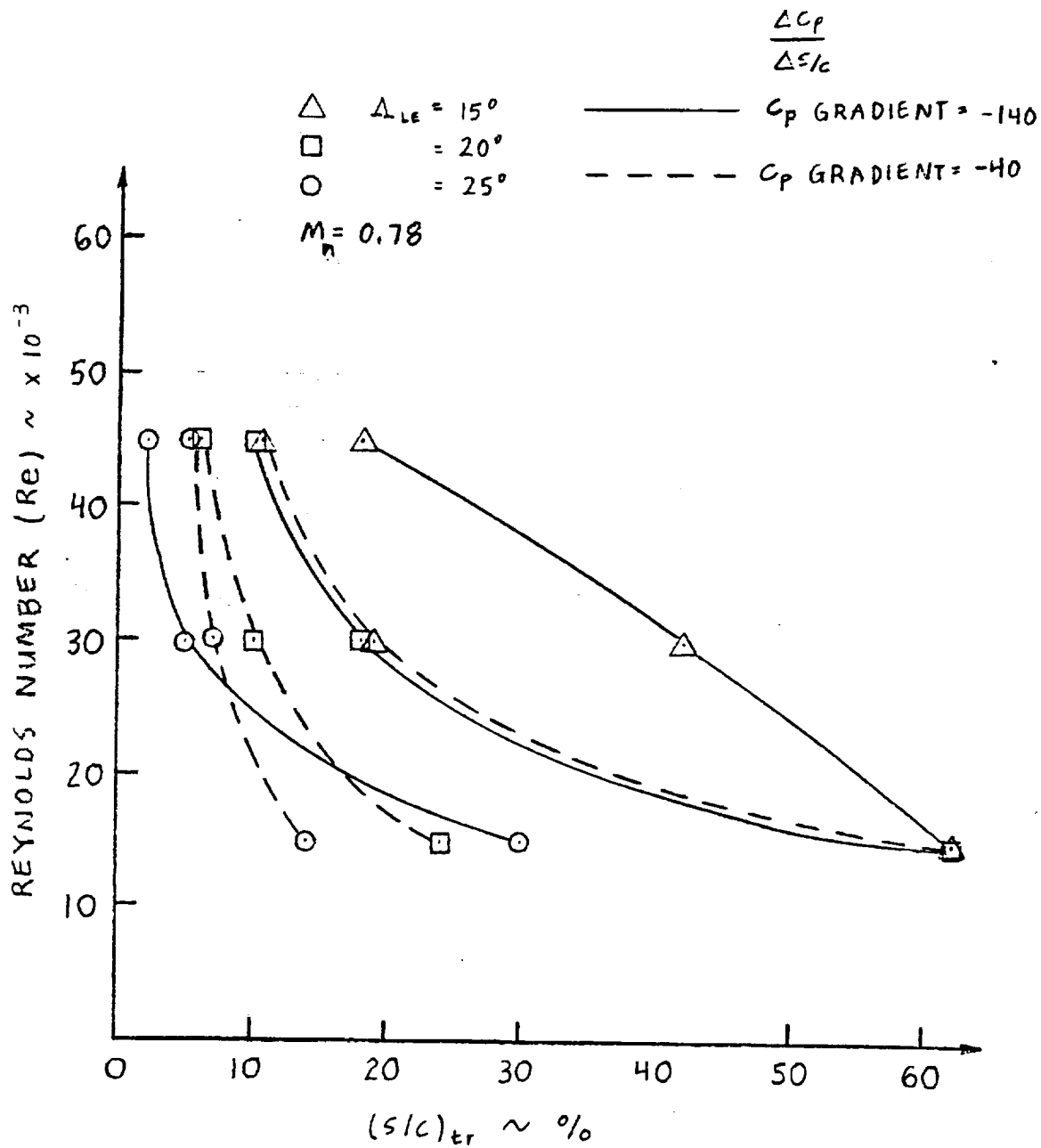
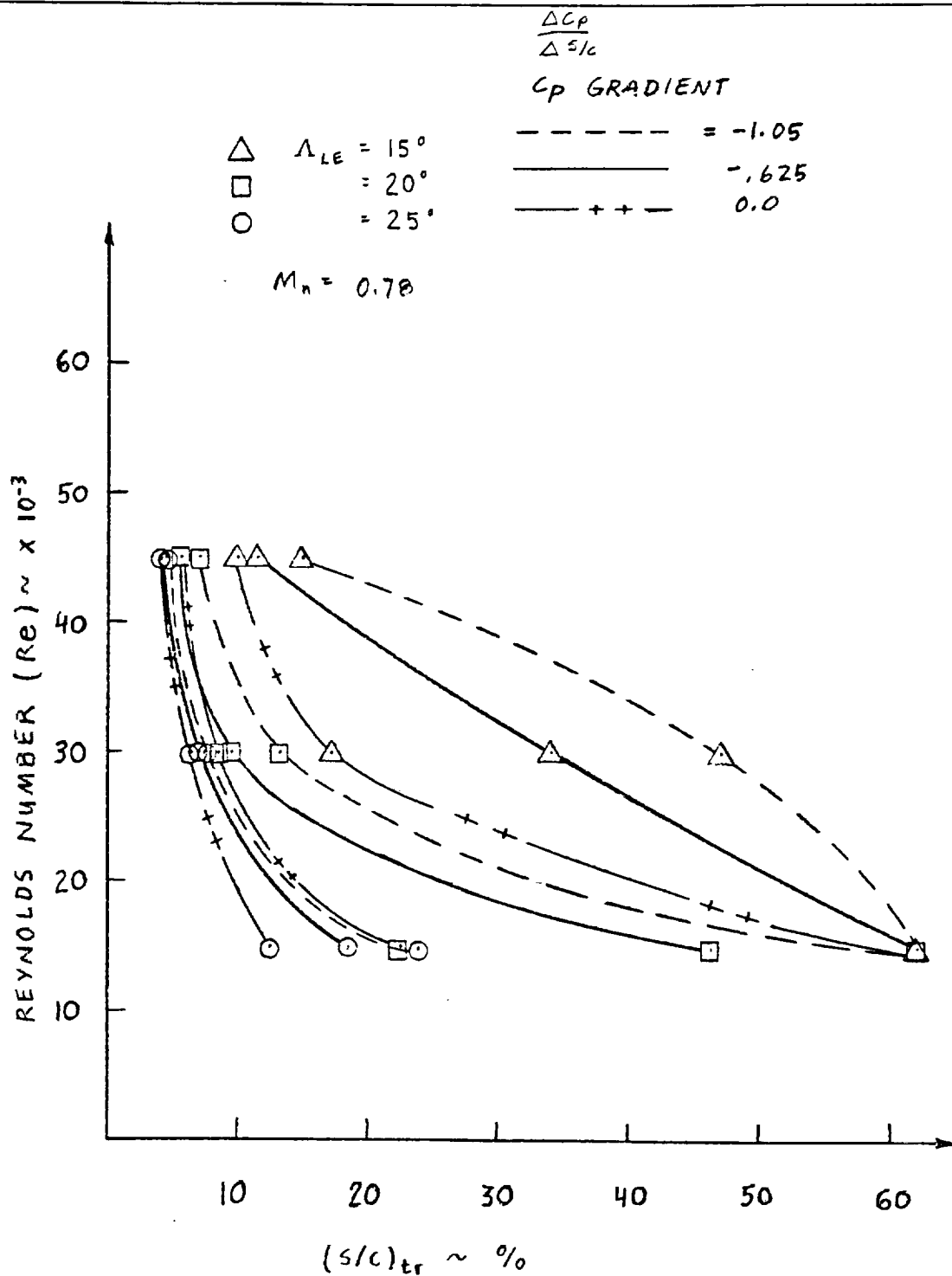


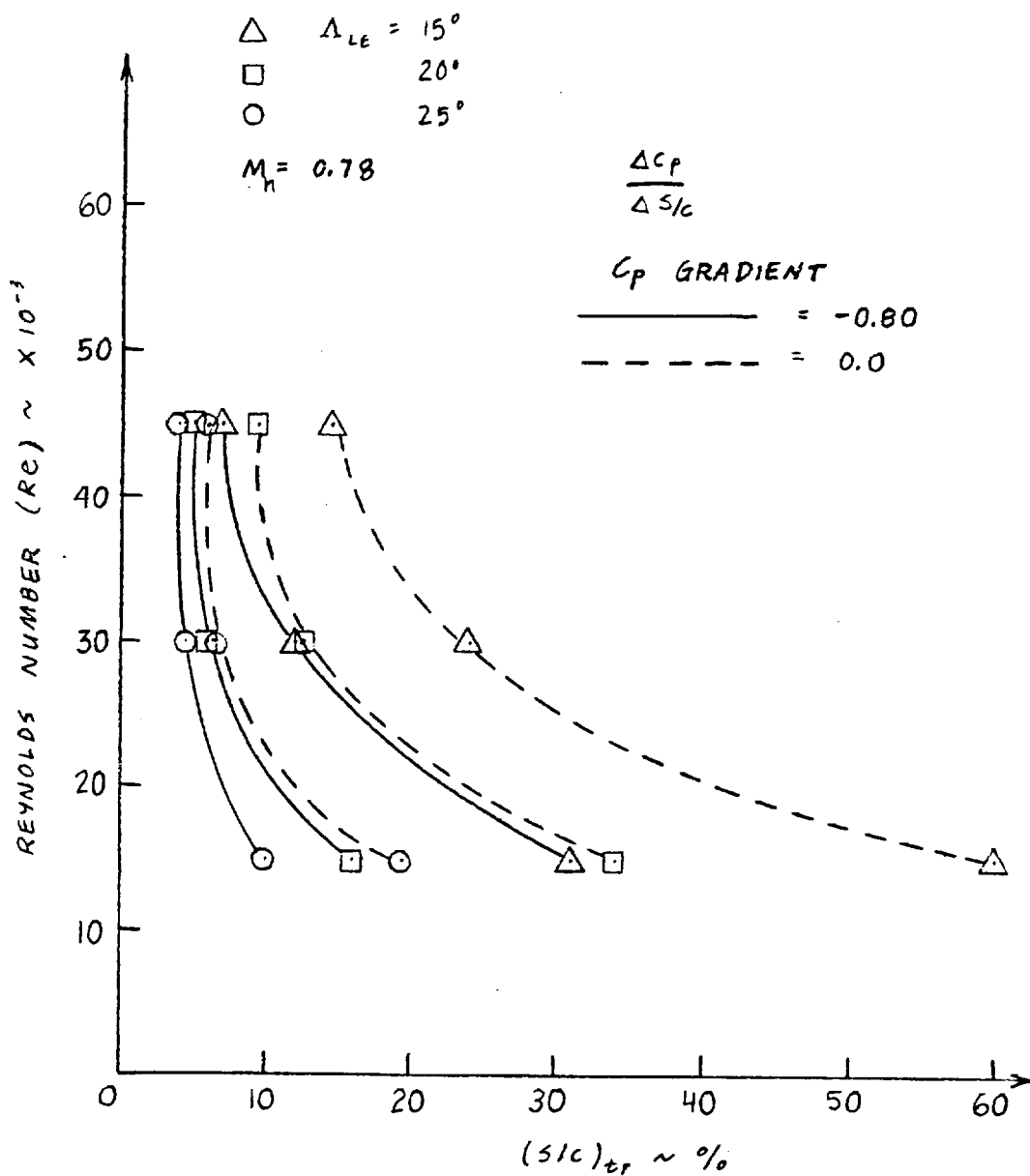
Figure 5.2 Forward chord pressure distribution optimized for different Schlichting conditions



CALC	KWILLIAMS	10/14/72	REVISED	DATE	Figure 5.3 Effect of initial upper surface pressure gradient, sweep angle and Reynolds number on transition	
CHECK						
APPD						
APPD						
					UNIVERSITY OF KANSAS	PAGE 119



CALC	K. WILLIAMS	10/14/93	REVISED	DATE	Figure 5.4 Effect of mid-chord upper surface pressure gradient, sweep angle and Reynolds number on transition	
CHECK						
APPD						
APPD						
					UNIVERSITY OF KANSAS	PAGE 120



CALC	K WILLIAMS	10/17/83	REVISED	DATE	Figure 5.5 Effect of lower surface pressure gradient, Reynolds number and sweep angle on extent of laminar flow	
CHECK						
APPD						
APPD						
					UNIVERSITY OF KANSAS	PAGE 121

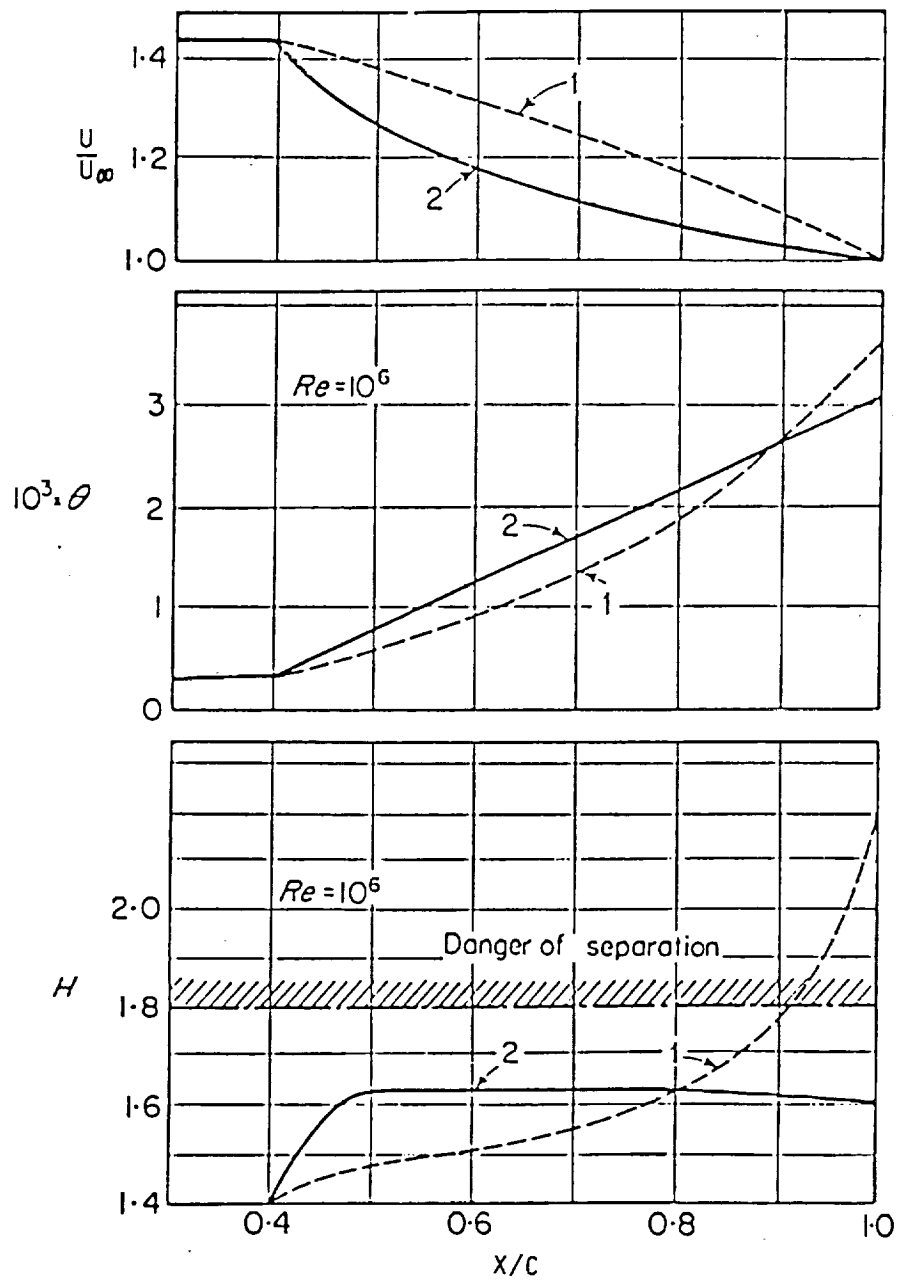


Figure 5.6 Illustration of the effect of recovery velocity distribution on development of turbulent boundary layer for low chord Reynolds number. (ref. 36)

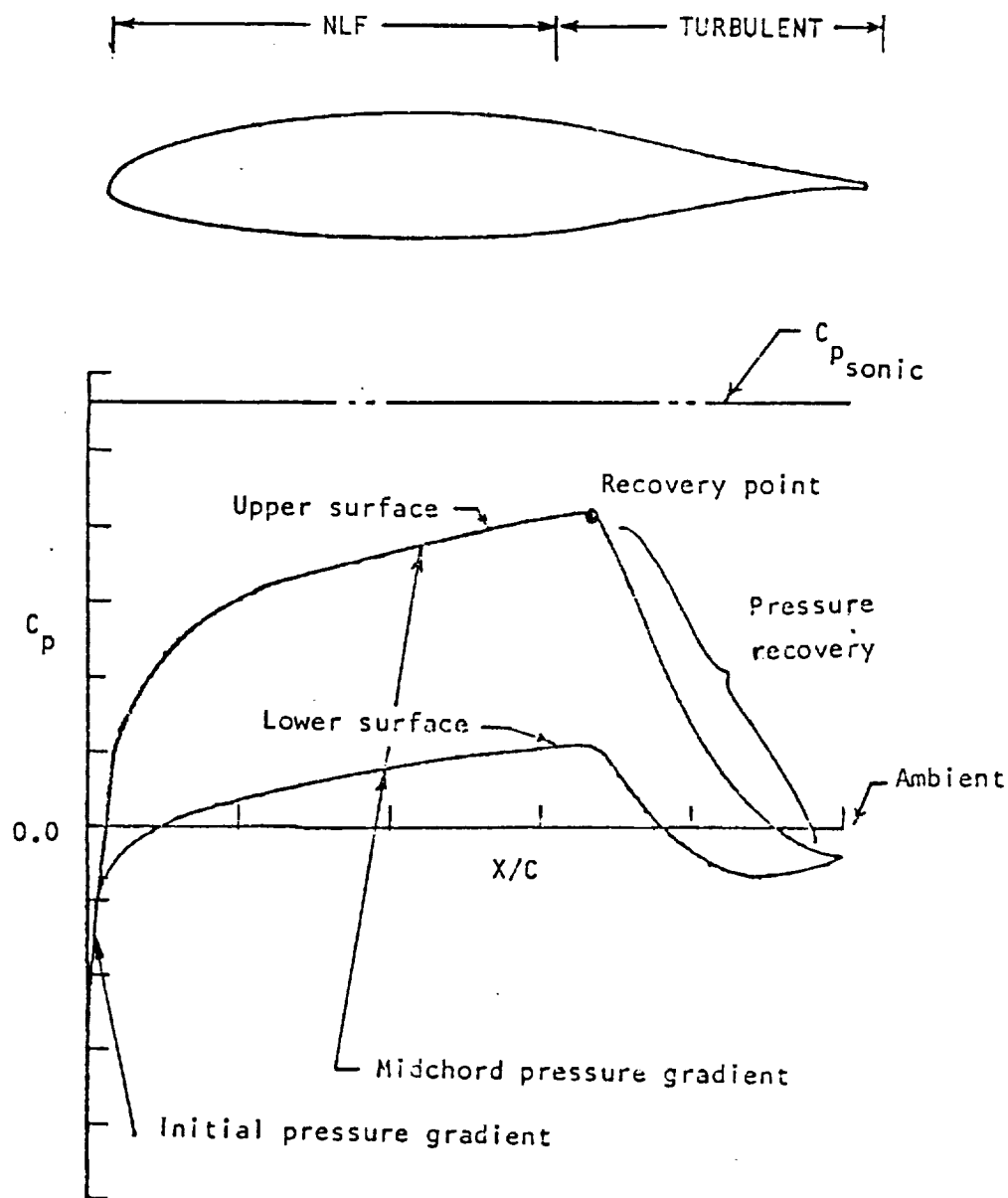


Figure 5.7 Characteristics of typical NLF pressure distribution for unswept and moderately swept wings

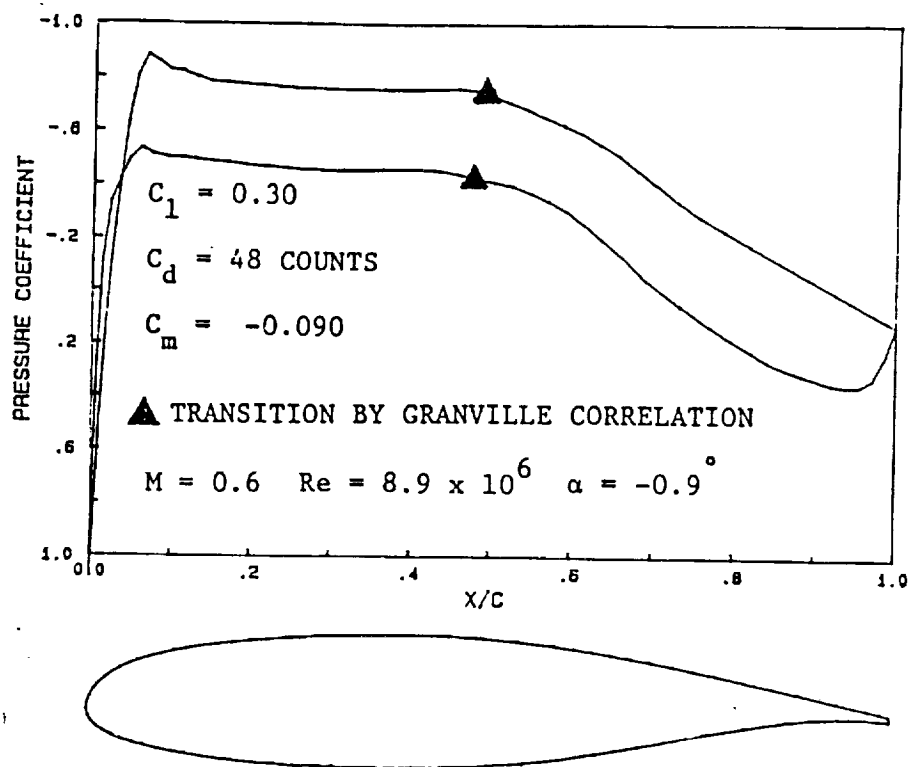


Figure 6.1 MS(1)-0317 pressure distribution as calculated by the NCS code.

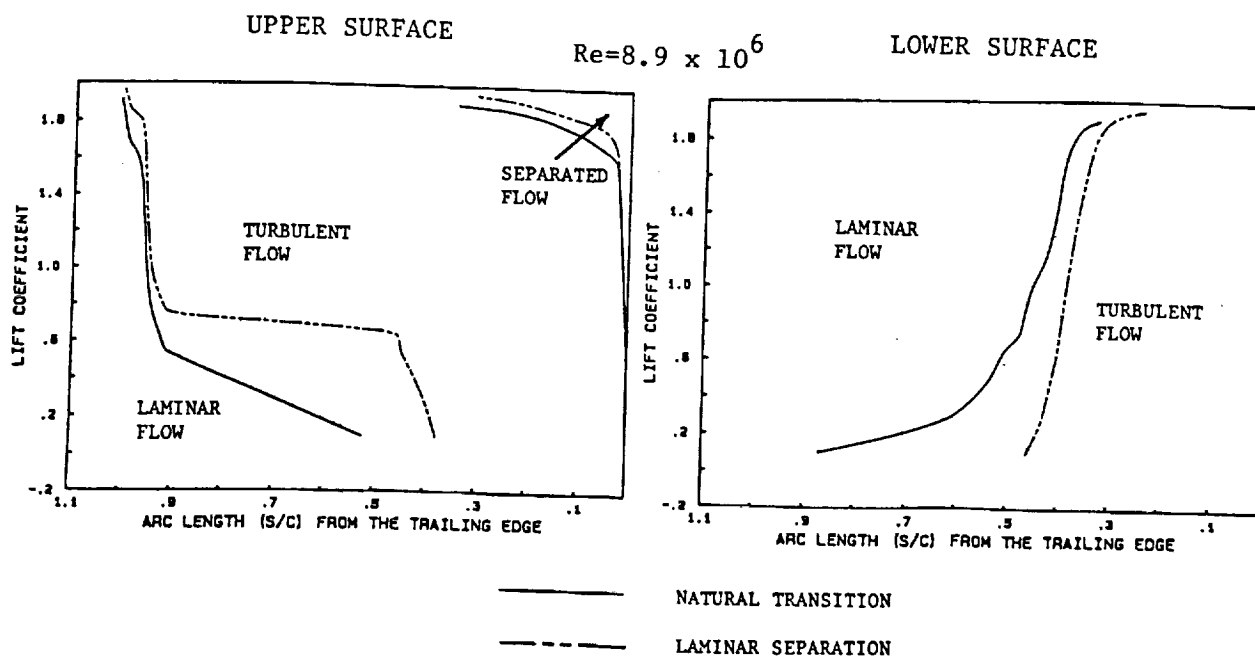


Figure 6.2 Locations of transition and turbulent separation on the MS(1)-0317 as calculated by the Eppler code.

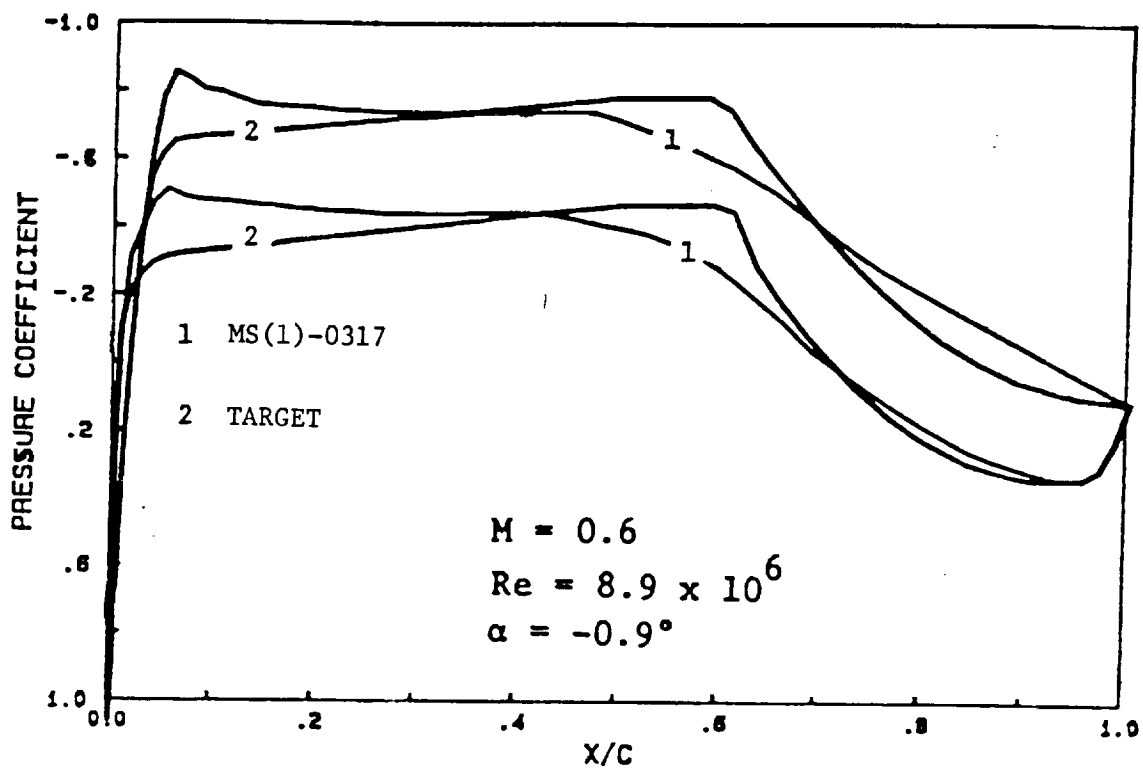


Figure 6.3 MS(1)-0317 pressure distribution and first target pressure distribution.

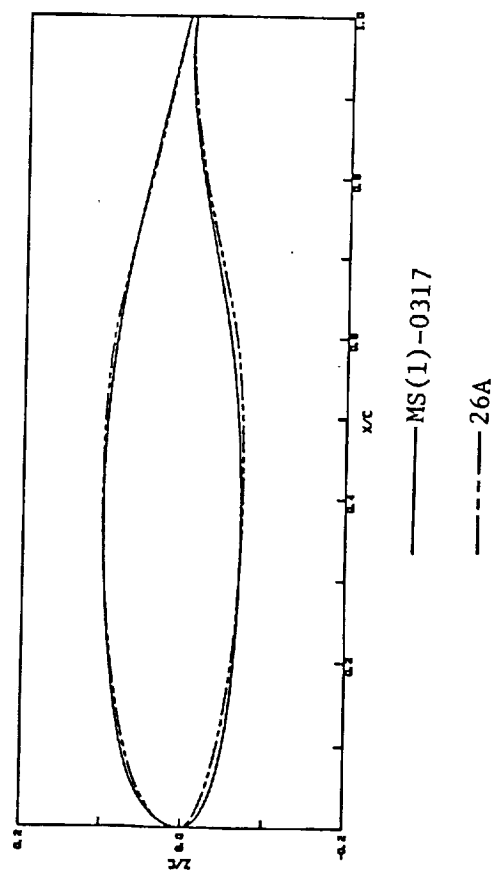
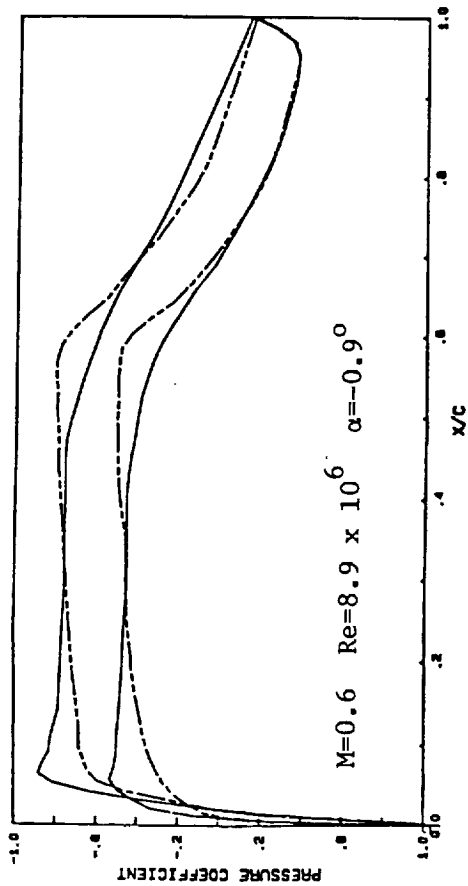


Figure 6.4 Comparison of MS(1)-0317 and 26A pressure distributions and contours.

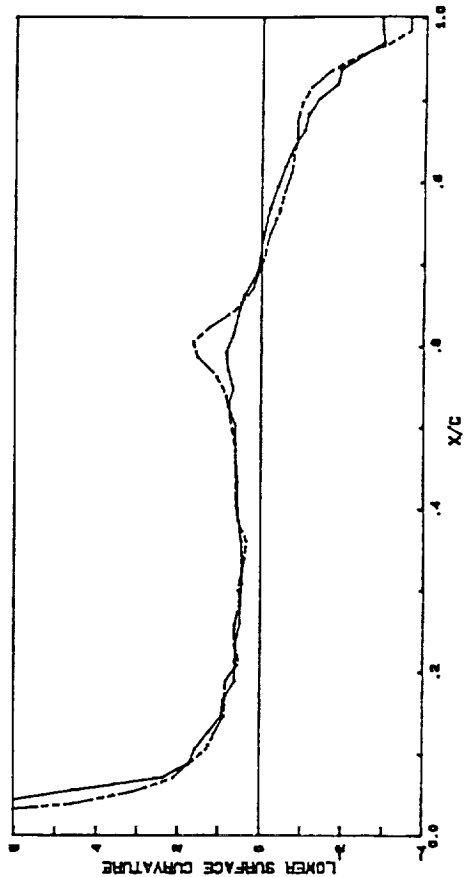
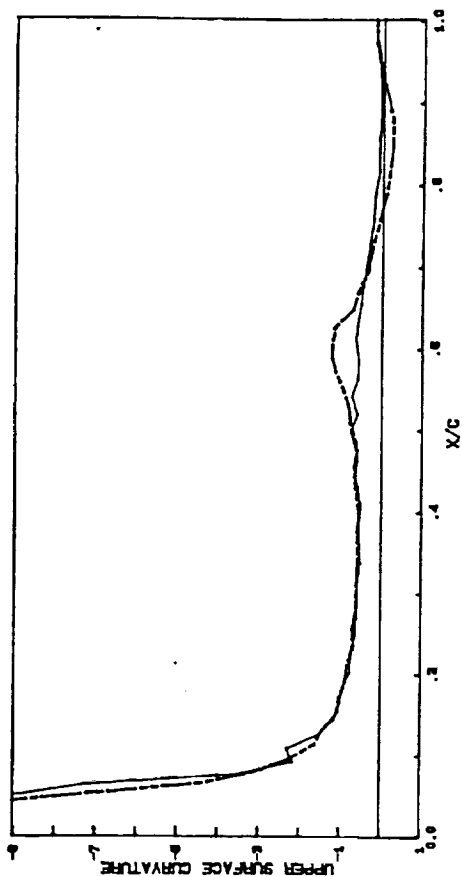


Figure 6.5 Comparison of MS(1)-0317 and 26A curvature distributions.

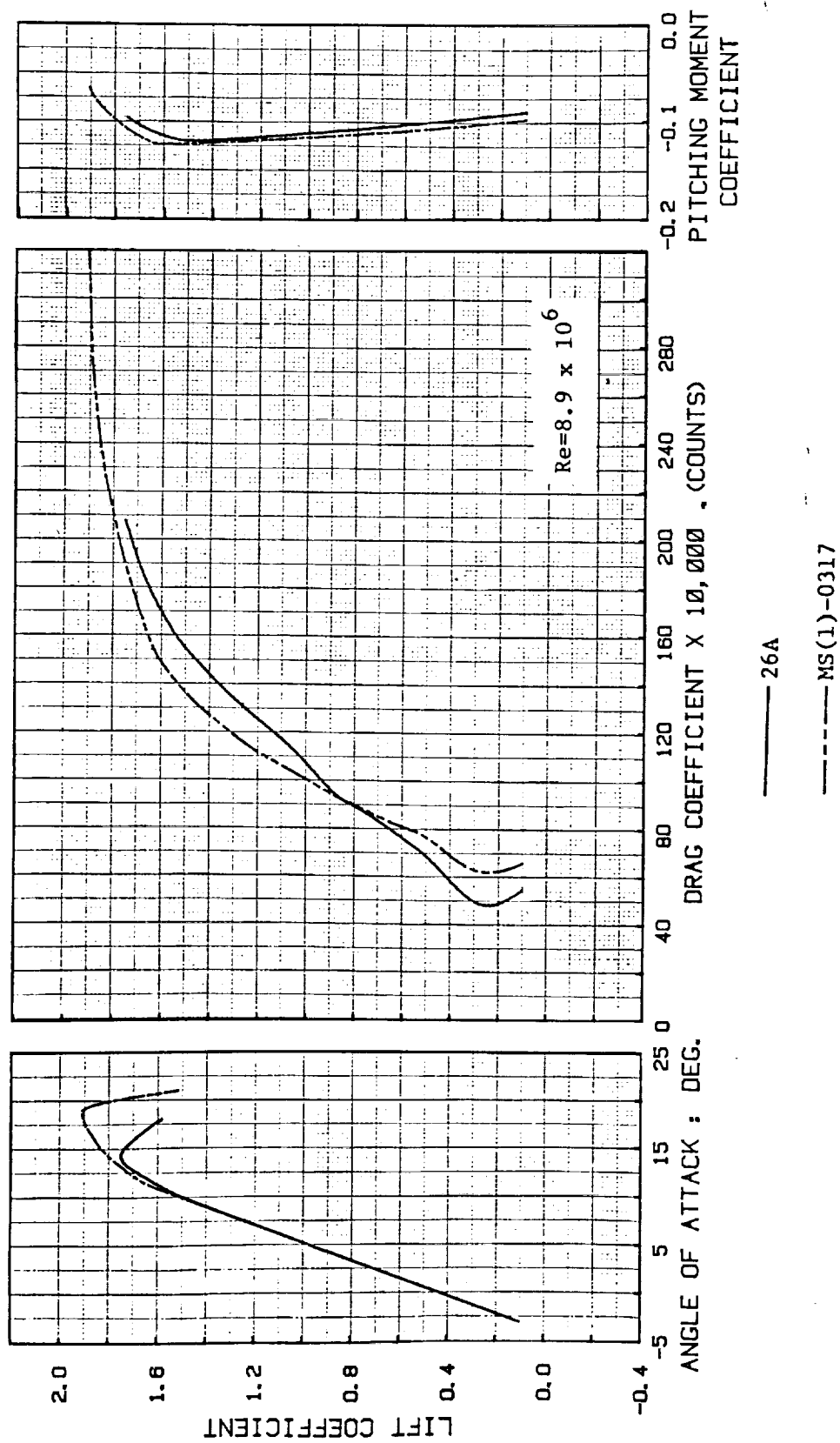


Figure 6.6 Aerodynamic characteristics of 26A and MS(1)-0317 as calculated by the Eppler code using natural transition.

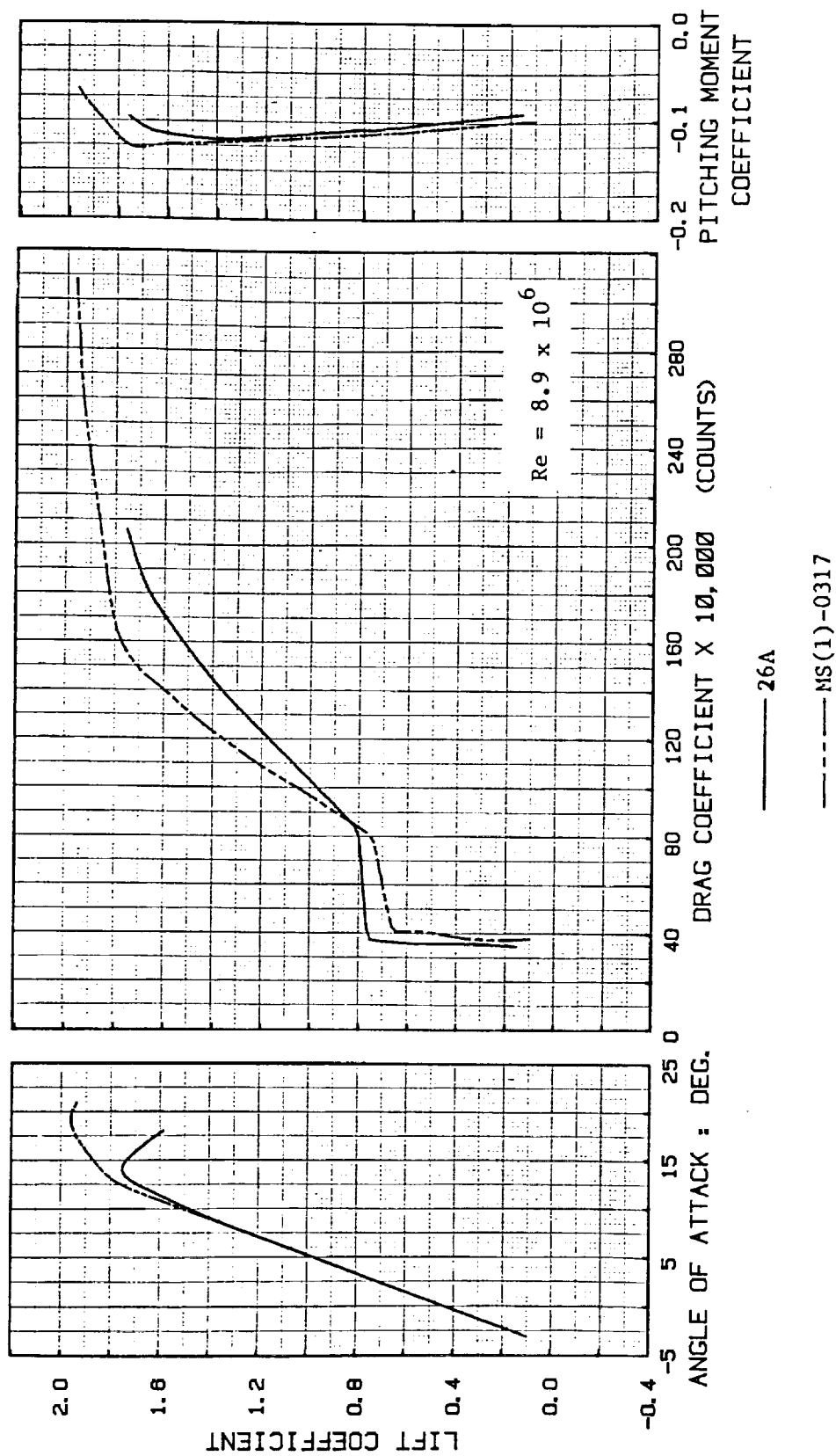


Figure 6.7 Aerodynamic characteristics of 26A and MS(1)-0317 as calculated by the Eppler code using the laminar separation criterion.

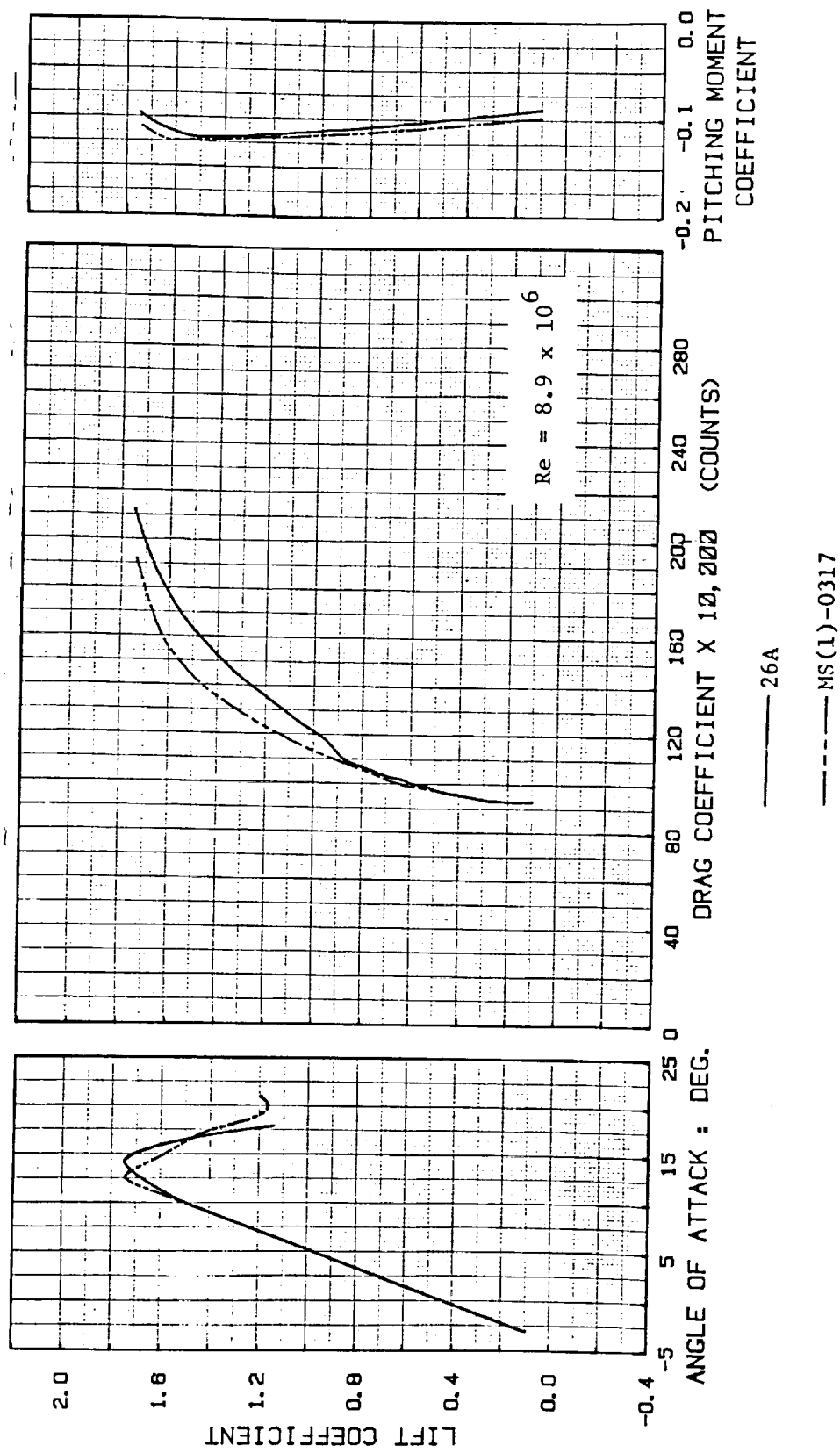


Figure 6.8 Aerodynamic characteristics of 26A and MS(1)-0317 as calculated by the Eppler code with transition fixed at 5-percent chord.

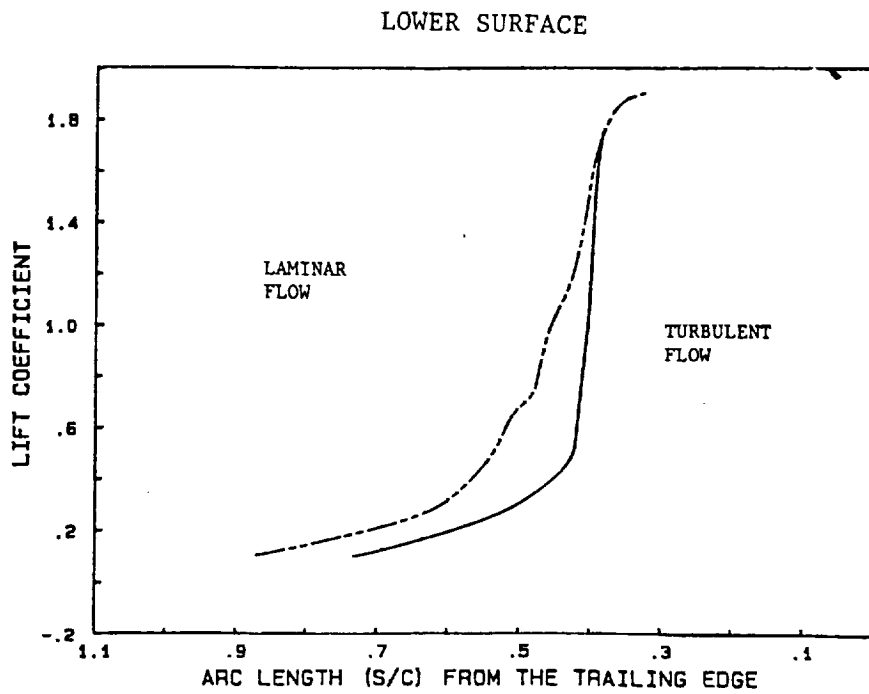
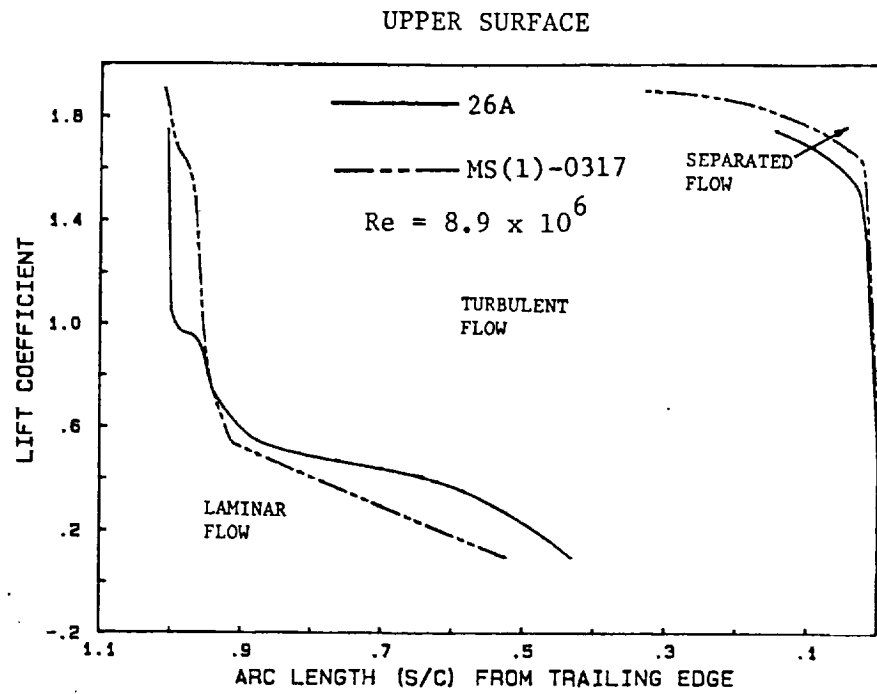


Figure 6.9 Transition and turbulent separation locations for 26A and MS(1)-0317 as calculated by the Eppler code using natural transition.

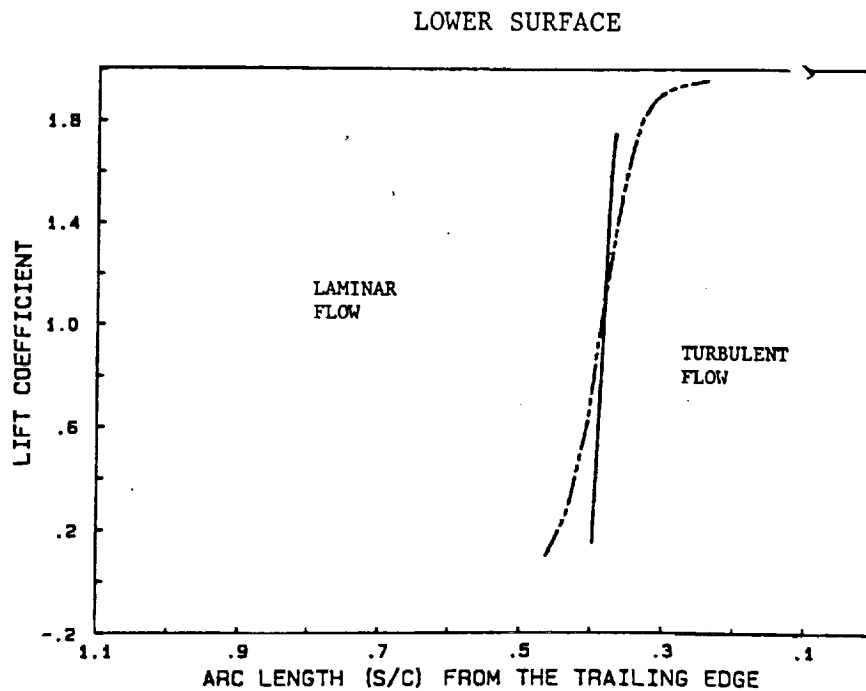
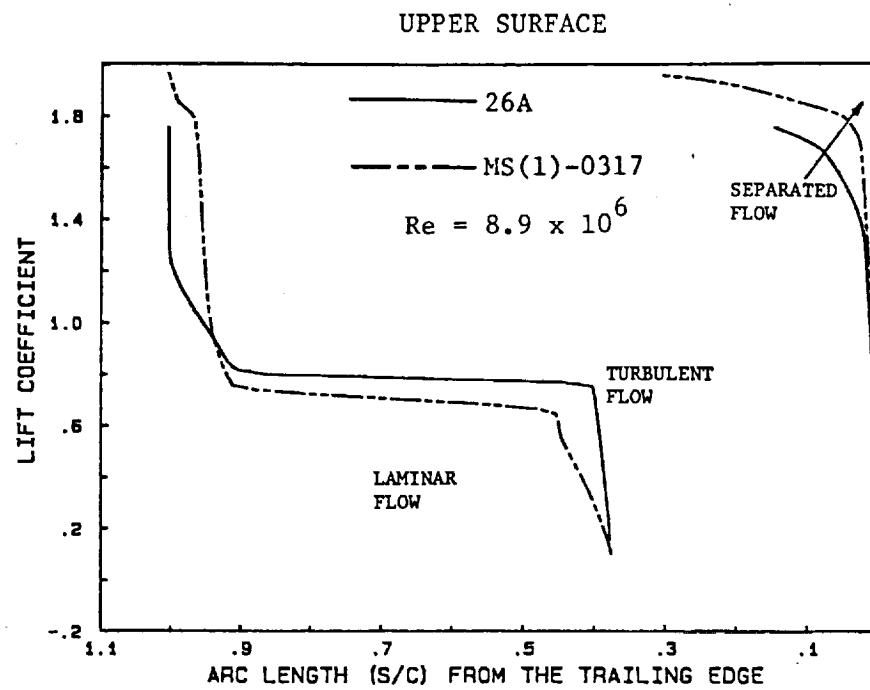


Figure 6.10 Transition and turbulent separation locations for 26A and MS(1)-0317 as calculated by the Eppler code using the laminar separation criterion.

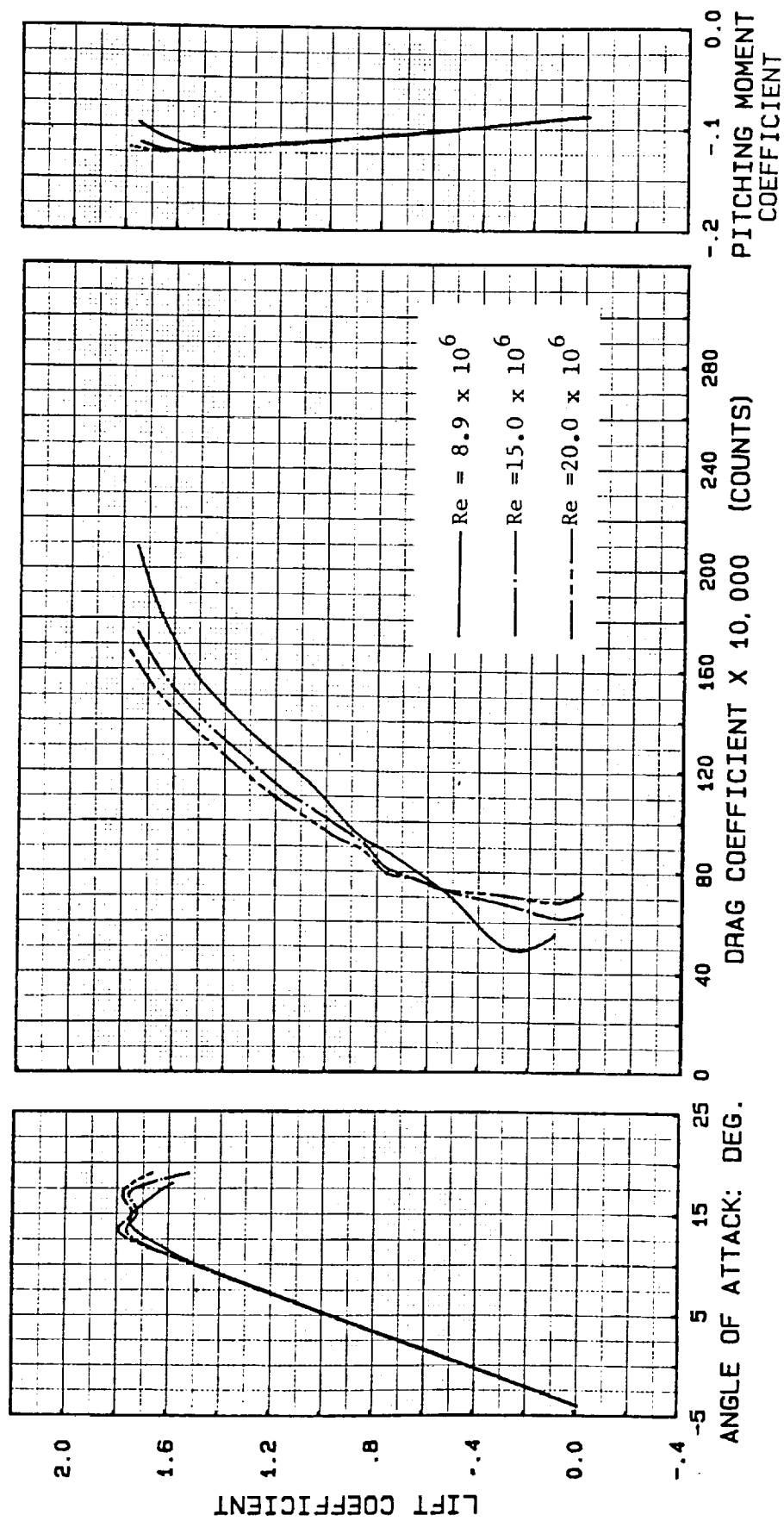


Figure 6.11 Effect of Reynolds number on the aerodynamic characteristics of 26A as calculated by the Eppler code using natural transition.

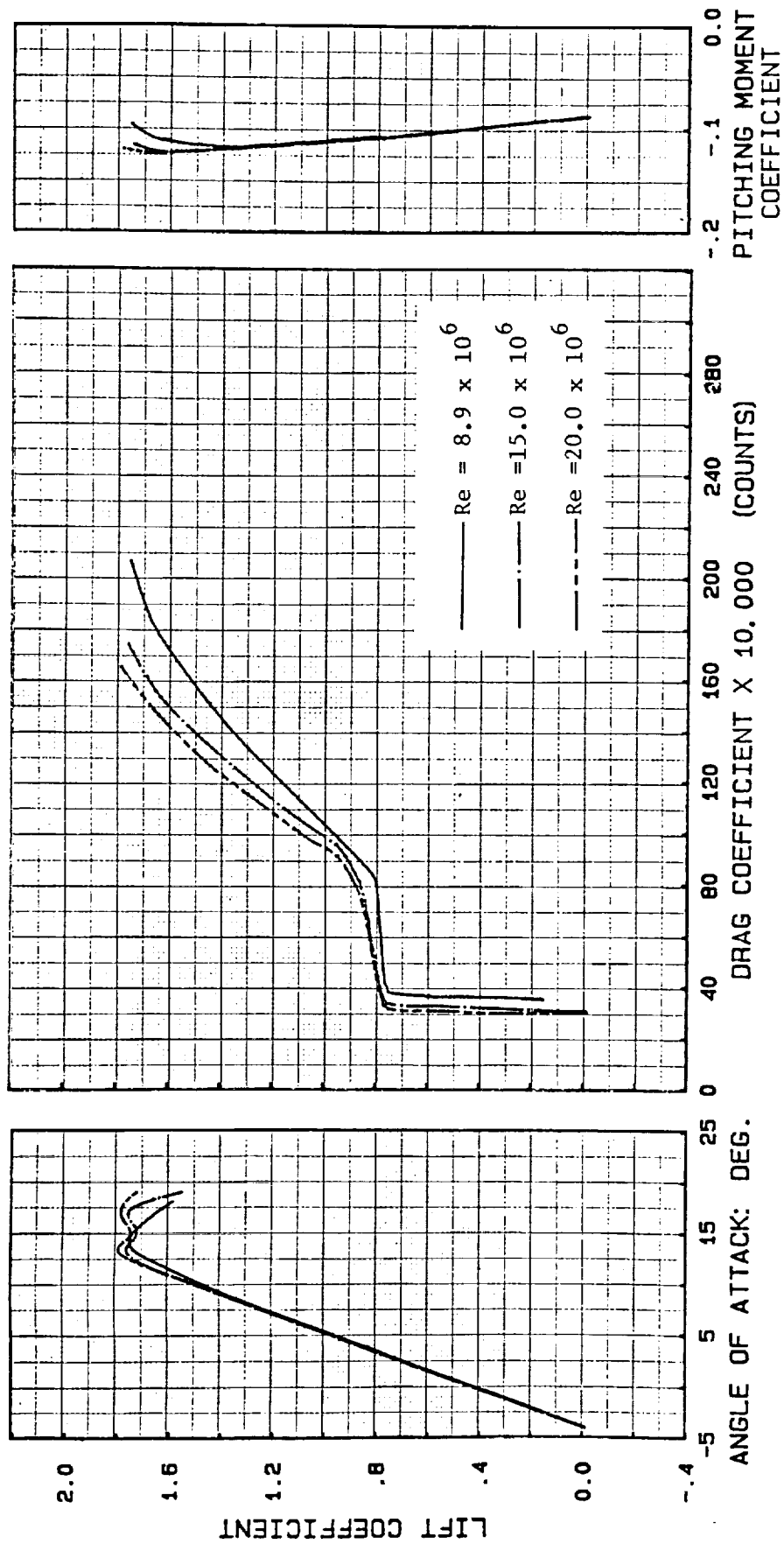


Figure 6.12 Effect of Reynolds number on the aerodynamic characteristics of 26A as calculated by the Eppler code using the laminar separation criterion.

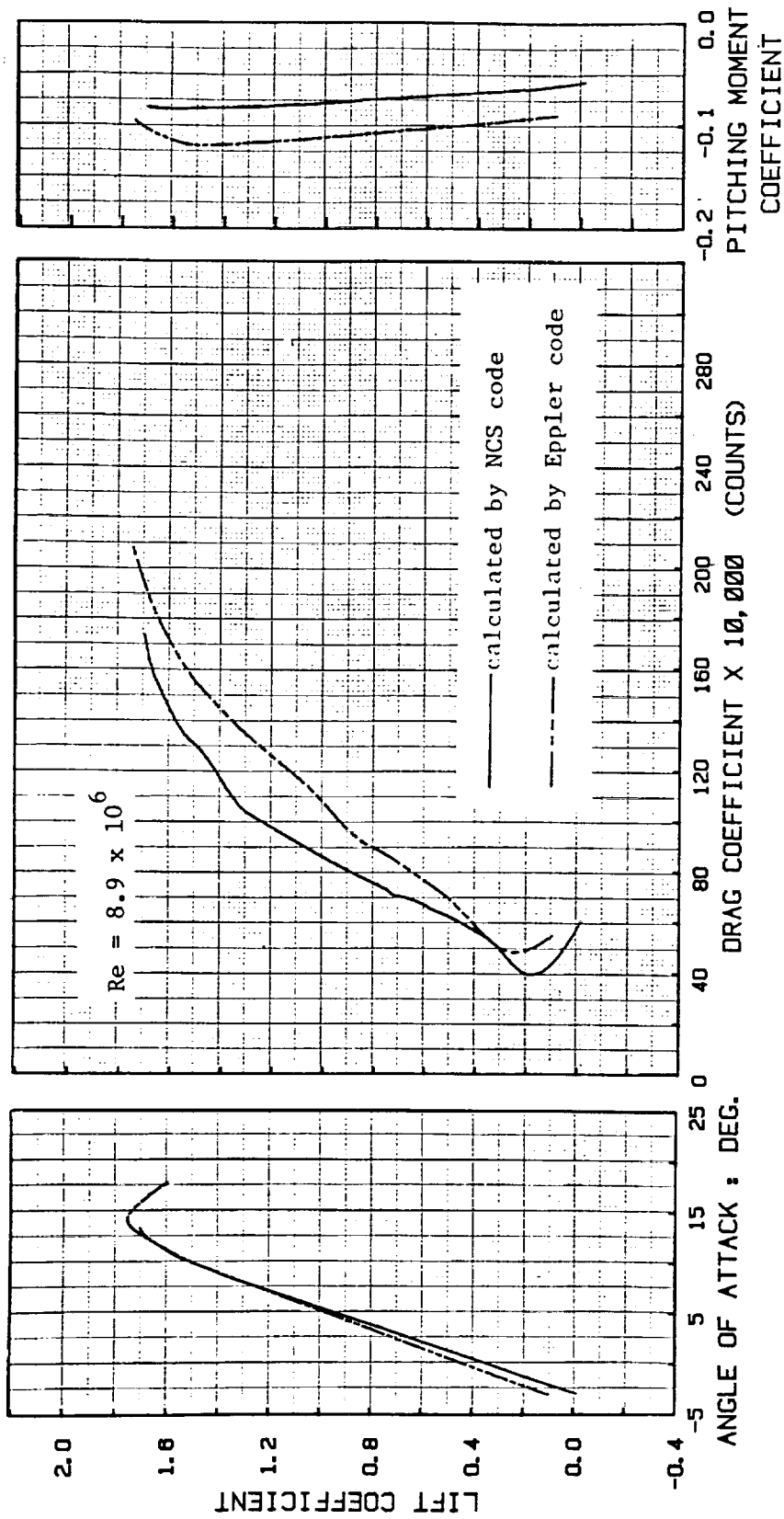


Figure 6.13 Comparison of NCS-predicted characteristics at $M=0.2$ and incompressible Eppler predictions for 26A using natural transition.

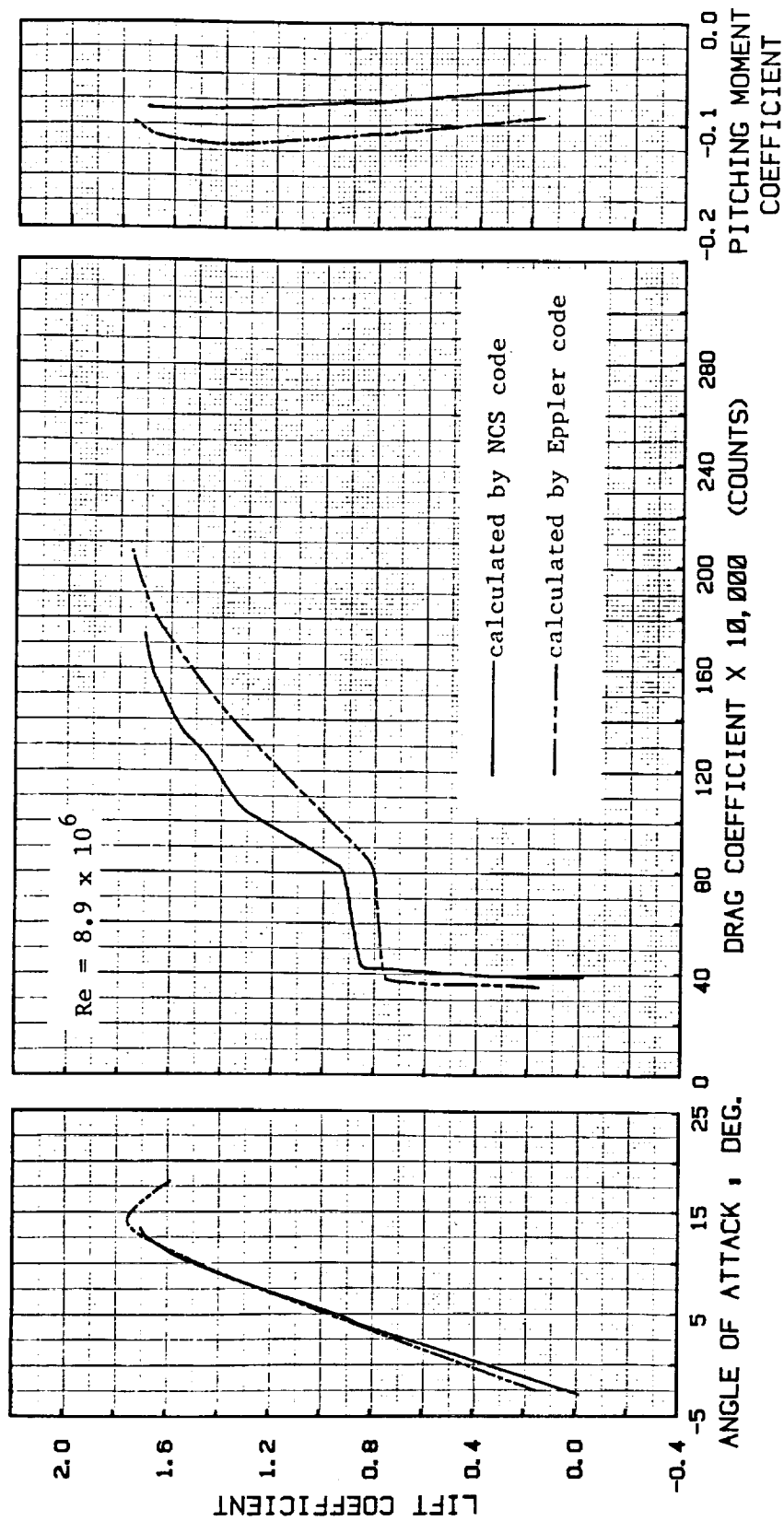


Figure 6.14 Comparison of NCS-predicted characteristics at $M=0.2$ and incompressible Eppler predictions for 26A using the laminar separation criterion.

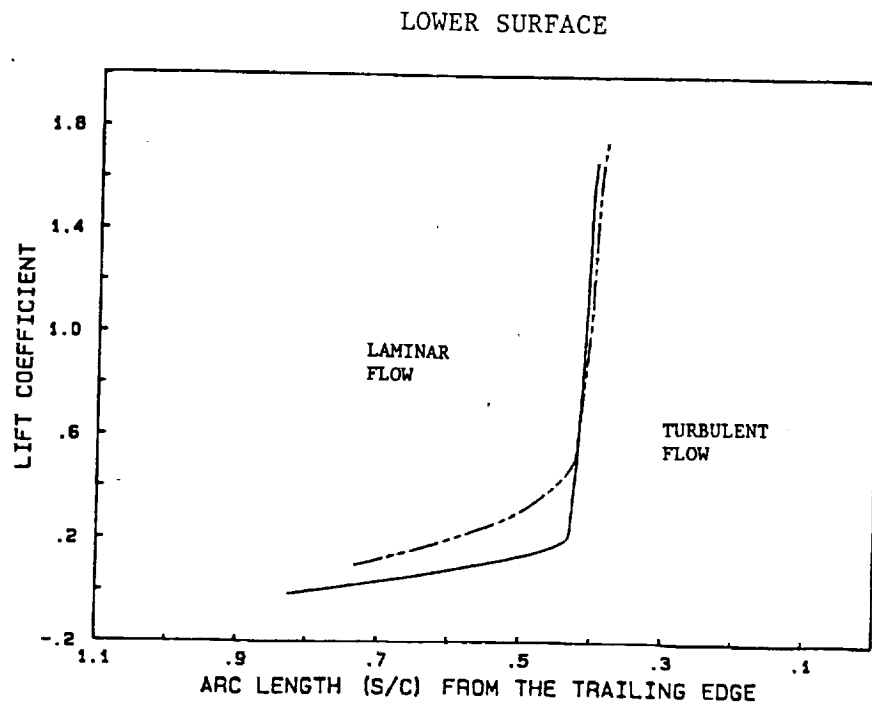
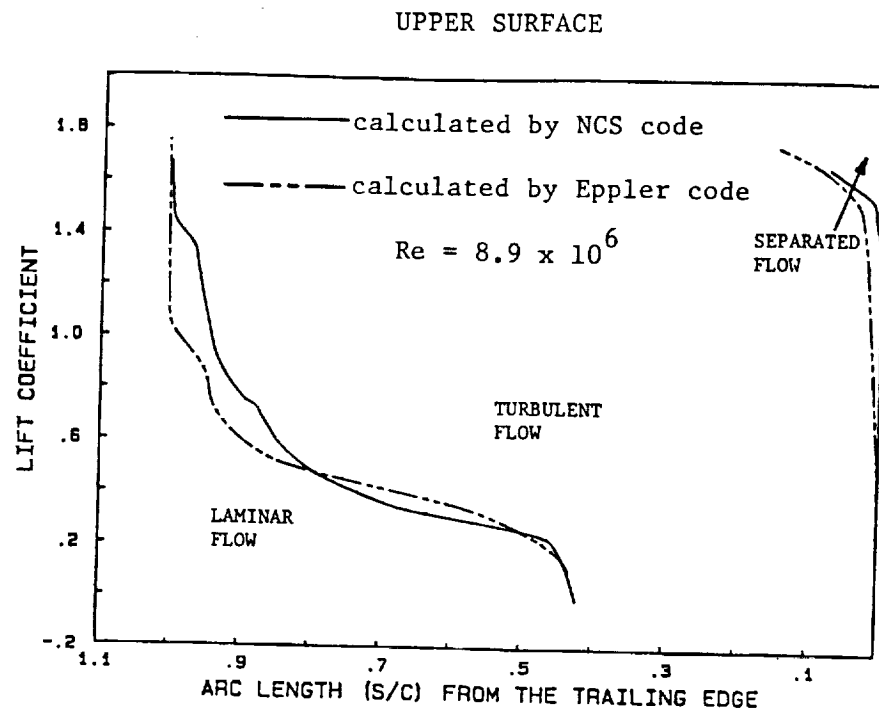


Figure 6.15 Transition and turbulent separation locations for 26A as calculated by the NCS code at $M=0.2$ and by the incompressible Eppler code using natural transition.

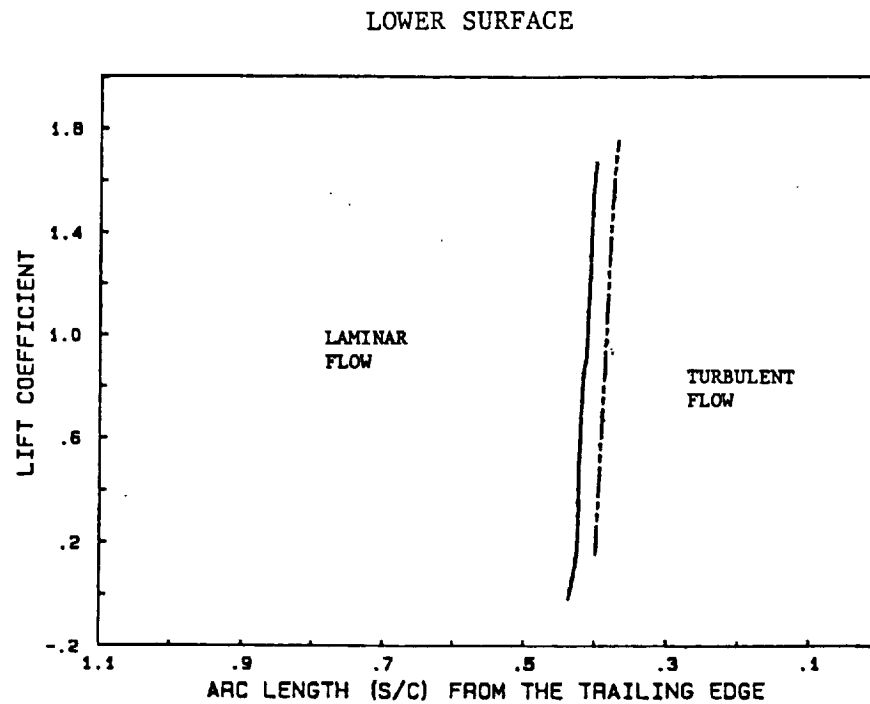
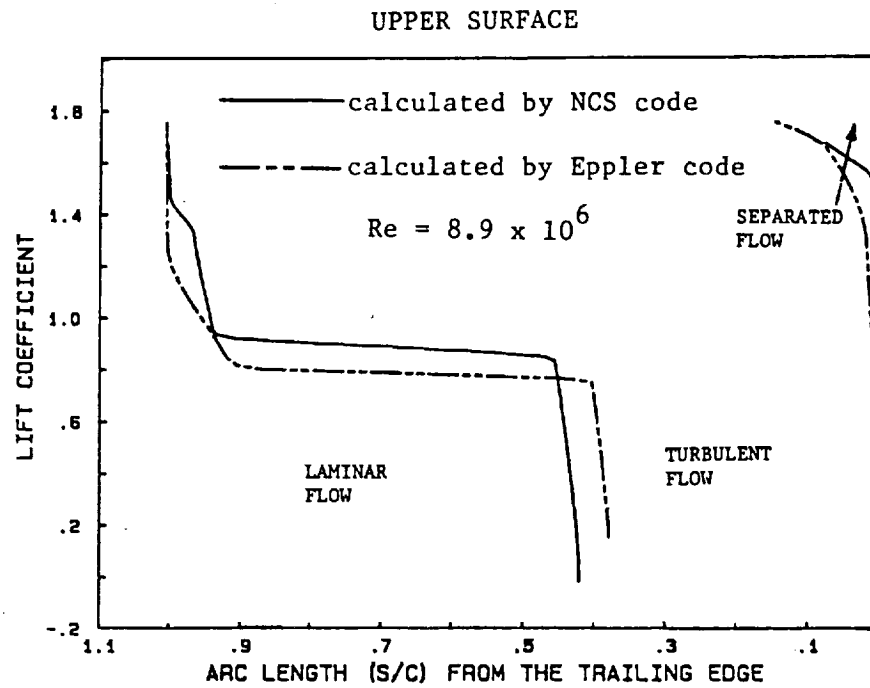


Figure 6.16 Transition and turbulent separation locations for 26A as calculated by the NCS code at $M=0.2$ and by the incompressible Eppler code using the laminar separation criterion.

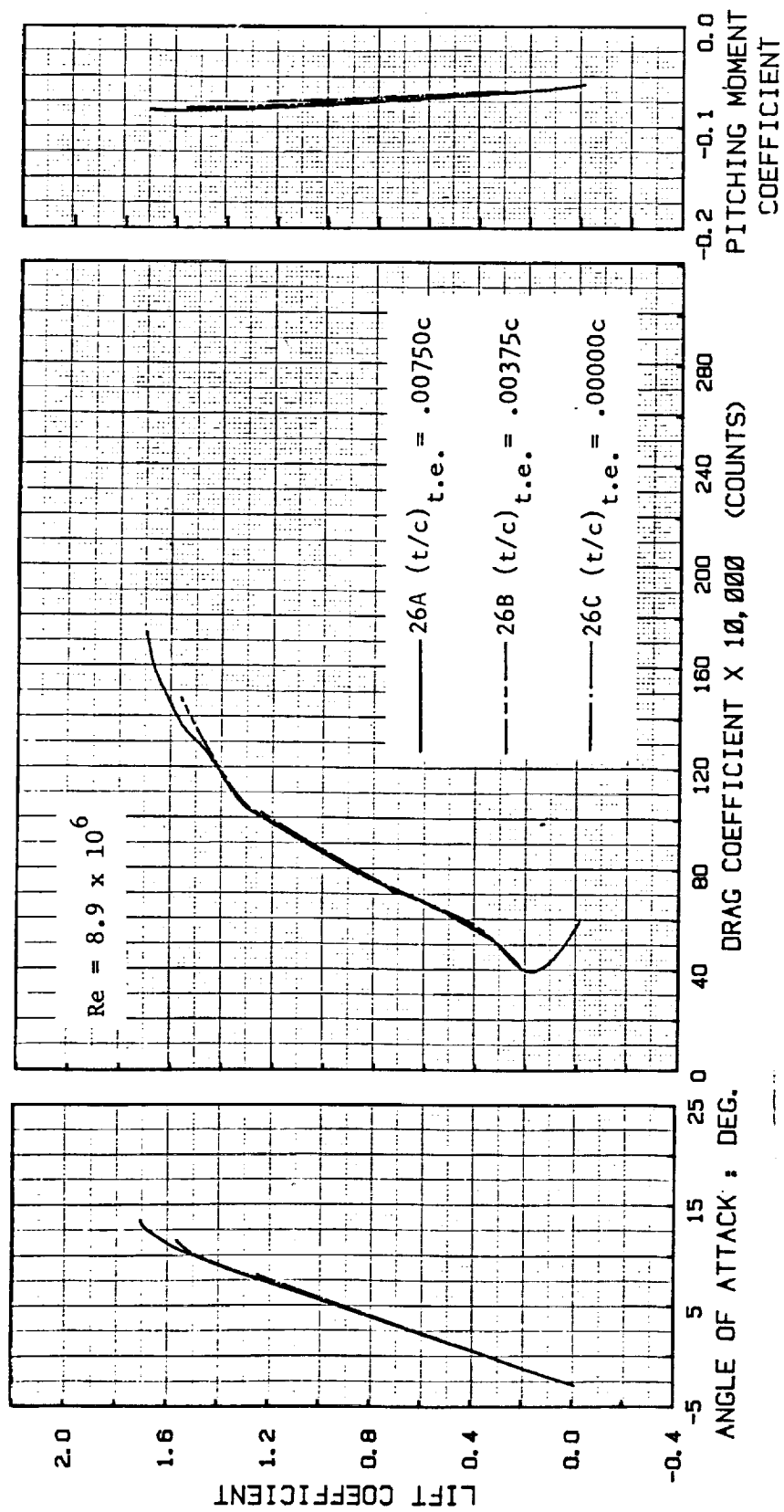


Figure 6.17 Effect of trailing-edge thickness on the aerodynamic characteristics of 26 as calculated by the NCS code at $M=0.2$ using natural transition.

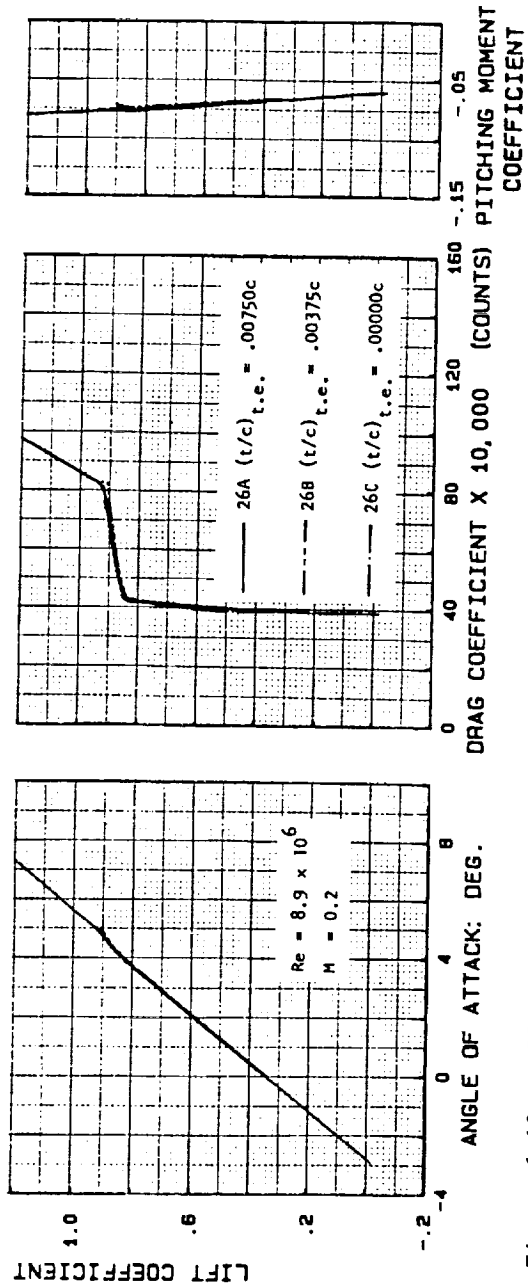


Figure 6.18 Effect of trailing-edge thickness on the aerodynamic characteristics of 26 as calculated by the NCS code at $M=0.2$ using the laminar separation criterion.

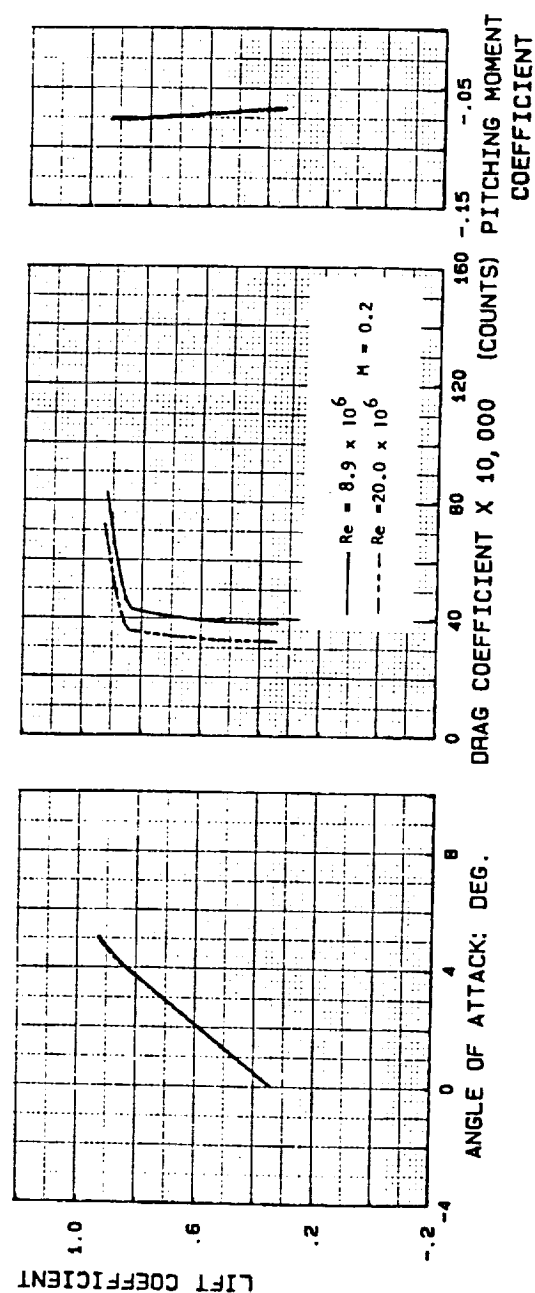


Figure 6.19 Effect of Reynolds number on the aerodynamic characteristics of 26B as calculated by the NCS code at $M=0.2$ using the laminar separation criterion.

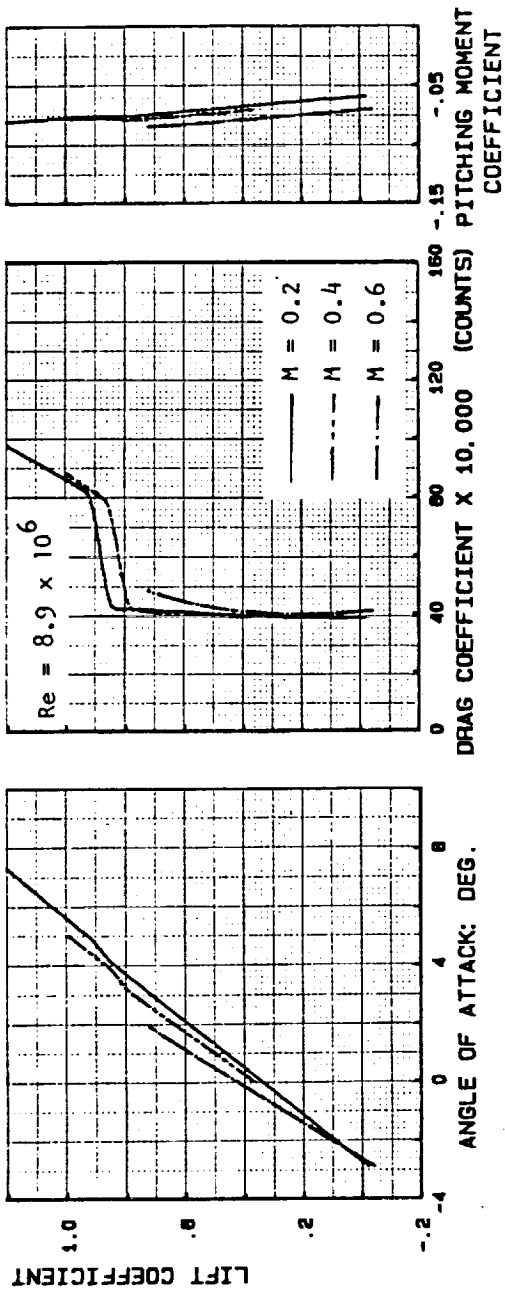


Figure 6.20 Effect of Mach number on the aerodynamic characteristics of 26A as predicted by the NCS code using the laminar separation criterion.

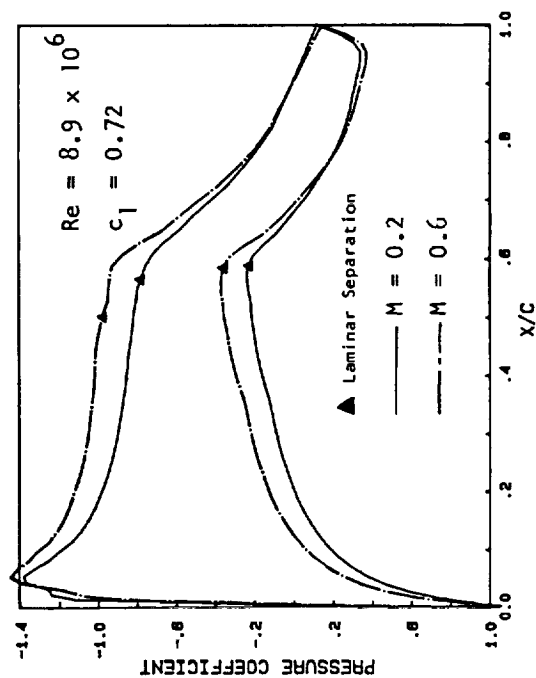


Figure 6.21 Effect of Mach number on the pressure distribution of 26A as predicted by the NCS code using natural transition.

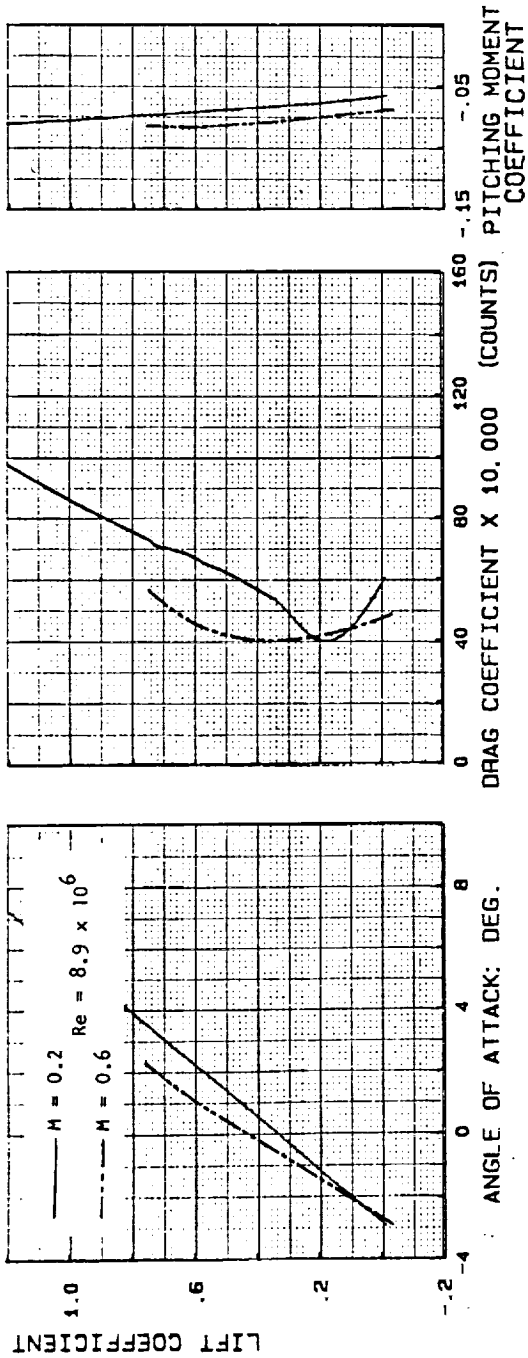


Figure 6.22 Effect of Mach number on the aerodynamic characteristics of 26A as predicted by the NCS code using natural transition.

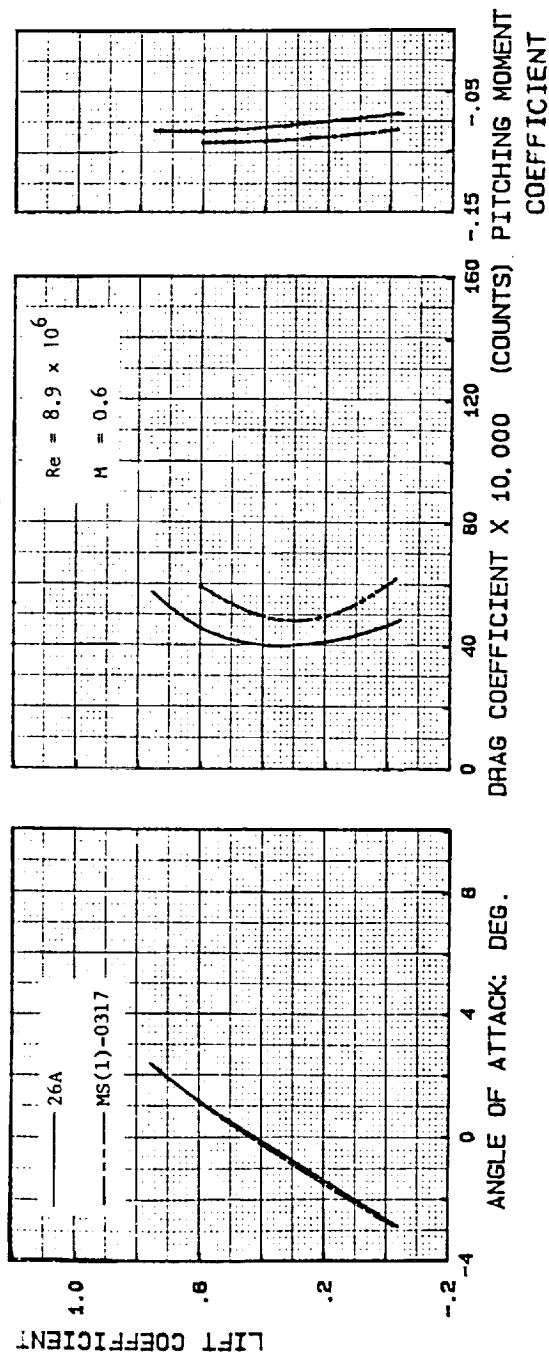


Figure 6.23 Aerodynamic characteristics of 26A and MS(1)-0317 as predicted by the NCS code using natural transition.

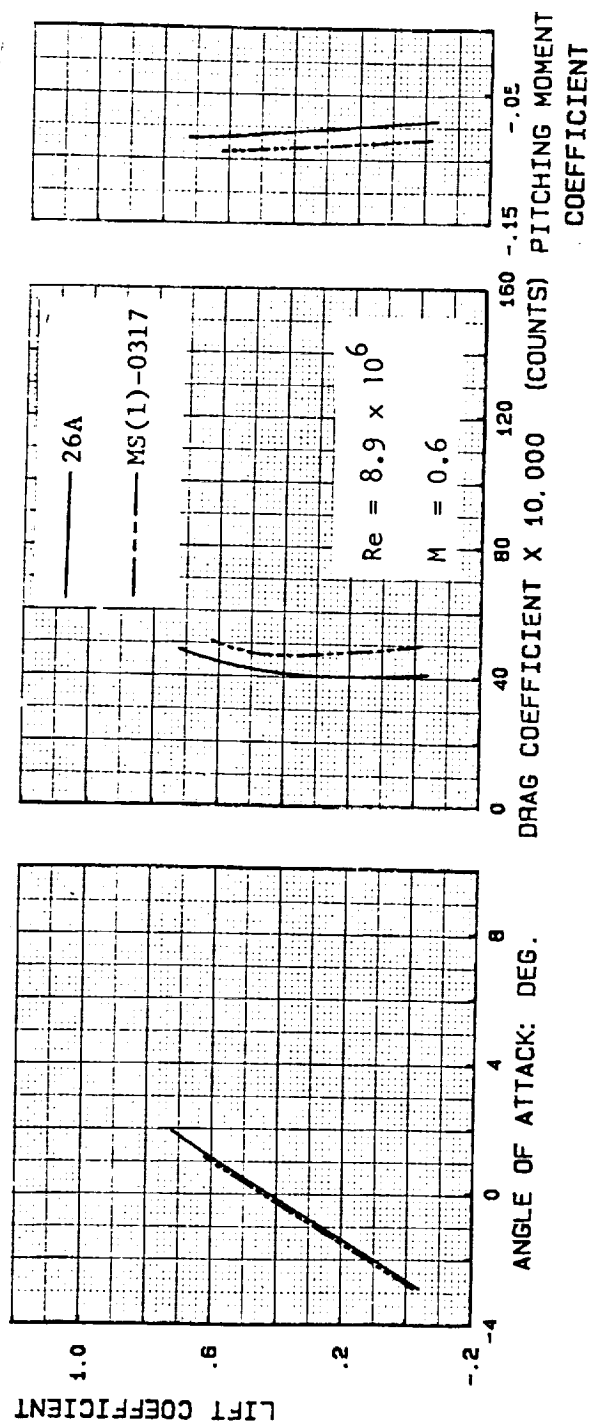


Figure 6.24 Aerodynamic characteristics of 26A and MS(1)-0317 as predicted by the NCS code using the laminar separation criterion.

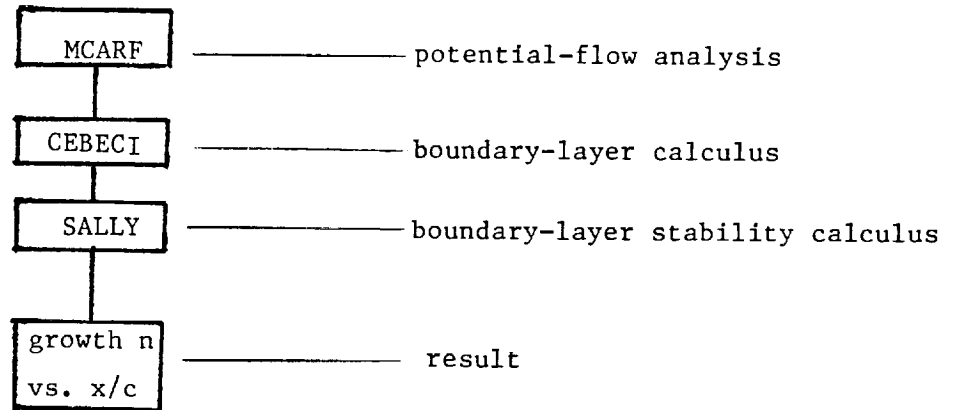


Figure 6.25 Procedure to determine T.S. disturbance growth

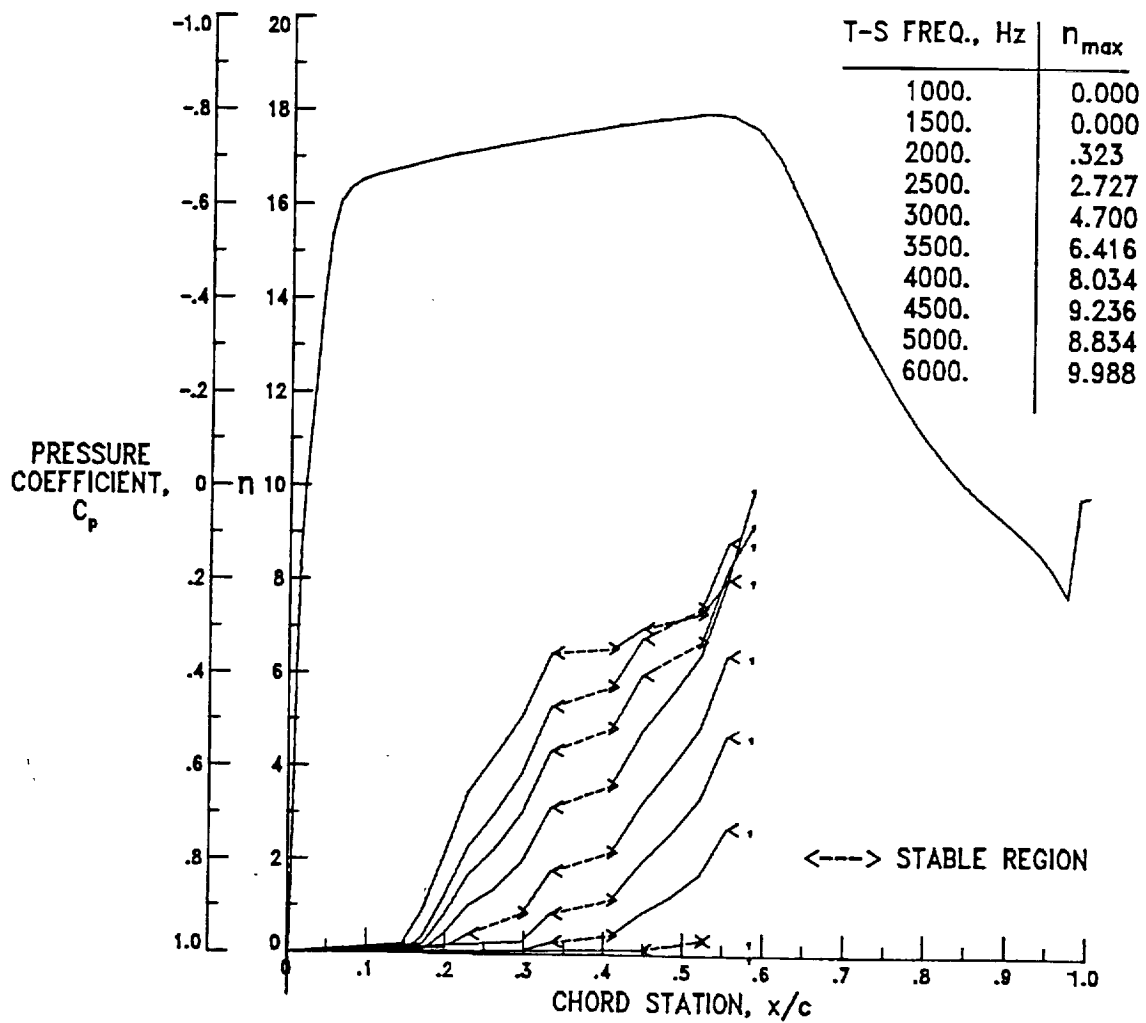


Figure 6.26 Amplification Factor n , Upper Surface Airfoil 26 A
 $c_1 = 0.28$, $Re = 8.9 \times 10^6$, $M = 0.60$

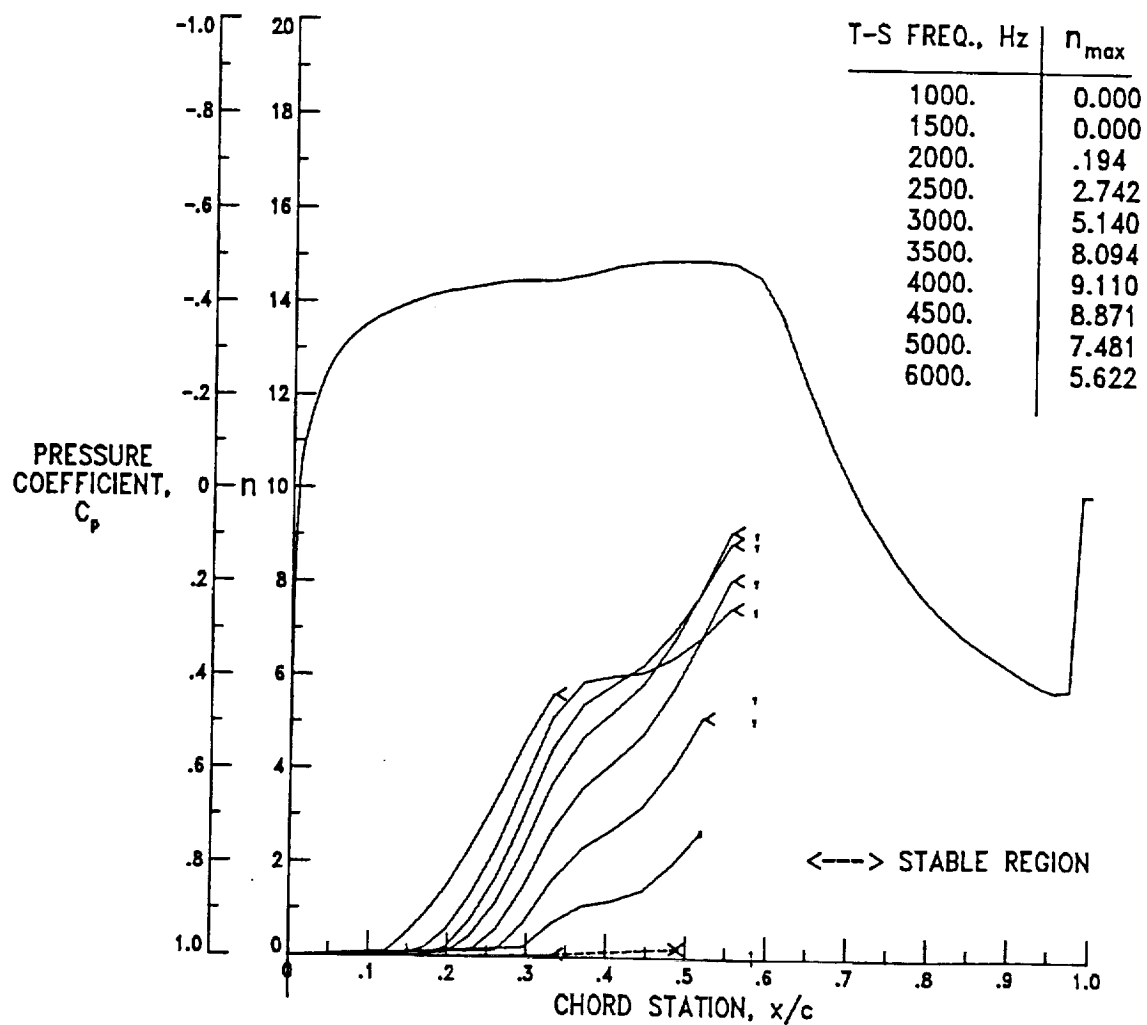


Figure 6.27 Amplification Factor n , Lower Surface Airfoil 26 A

$$c_1 = 0.28, \quad Re = 8.9 \times 10^6, \quad M = 0.60$$

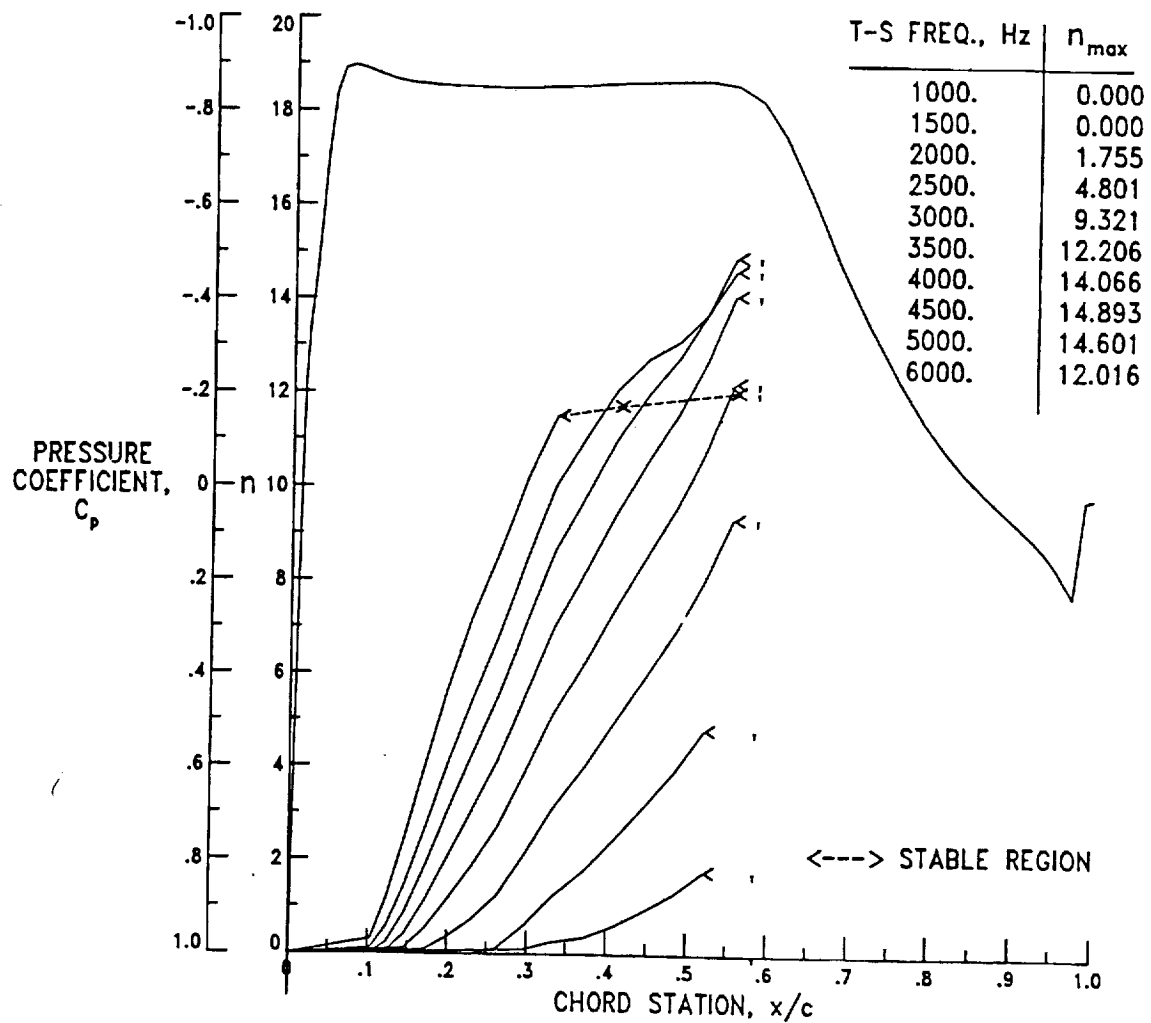


Figure 6.28 Amplification Factor n , Upper Surface Airfoil 26 A
 $c_1 = 0.45$, $Re = 8.9 \times 10^6$, $M = 0.60$

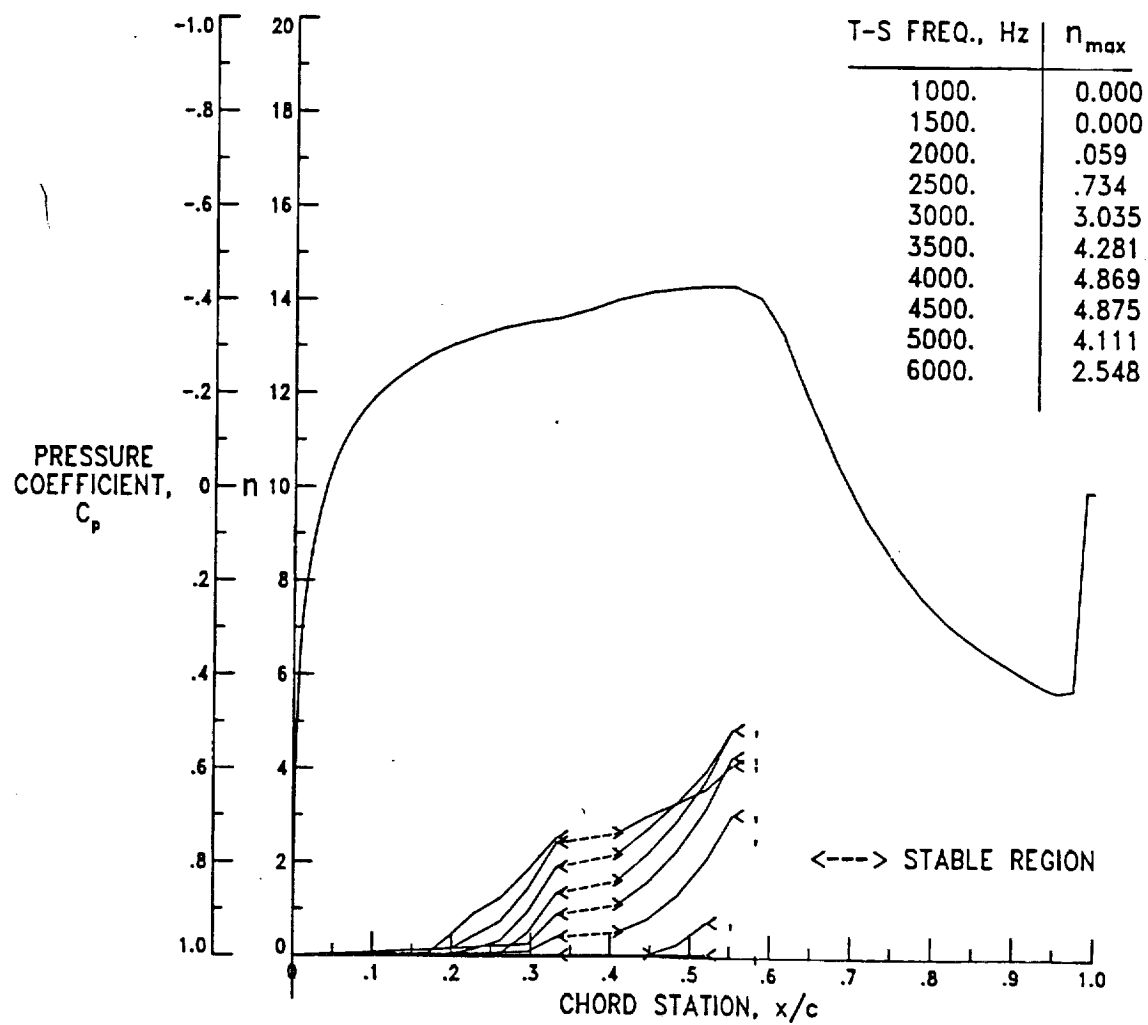


Figure 6.29 Amplification Factor n , Lower Surface Airfoil 26 A

$$c_1 = 0.45, Re = 8.9 \times 10^6, M = 0.60$$

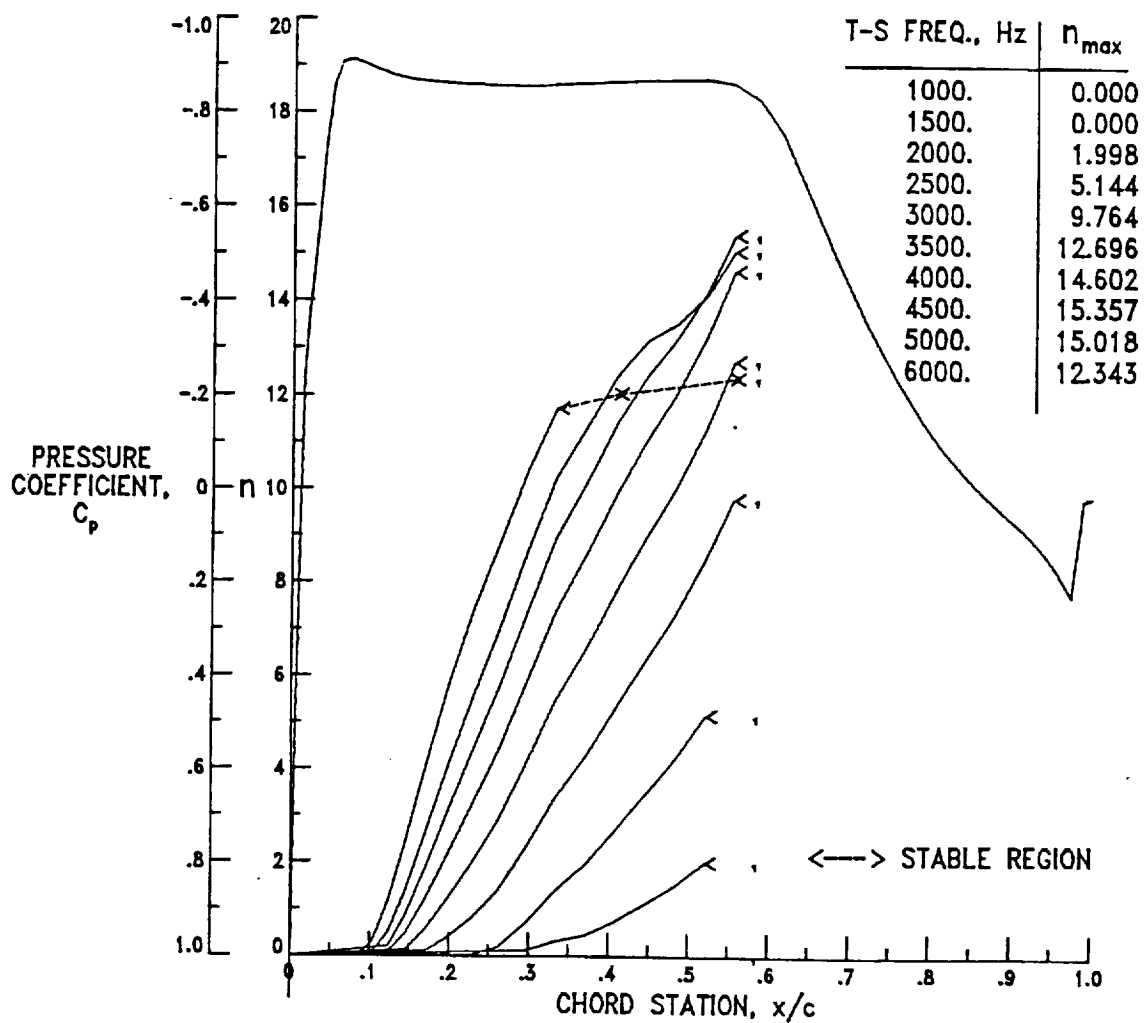


Figure 6.30 Amplification Factor n , Upper Surface Airfoil 26 A

$$c_1 = 0.46, Re = 8.9 \times 10^6, M = 0.60$$

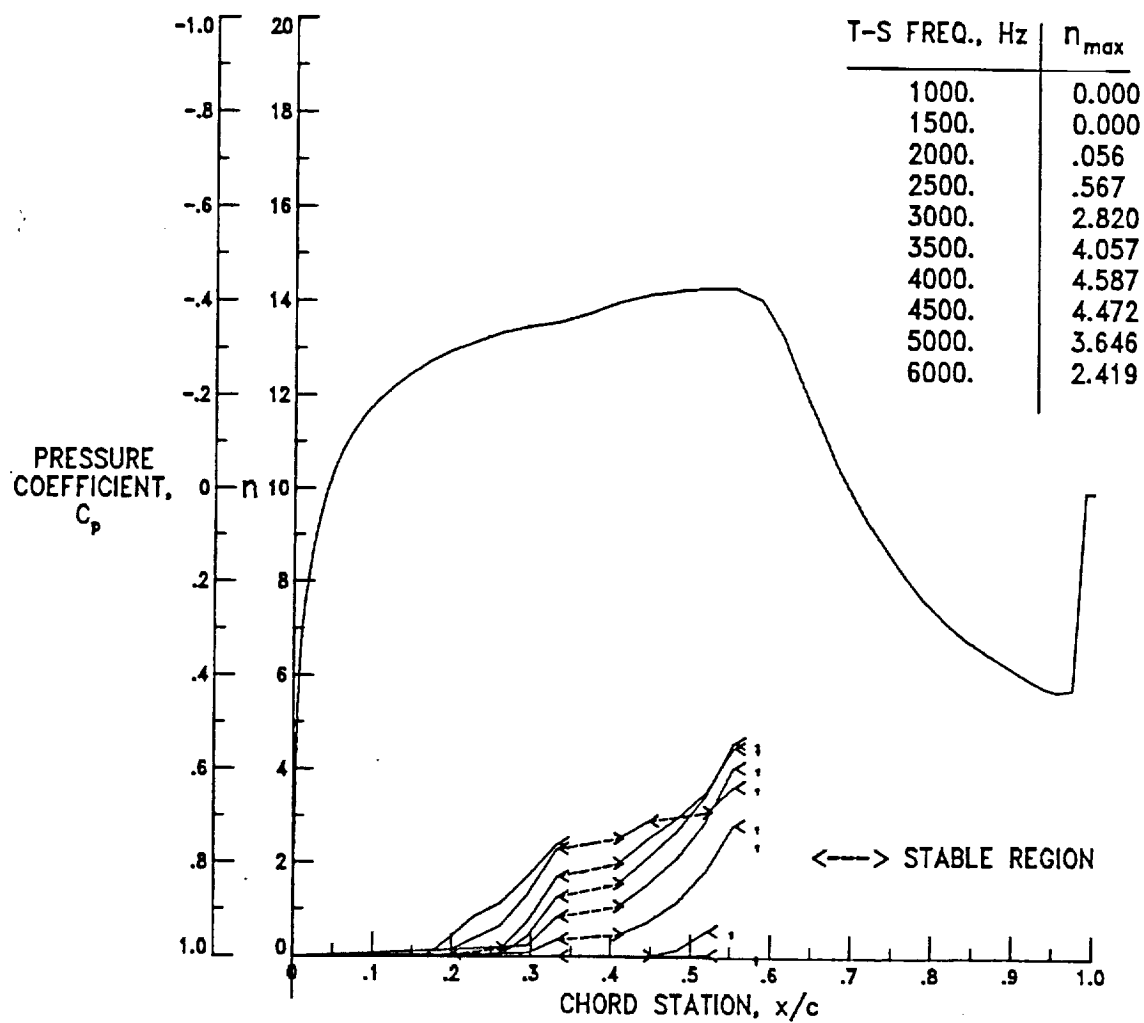


Figure 6.31 Amplification Factor n , Lower Surface Airfoil 26A
 $c_l = 0.46$, $Re = 8.9 \times 10^6$, $M = 0.60$

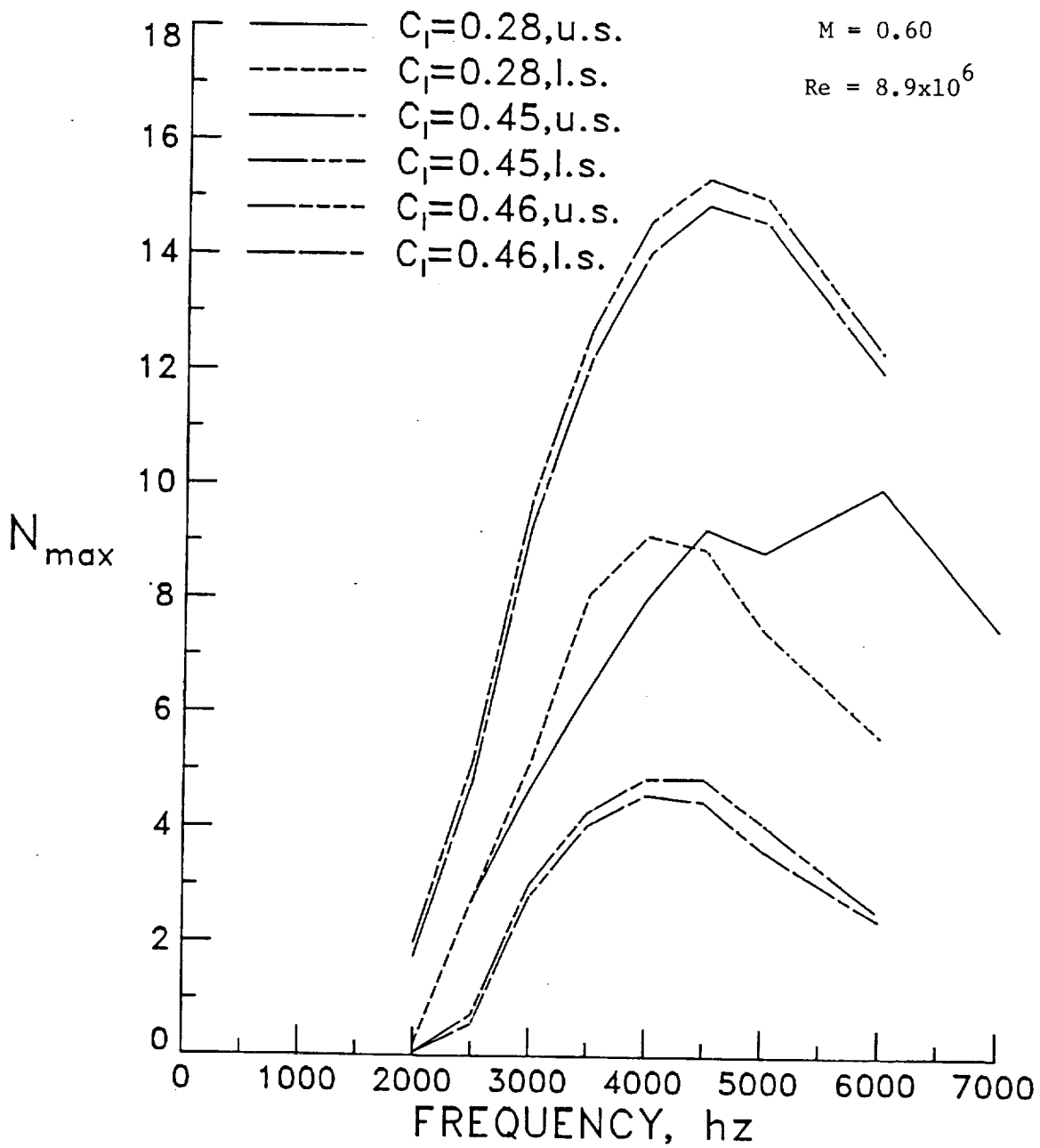


Figure 6.32 Frequency Dependence of n_{max} for airfoil 26A

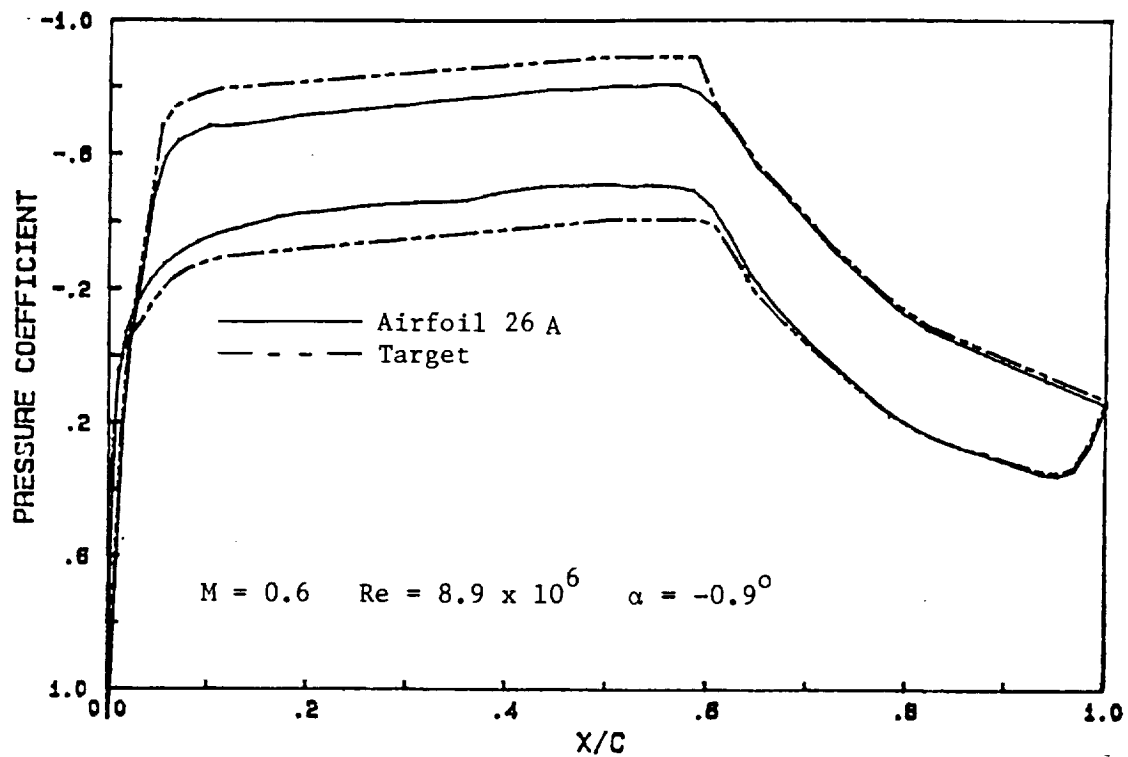


Figure 6.33 Airfoil 26 pressure distribution and target pressure distribution for airfoil 32.

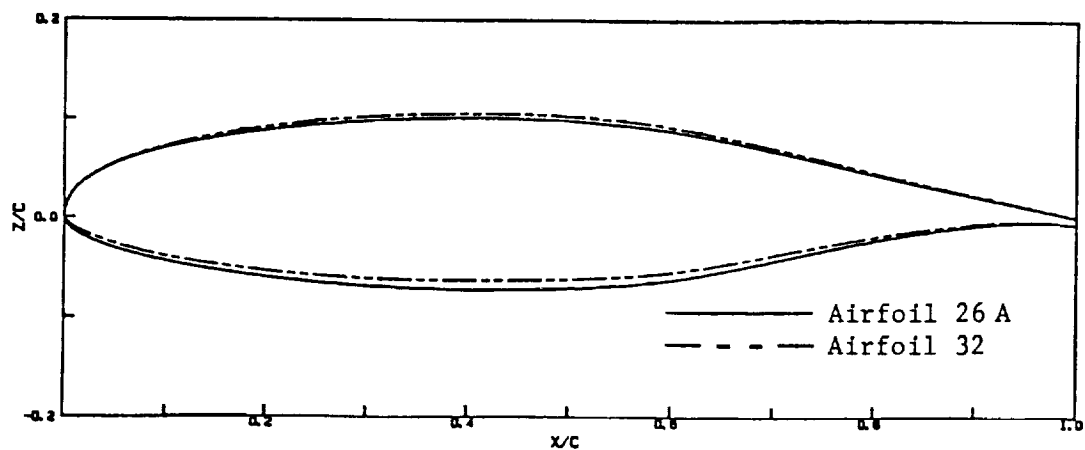


Figure 6.34 Airfoils 26 and 32.

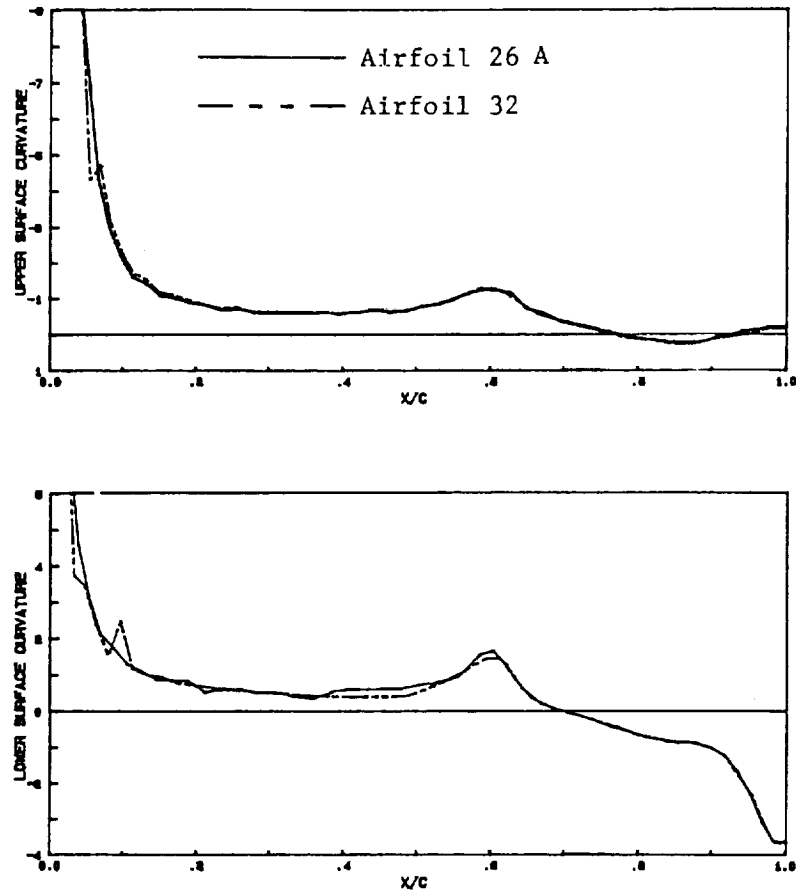


Figure 6.35 Curvature distributions of airfoils 26 & 32.

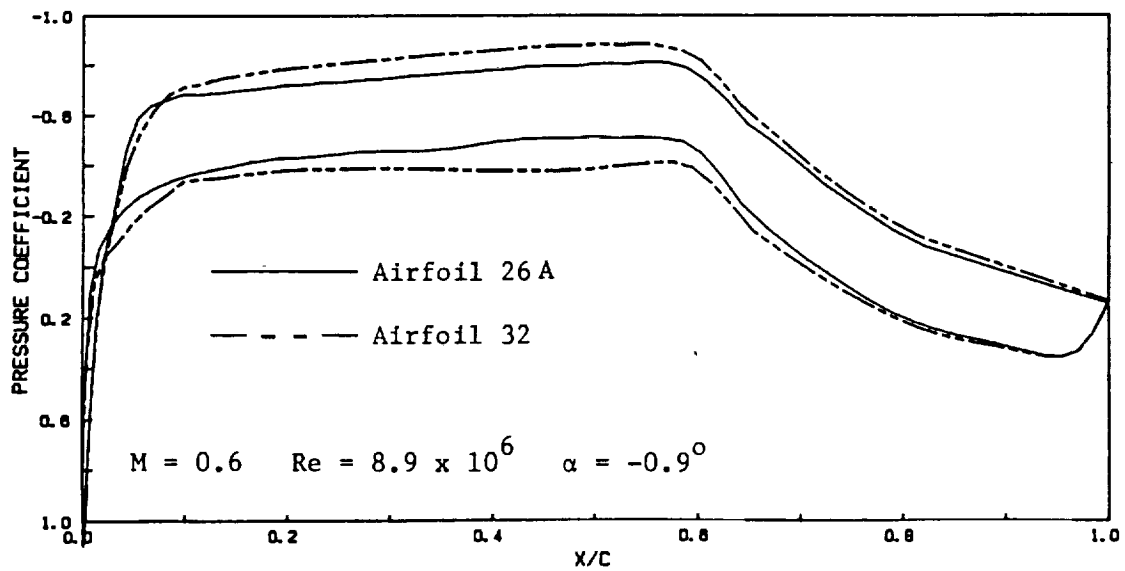


Figure 6.36 Pressure distributions of airfoils 26 & 32 as calculated by the NCS code using natural transition.

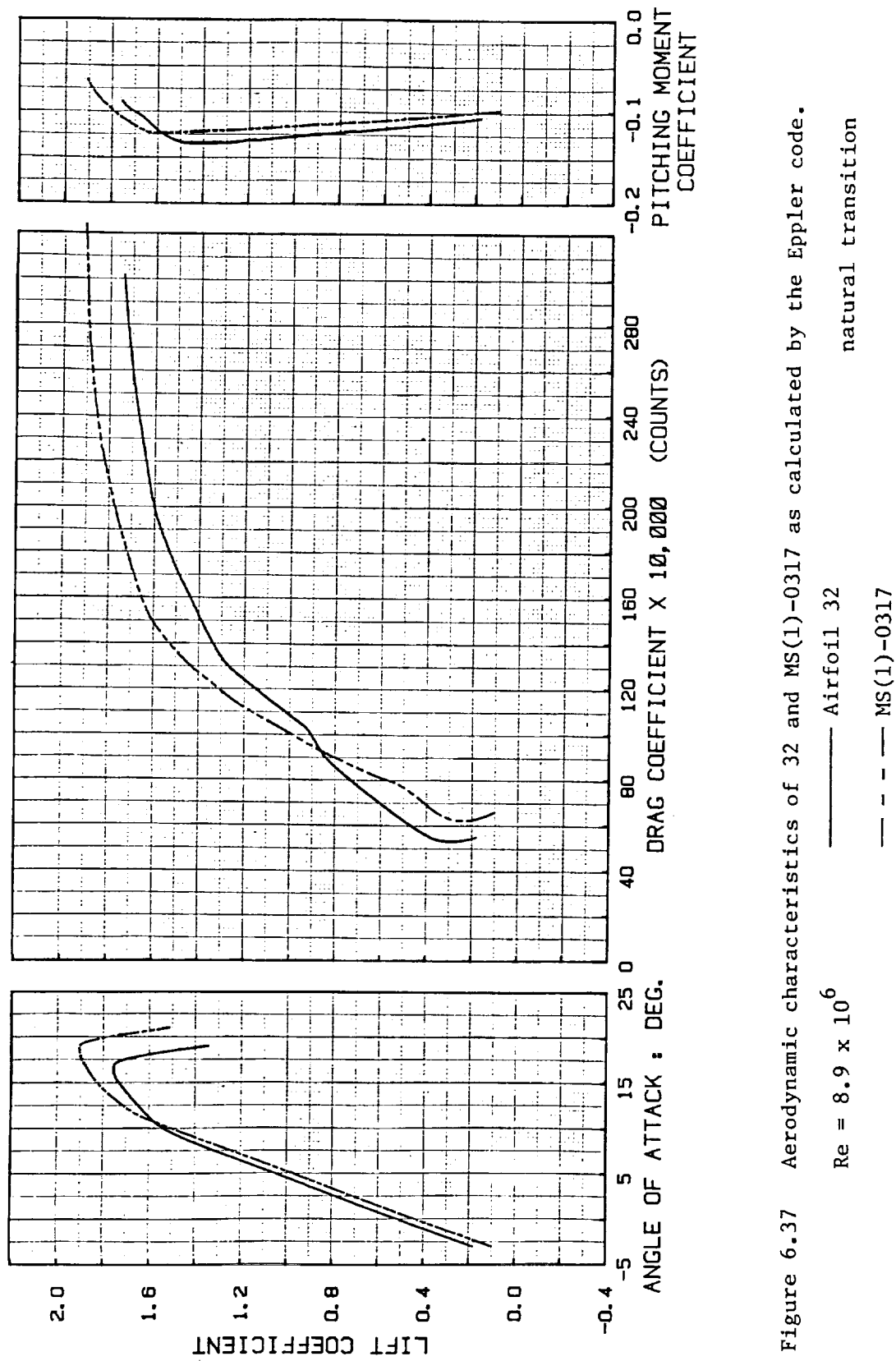


Figure 6.37 Aerodynamic characteristics of 32 and MS(1)-0317 as calculated by the Epppler code.

$Re = 8.9 \times 10^6$

natural transition

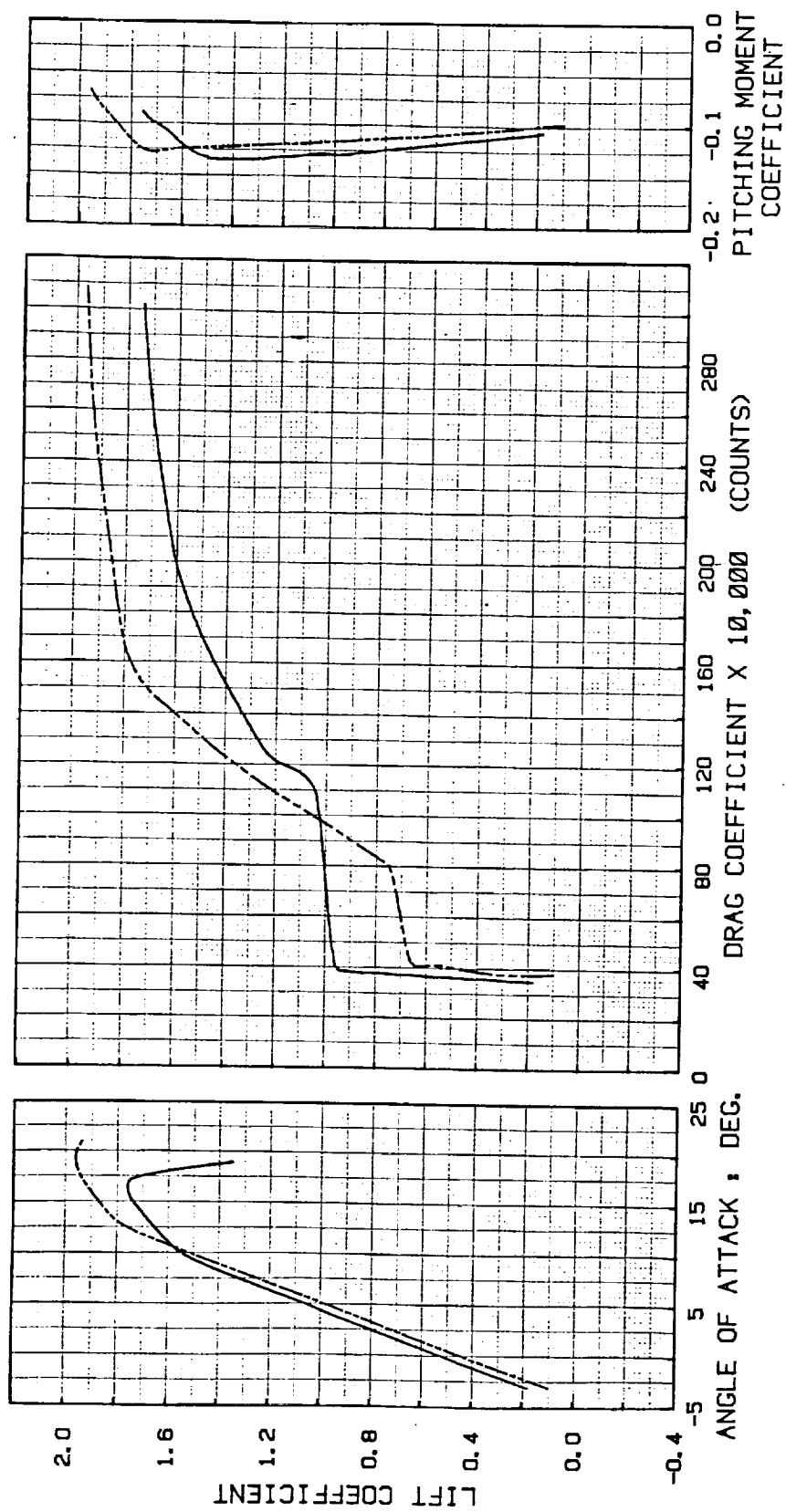


Figure 6.38 Aerodynamic characteristics of 32 and MS(1)-0317 as calculated by the Eppler code.

Re = 8.9×10^6

laminar separation

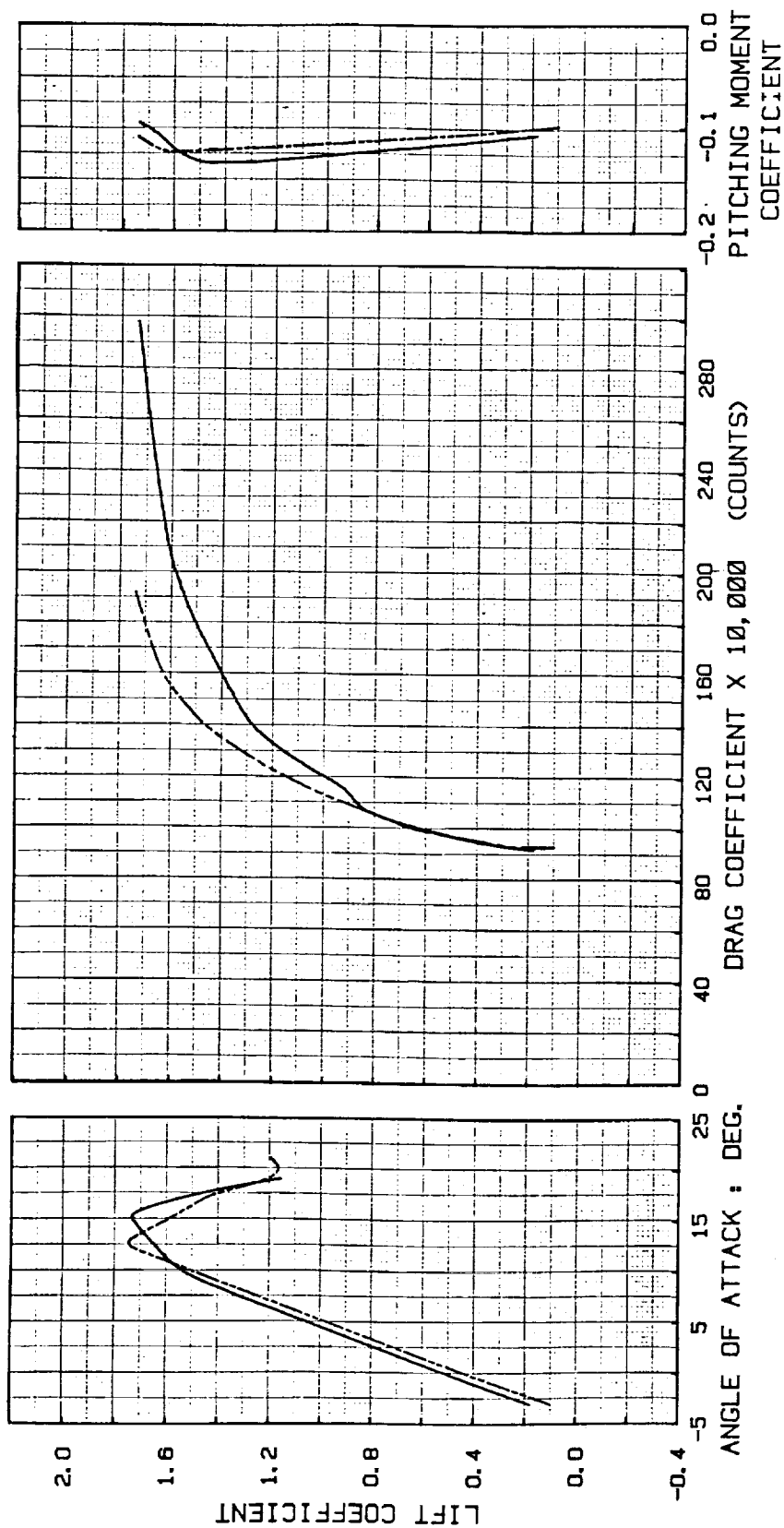


Figure 6.39 Aerodynamic characteristics of 32 and MS(1)-0317 as calculated by the Eppler code.

$Re = 8.9 \times 10^6$

— Airfoil 32

- - - MS(1)-0317

transition fixed at $.05c$

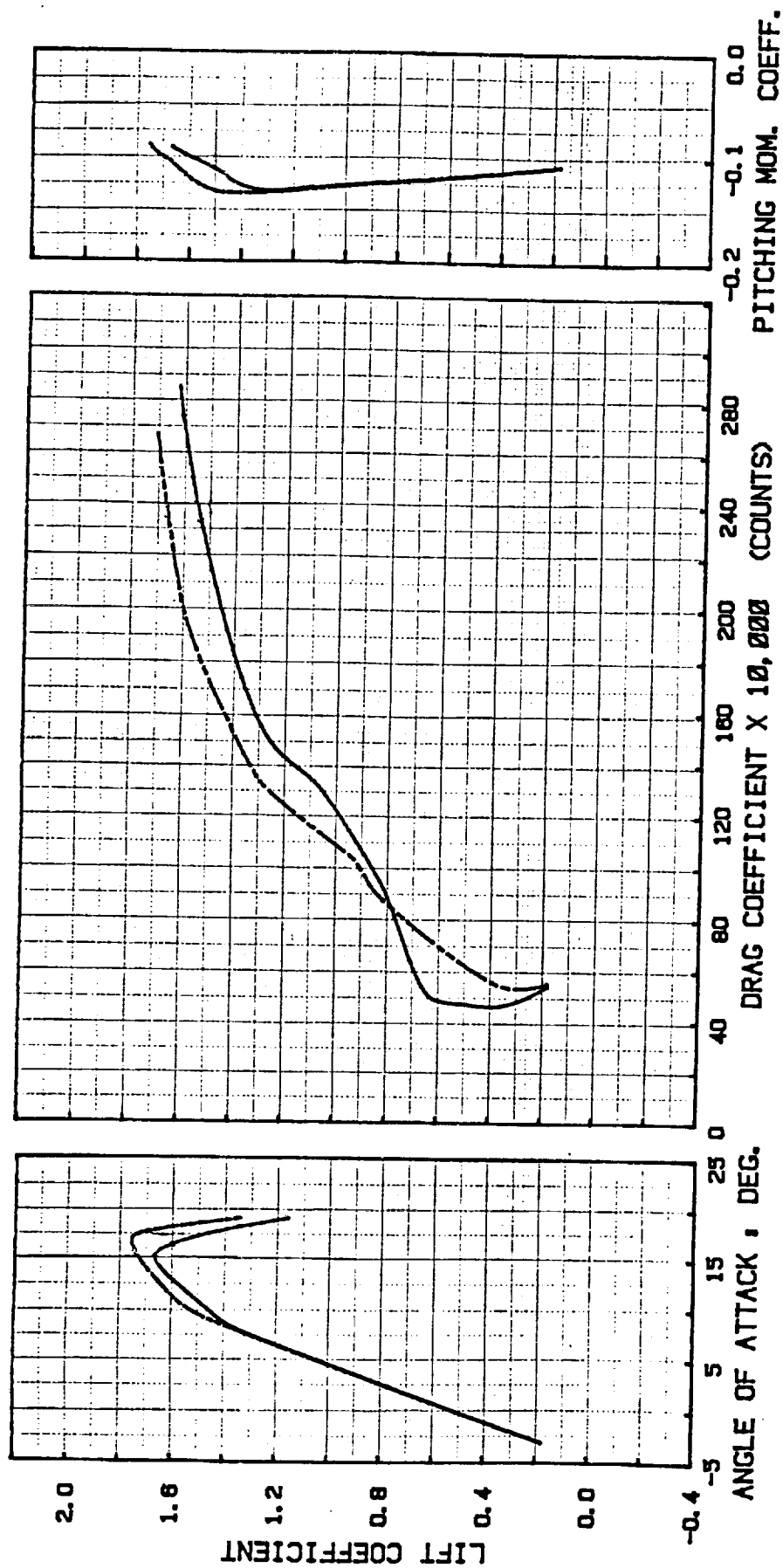


Figure 6.40 Effect of Reynolds number on the aerodynamic characteristics of 32 as predicted by the Eppler code.

— $Re = 4.0 \times 10^6$

- - - $Re = 8.9 \times 10^6$

natural transition

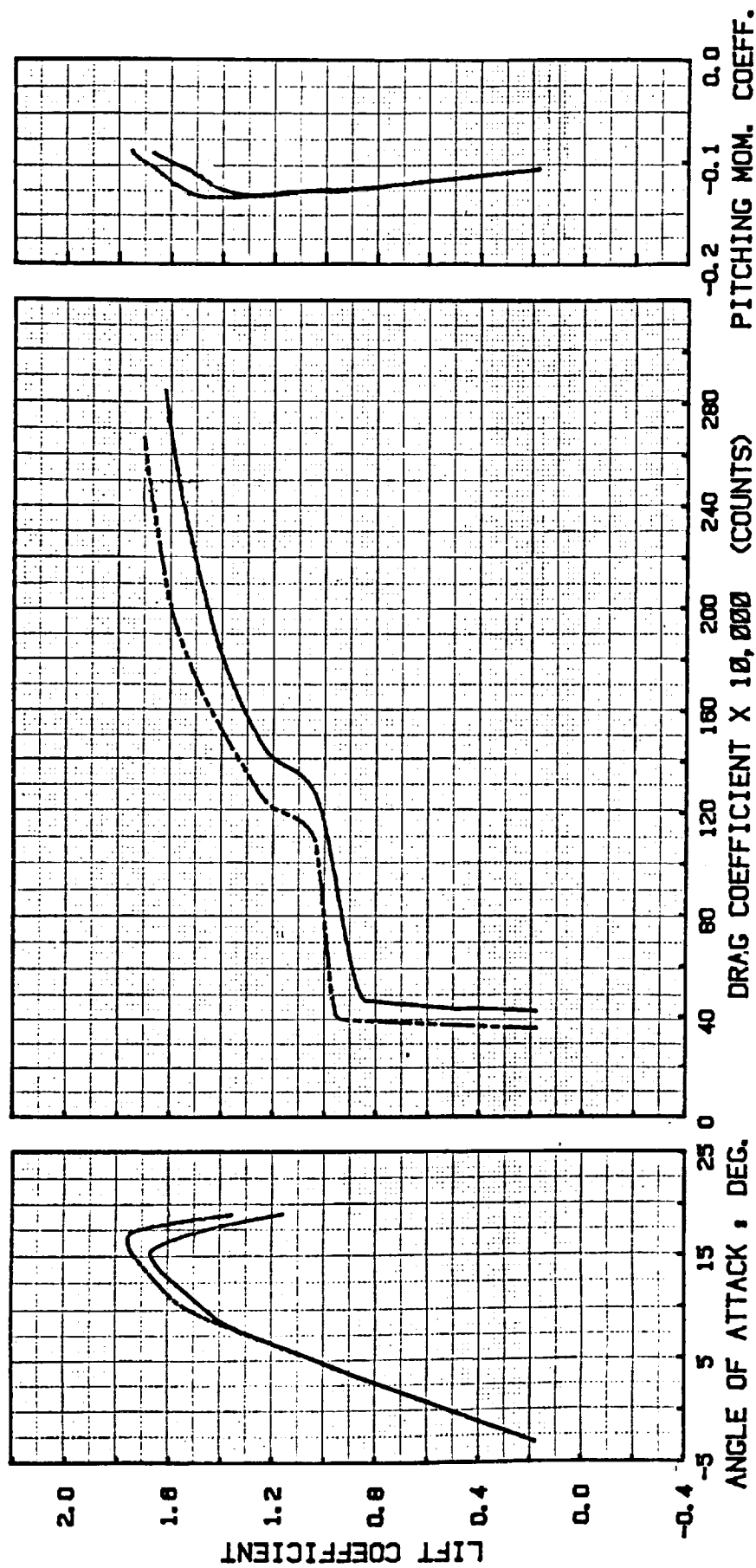


Figure 6.41 Effect of Reynolds number on the aerodynamic characteristics of 32 as predicted by the Eppler code.

— $Re = 4.0 \times 10^6$

- - - $Re = 3.9 \times 10^6$

laminar separation

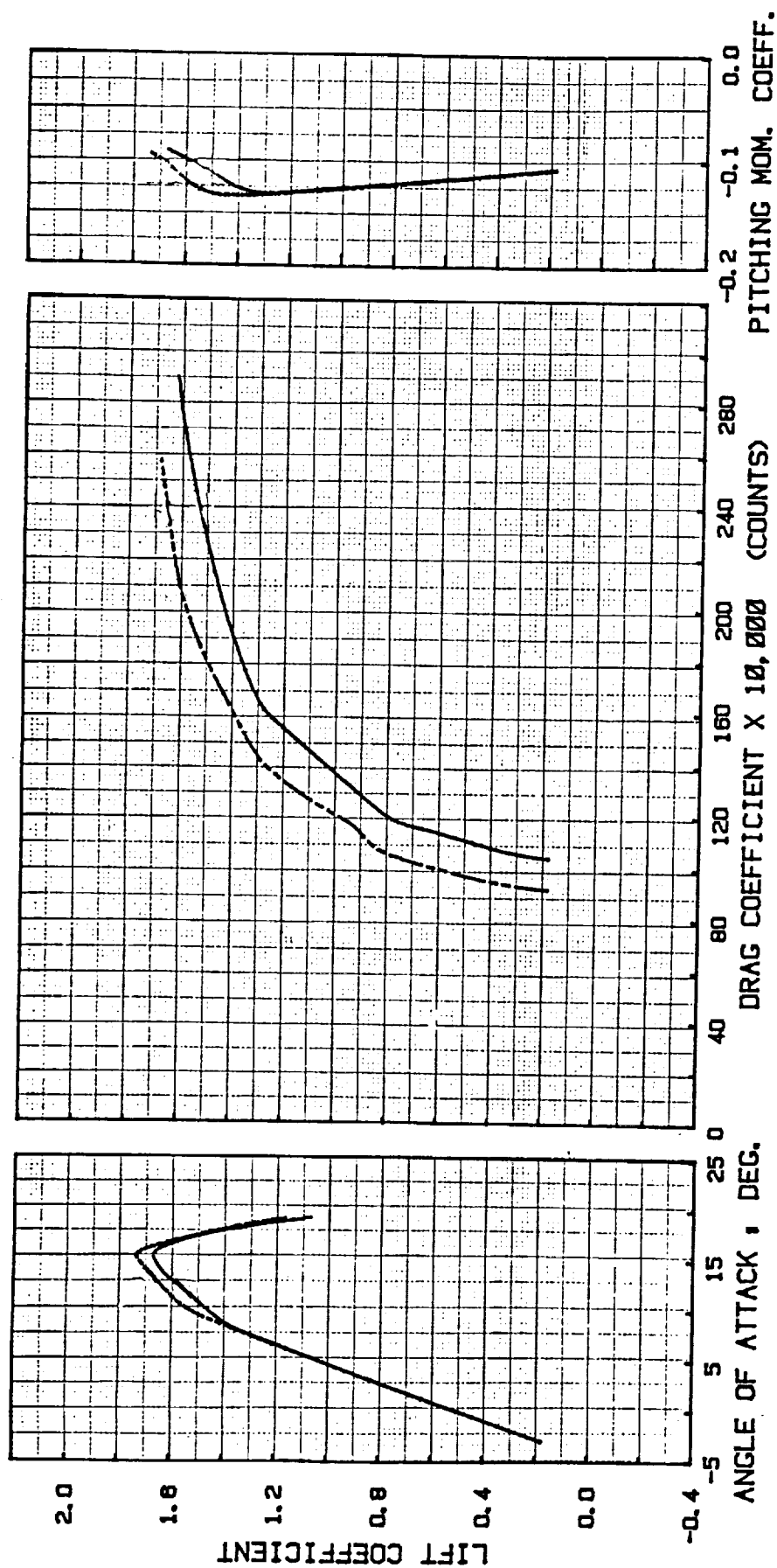


Figure 6.42 Effect of Reynolds number on the aerodynamic characteristics of 32 as predicted by the Eppler code.

— $Re = 4.0 \times 10^6$

- - - $Re = 8.9 \times 10^6$

transition fixed at .05c

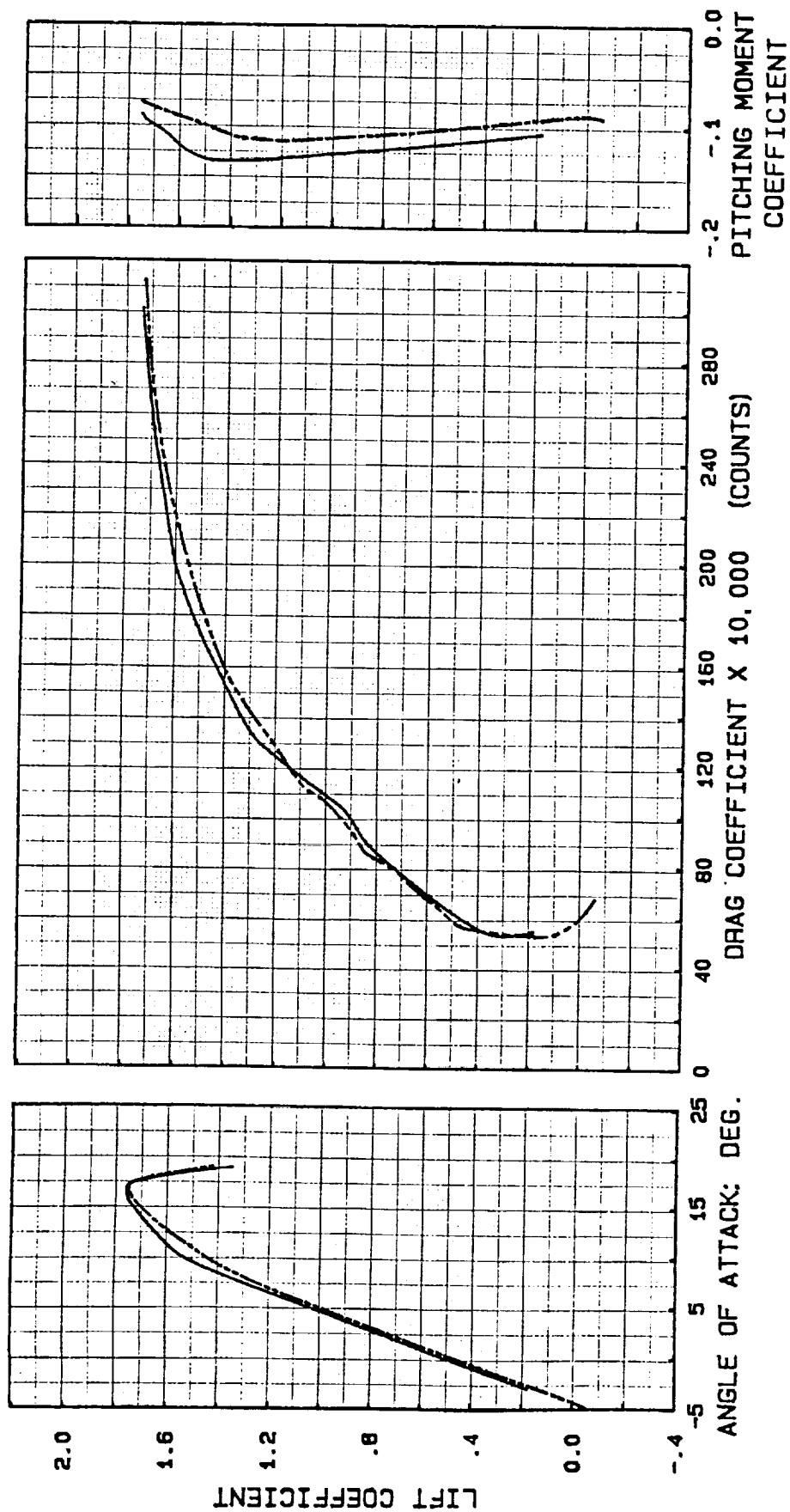


Figure 6.43 Effect of trailing-edge thickness on the aerodynamic characteristics of airfoil 32 as predicted by the Epppler code.

Re = 8.9×10^6

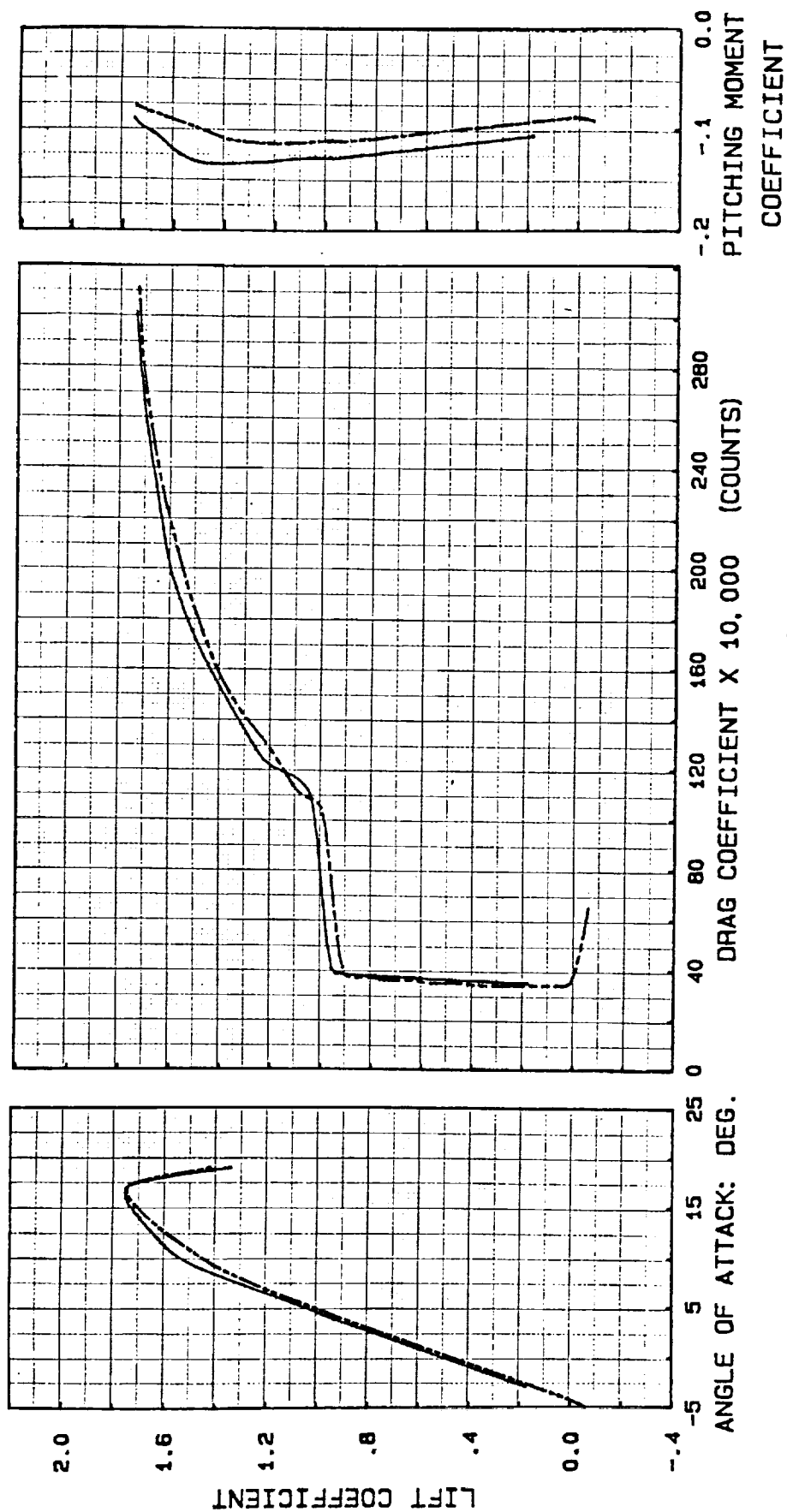


Figure 6.44 Effect of trailing-edge thickness on the aerodynamic characteristics of airfoil 32 as predicted by the Eppler code.

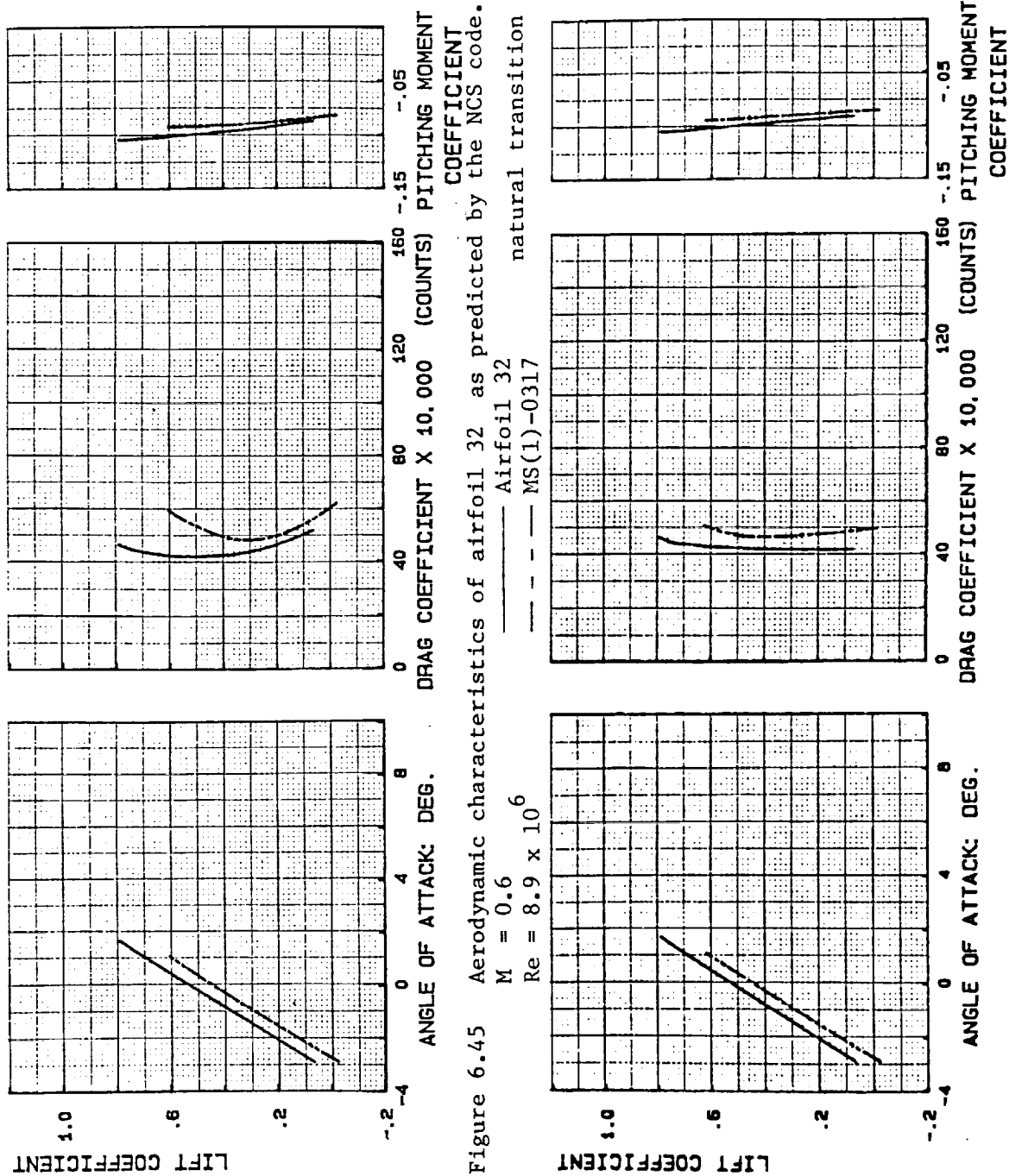


Figure 6.46 Aerodynamic characteristics of airfoil 32 as predicted by the NCS code.
 $M = 0.6$
 $Re = 8.9 \times 10^6$
 — Airfoil 32
 - - - MS(1)-0317
 ... laminar separation

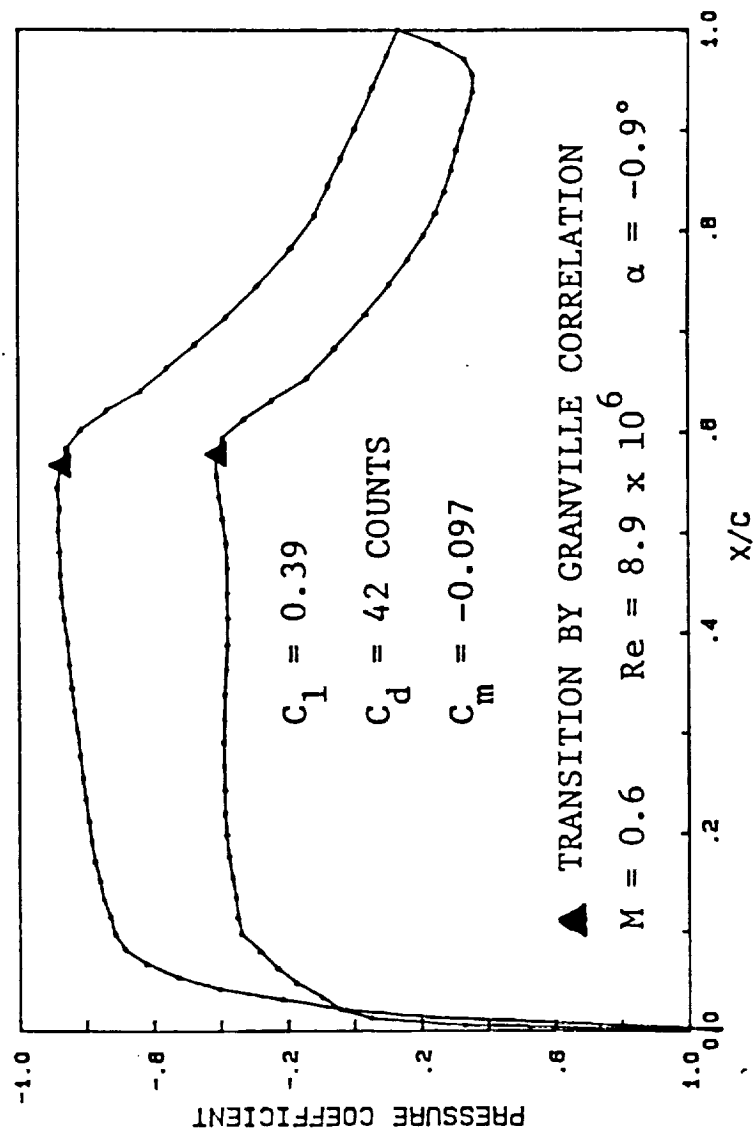
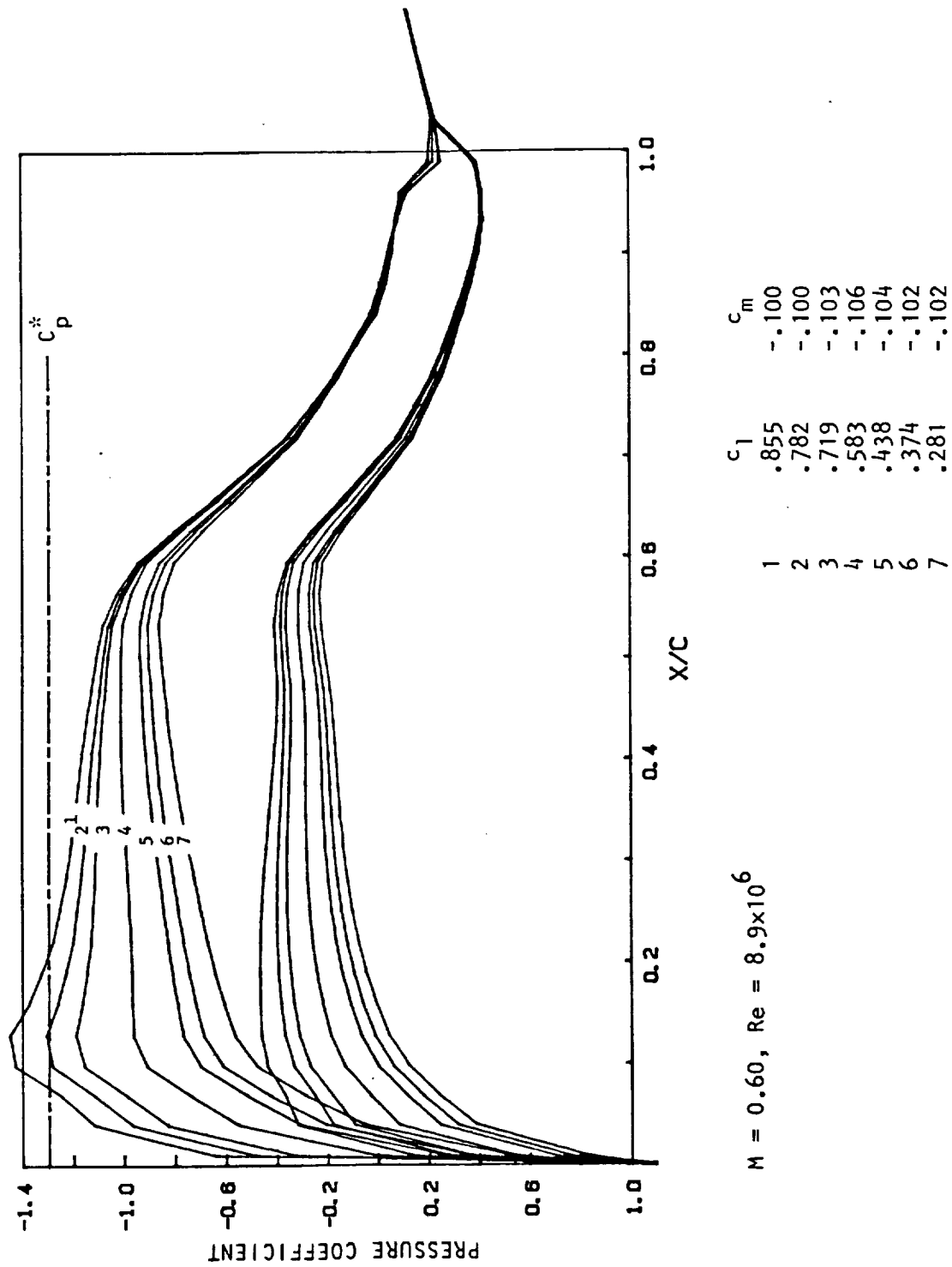


Figure 6.47 Pressure distribution for airfoil 32 as calculated by the NCS code using natural transition.



$M = 0.60, Re = 8.9 \times 10^6$

Figure 6.48 Calculated pressure distributions airfoil 32;
TRANSEP code (medium grid)

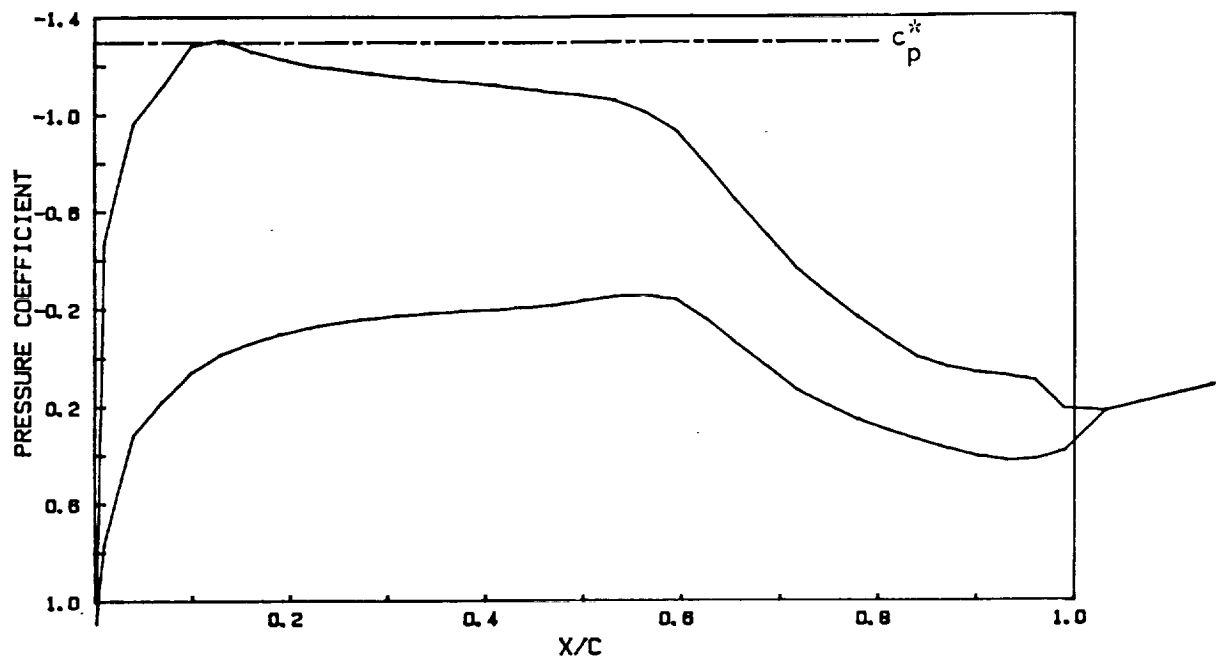


Figure 6.49 Critical flow condition airfoil 32, $M = 0.60$
 TRANSEP code (medium grid)
 $Re = 8.9 \times 10^6$; $c_l = .78$, $c_m = -.100$

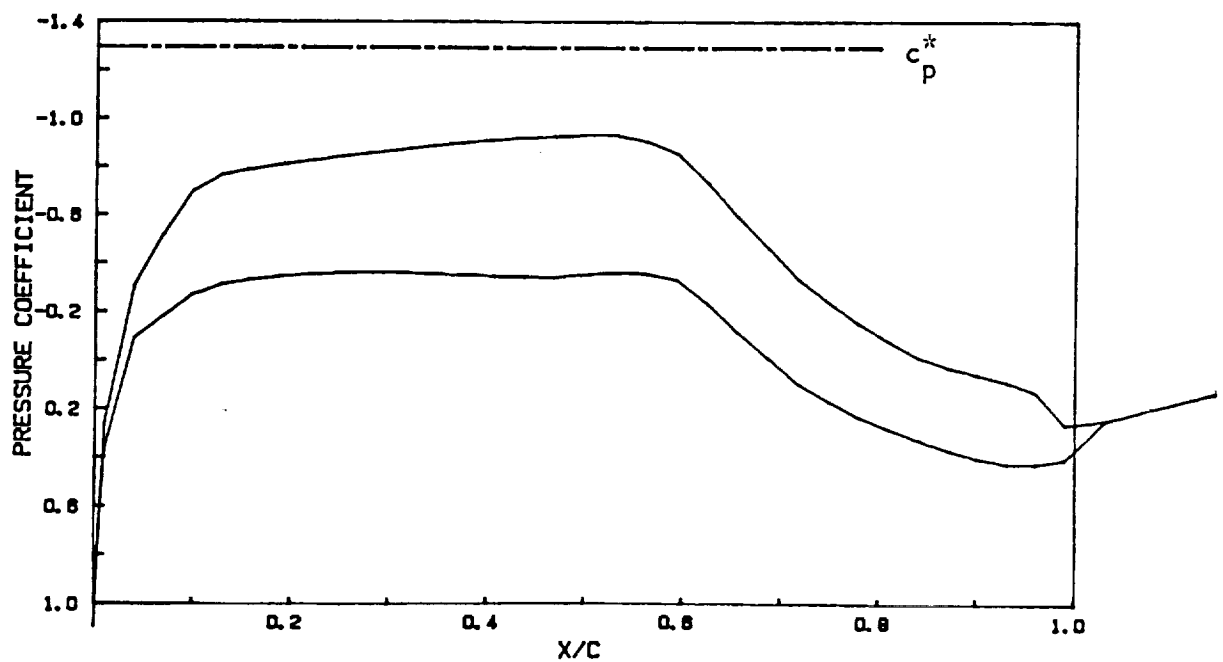


Figure 6.50 Pressure distribution design condition airfoil 32
 TRANSEP code (medium grid)
 $M = 0.60$; $Re = 8.9 \times 10^6$; $\alpha = -0.9^\circ$

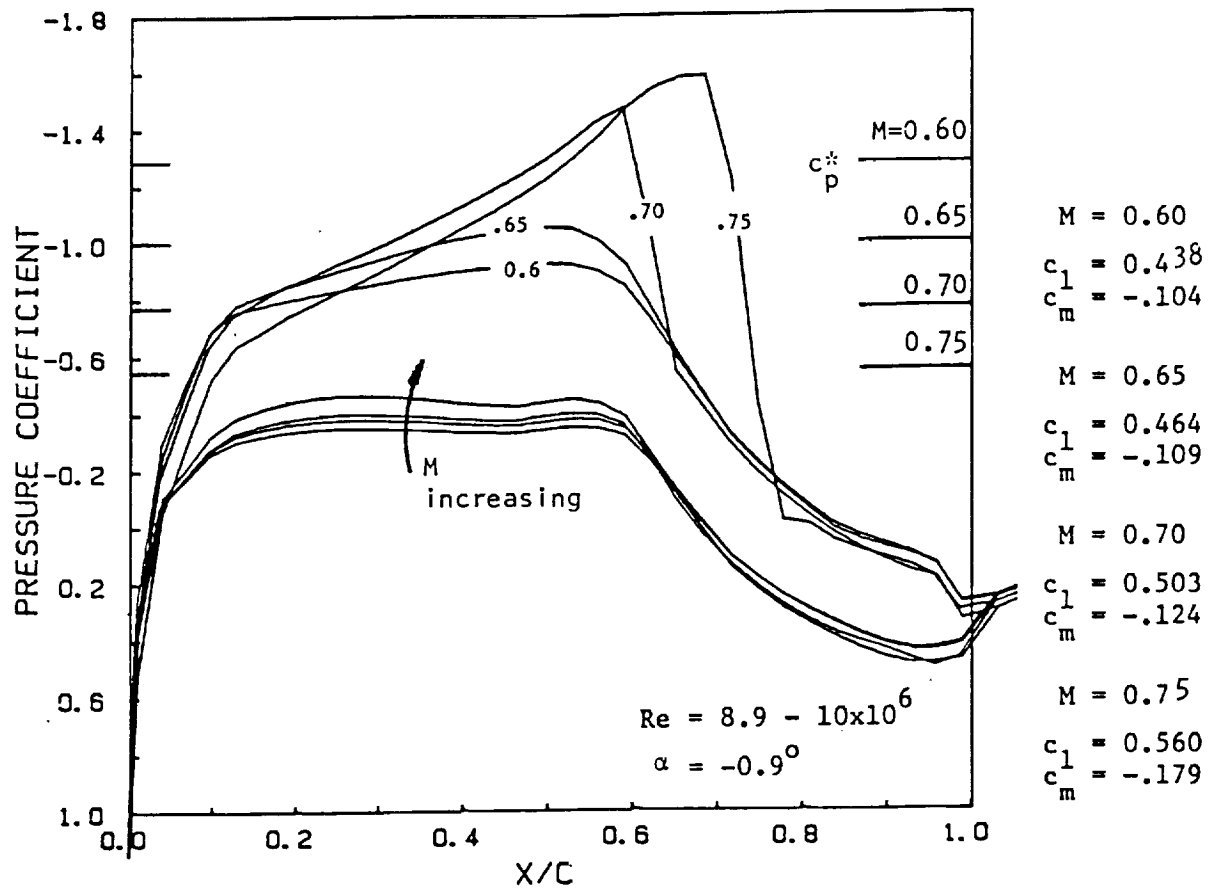


Figure 6.51 Pressure distributions for several Mach numbers
TRANSEP code (medium grid)
Airfoil 32

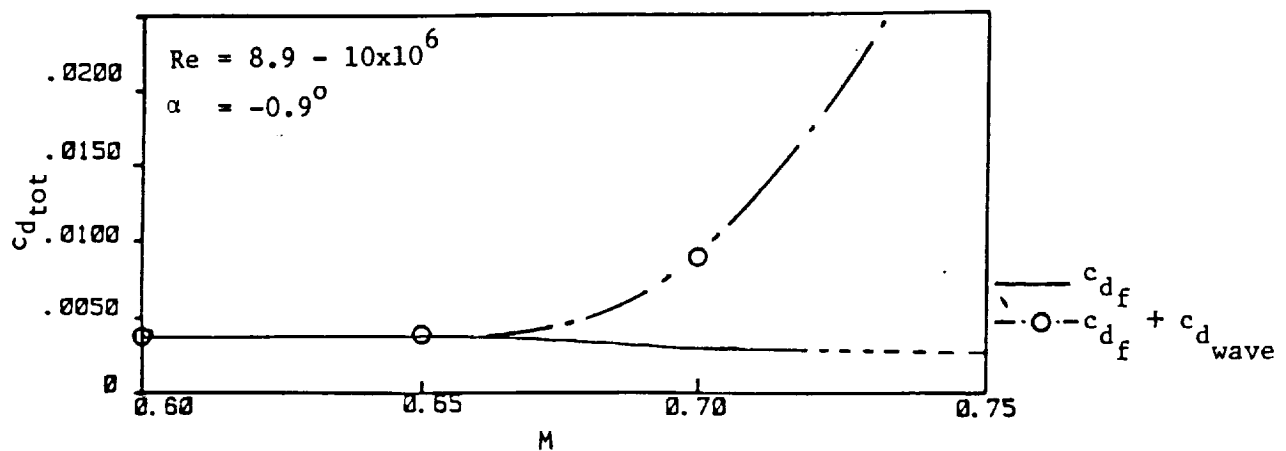


Figure 6.52 Drag rise estimate airfoil 32
TRANSEP (medium grid)

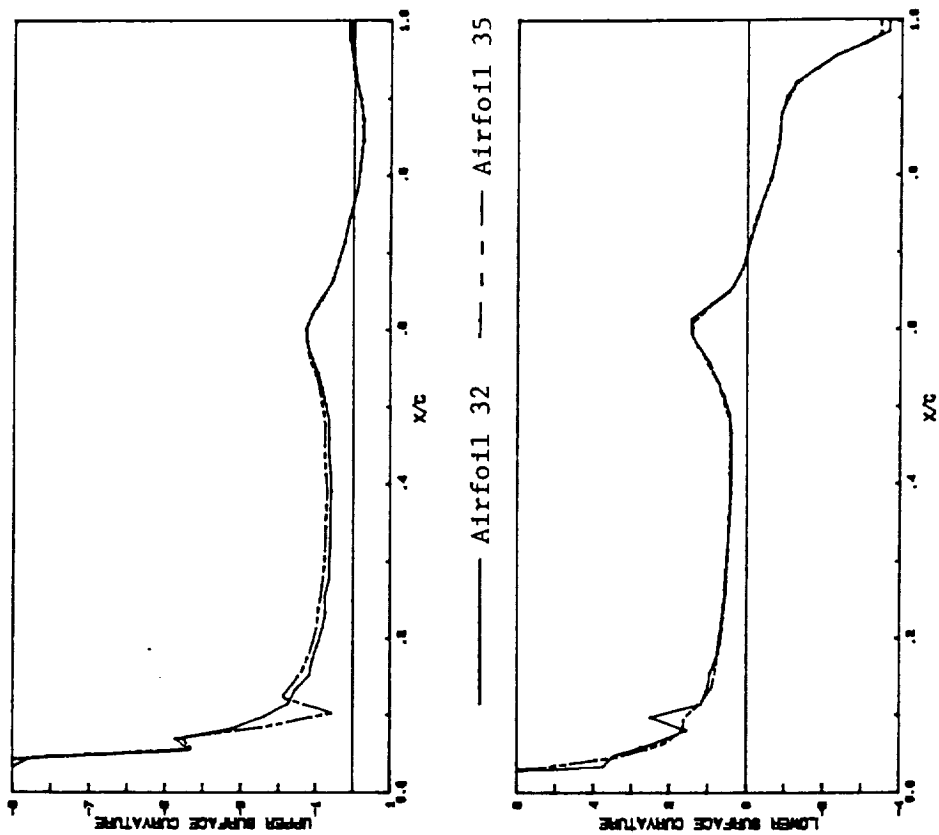


Figure 6.54 Curvature distributions of airfoils 32 & 35.

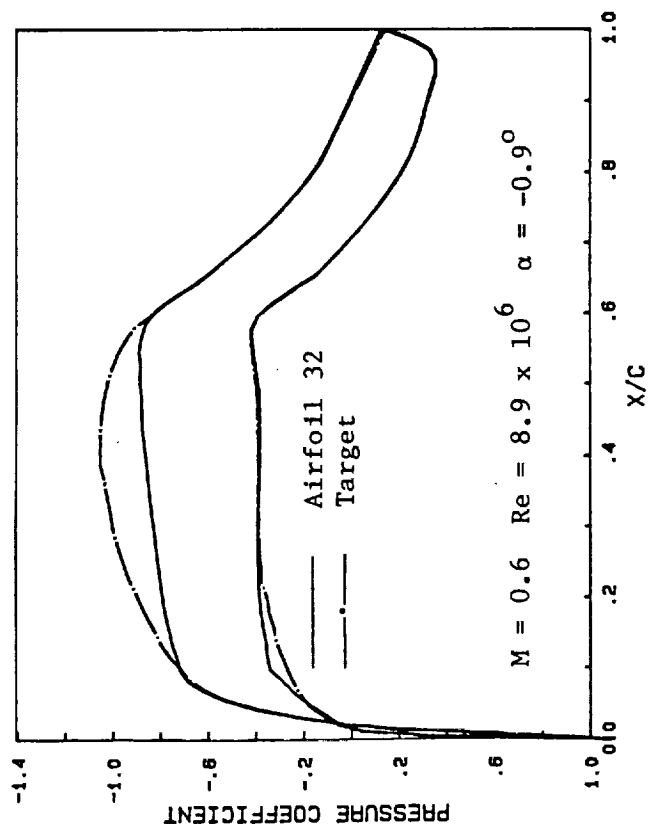


Figure 6.53 Airfoil 32 pressure distribution and target pressure distribution.

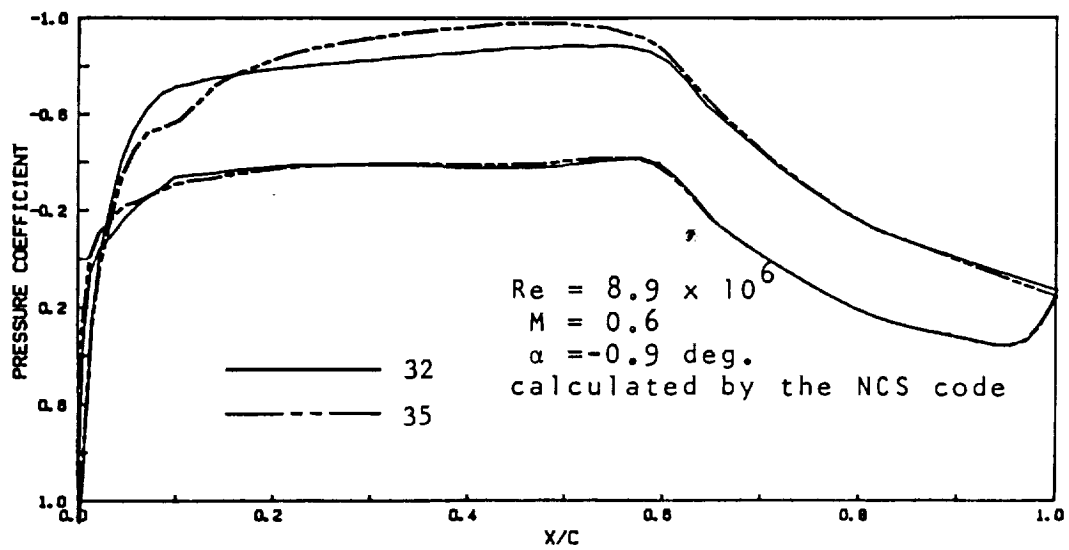


Figure 6.55 Comparison of airfoils 32 and 35 pressure distributions

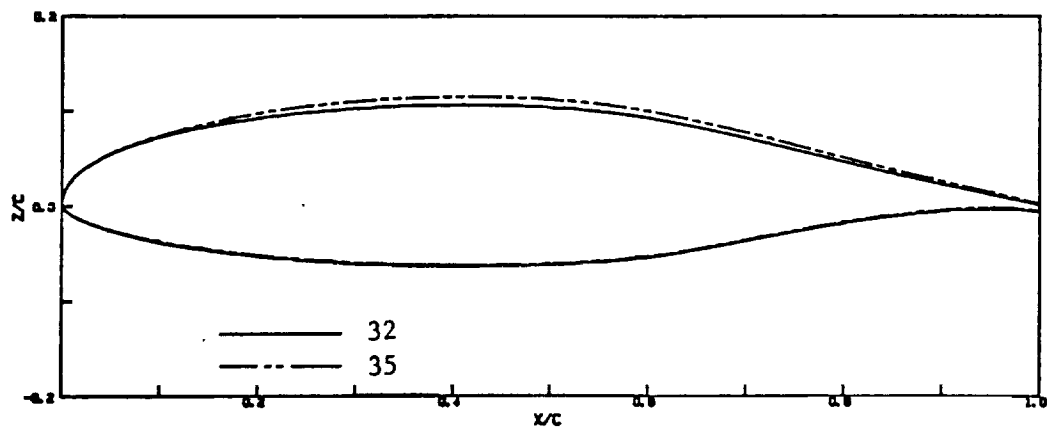


Figure 6.56 Airfoil 32 and 35 contours

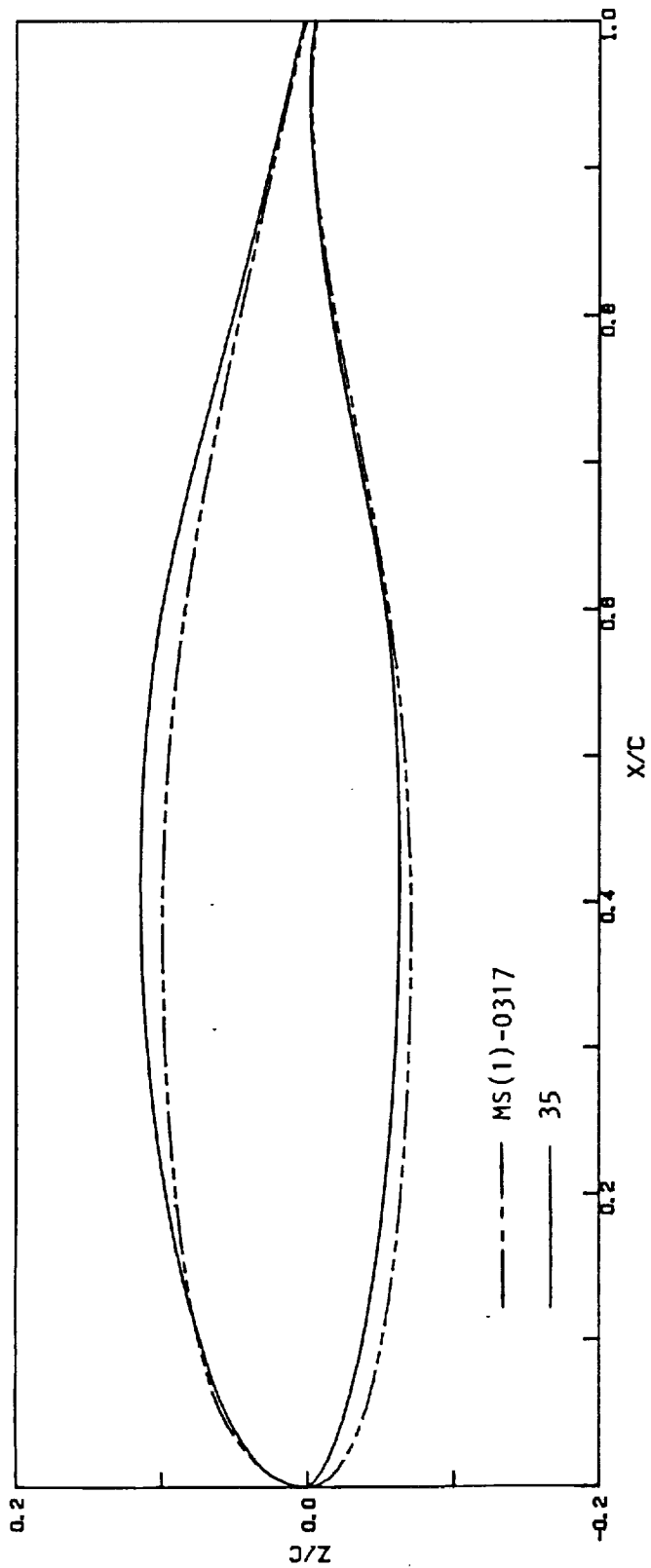


Figure 6.57 Comparison of MS(1)-0317 and 35 contours

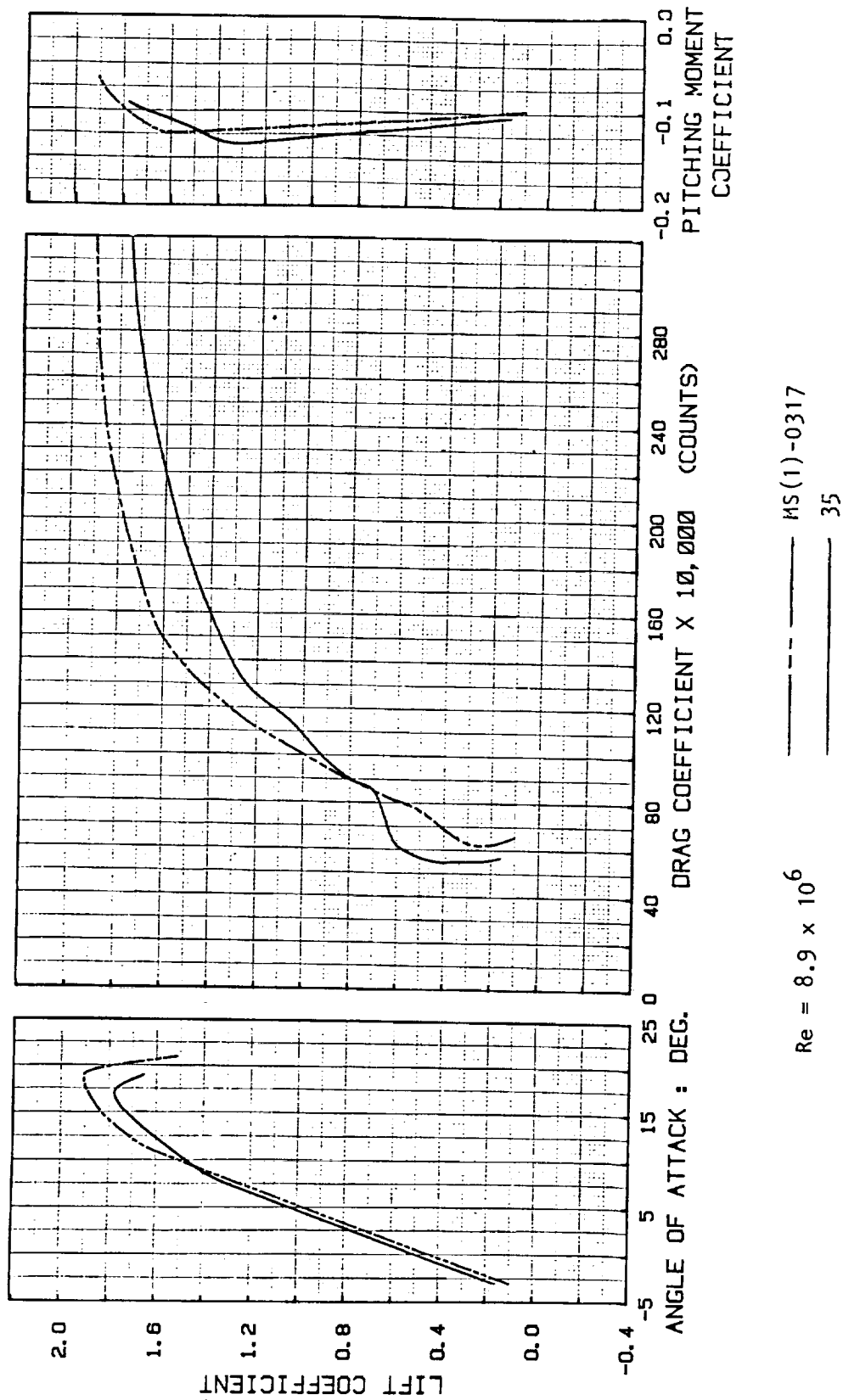


Figure 6.58 Aerodynamic characteristics of 35 and MS(1)-0317 as calculated by the Eppler code using natural transition

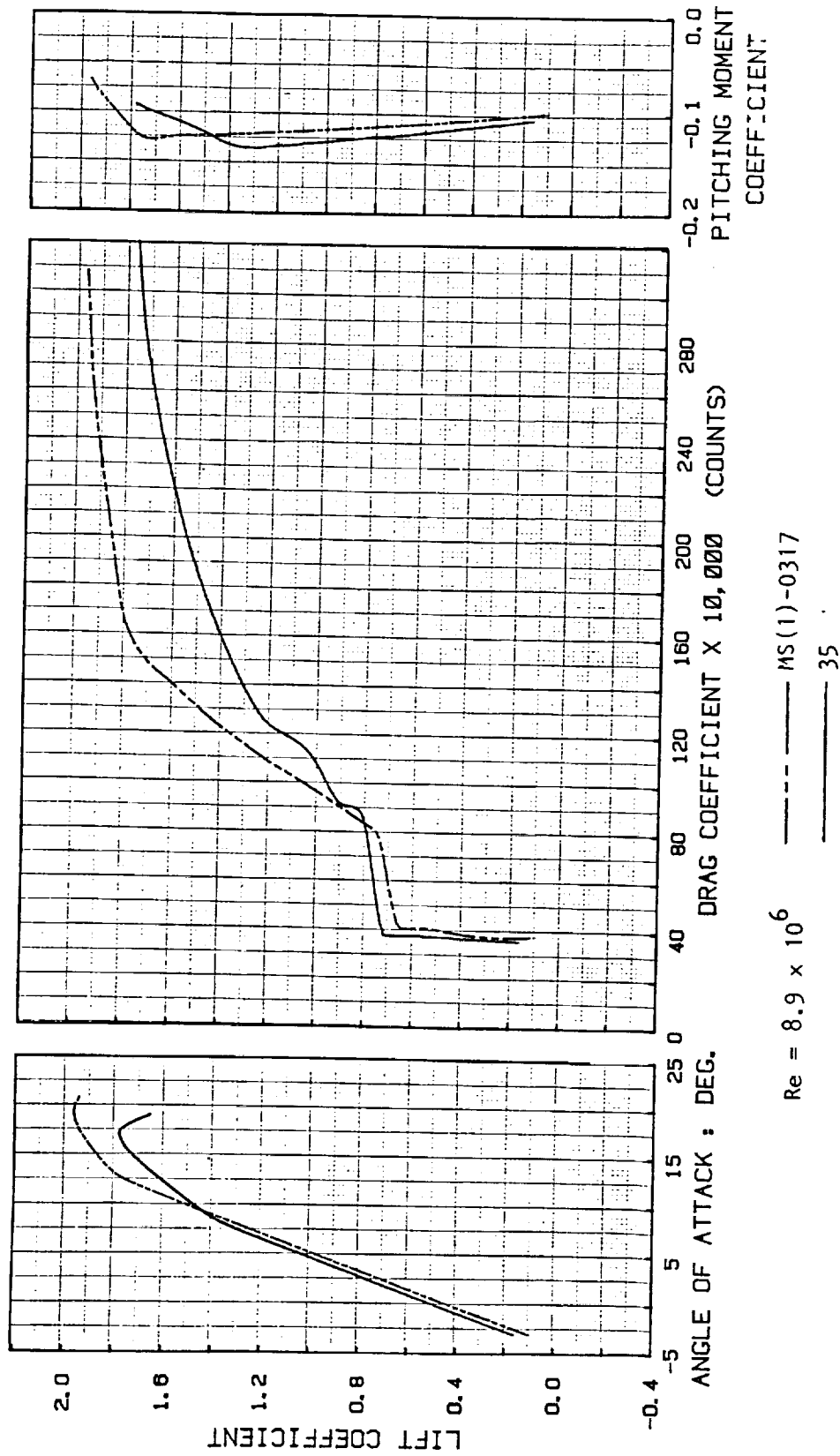


Figure 6.59 Aerodynamic characteristics of 35 and MS(1)-0317 as calculated by the Eppler code using laminar separation

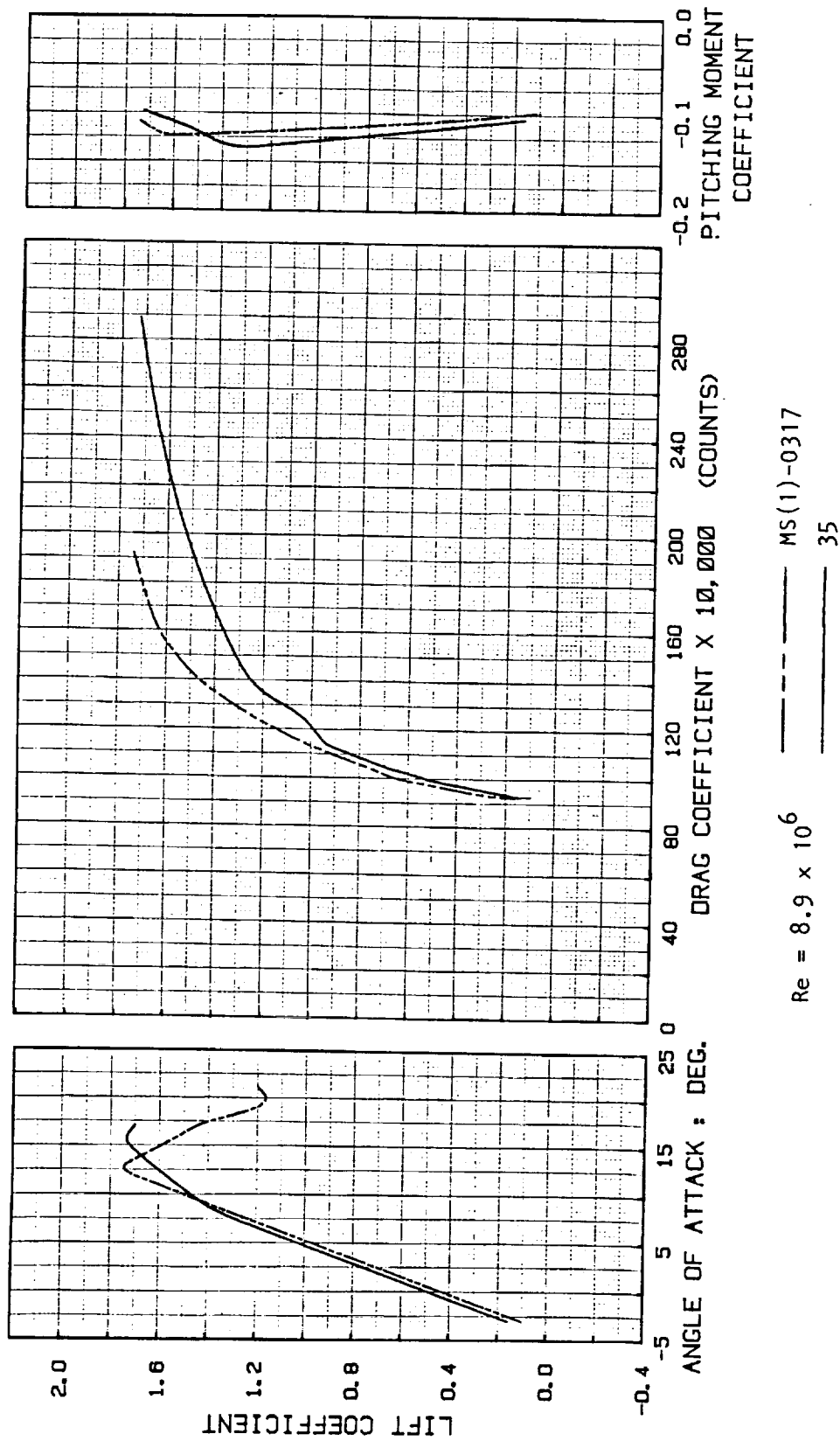


Figure 6.60 Aerodynamic characteristics of 35 and MS(1)-0317 as calculated by the Eppler code using fixed transition at 5-percent chord on both surfaces

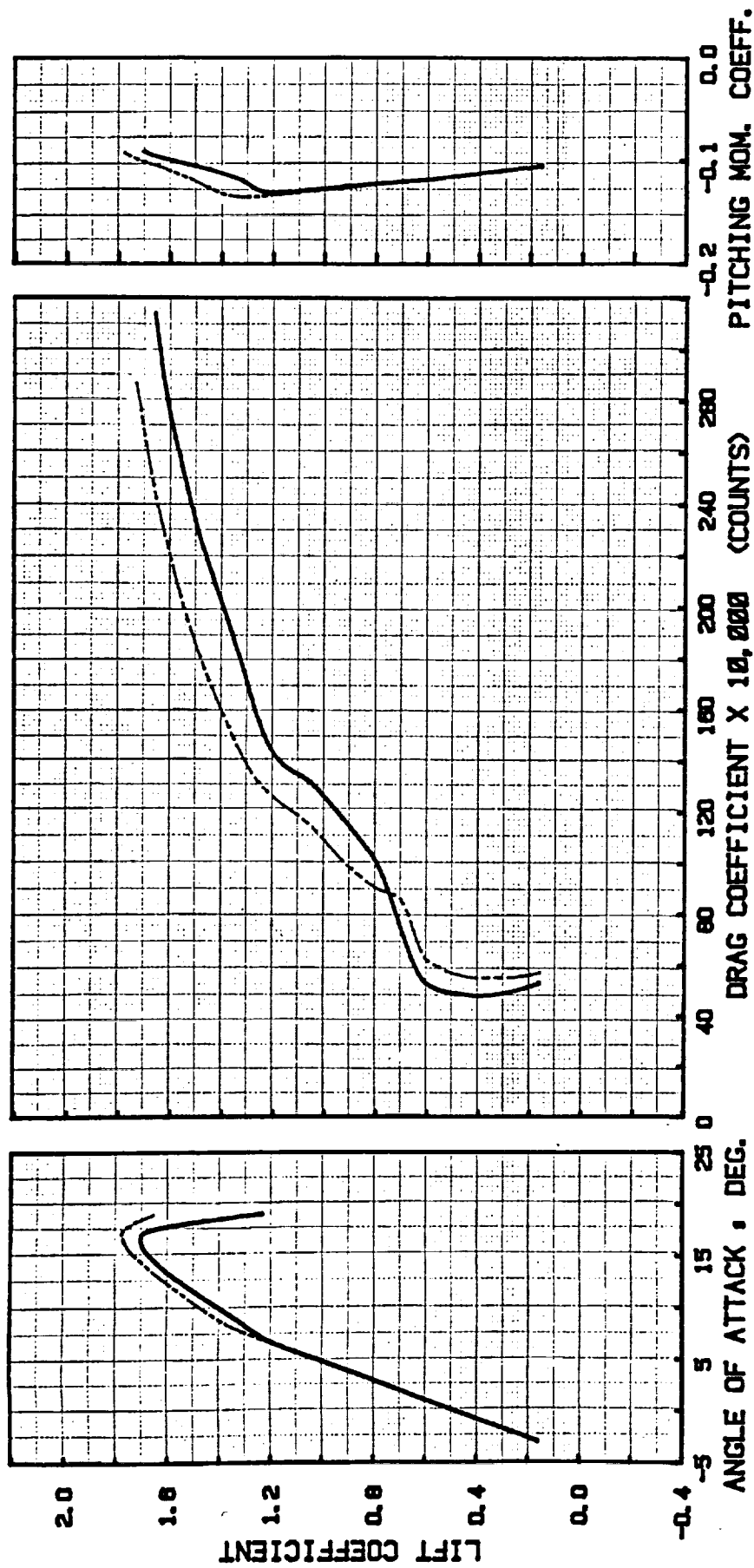


Figure 6. 61 Effect of Reynolds number on the aerodynamic characteristics of 35 as predicted by the Eppler code.

— $Re = 4.0 \times 10^6$
 - - - $Re = 8.9 \times 10^6$
 natural transition

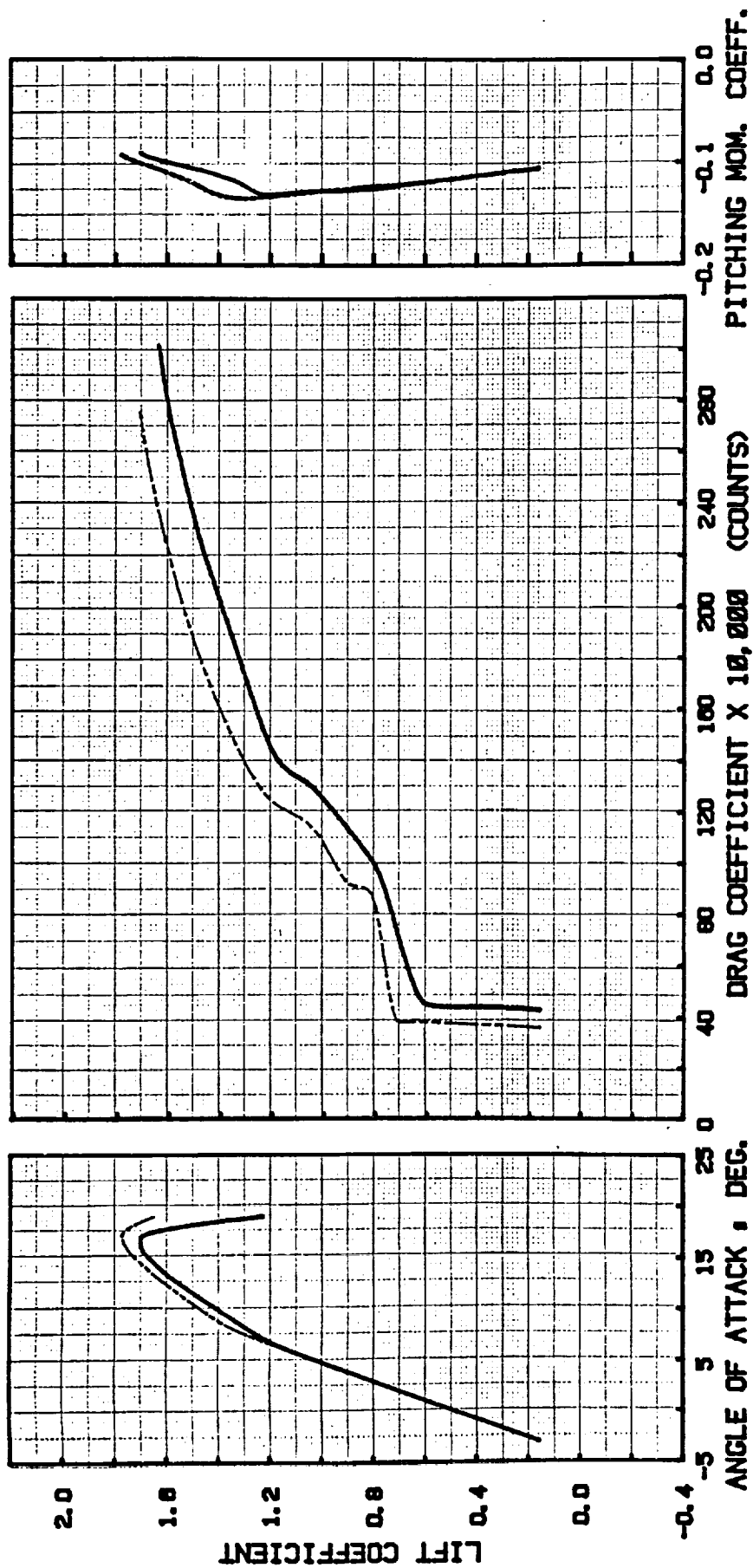


Figure 6. 62 Effect of Reynolds number on the aerodynamic characteristics of 35 as predicted by the Eppler code.

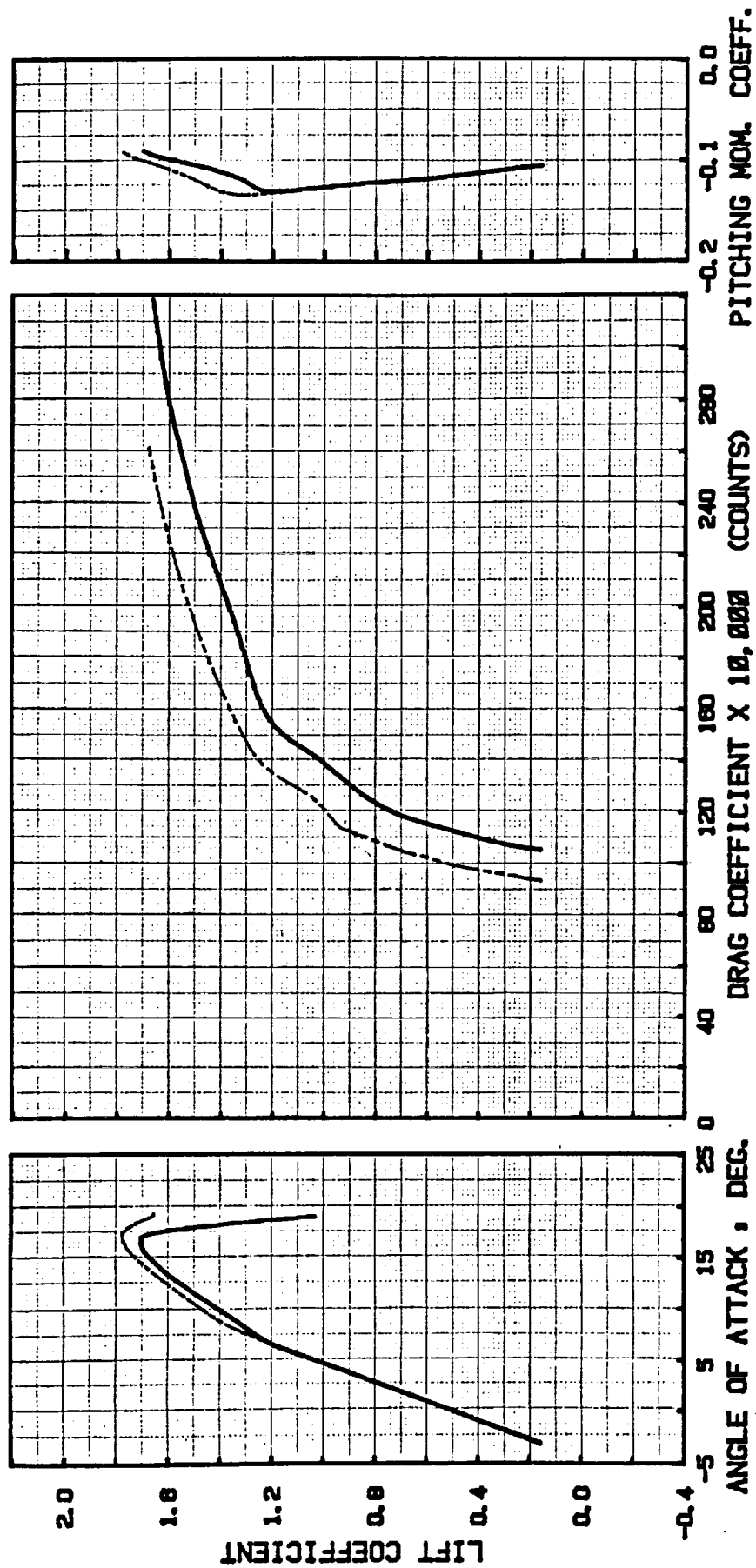


Figure 6.63 Effect of Reynolds number on the aerodynamic characteristics of 35 as predicted by the Eppler code.

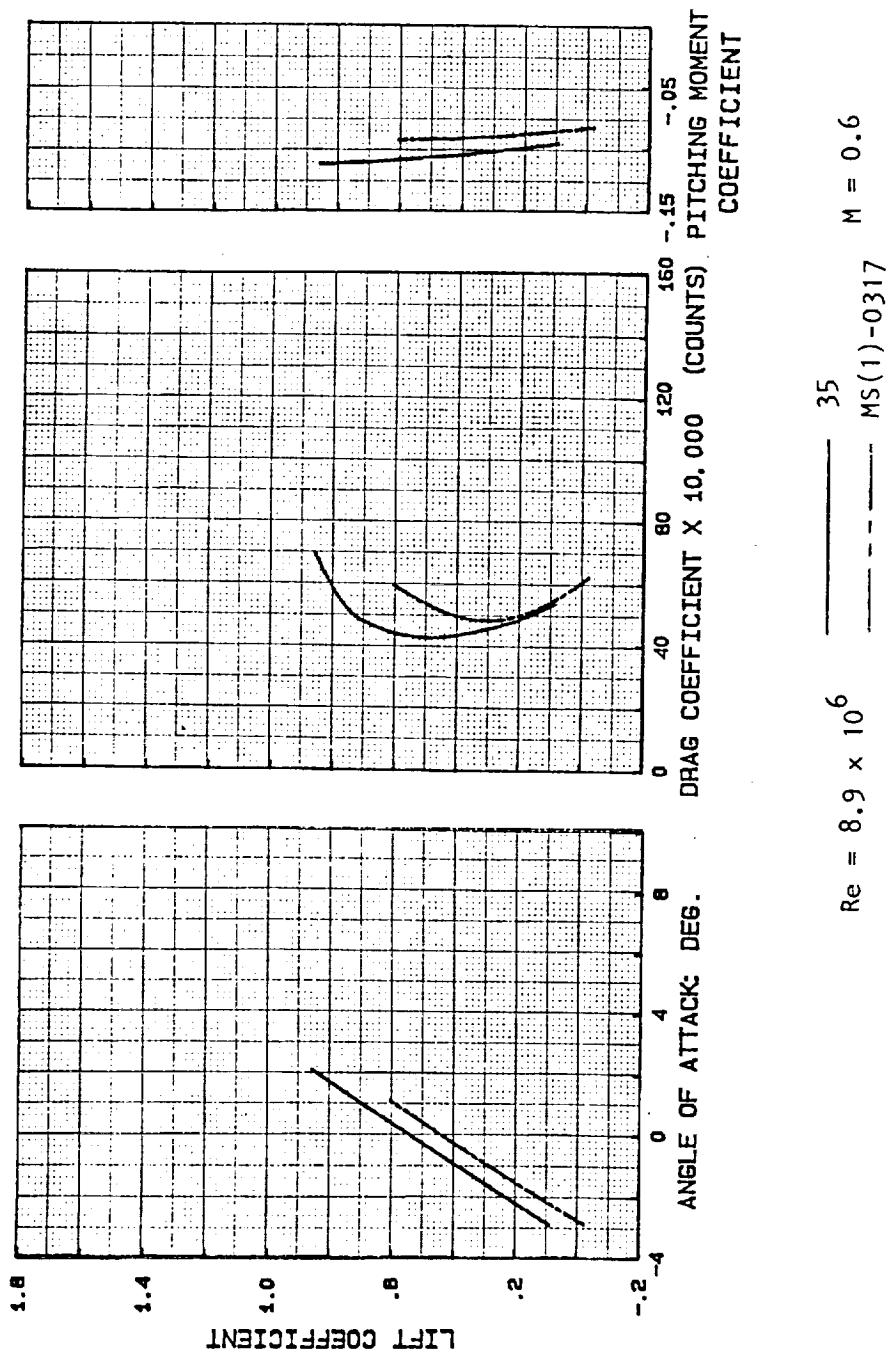


Figure 6.64 Aerodynamic characteristics of 35 and MS(1)-0317 as calculated by NCS code using natural transition

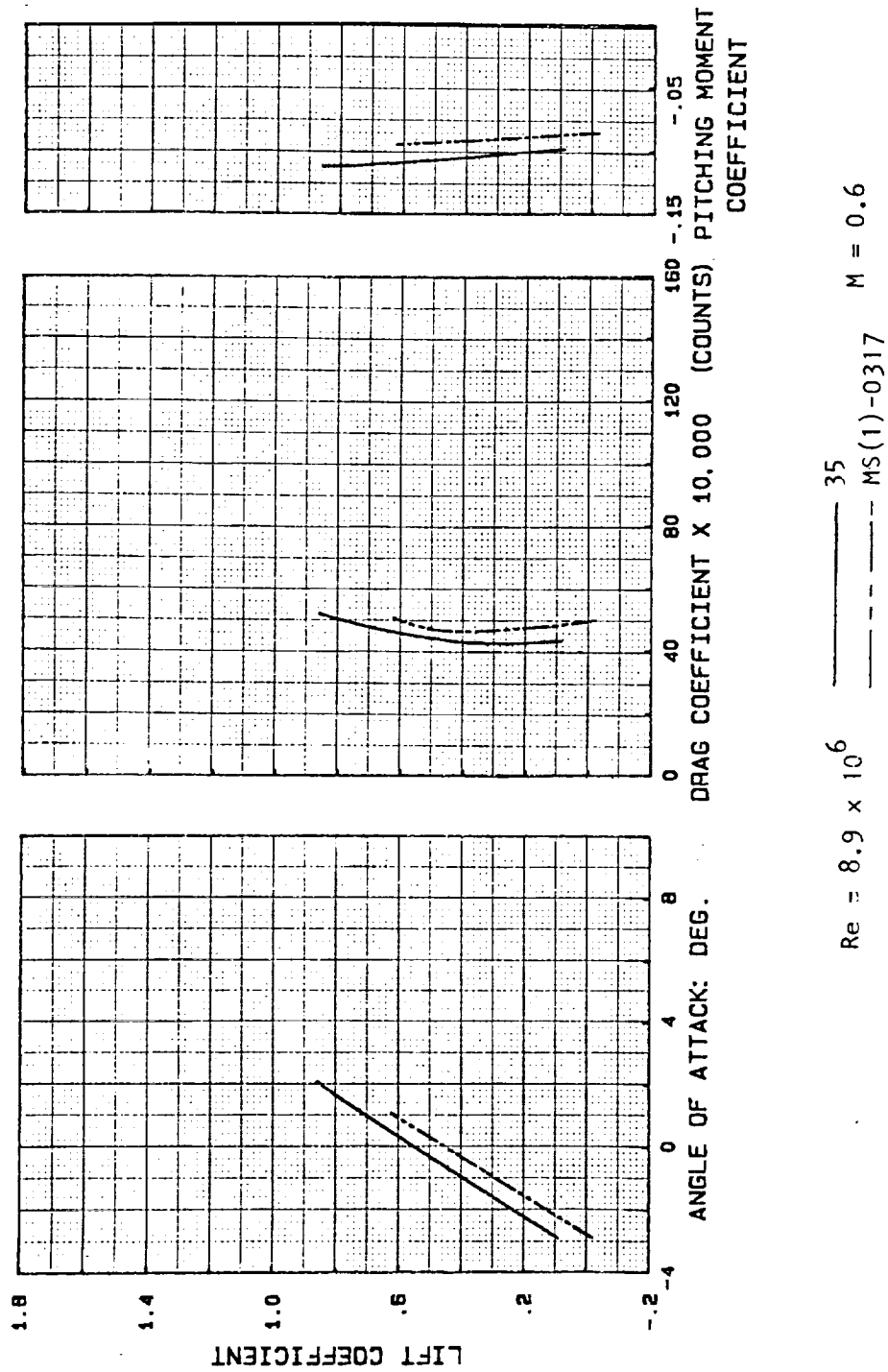


Figure 6.65 Aerodynamic characteristics of 35 and MS(1)-0317 as calculated by NCS code using laminar separation

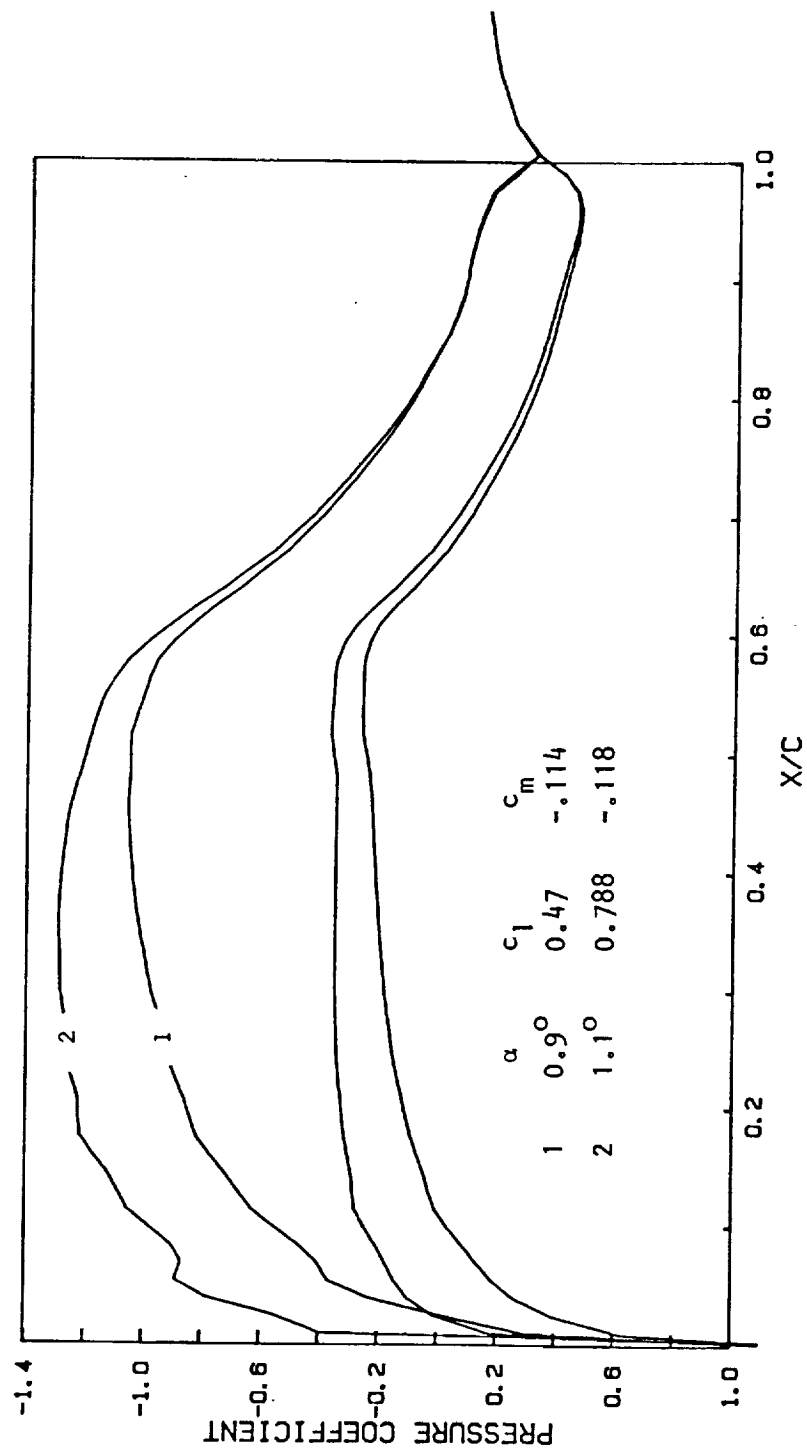


Figure 6.66 Pressure distributions airfoil 35 for different α .
 $M = 0.60$; $Re = 8.9 \times 10^6$.
 TRANSEP (fine grid)

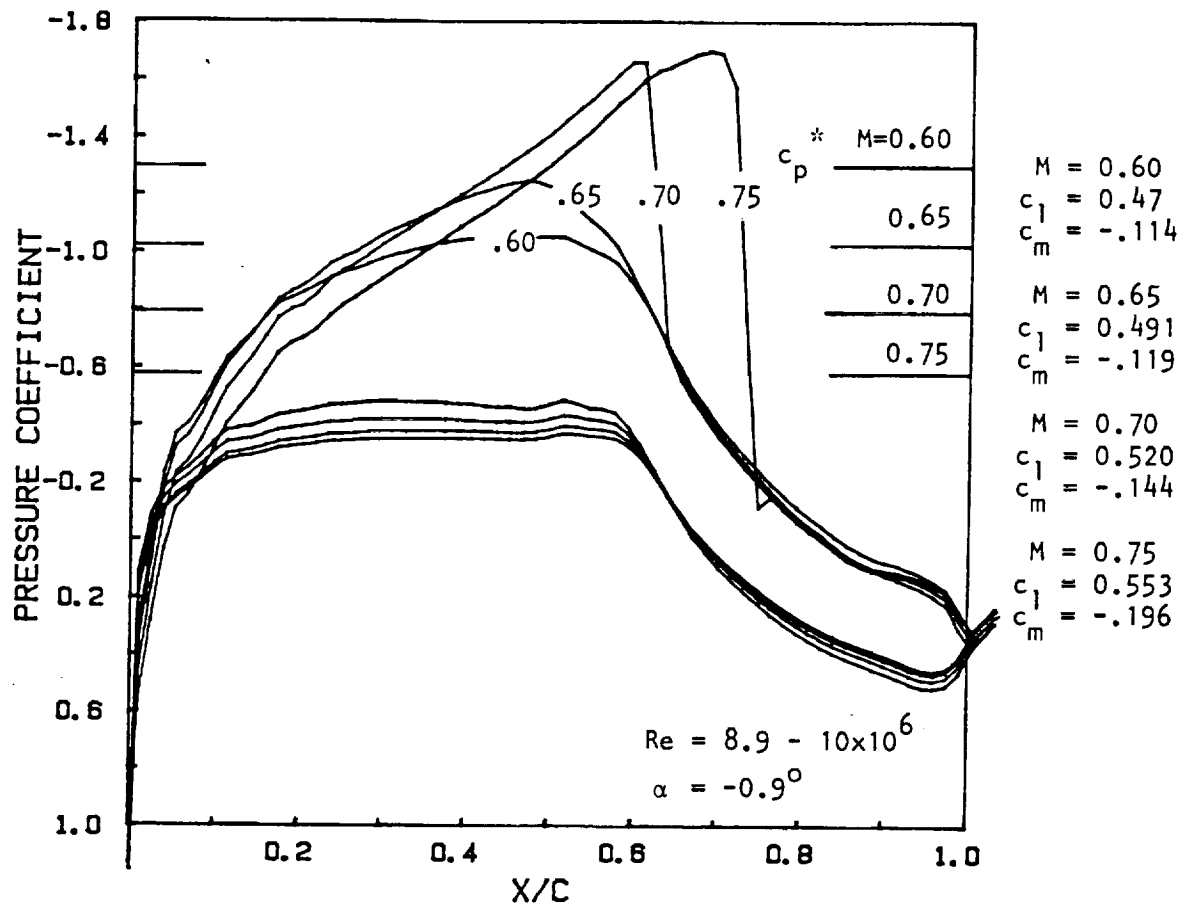


Figure 6.67 Pressure distributions airfoil 35 for increasing Mach number
TRANSEP code (fine grid)

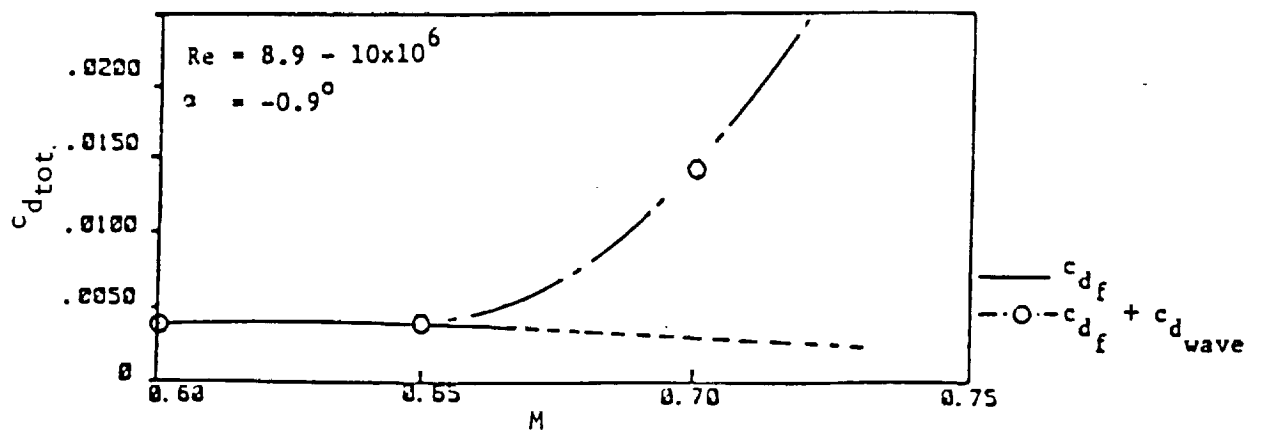


Figure 6.68 Drag rise estimate airfoil 35
TRANSEP (fine grid)

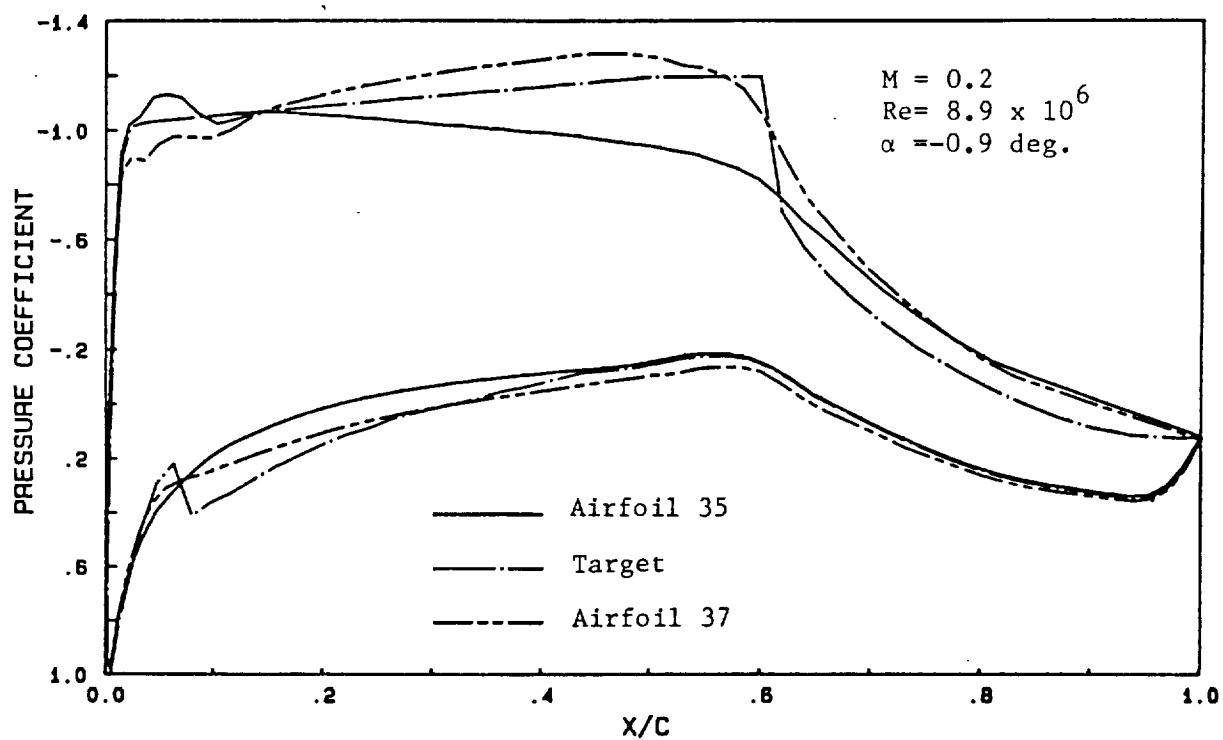


Figure 6.69 Airfoil 35 pressure distribution, target pressure distribution, and resulting pressure distribution for airfoil 37.

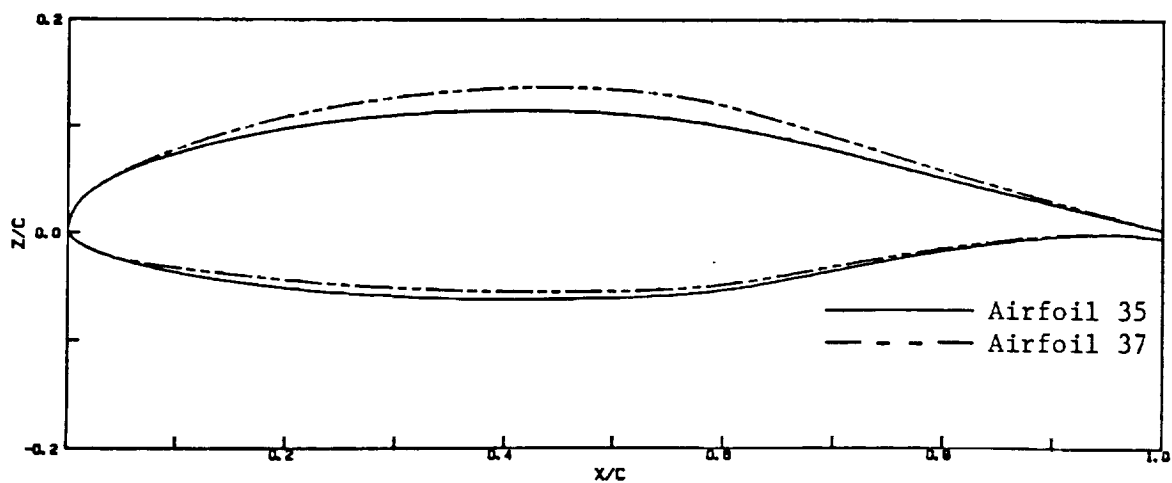


Figure 6.70 Airfoils 35 and 37

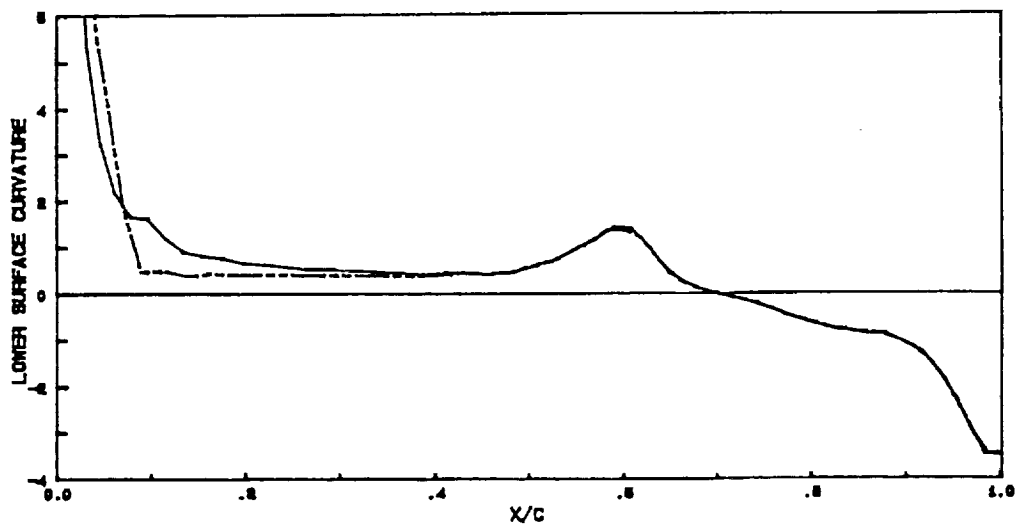
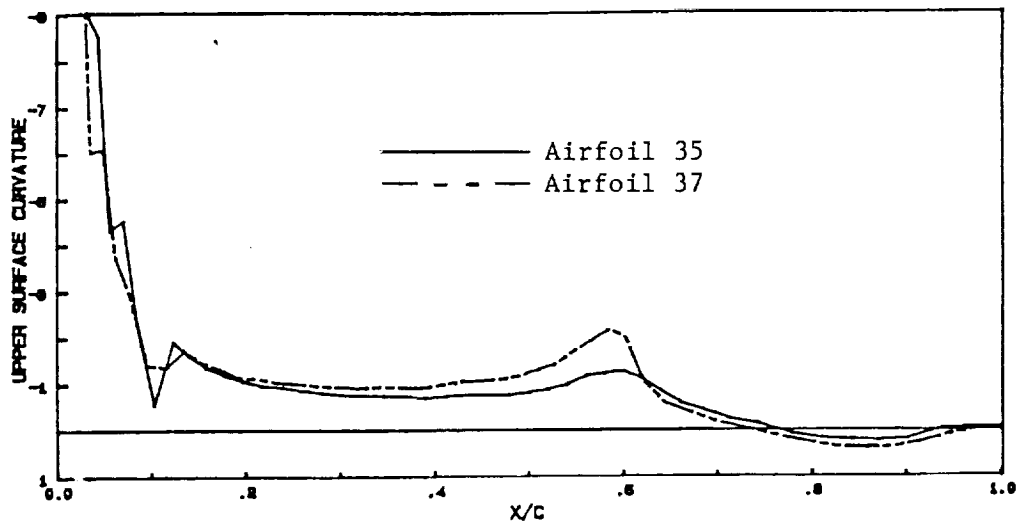


Figure 6.71 Curvature distributions of airfoils 35 and 37.

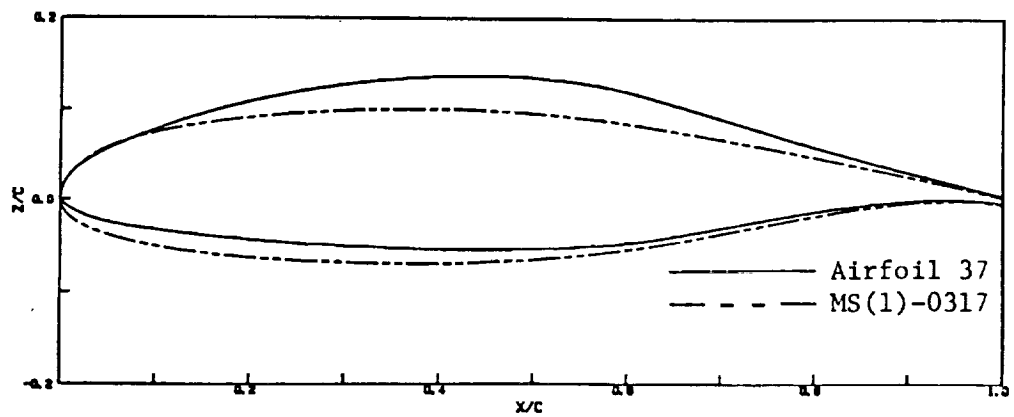


Figure 6.72 Airfoils 37 and MS(1)-0317.

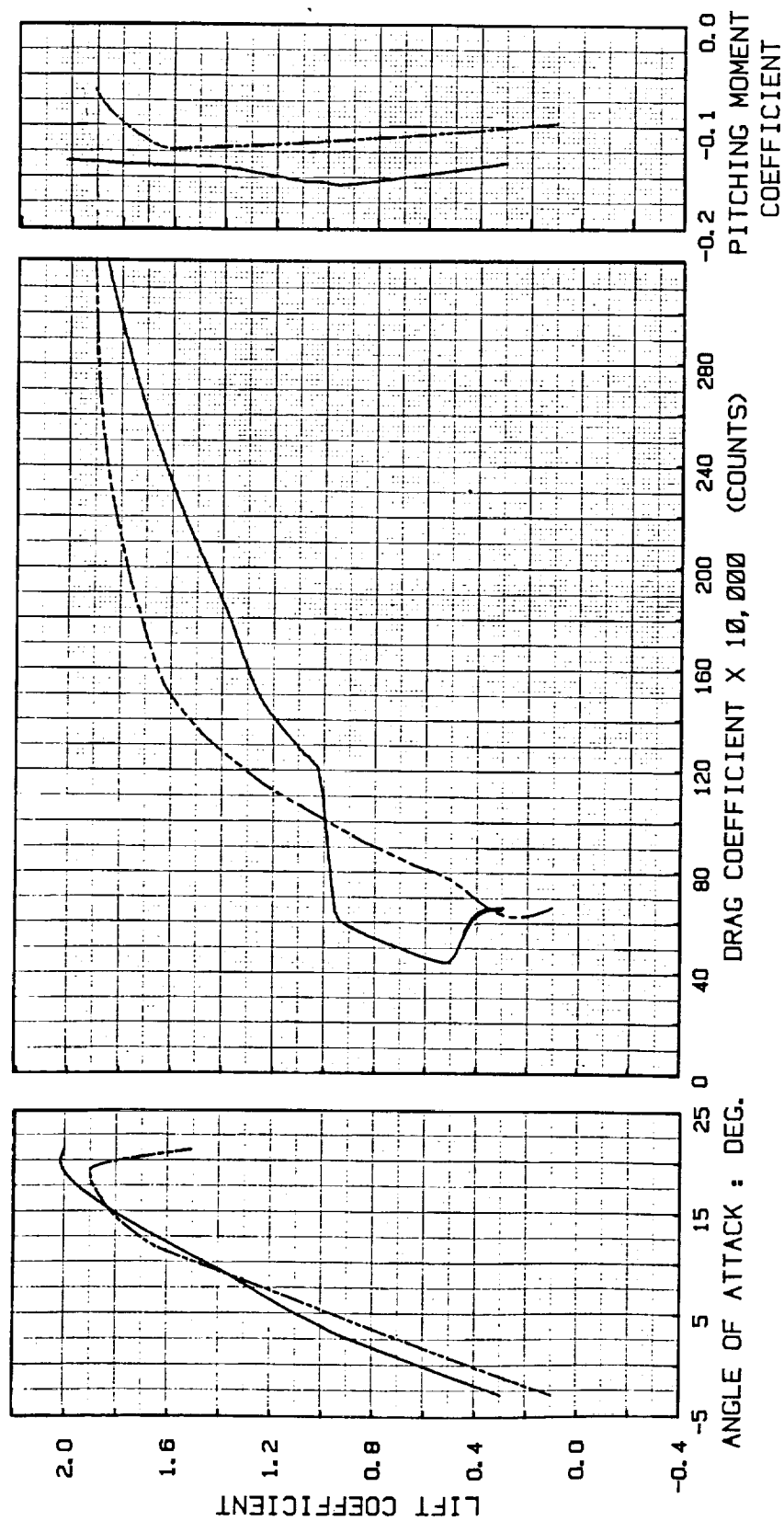
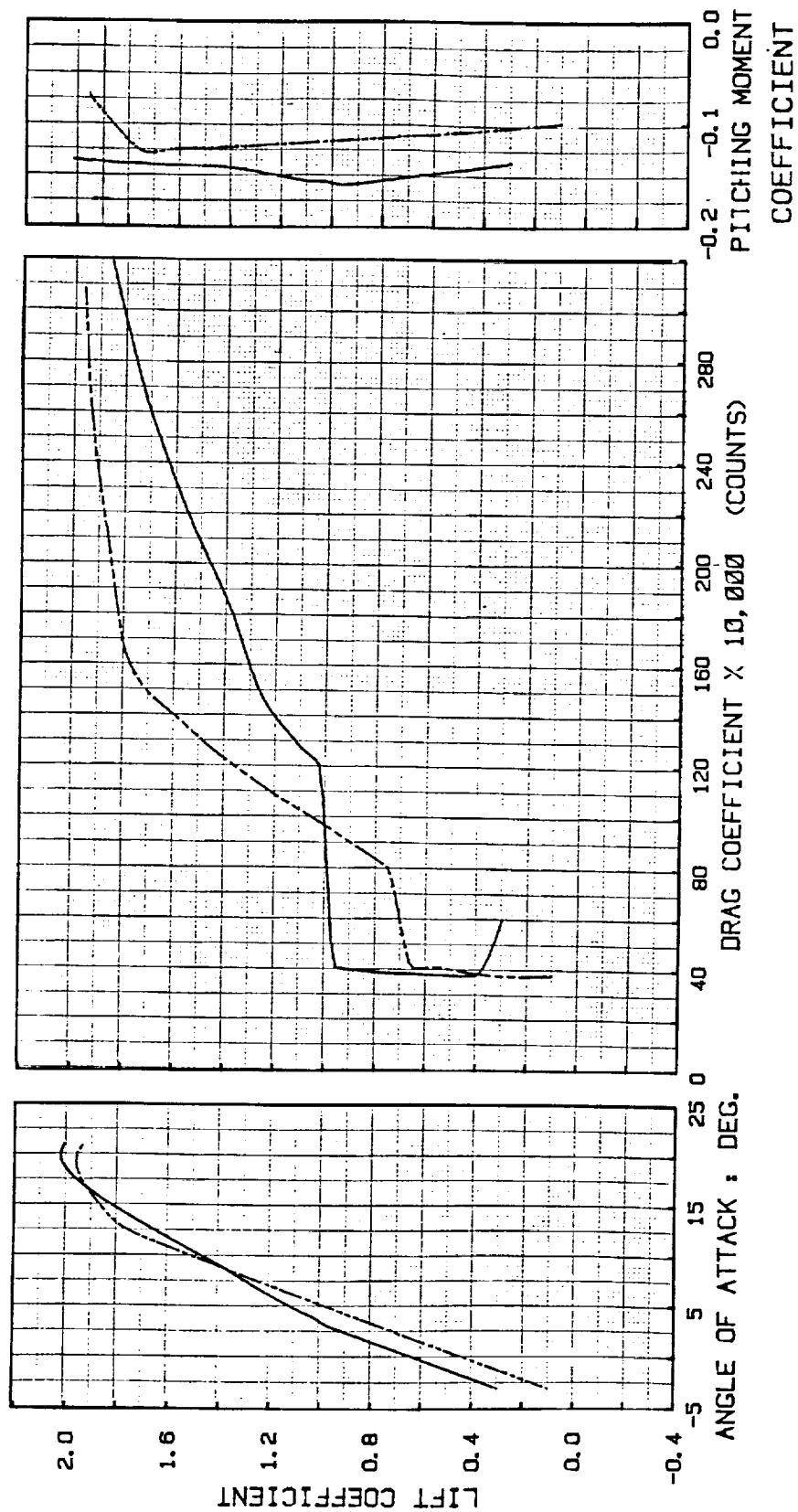


Figure 6.73 Aerodynamic characteristics of 37 and MS(1)-0317 as calculated by the Eppler code using natural transition.

$Re = 8.9 \times 10^6$

— Airfoil 37

- - - MS(1)-0317



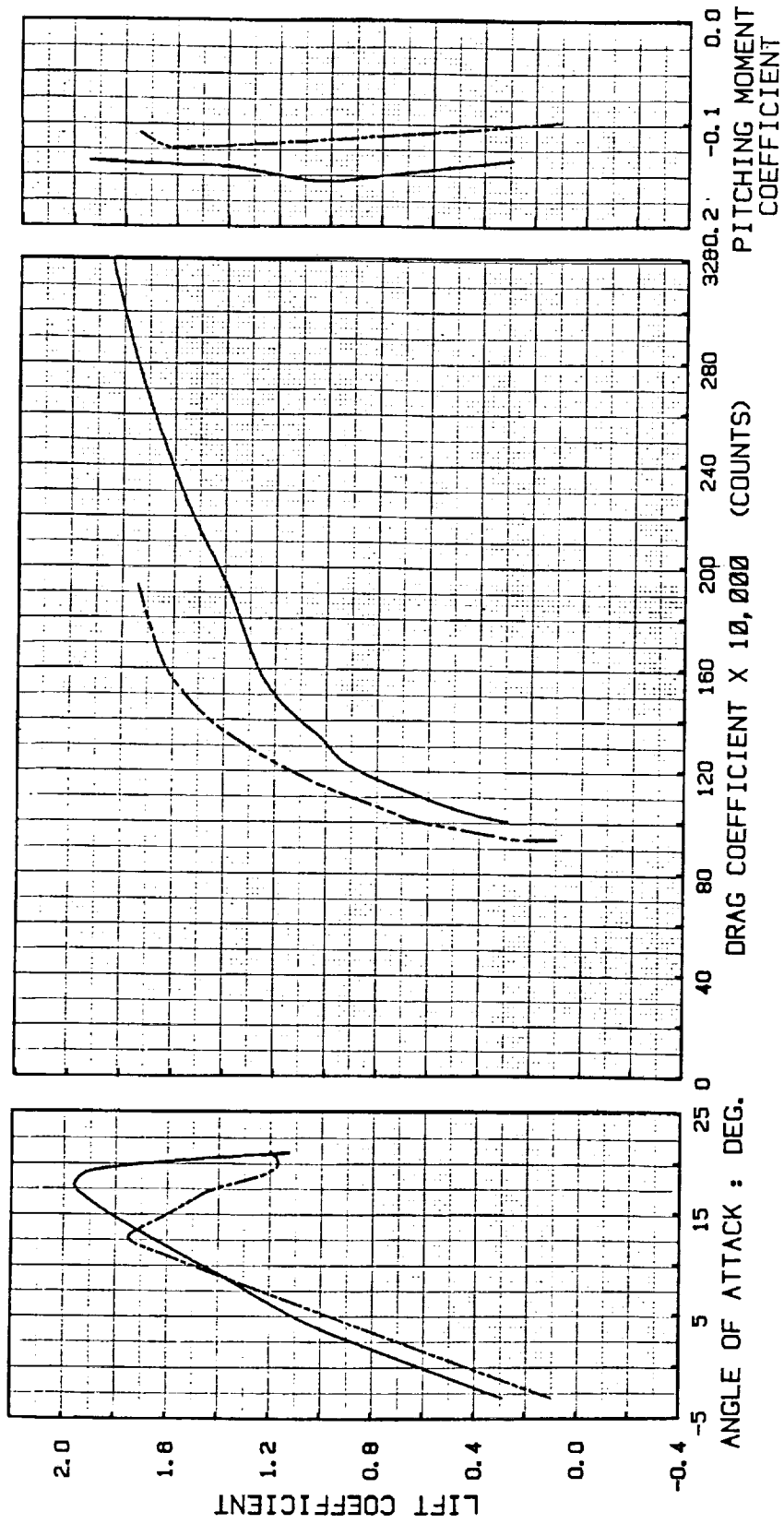


Figure 6.75 Aerodynamic characteristics of 37 and MS(1)-0317 as calculated by the Eppler code using fixed transition at 5-percent chord on both surfaces.

$$Re = 8.9 \times 10^6$$

— Airfoil 37
 - - - MS(1)-0317

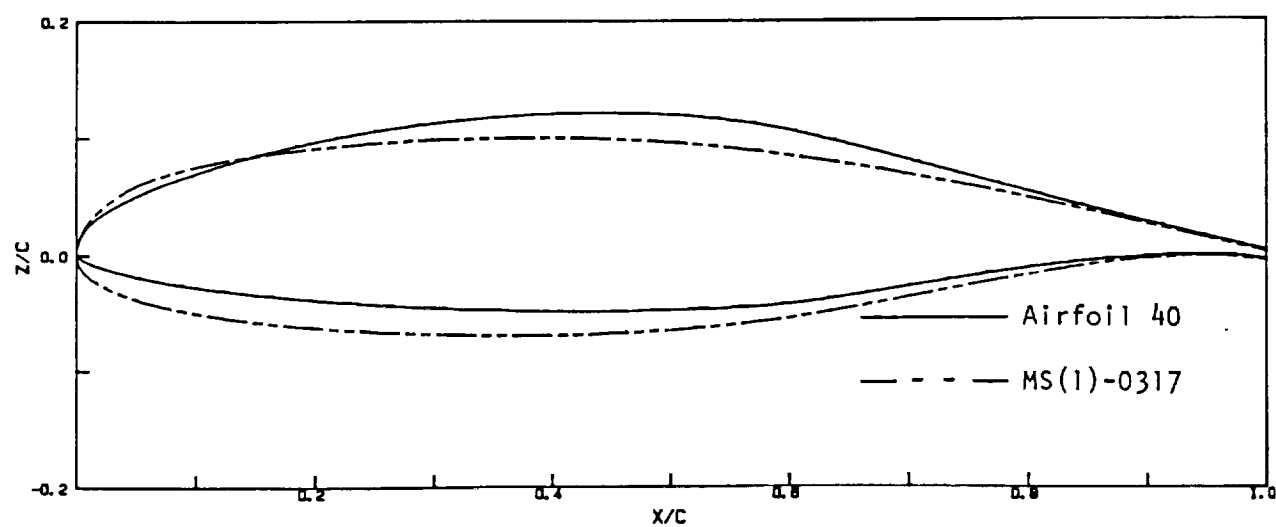
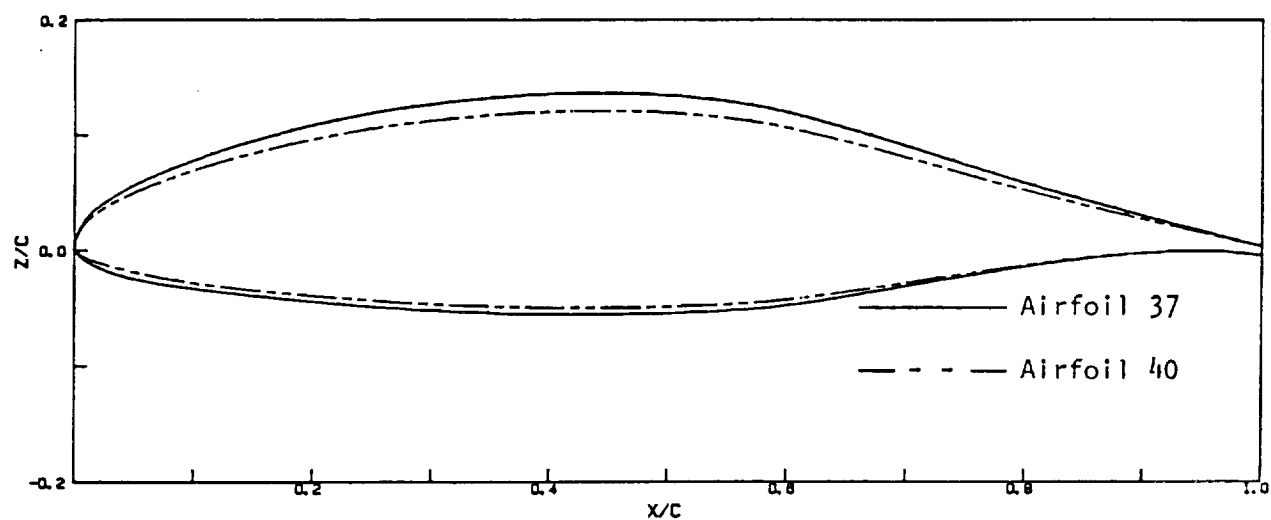


Figure 6.76 Airfoils 37, 40, and MS(1)-0317.

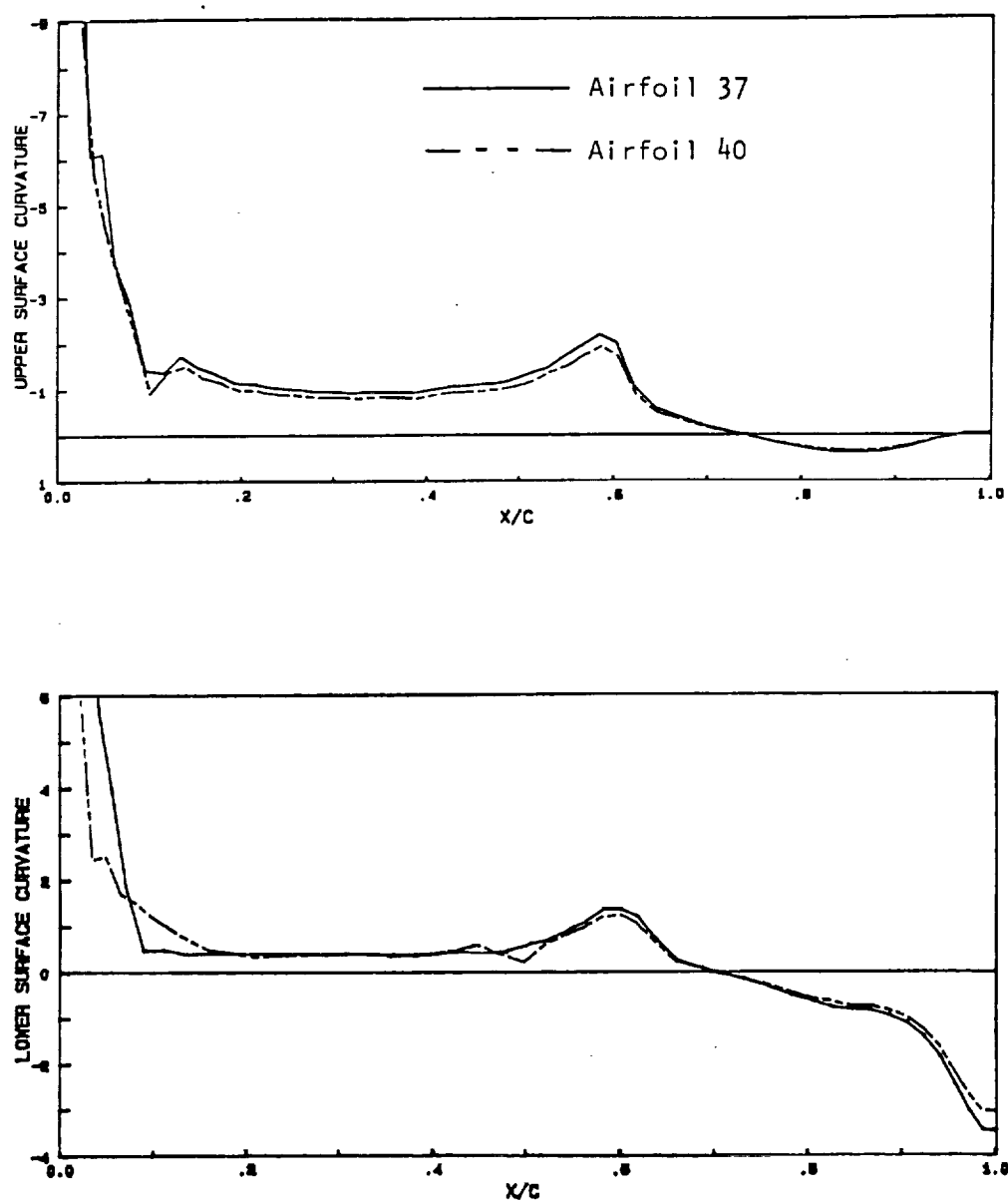


Figure 6.77 Curvature distributions of 37 and 40.

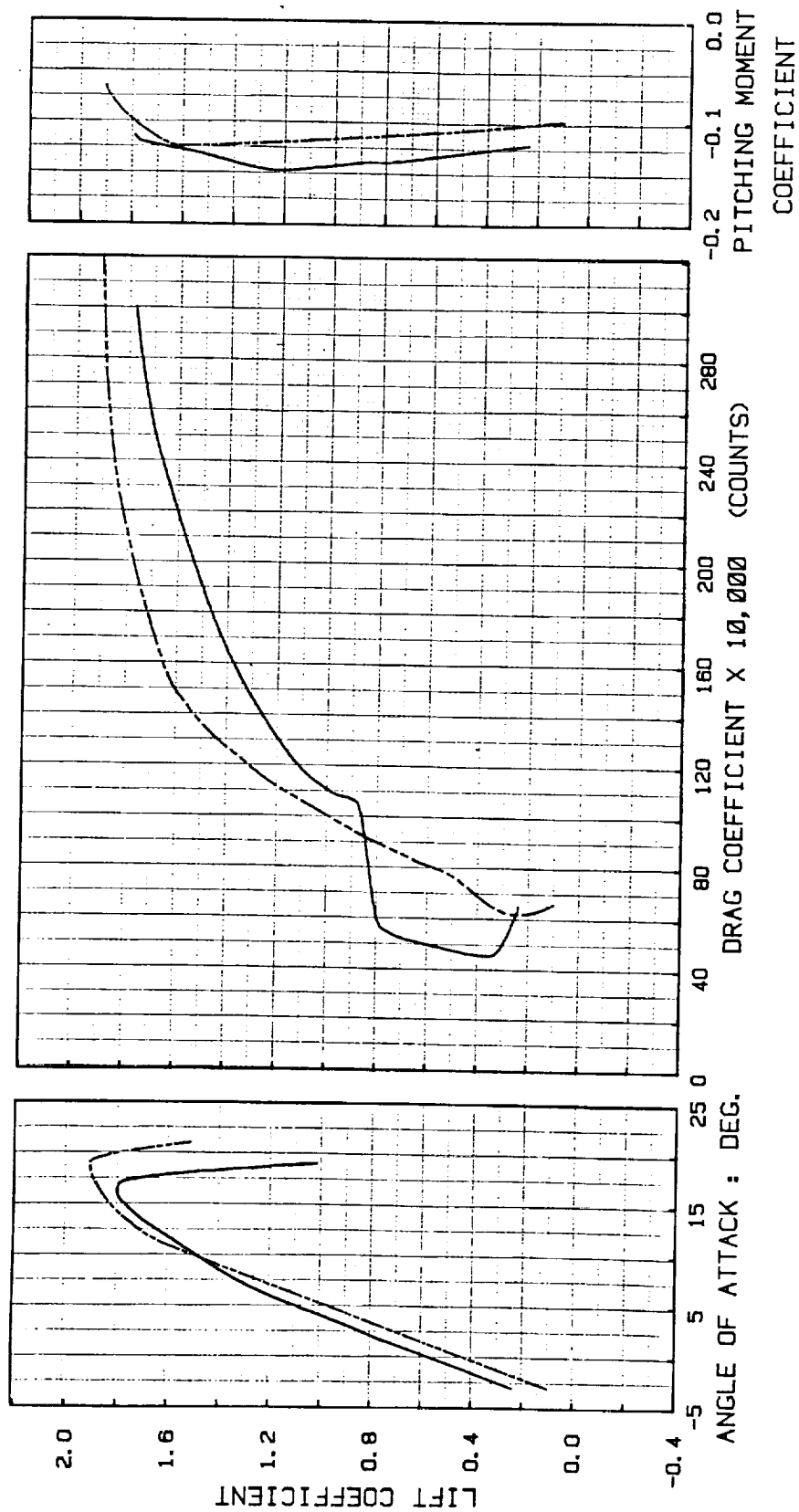


Figure 6.78 Aerodynamic characteristics of 40 and MS(1)-0317 as calculated by the Eppler code using natural transition.

$Re = 8.9 \times 10^6$

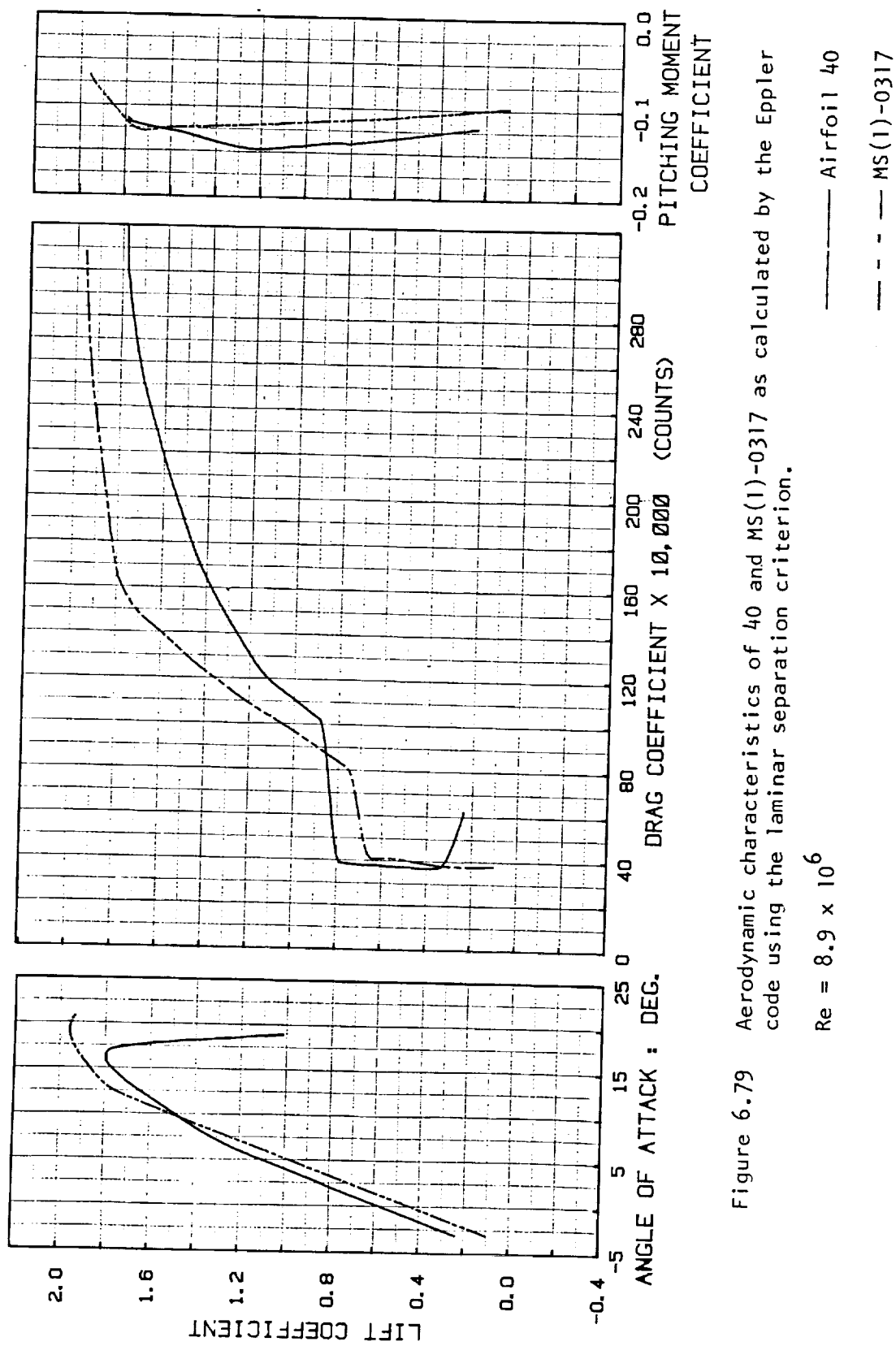


Figure 6.79 Aerodynamic characteristics of 40 and MS(1)-0317 as calculated by the Eppler code using the laminar separation criterion.

$Re = 8.9 \times 10^6$

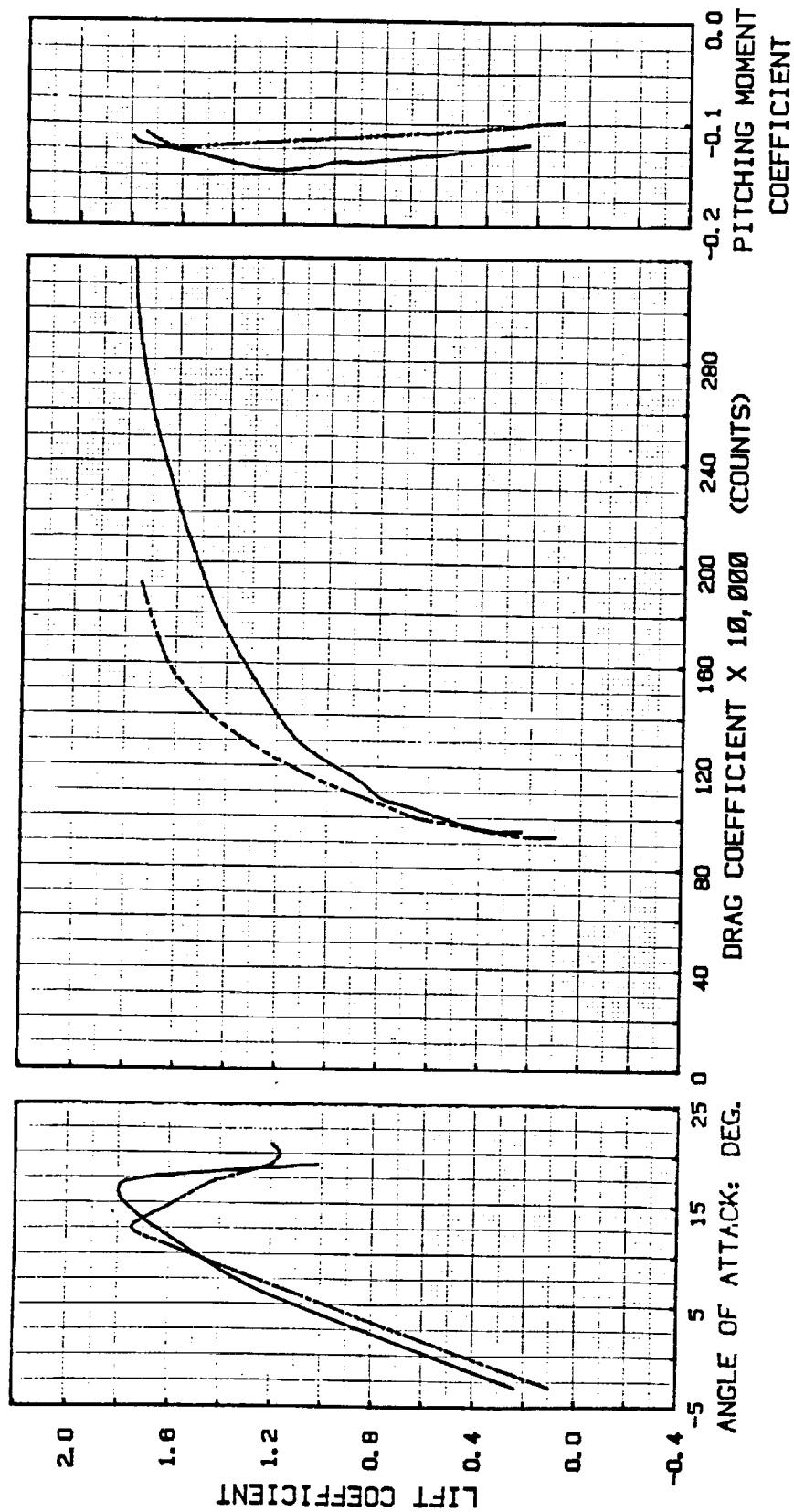


Figure 6.80 Aerodynamic characteristics of 40 and MS(1)-0317 as calculated by the Eppler code with transition fixed at 5-percent chord.

$Re = 8.9 \times 10^6$

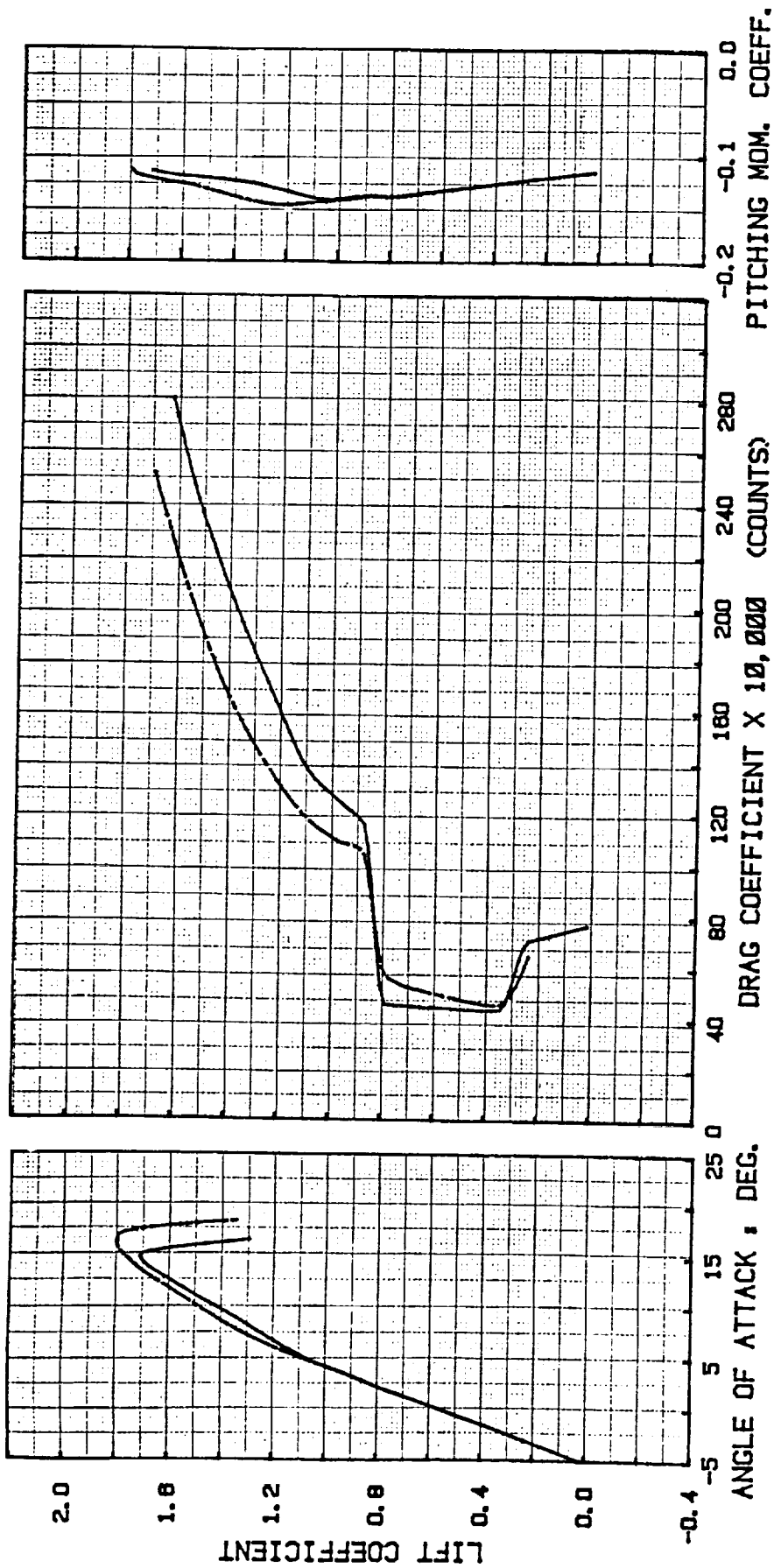


Figure 6.81 Effect of Reynolds number on the aerodynamic characteristics of 40 as predicted by the Eppler code using natural transition.

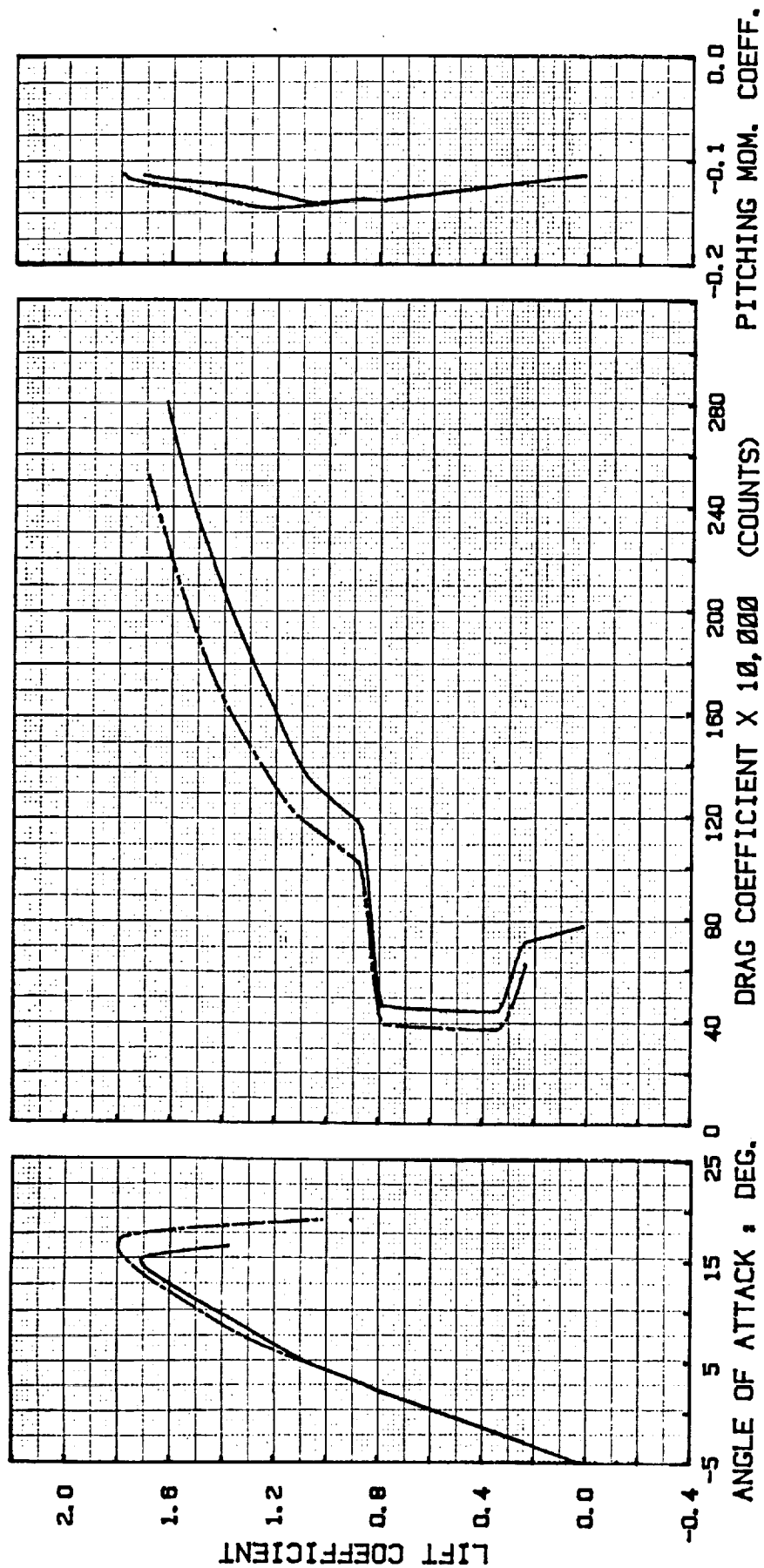


Figure 6.82 Effect of Reynolds number on the aerodynamic characteristics of 40 as calculated by the Eppler code using the laminar separation criterion.

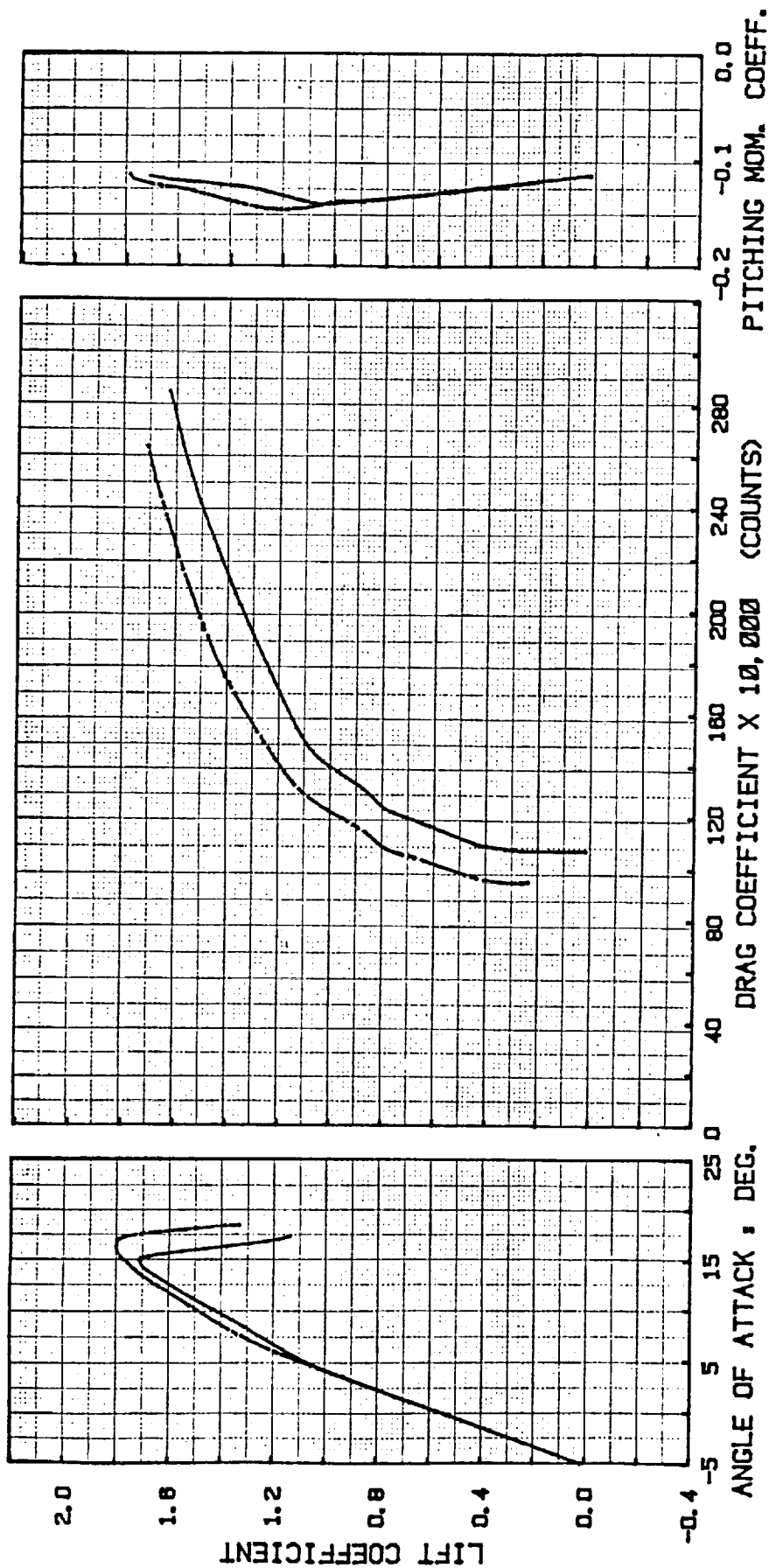


Figure 6.83 Effect of Reynolds number on the aerodynamic characteristics of 40 as calculated by the Eppler code with transition fixed at 5-percent chord.

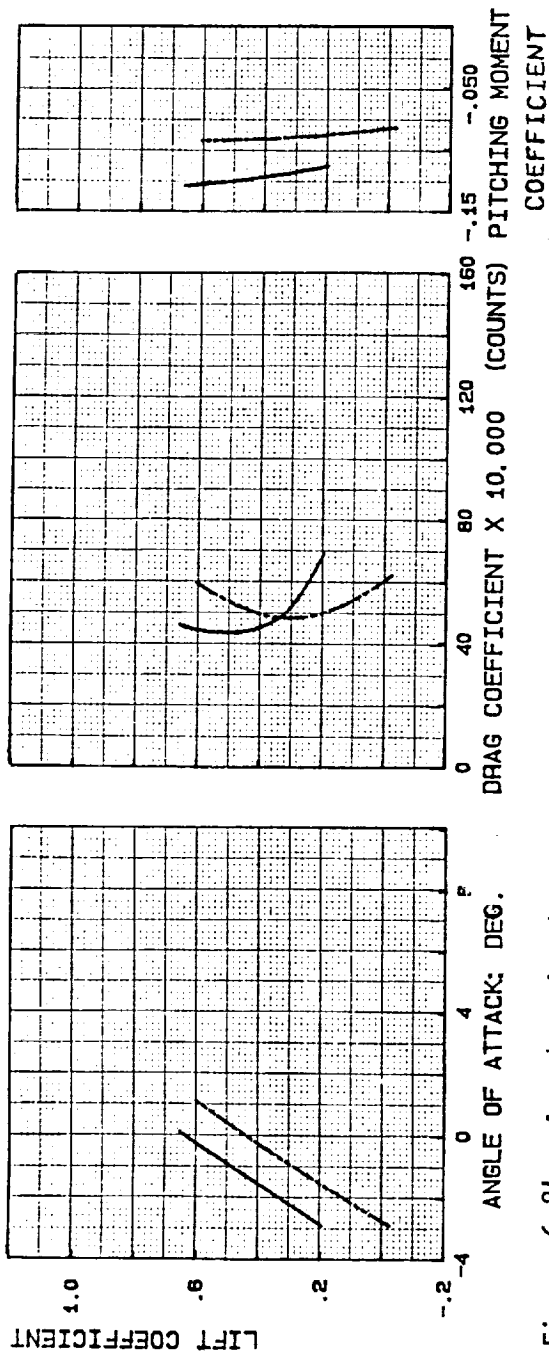


Figure 6.84 Aerodynamic characteristics of airfoil 40 as predicted by the NCS code.
 $M = 0.6$
 $Re = 8.9 \times 10^6$

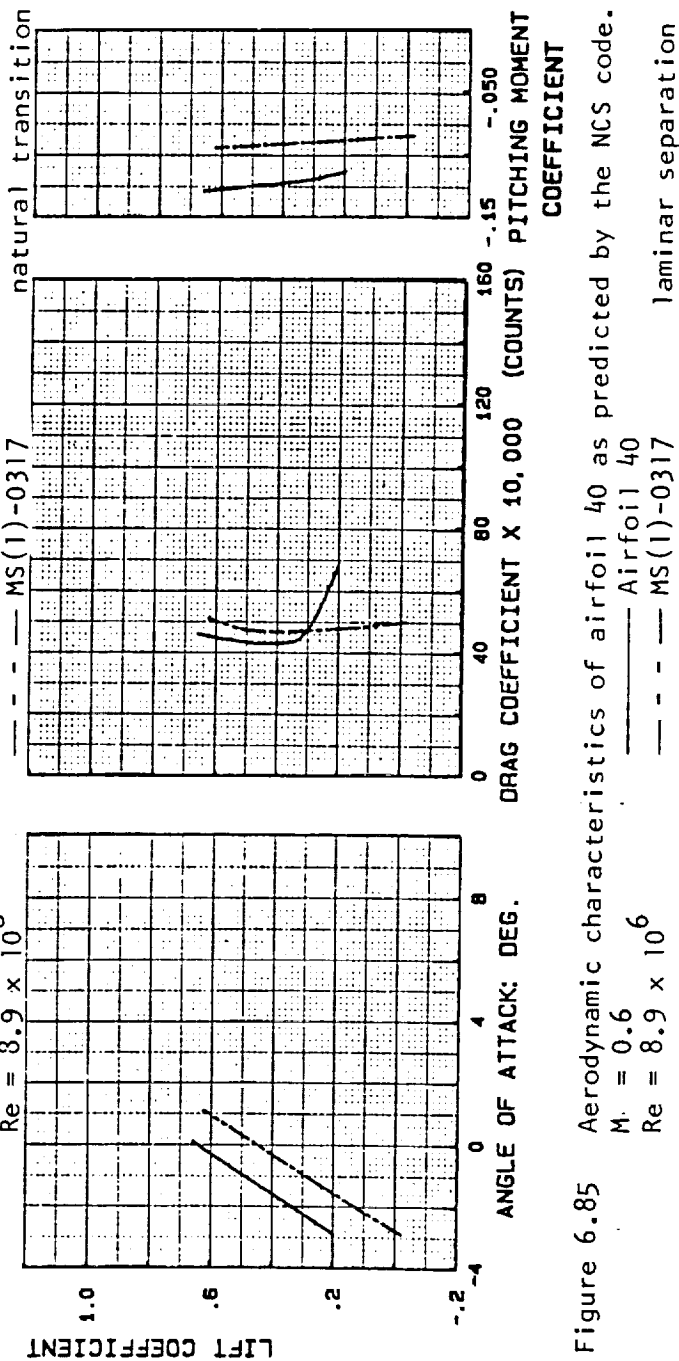


Figure 6.85 Aerodynamic characteristics of airfoil 40 as predicted by the NCS code.
 $M = 0.6$
 $Re = 8.9 \times 10^6$

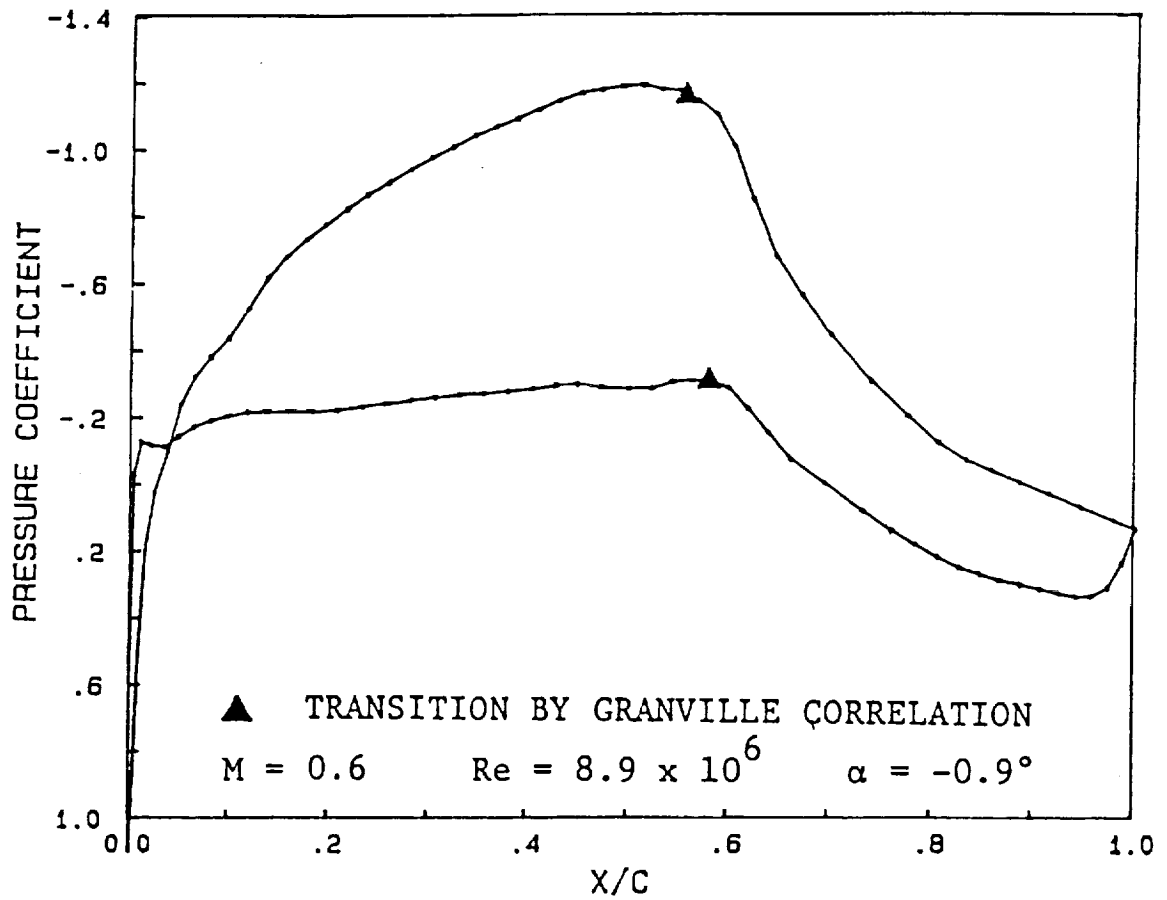


Figure 6.86 Design pressure distribution airfoil 40.
NCS predicted transition at begin pressure recovery.

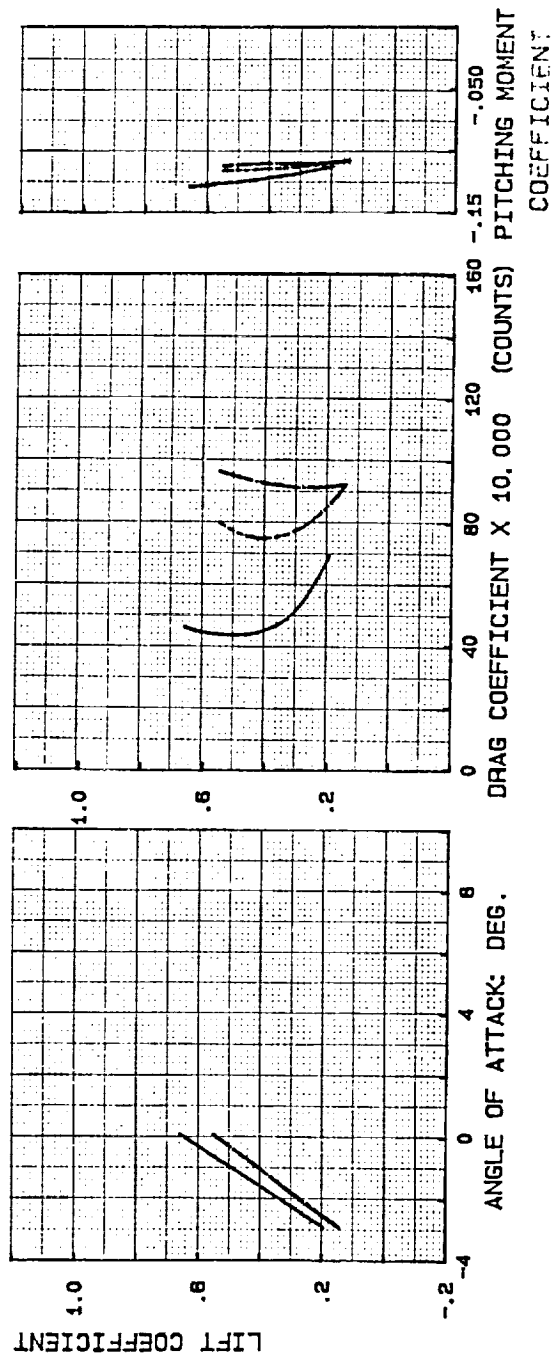


Figure 6.87

Aerodynamic characteristics of airfoil $14\%as$ predicted by the NCS code

$M = 0.6$

$Re = 8.9 \times 10^6$

Effect of fixing transition to $5\%c$:

- transition upper surface only
- - - transition both surfaces
- no transition

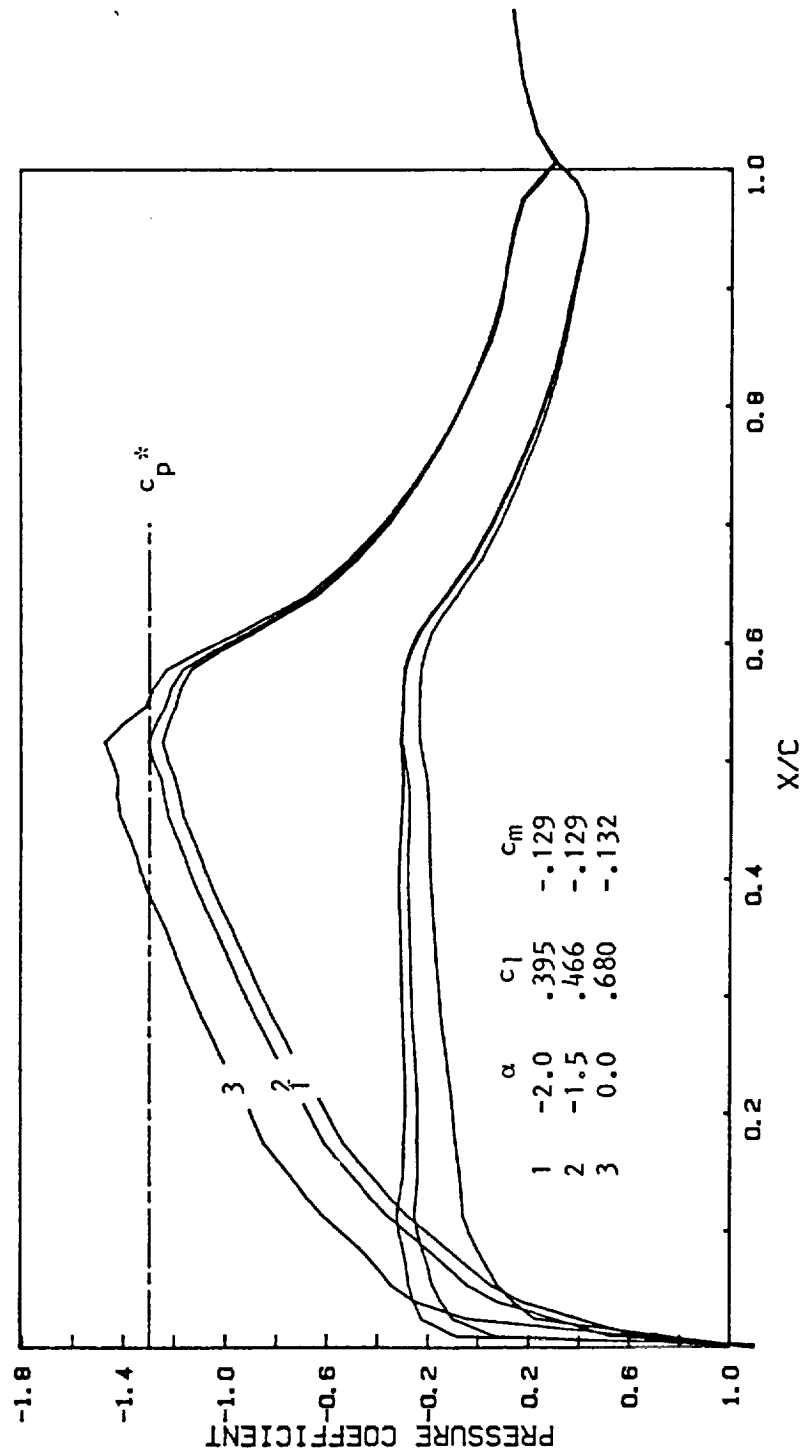


Figure 6.88 Pressure distributions of airfoil 40 for different α .
 $M = 0.60$; $Re = 8.9 \times 10^6$
 TRANSEP (fine grid)

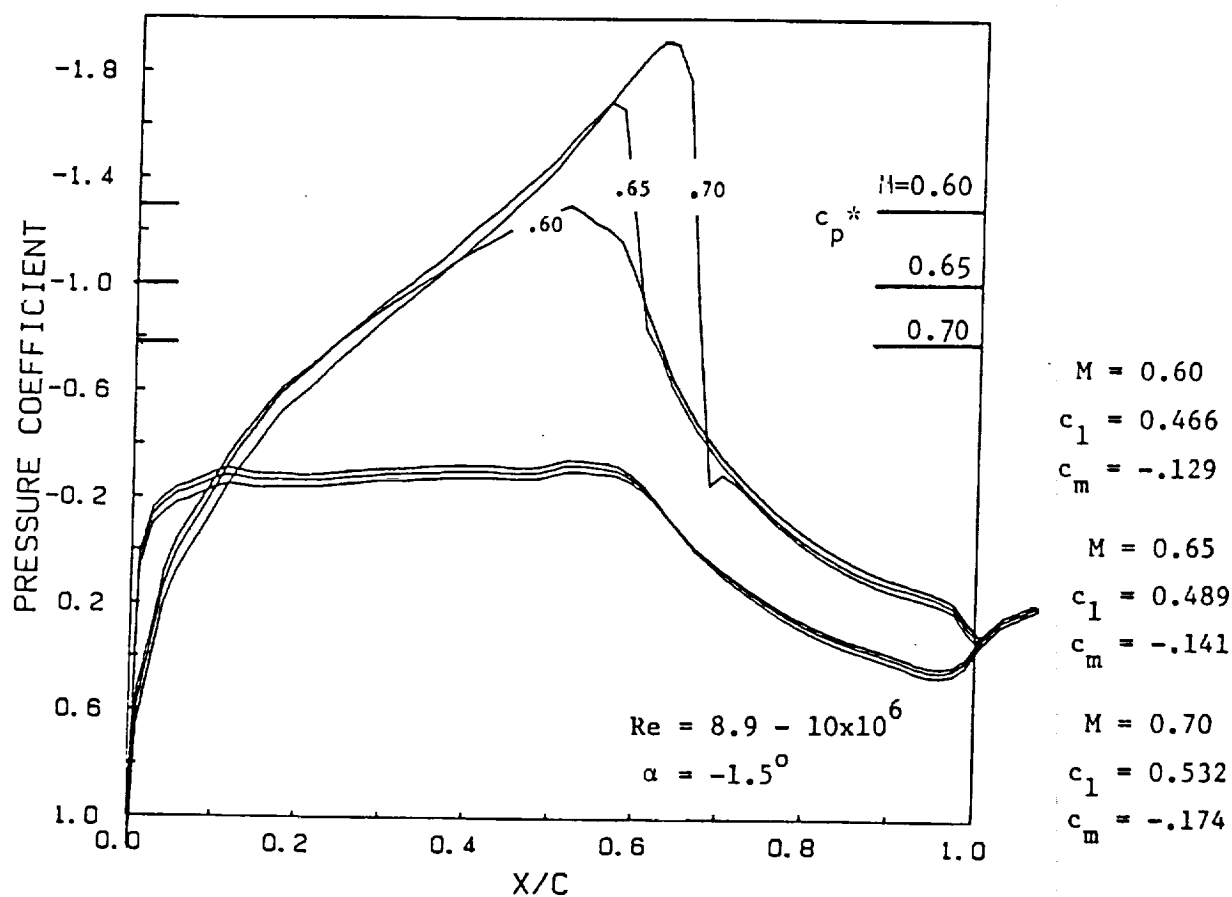


Figure 6.89 Pressure distributions of airfoil 40 for increasing Mach number
TRANSEP code (fine grid)

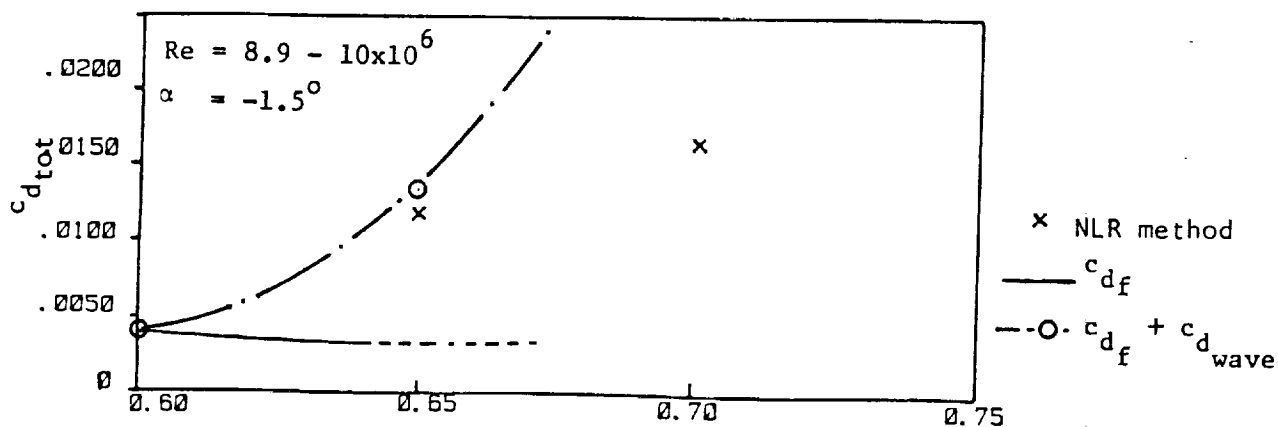


Figure 6.90 Drag rise estimate airfoil 40
TRANSEP (fine grid) and NLR method

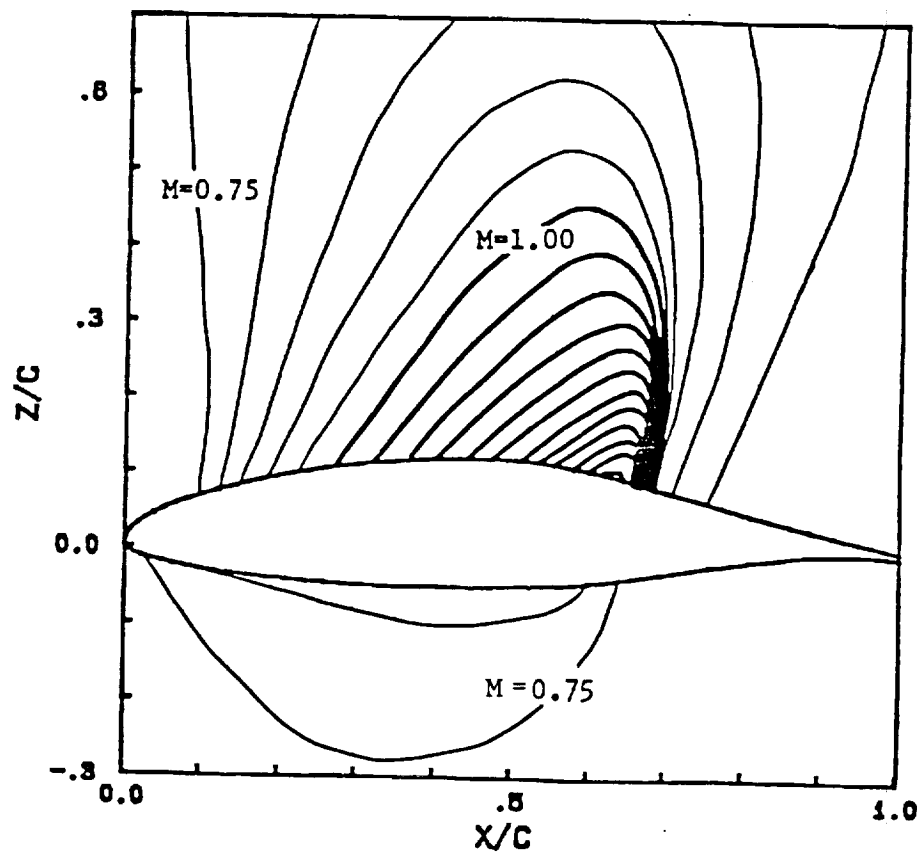


Figure 6.91

Supersonic pocket and strong shock wave
over airfoil 40 at $M = 0.70$

Iso-Mach lines calculated by TRANSEP
(increments of .05)

$\alpha = -1.5^\circ$

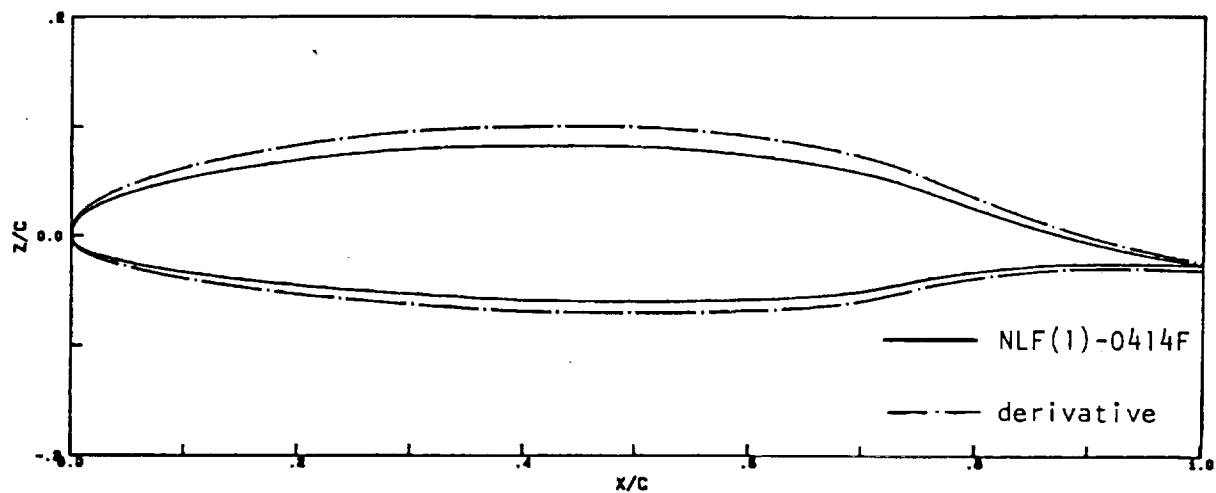


Figure 6.92 Airfoils NLF(1)-0414F and derivative.

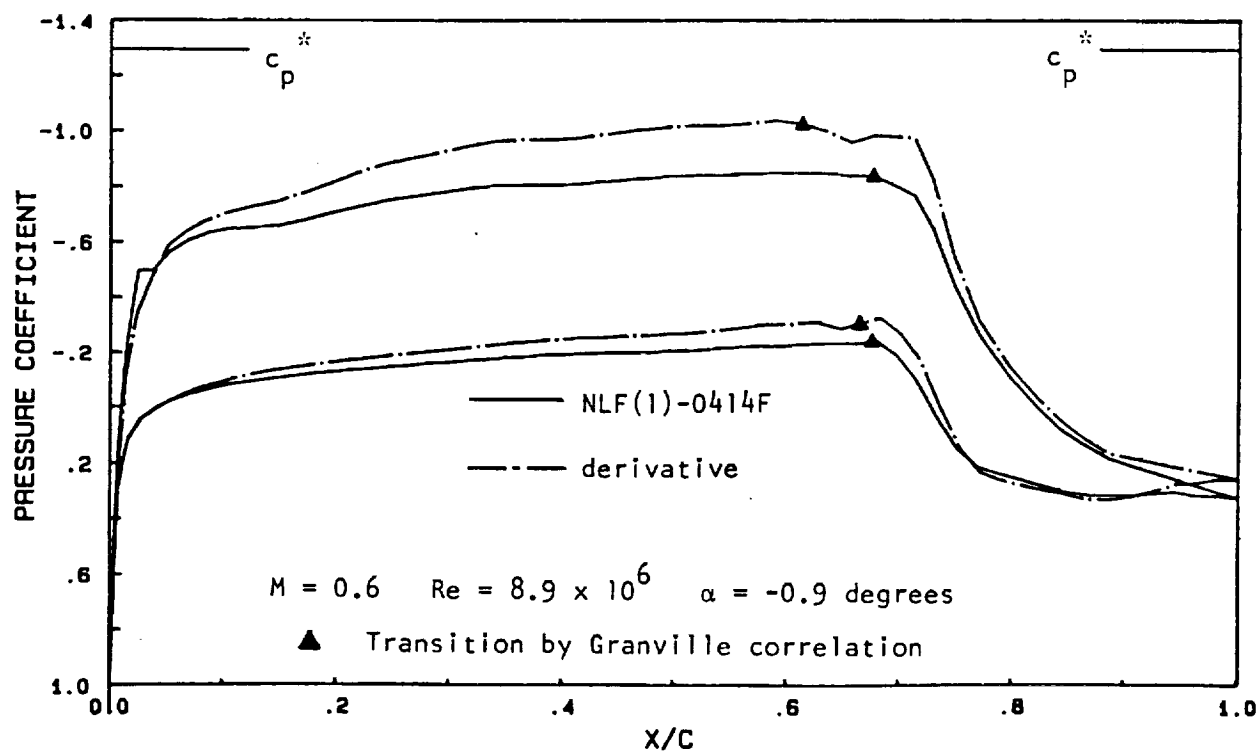


Figure 6.93 Aerodynamic characteristics of NLF(1)-0414F and derivative as calculated by the NCS code using natural transition.

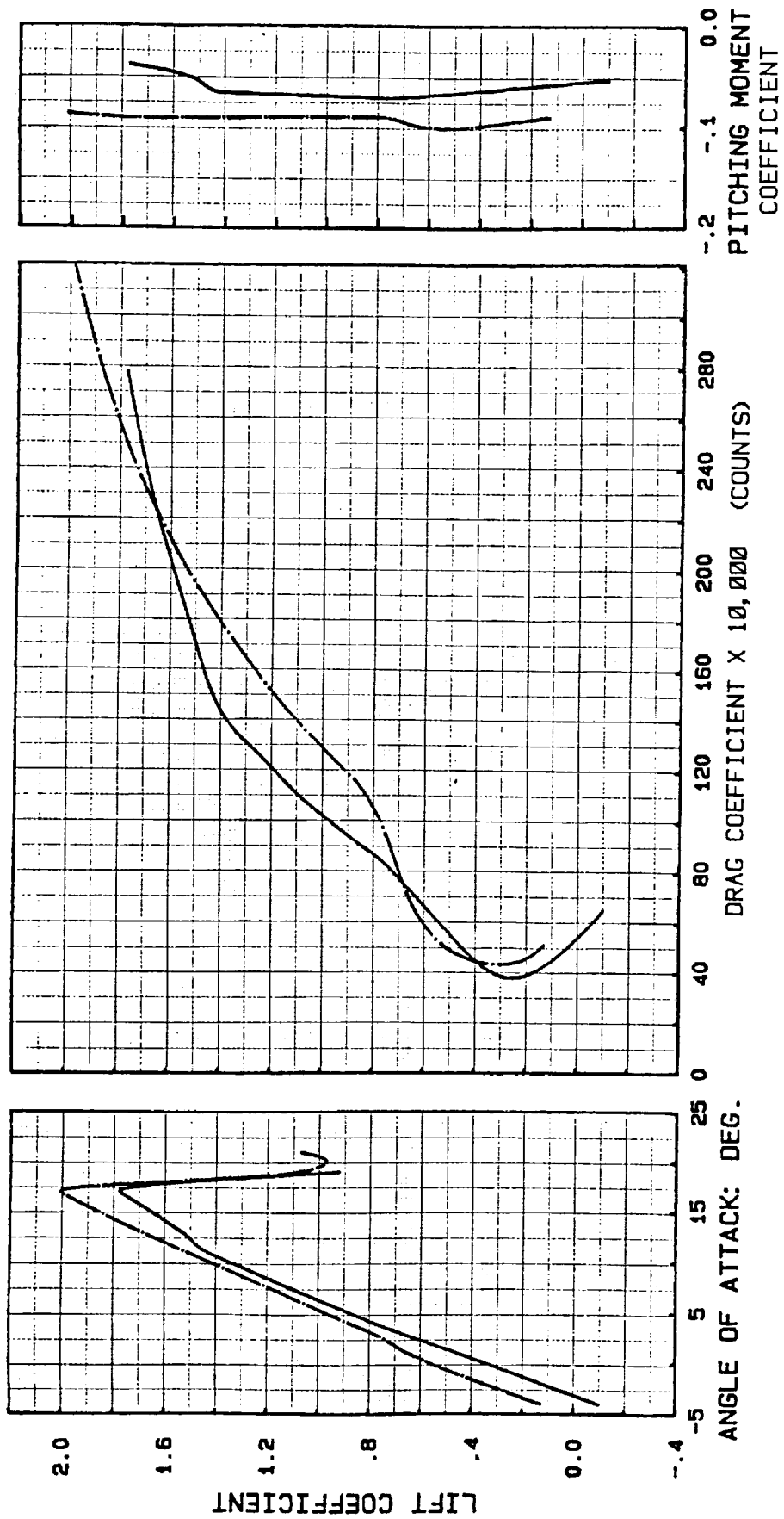


Figure 6.94 Aerodynamic characteristics of NLF(1)-0414F and derivative as calculated by the Eppler code using natural transition.

Re = 8.9×10^6

— NLF(1)-0414F
 - - - derivative

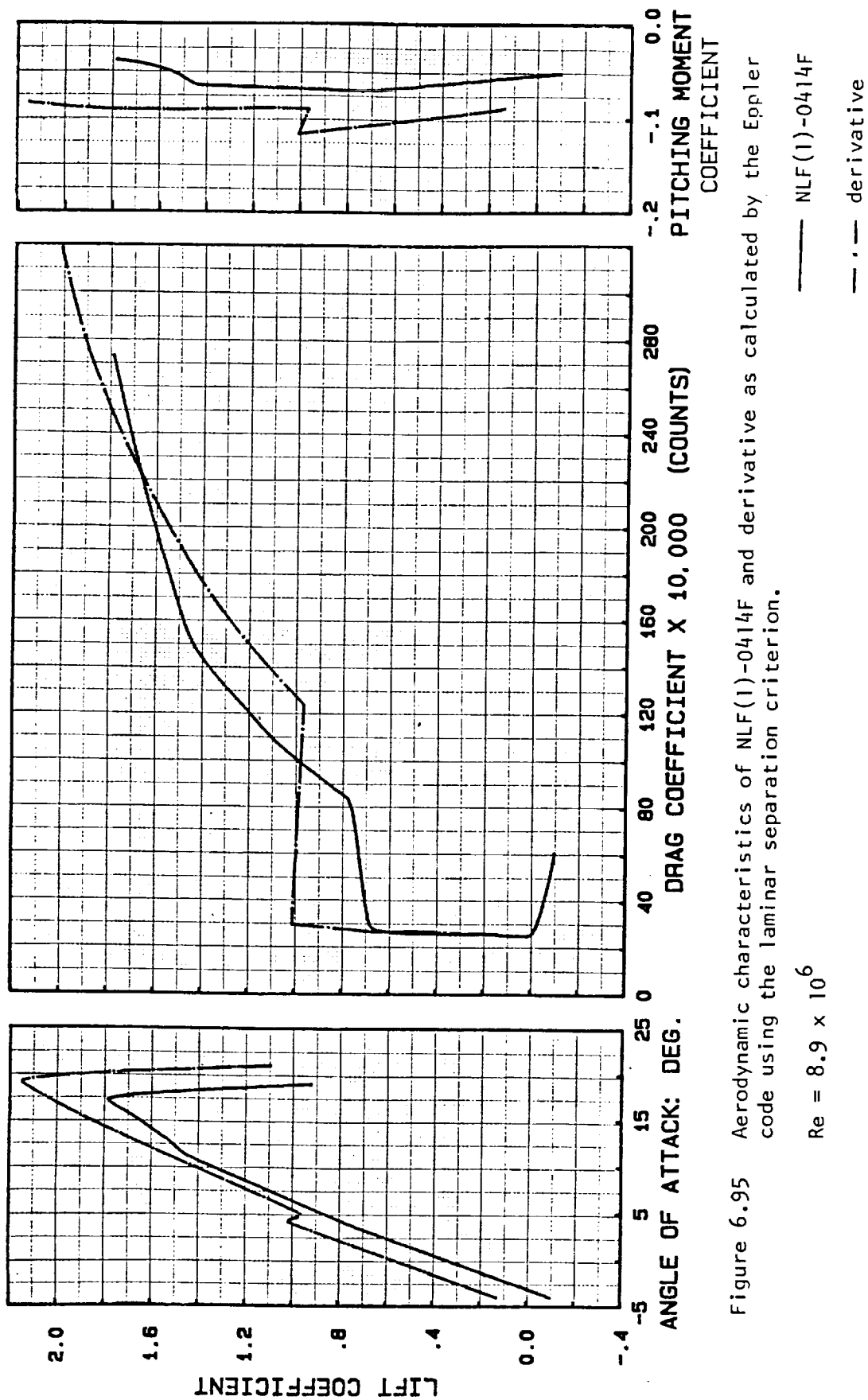


Figure 6.95 Aerodynamic characteristics of NLF(1)-0414F and derivative as calculated by the Eppler code using the laminar separation criterion.

$Re = 8.9 \times 10^6$

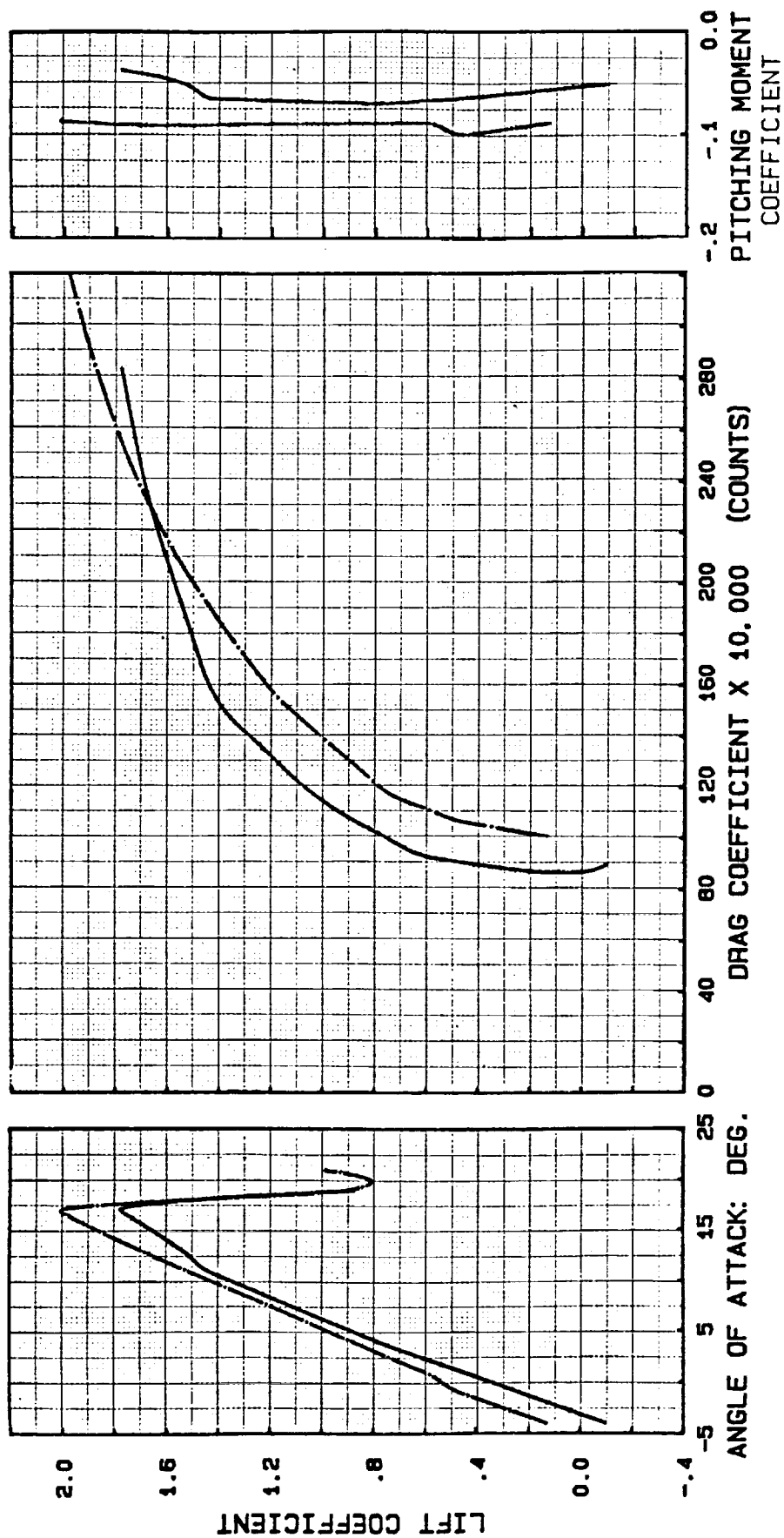


Figure 6.96 Aerodynamic characteristics of NLF(1)-0414F and derivative as calculated by the Eppler code with transition fixed at 5-percent chord.

$$Re = 8.9 \times 10^6$$

—— NLF(1)-0414F
 ---- derivative

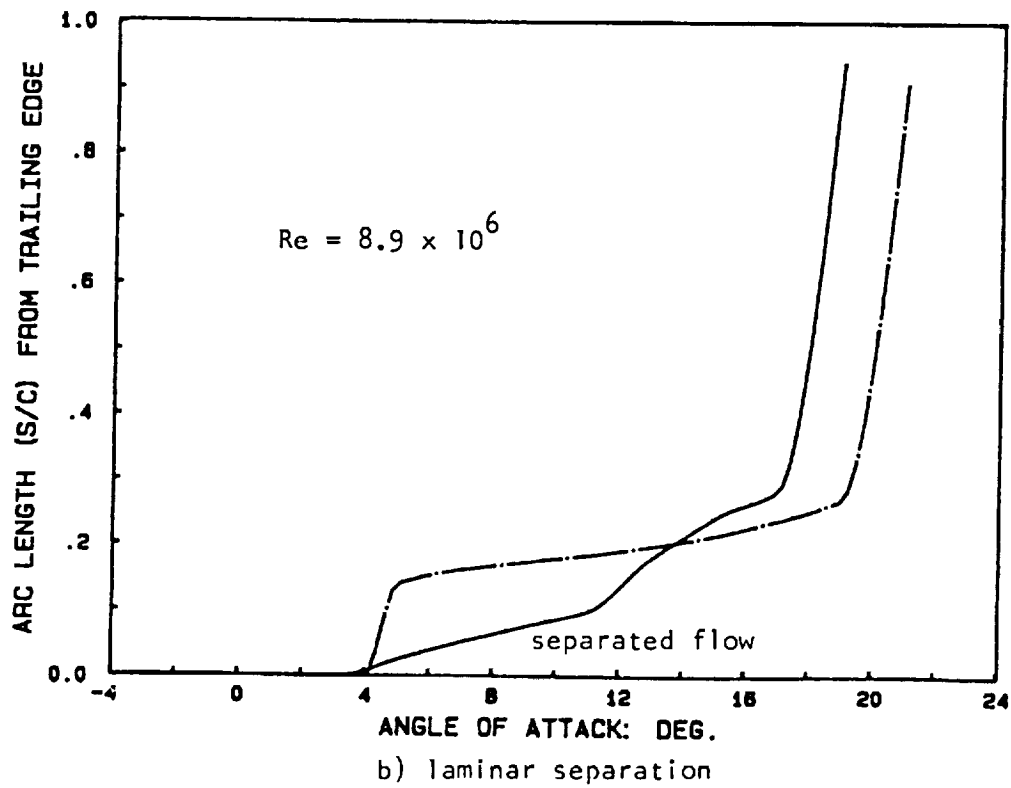
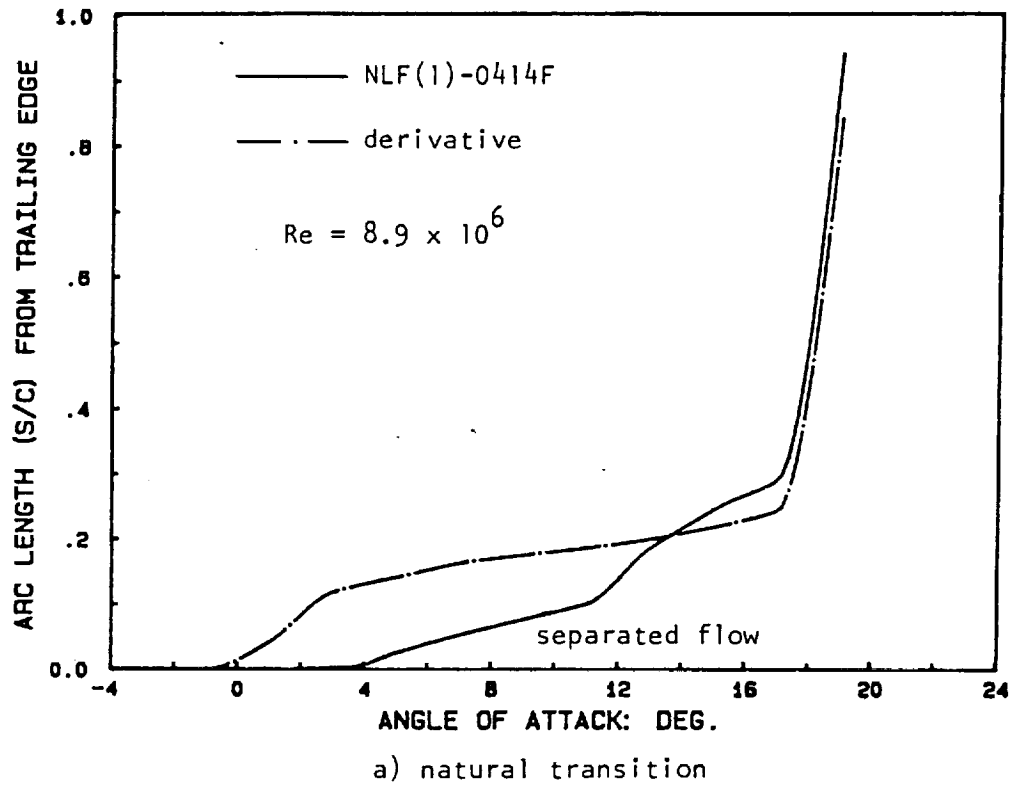
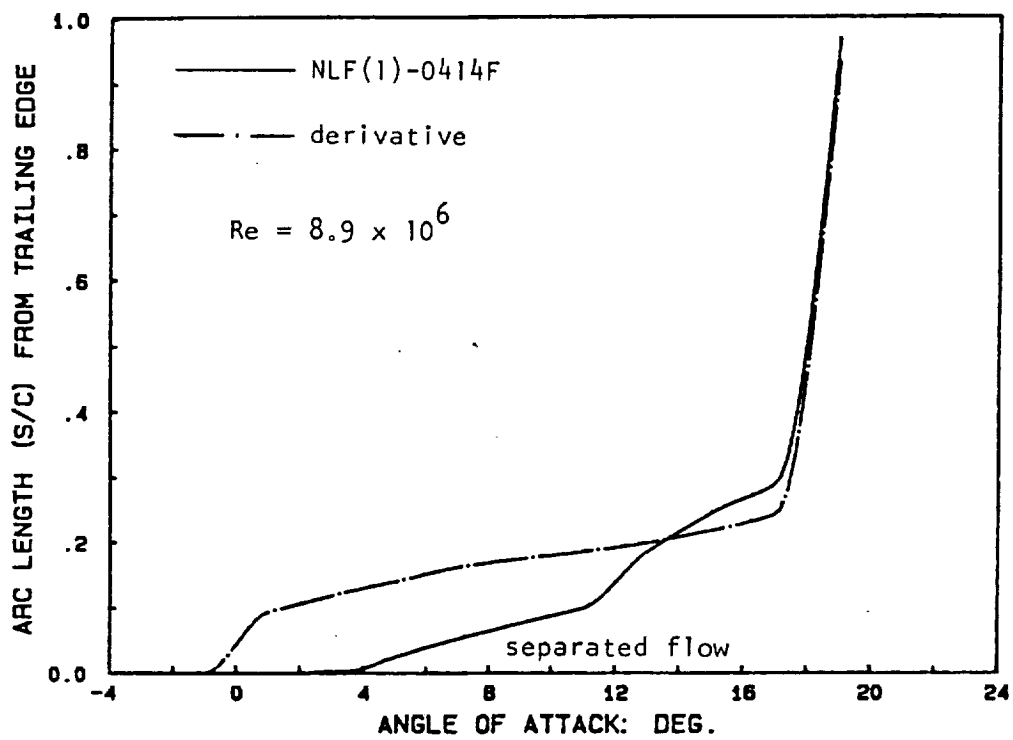


Figure 6.97 Location of turbulent separation for NLF(1)-0414F and derivative as calculated by the Eppler code.



c) transition fixed at 5-percent chord

Figure 6.97 (concluded)

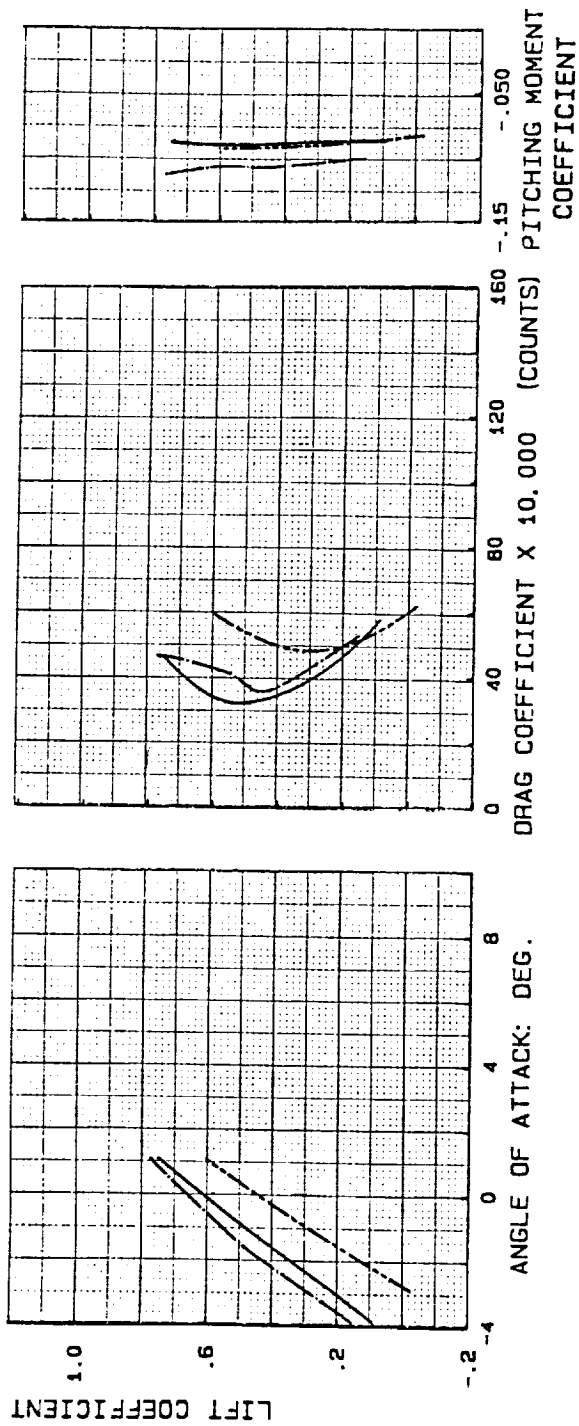


Figure 6.98 Aerodynamic characteristics of NLF(1)-0414F and derivative as predicted by the NCS code using natural transition.

$M = 0.6$
 $Re = 8.9 \times 10^6$

— NLF(1)-0414F
 - - - derivative
 - - - MS(1)-0317

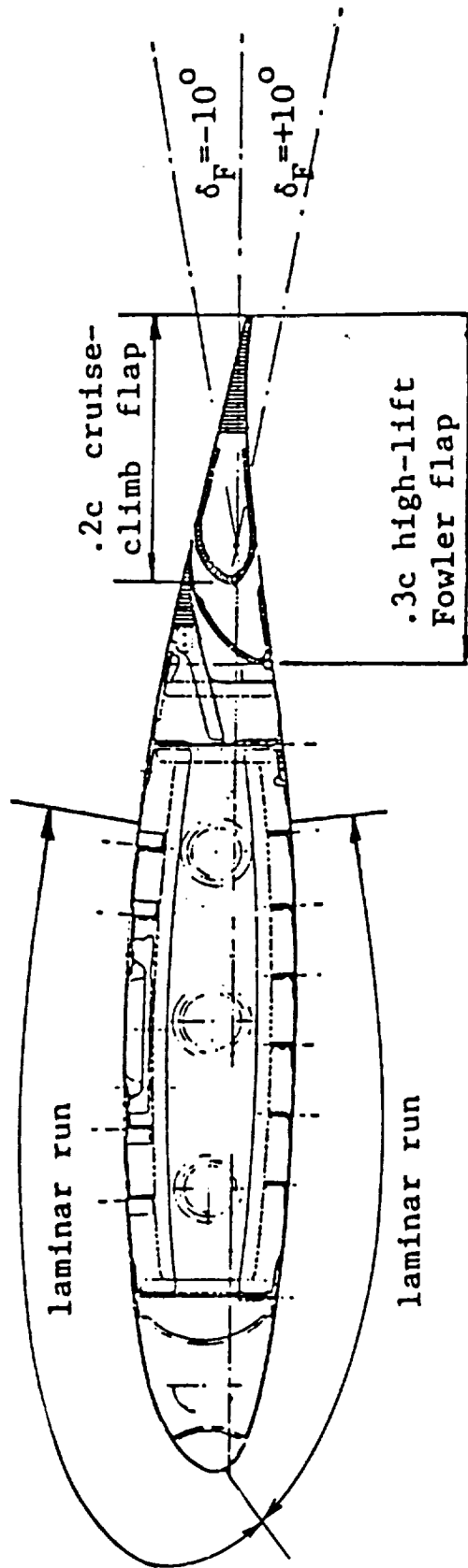
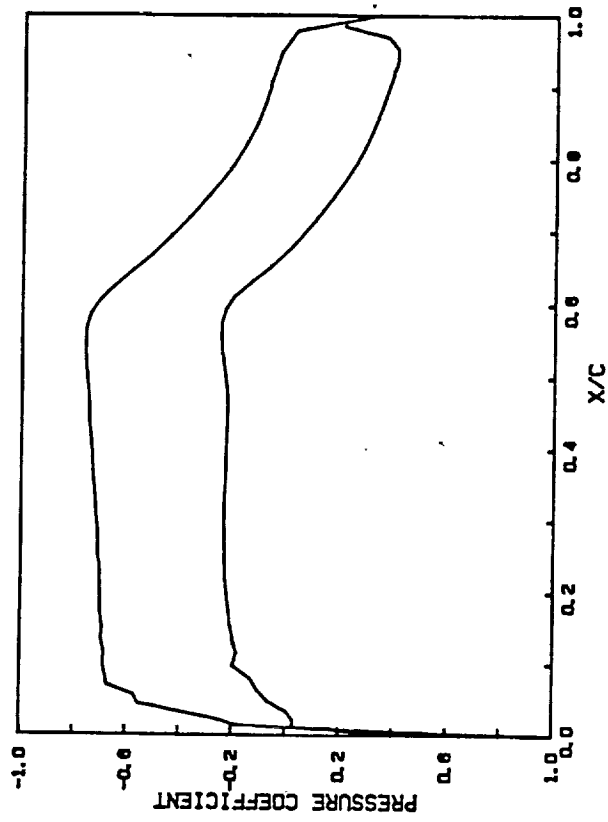
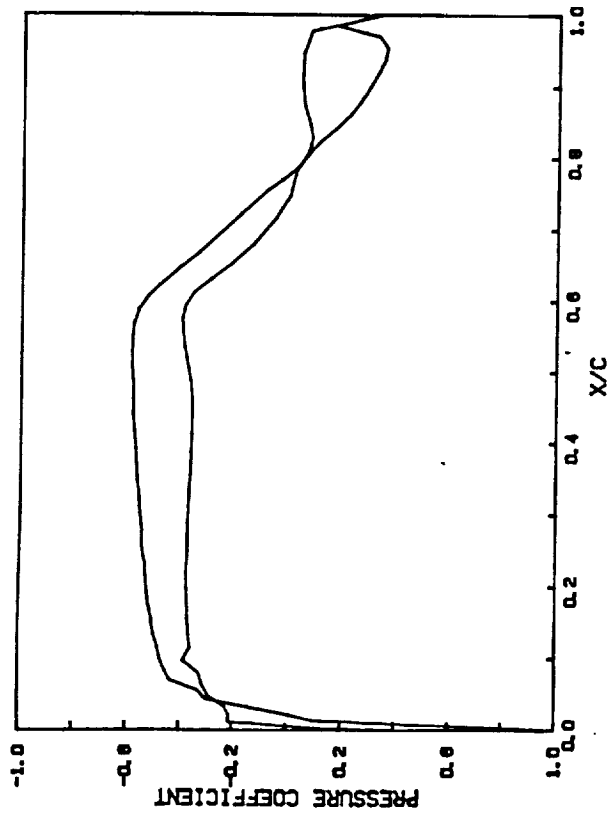


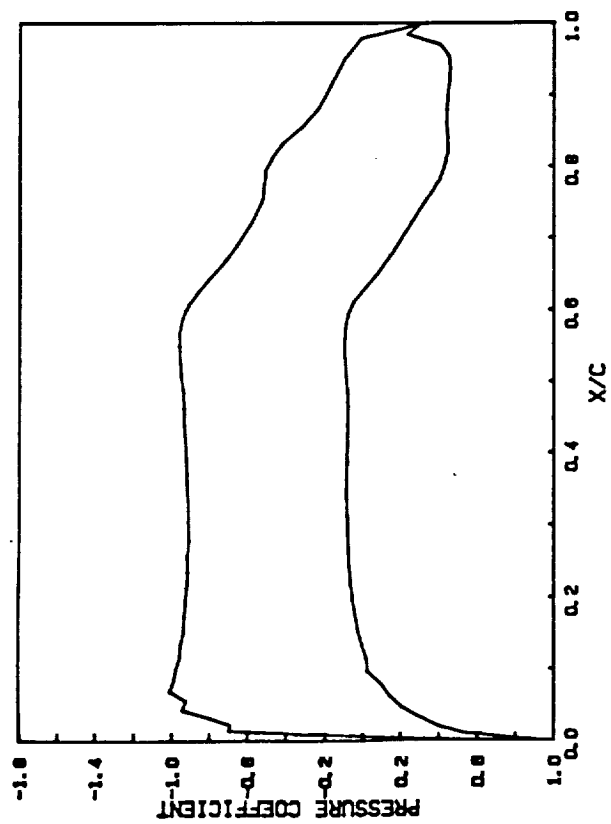
Figure 7.1 .20c cruise/climb flap incorporated into .30c Fowler flap



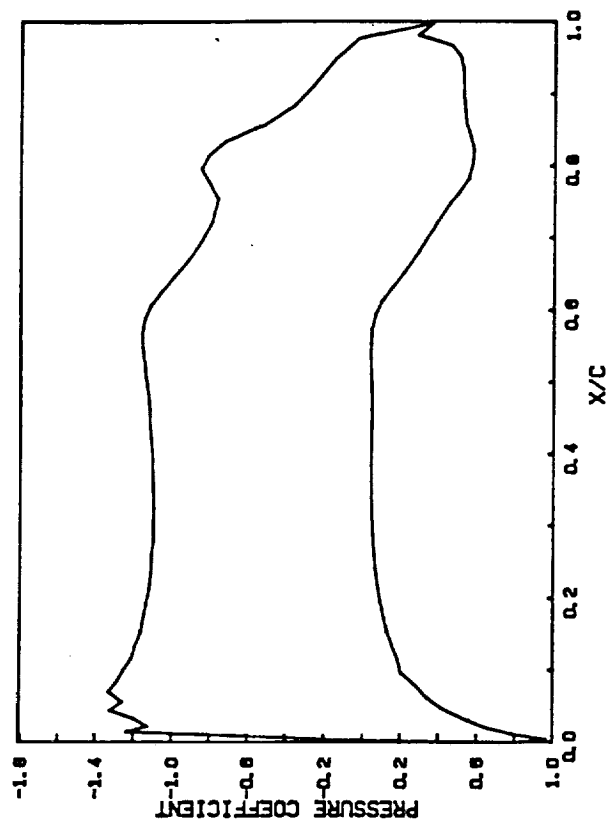
- a) $\delta_F = -5$ deg.; $\alpha = -0.90$ deg.; $C_l = 0.116$; $C_m = -0.0461$ b) $\delta_F = 0$ deg.; $\alpha = -1.00$ deg.; $C_l = 0.396$; $C_m = -0.1125$

calculated by Epppler code

Figure 7.2 Calculated inviscid pressure distributions of airfoil 32 with deflection of a 20% chord cruise/climb flap. $Re = 8.9 \times 10^6$



c) $\delta_F = 5 \text{ deg.}; \alpha = -0.90 \text{ deg.}; C_l = 0.717; C_m = -0.1775$



d) $\delta_F = 10 \text{ deg.}; \alpha = -1.00 \text{ deg.}; C_l = 1.006; C_m = -0.2397$

Figure 7.2 Concluded

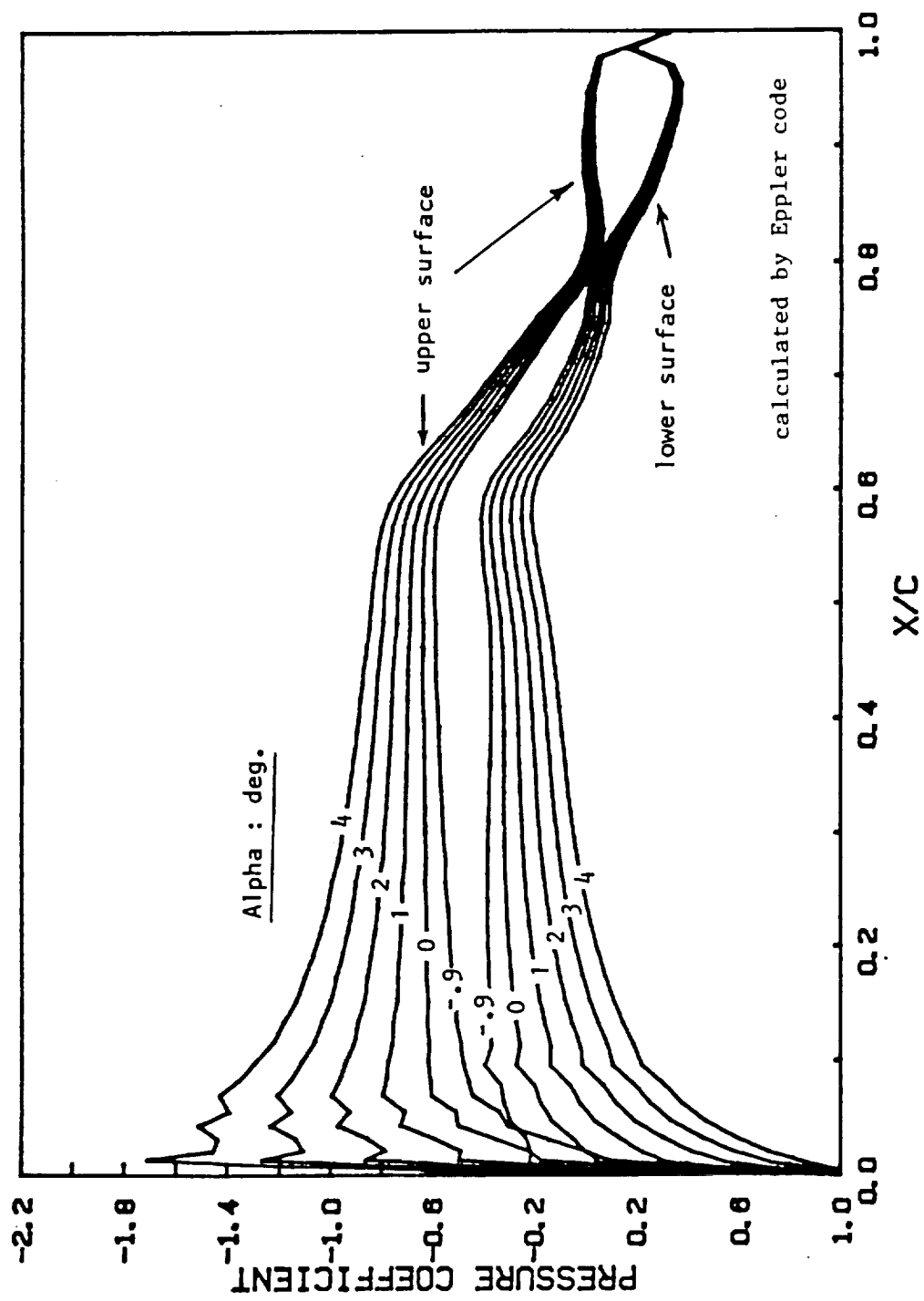


Figure 7.3 Inviscid pressure distributions of airfoil 32 with $\delta_F = -5$ deg.

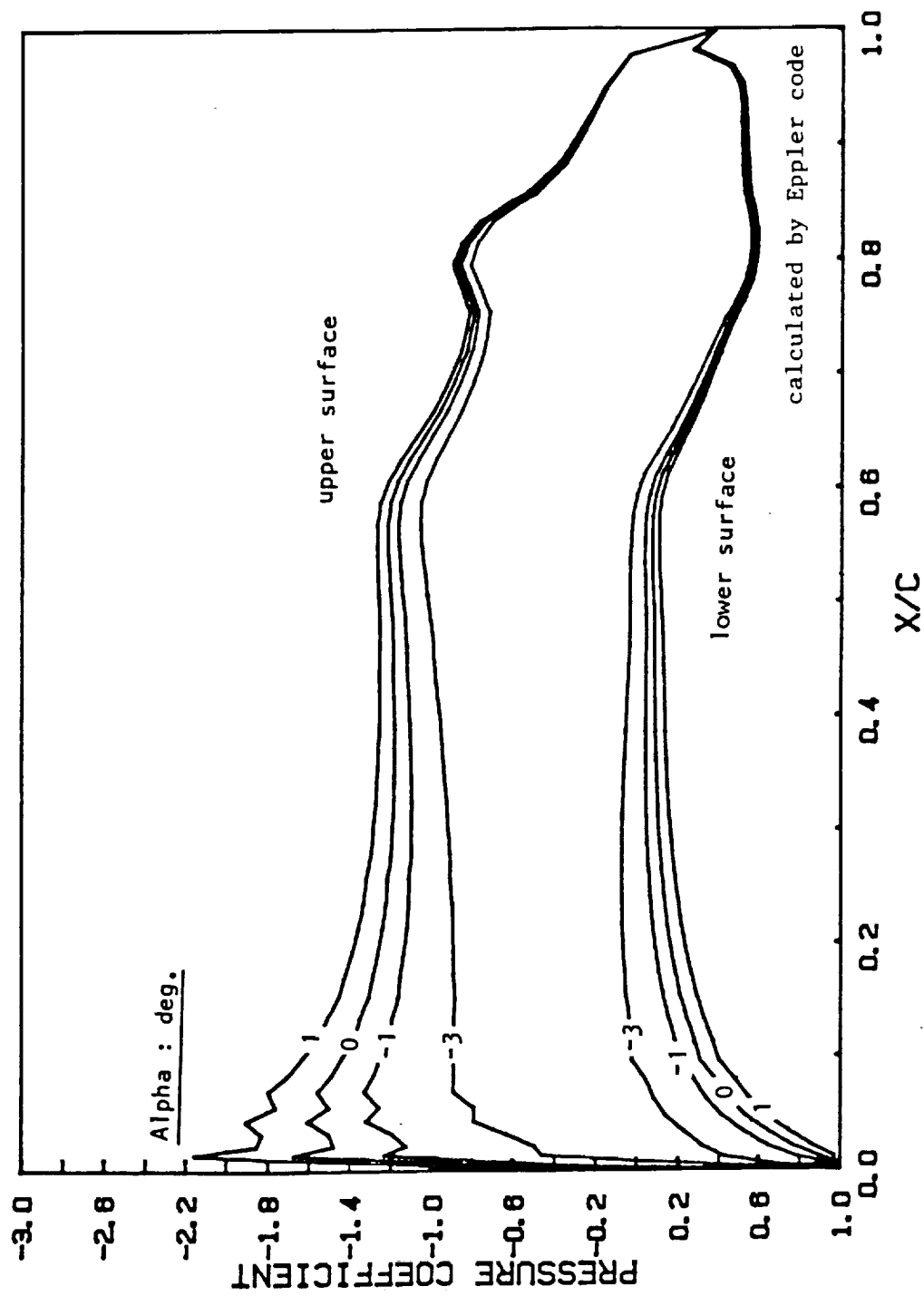
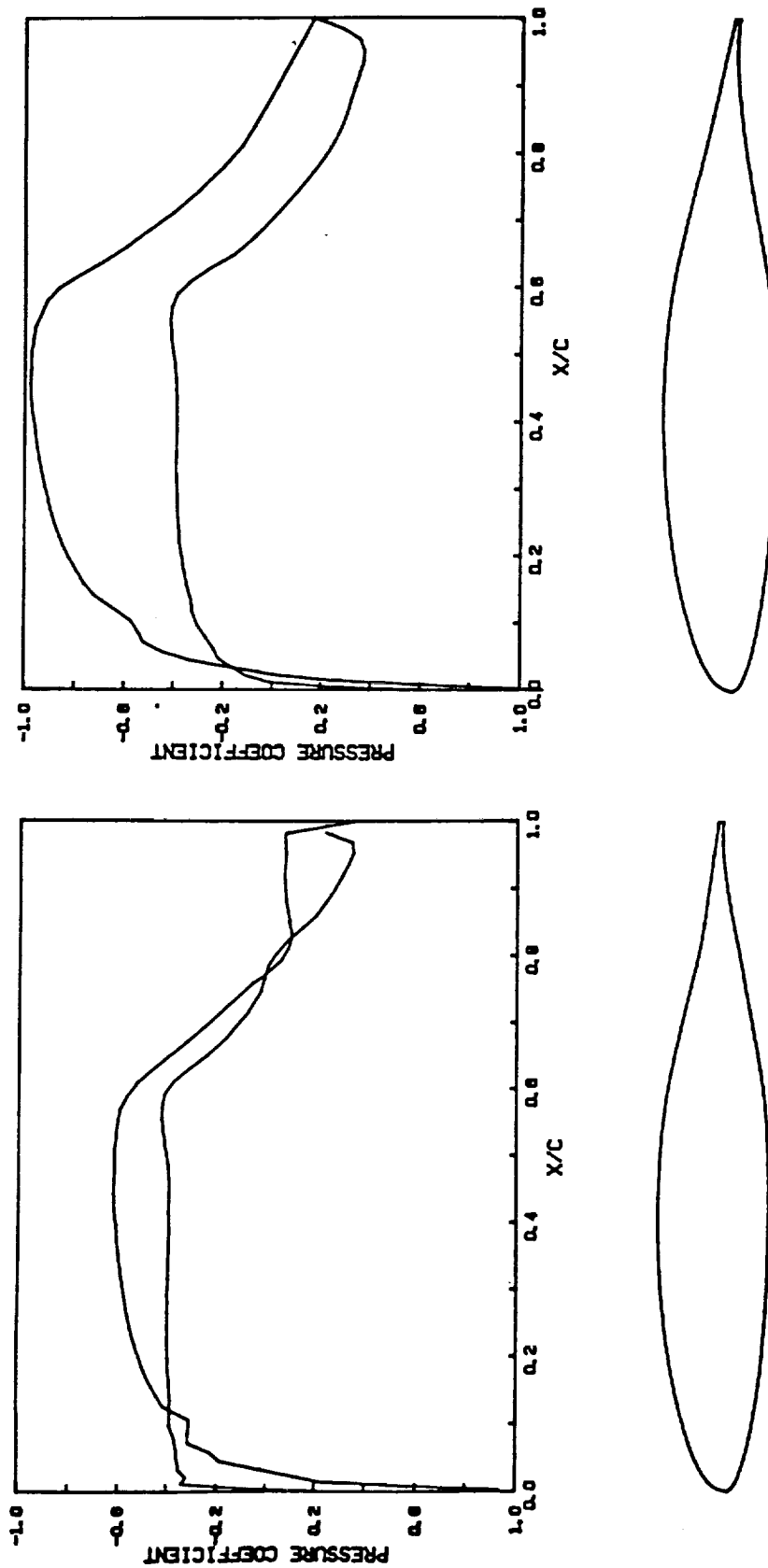
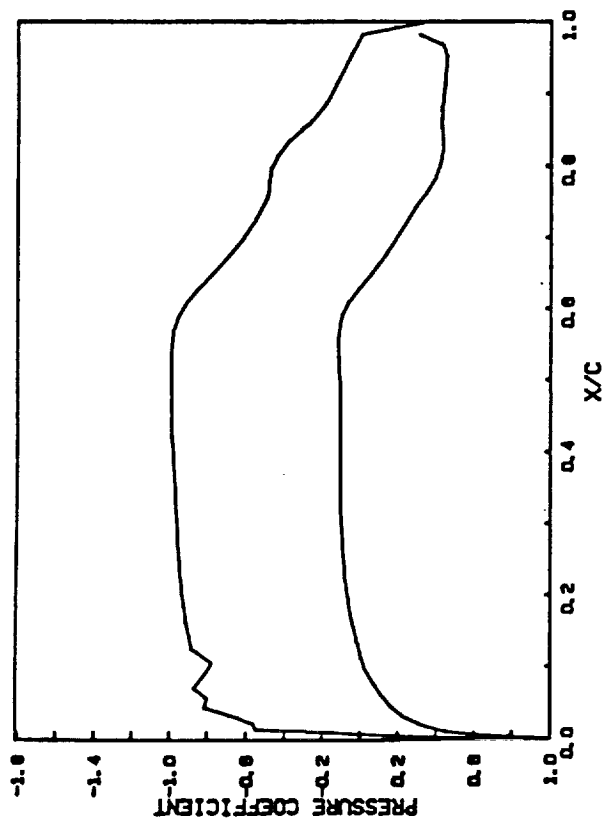
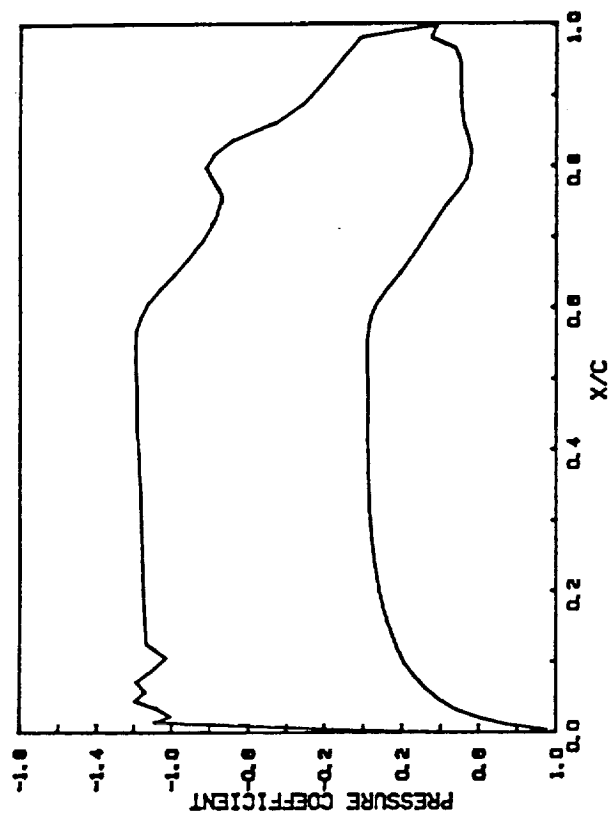


Figure 7.4 Inviscid pressure distributions of airfoil 32 with $\delta_F = 10^\circ$.



a) $\delta_F = -5 \text{ deg.}; \alpha = -1.00 \text{ deg.}; C_l = 0.085; C_m = -0.0444$ b) $\delta_F = 0 \text{ deg.}; \alpha = -0.90 \text{ deg.}; C_l = 0.405; C_m = -0.1051$
calculated by Epppler code

Figure 7.5 Inviscid pressure distributions of airfoil 35 with deflection of a 20% chord cruise/climb flap. $Re = 8.9 \times 10^6$



c) $\delta_F = 5 \text{ deg.}; \alpha = -0.90 \text{ deg.}; C_l = 0.696; C_m = -0.1766$ d) $\delta_F = 10 \text{ deg.}; \alpha = -0.90 \text{ deg.}; C_l = 0.997; C_m = -0.2397$

Figure 7.5 Concluded

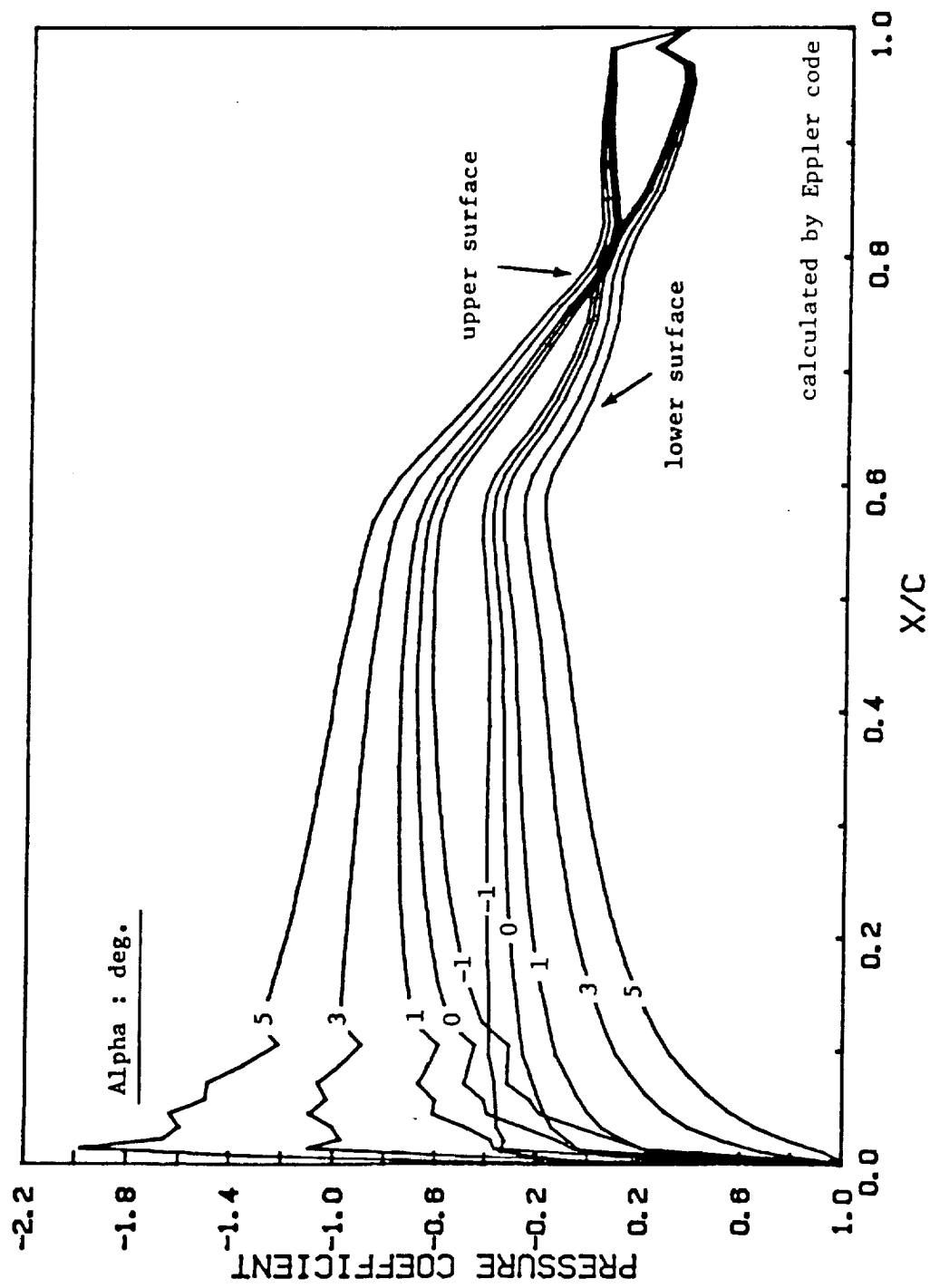


Figure 7.6 Inviscid pressure distribution of airfoil 35 with $\delta_F = -5$ deg.

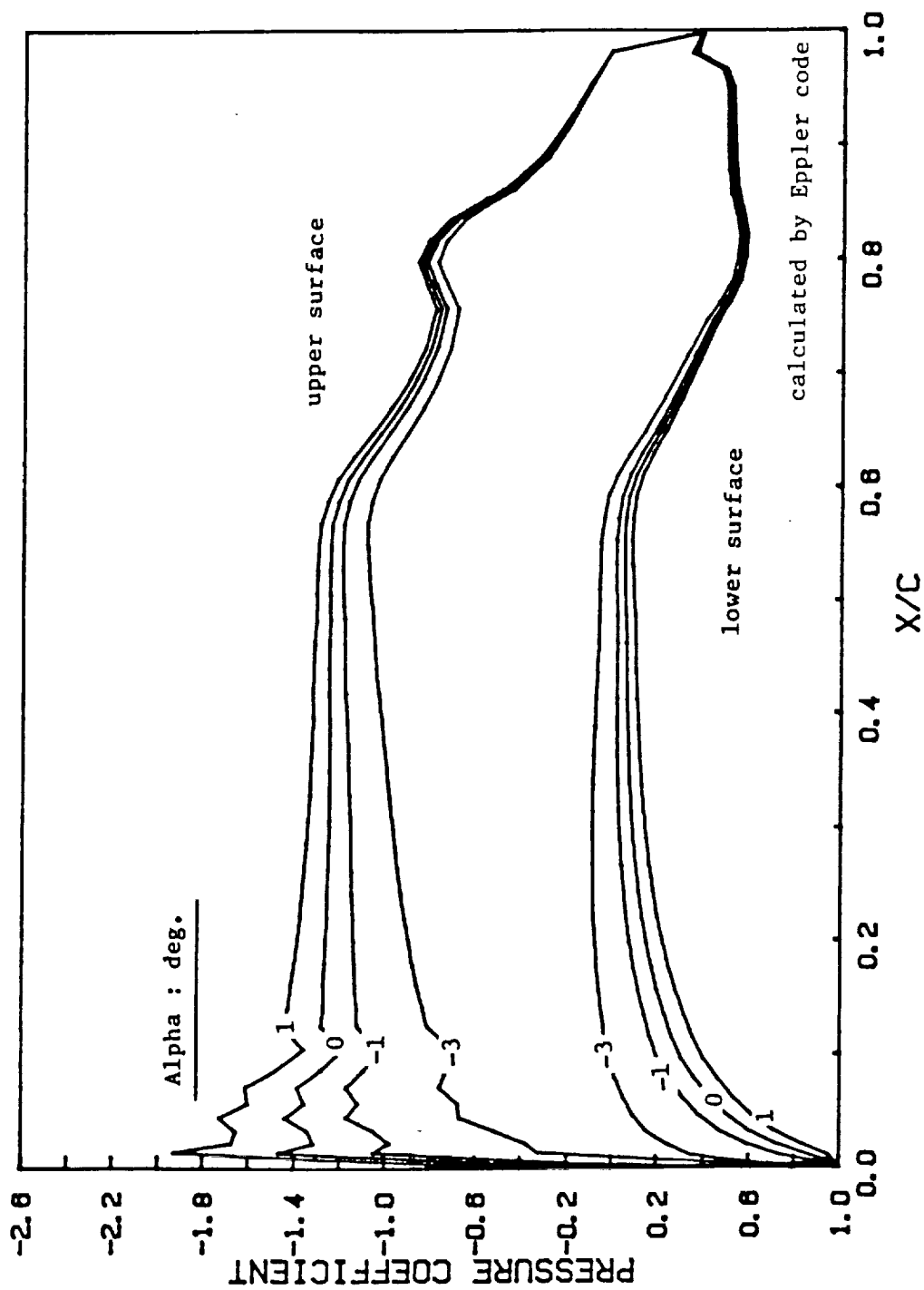
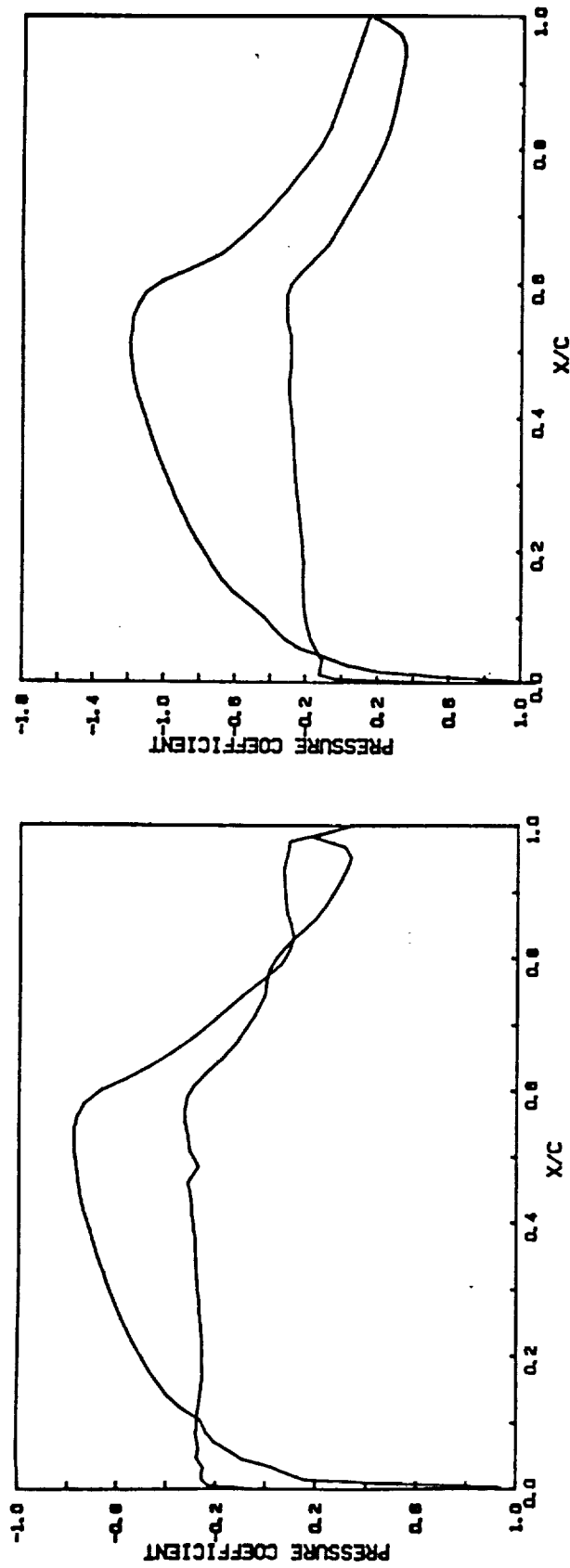


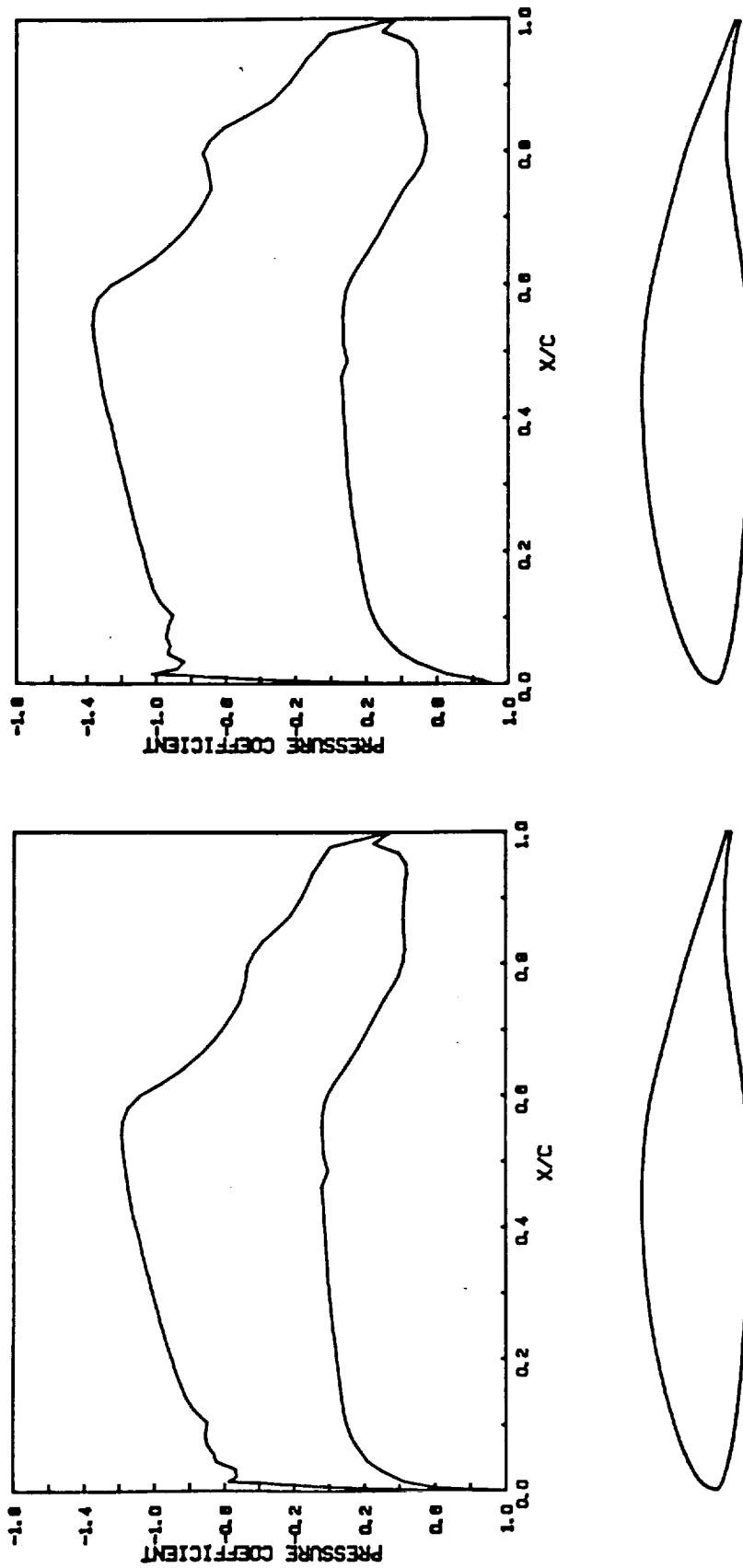
Figure 7.7 Inviscid pressure distributions of airfoil 35 with $\delta_F = 10$ deg.



a) $\delta_F = -5$ deg. ; $\alpha = -0.90$ deg. ; $C_l = 0.172$; $C_m = -0.0602$ b) $\delta_F = 0$ deg. ; $\alpha = -0.90$ deg. ; $C_l = 0.5616$; $C_m = -0.1258$

calculated by Eppler code

Figure 7.8 Calculated inviscid pressure distributions of airfoil 40 with deflection of a 20% cruise/climb flap. $Re = 8.9 \times 10^6$



c) $\delta_F = 5 \text{ deg.}$; $\alpha = -0.90 \text{ deg.}$; $C_l = 0.773$; $C_m = -.1934$ d) $\delta_F = 10 \text{ deg.}$; $\alpha = -1.00 \text{ deg.}$; $C_l = 1.060$; $C_m = -.2567$

Figure 7.8 Concluded

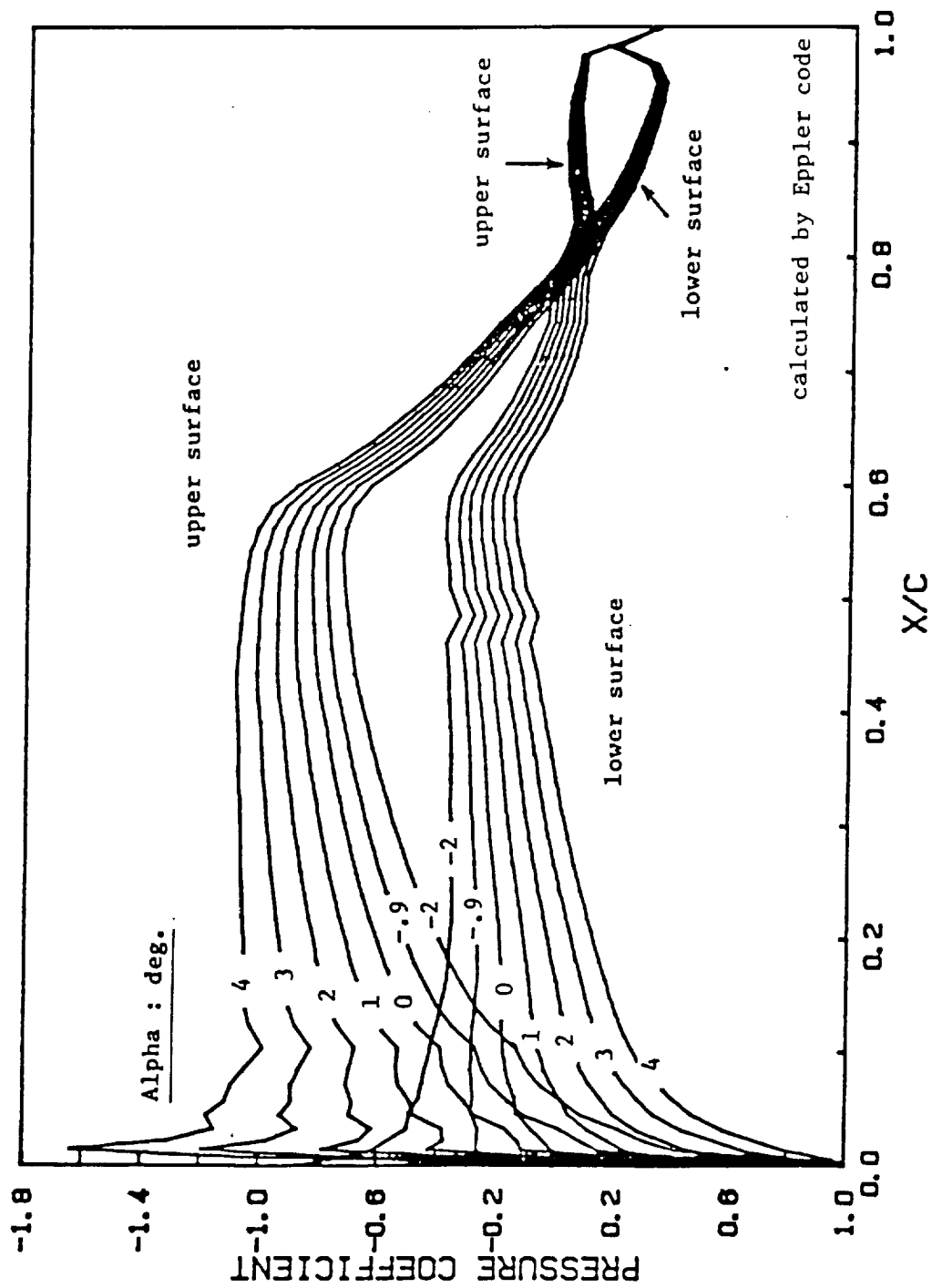


Figure 7.9 Inviscid pressure distribution of airfoil 40 with $\delta_F = -5$ deg.

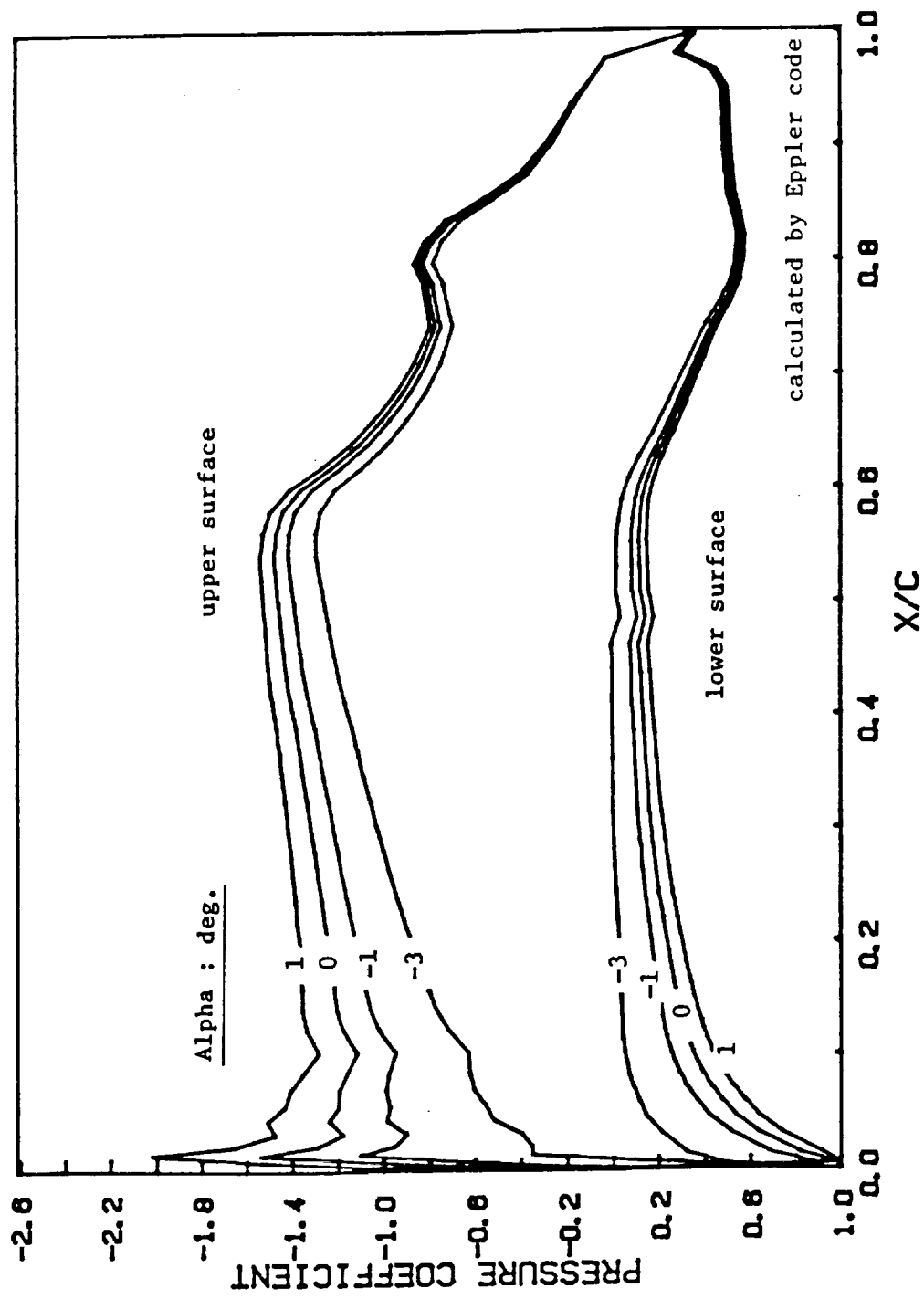
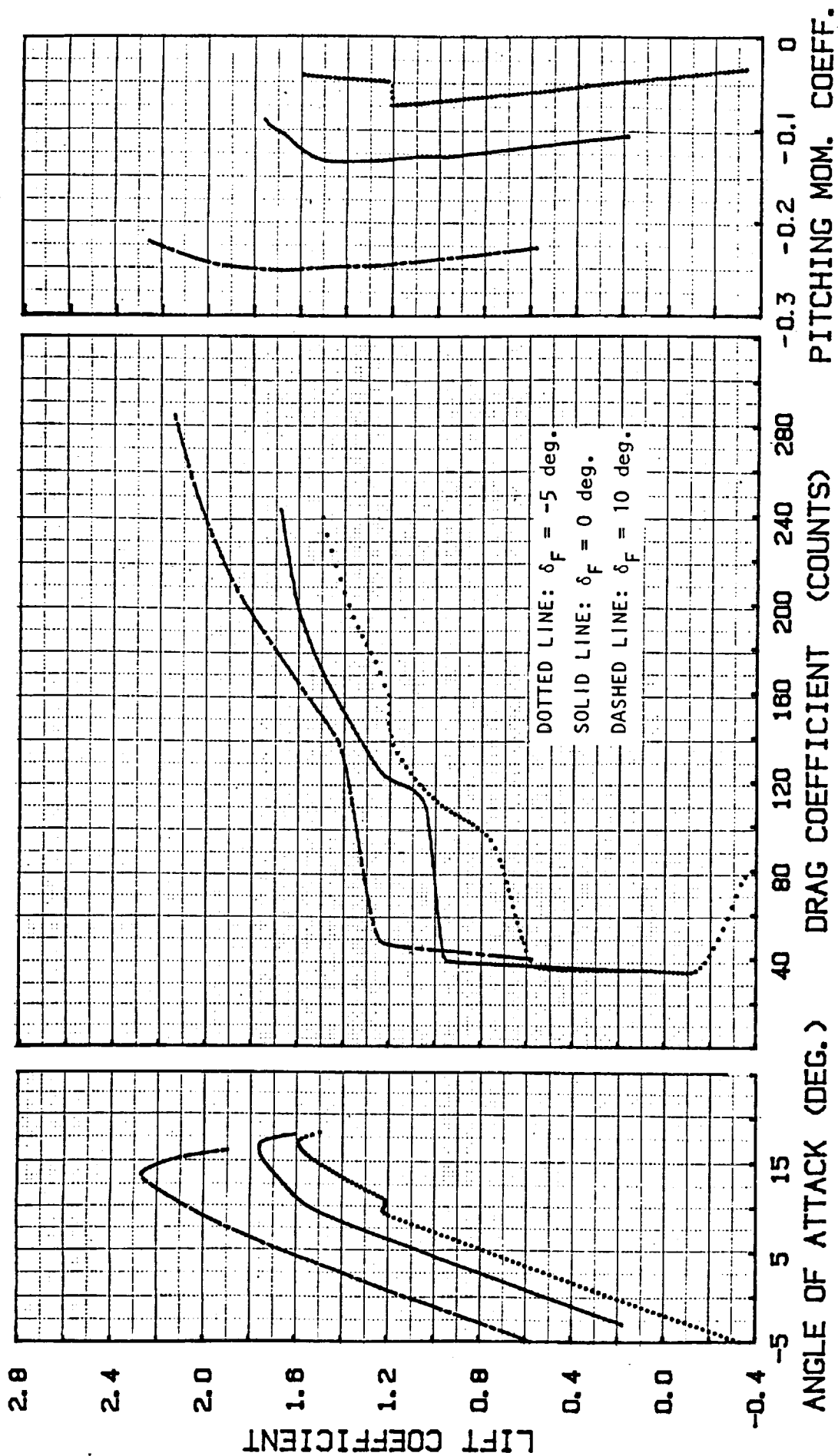


Figure 7.10 Inviscid pressure distribution of airfoil 40 with $\delta_F = 10$ deg.



a) LAMINAR SEPARATION

Figure 7.11 Calculated aerodynamic characteristics of airfoil 32 (for laminar separation, natural transition, and fixed transition criteria) with $\delta_F = -5, 0$, and 10 deg.
 $Re = 8.9 \times 10^6$ Eppler prediction

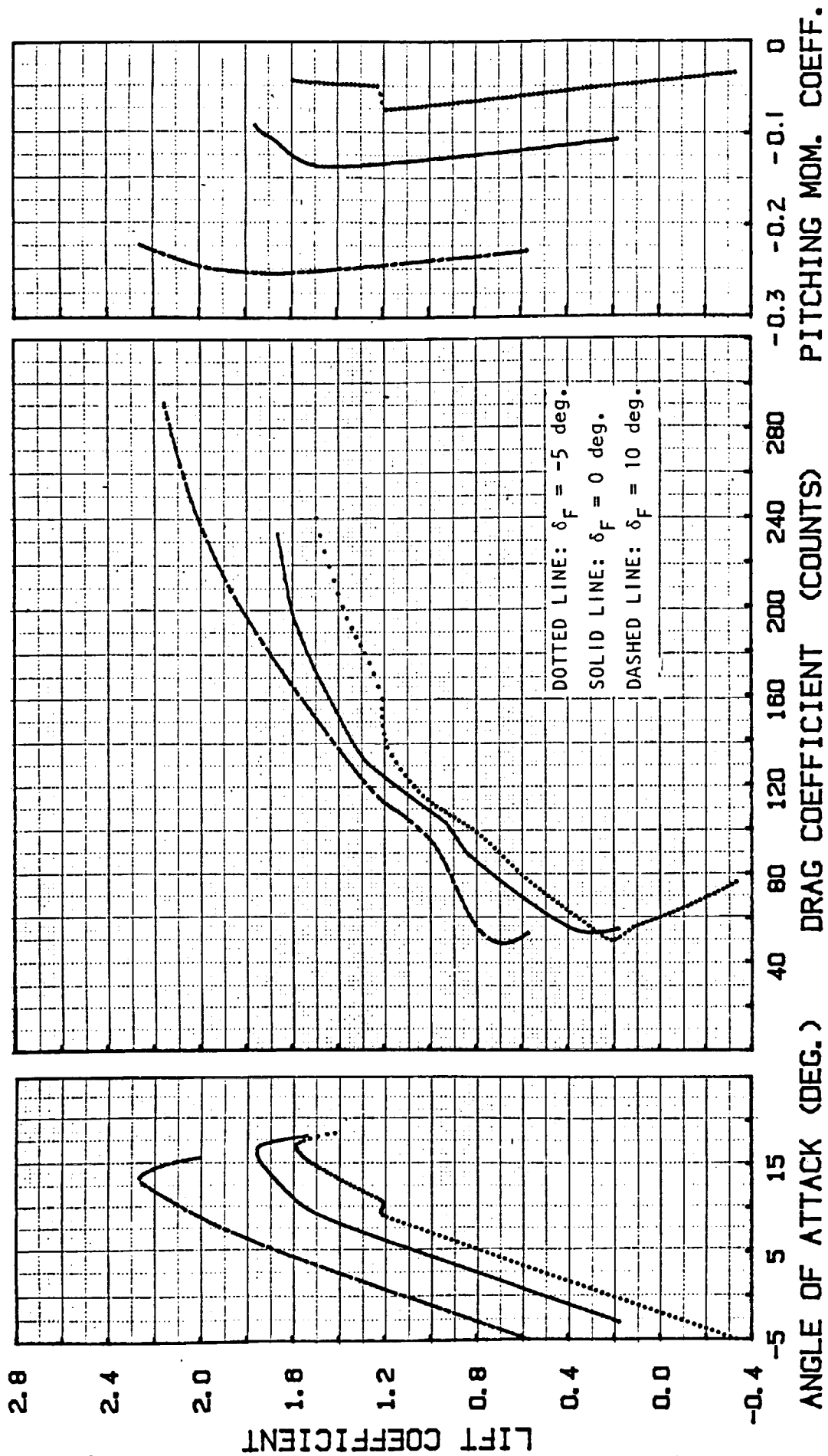


Figure 7.11 continued b) NATURAL TRANSITION

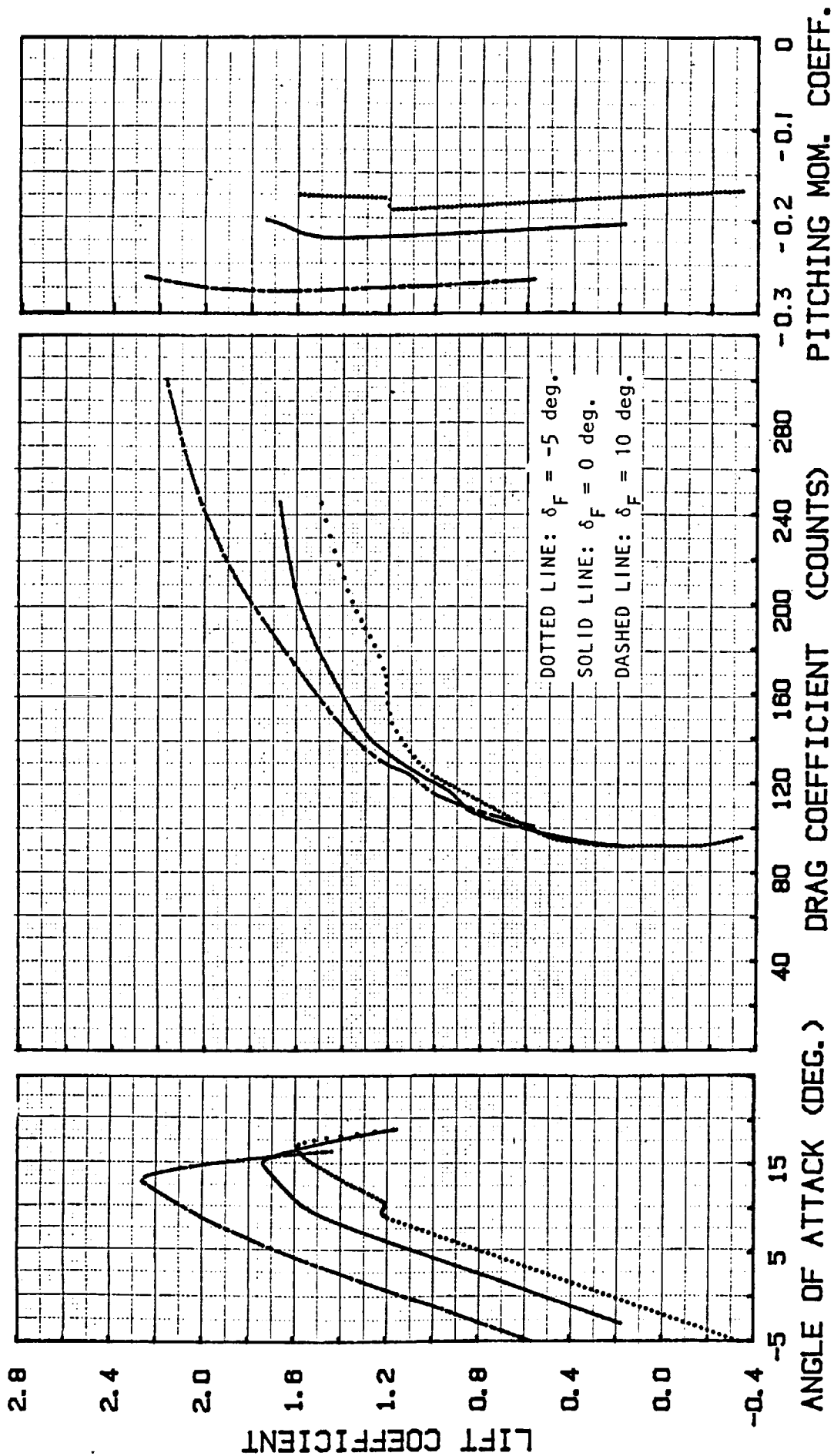
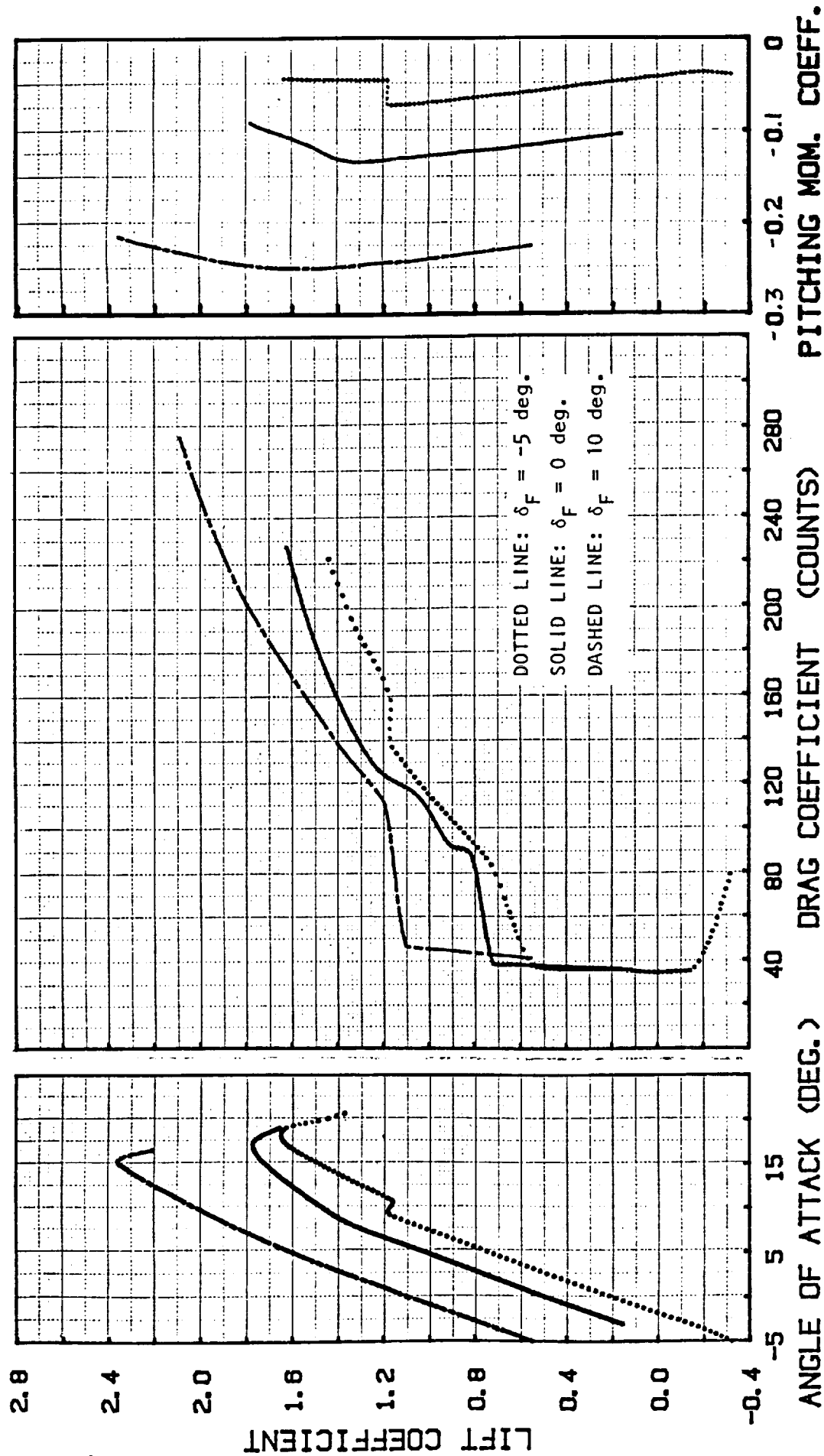


Figure 7.11 concluded c) FIXED TRANSITION (5% on both upper and lower surfaces)



a) LAMINAR SEPARATION

Figure 7.12 Calculated aerodynamic characteristics of airfoil 35 (for laminar separation, natural transition, and fixed transition criteria) with $\delta_F = -5, 0, \text{ and } 10 \text{ deg.}$
 $Re = 8.9 \times 10^6$ Eppler prediction

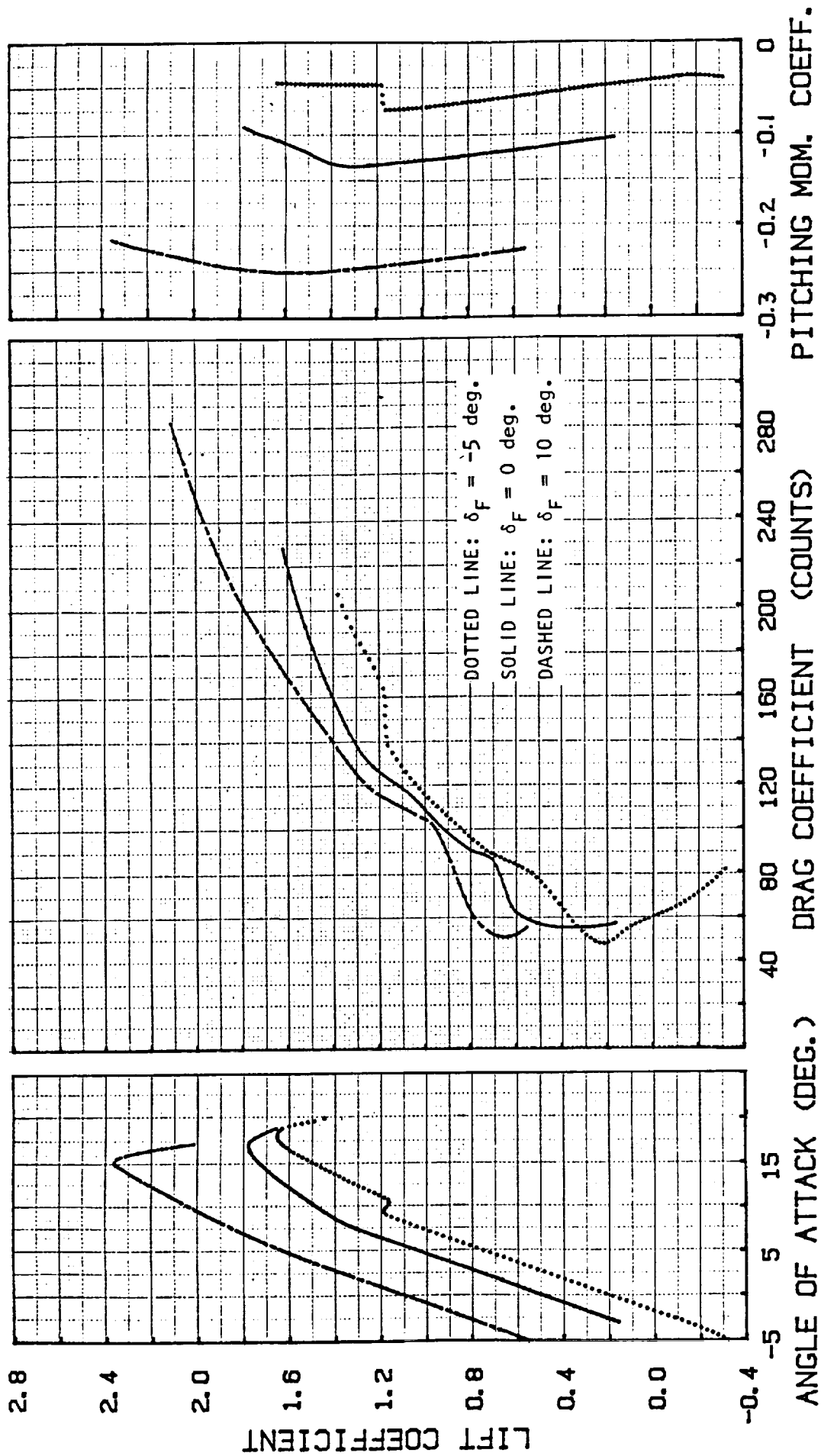


Figure 7.12 continued b) NATURAL TRANSITION

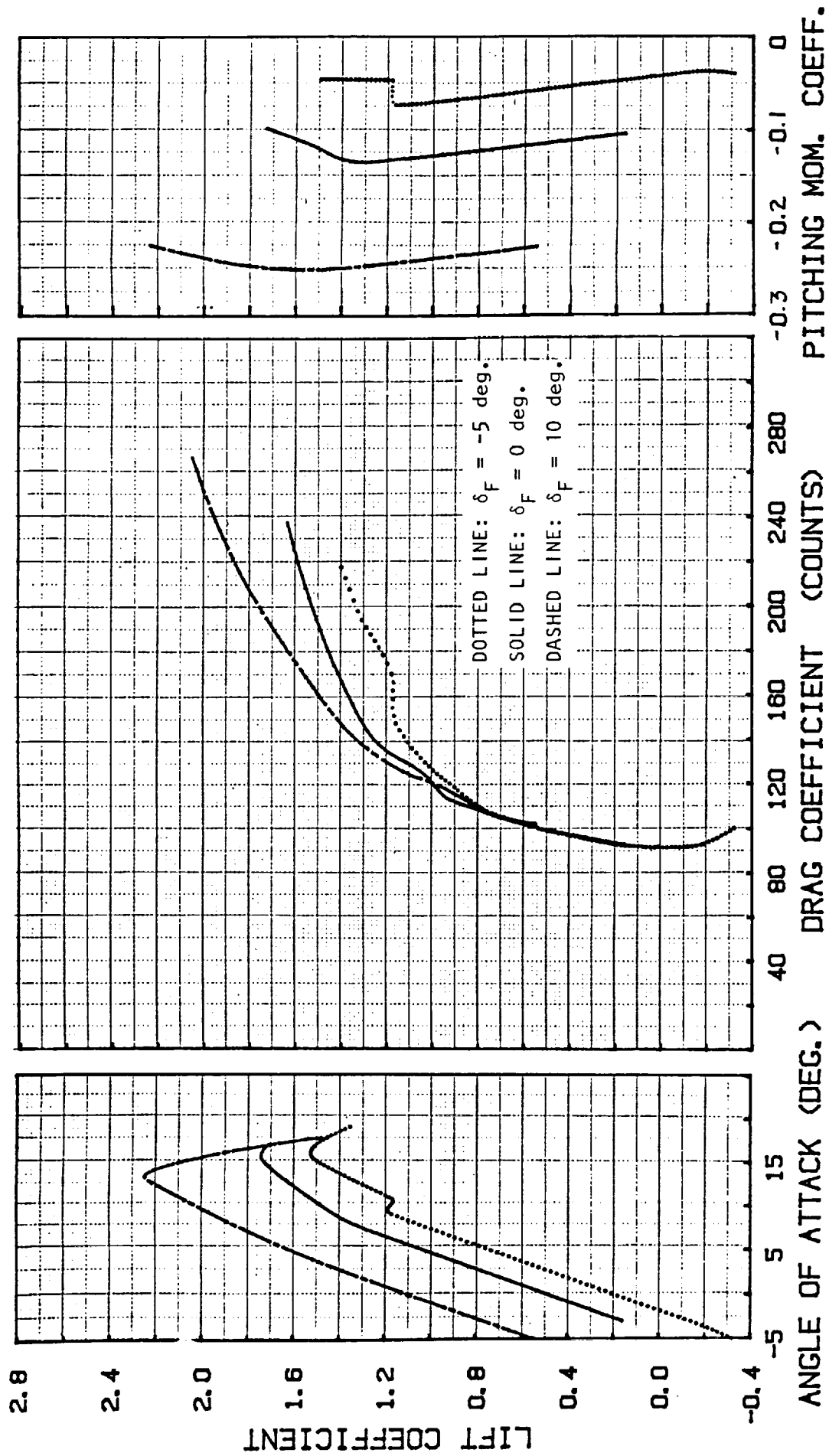
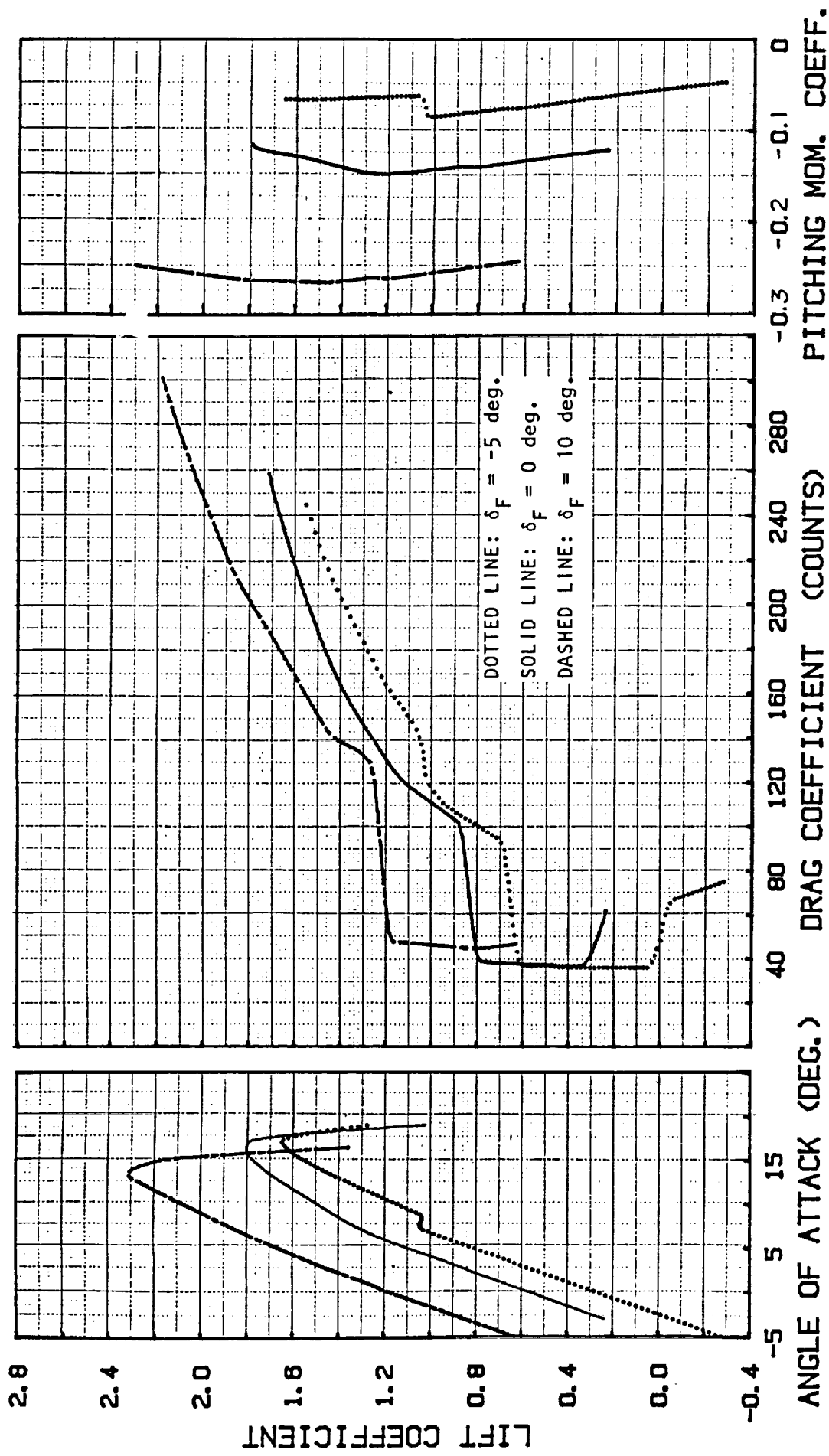


Figure 7.12 concluded c) FIXED TRANSITION (5% on both upper and lower surfaces)



a) LAMINAR SEPARATION

Figure 7.13 Calculated aerodynamic characteristics of airfoil 40 (for laminar separation, natural transition, and fixed transition criteria) with $\delta_F = -5, 0$, and 10 deg.
 $Re = 8.9 \times 10^6$ Eppler prediction

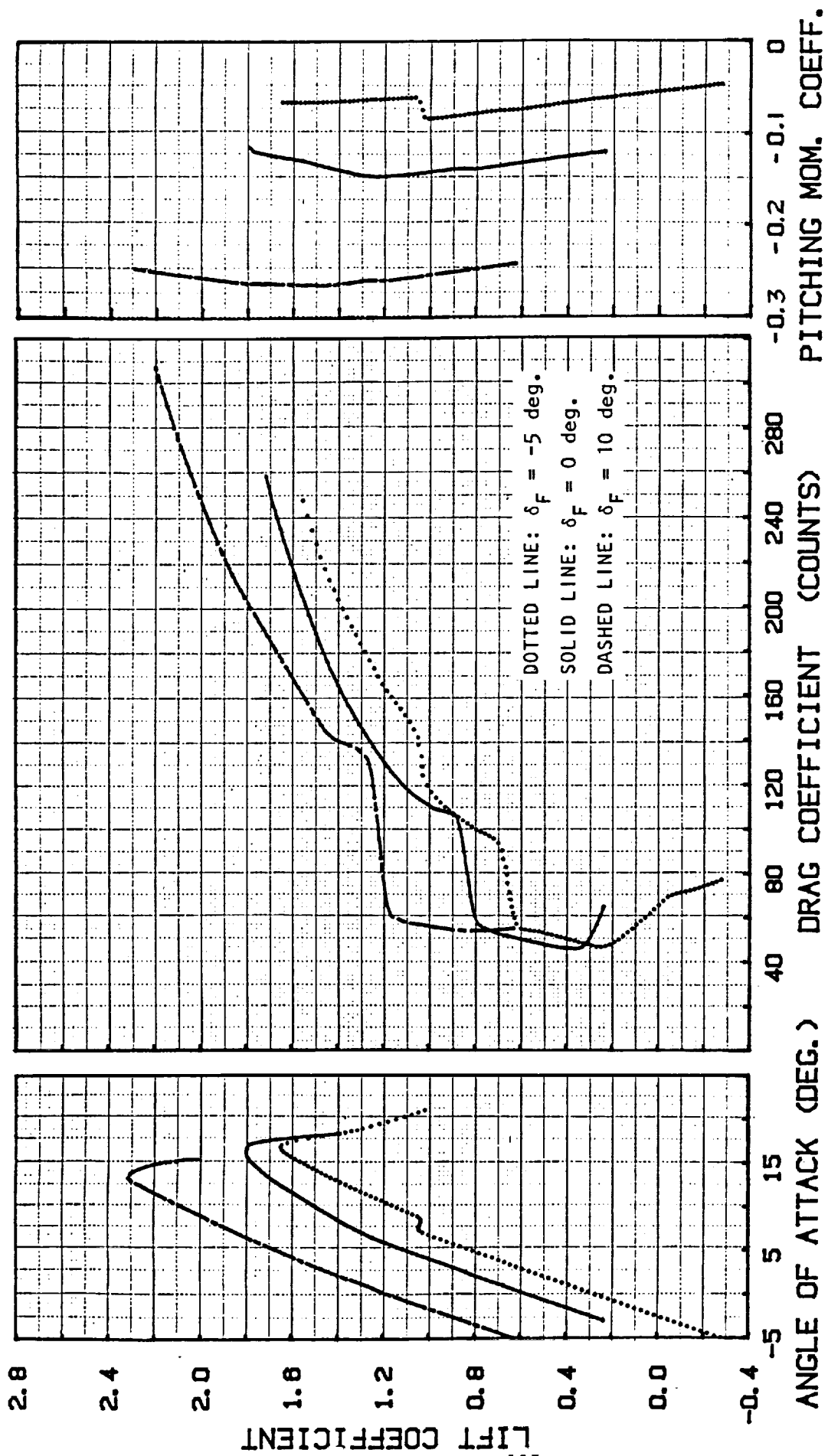


Figure 7.13 continued b) NATURAL TRANSITION

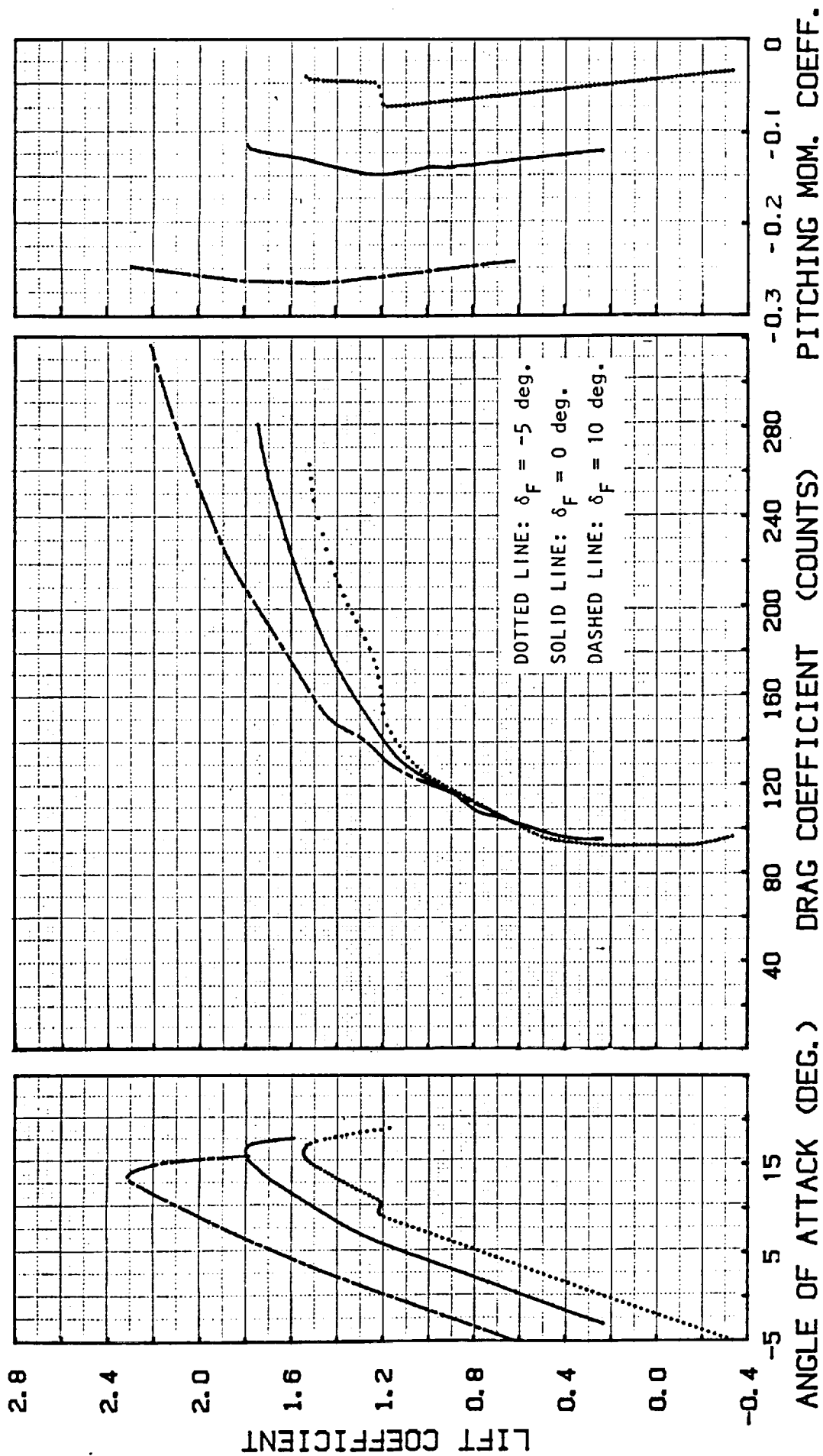


Figure 7.13 concluded c) FIXED TRANSITION (5% on both upper and lower surfaces)

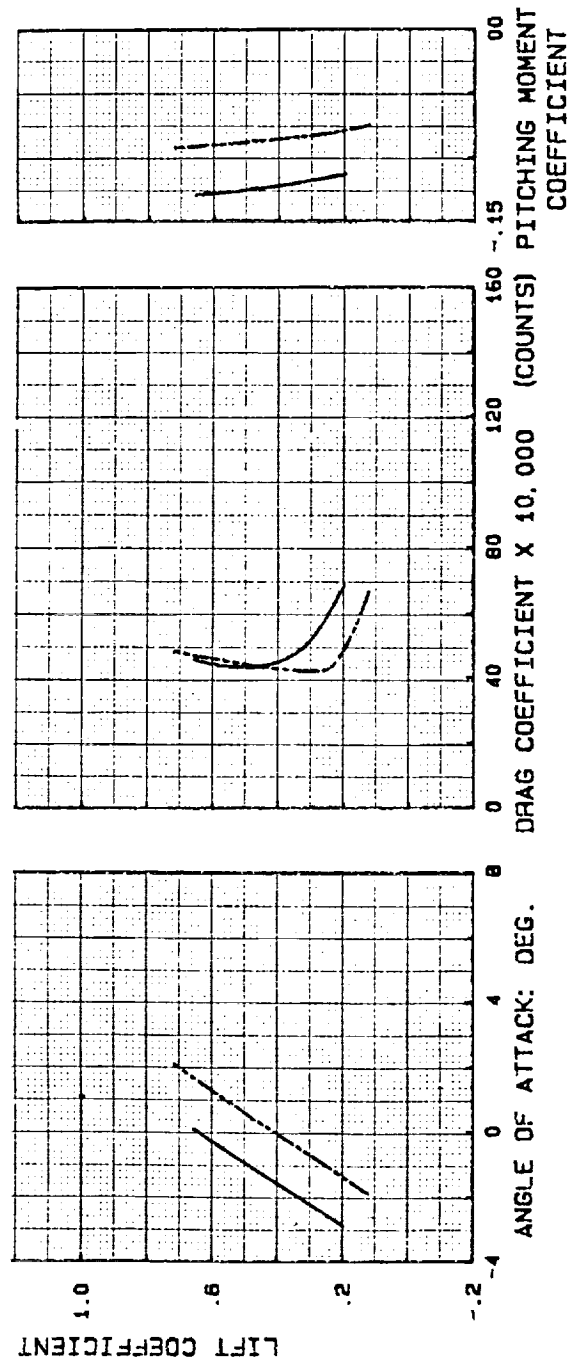


Figure 7.14a Effect of flap deflection on aerodynamic characteristics of airfoil 40 as predicted by the NCS code.

$c_f/c = 0.20$ $\delta_f = 0$ deg. $Re = 8.9 \times 10^6$
 $---$ $\delta_f = -3$ deg. $M = 0.6$

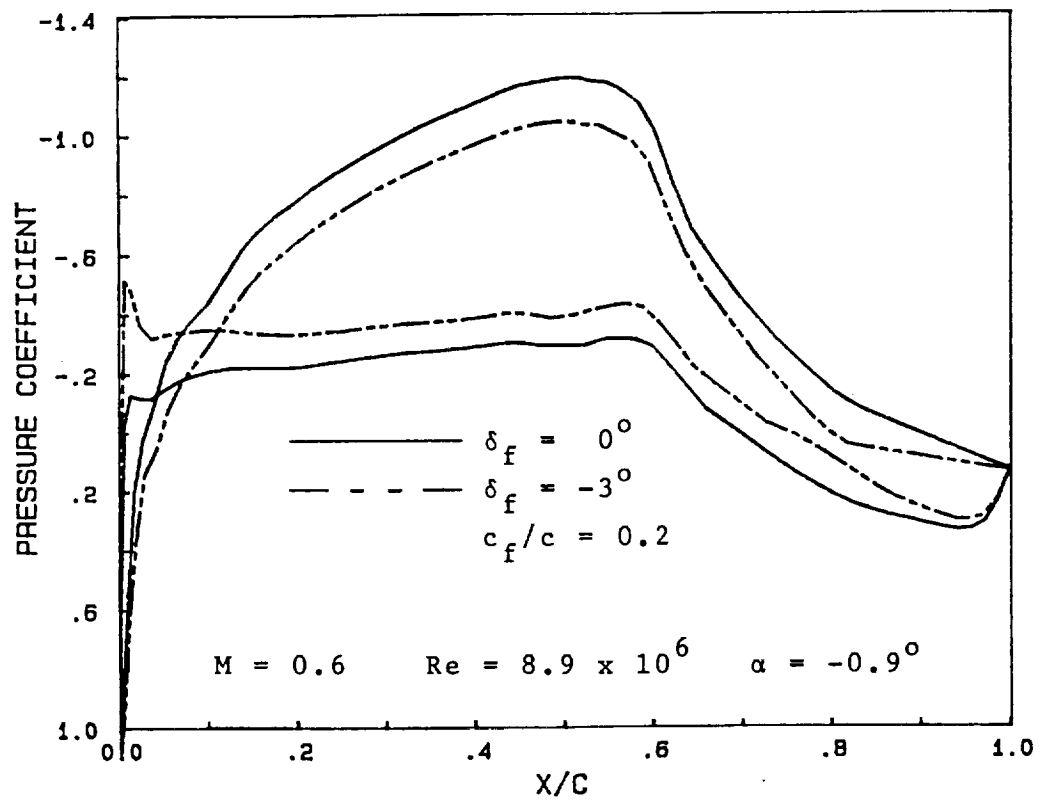


Figure 7.14b Effect of flap deflection on the pressure distribution of airfoil 40 as predicted by the NCS code.

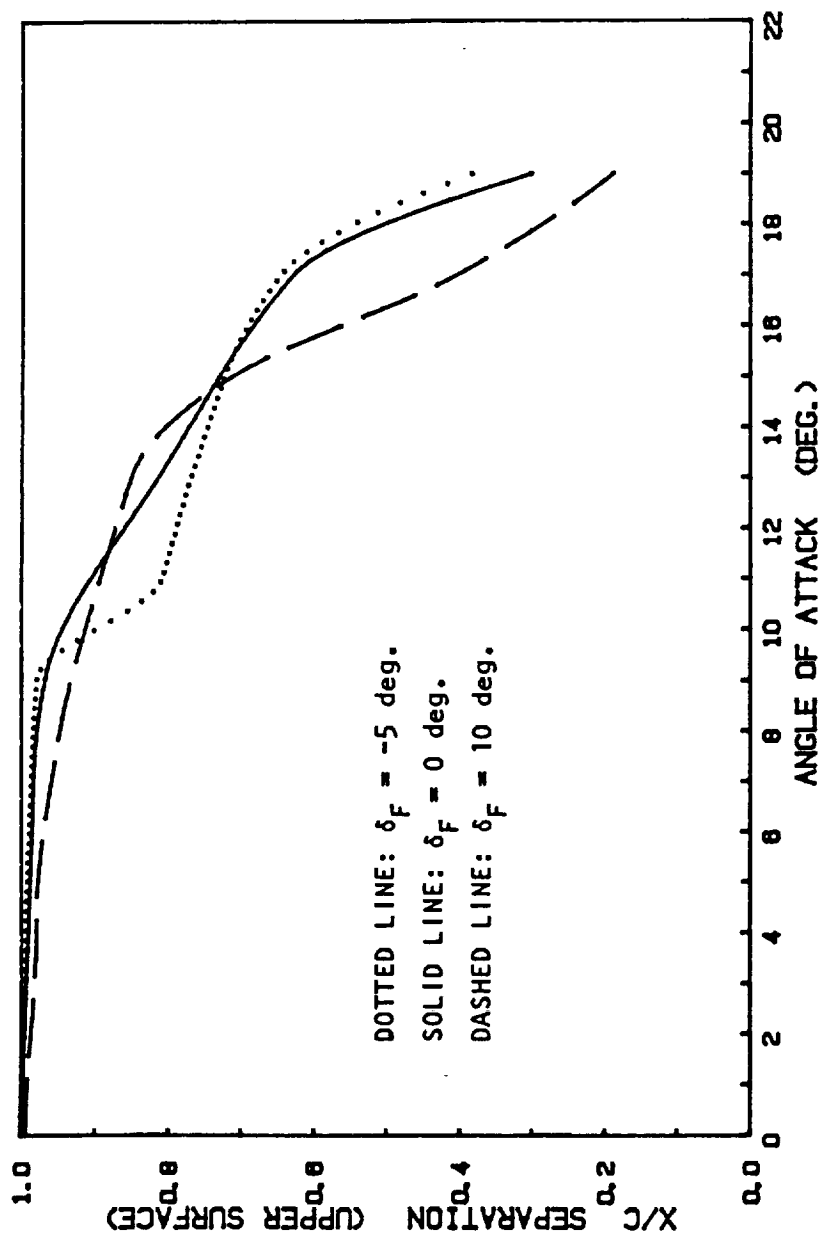


Figure 7.15 The change in predicted point of turbulent separation with changes in both angle of attack and flap deflection angle for airfoil 32. $Re = 8.9 \times 10^6$ Eppler prediction

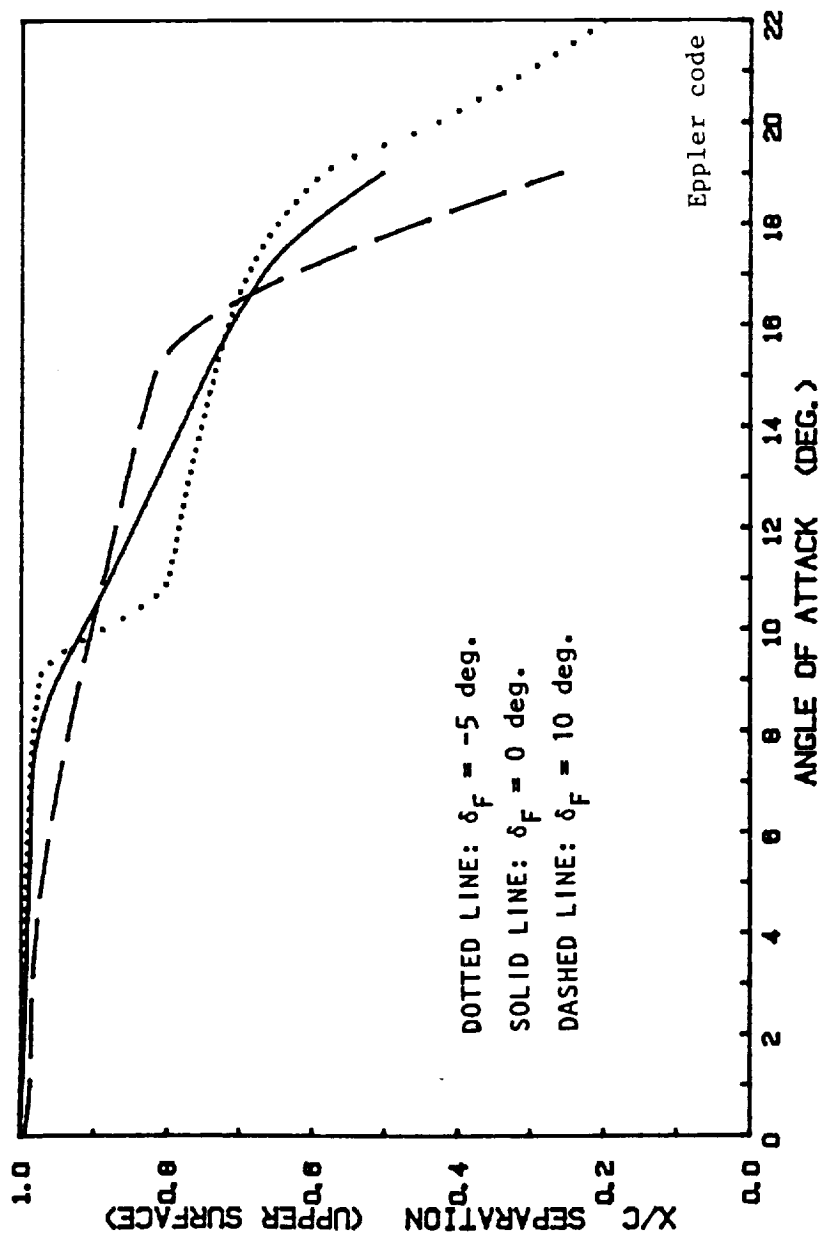


Figure 7.16 The change in predicted point of turbulent separation with changes in both angle of attack and flap deflection angle for airfoil 35. $Re = 8.9 \times 10^6$

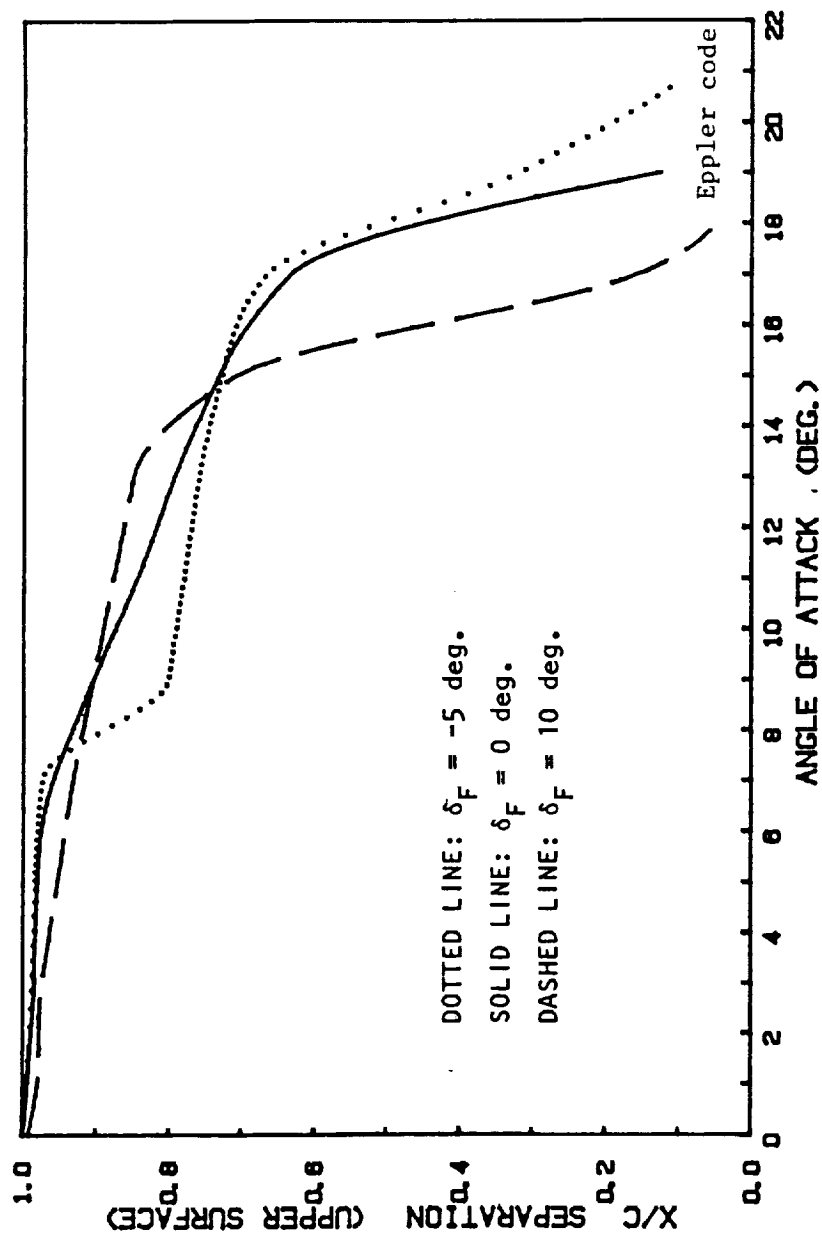


Figure 7.17 The change in predicted point of turbulent separation with changes in both angle of attack and flap deflection angle for airfoil 40. $Re = 8.9 \times 10^6$

APPENDIX I

COORDINATES OF K.U. NLF AIRFOILS

CONTENTS:

	<u>Page</u>
Coordinates of Airfoil KU 26.....	
Coordinates of Airfoil KU 32.....	
Coordinates of Airfoil KU 35.....	
Coordinates of Airfoil KU 37.....	
Coordinates of Airfoil KU 40.....	
Coordinates of KU Derivative NASA NLF(1)-0414F.....	
Nose Shape Parameters.....	

AIRFOIL 26A COORDINATES

UPPER SURFACE		LOWER SURFACE	
X/C	Z/C	X/C	Z/C
0.	0.00099	1.00000	-0.00654
0.00067	0.00708	0.98396	-0.00486
0.00317	0.01559	0.96884	-0.00413
0.00765	0.02418	0.95275	-0.00413
0.01335	0.03156	0.93535	-0.00479
0.02088	0.03783	0.91651	-0.00608
0.03128	0.04482	0.89635	-0.00794
0.04267	0.05129	0.87534	-0.01031
0.05403	0.05654	0.85402	-0.01310
0.06699	0.06144	0.83252	-0.01632
0.08144	0.06605	0.81053	-0.01999
0.09714	0.07034	0.78770	-0.02417
0.11414	0.07439	0.76343	-0.02895
0.13230	0.07820	0.73667	-0.03452
0.15132	0.08170	0.70353	-0.04163
0.17128	0.08496	0.66810	-0.04930
0.19177	0.08790	0.64251	-0.05469
0.21277	0.09055	0.62182	-0.05875
0.23455	0.09292	0.60329	-0.06193
0.25674	0.09501	0.58510	-0.06449
0.27924	0.09680	0.56599	-0.06663
0.30216	0.09830	0.54539	-0.06848
0.32523	0.09951	0.52382	-0.07001
0.34840	0.10042	0.50169	-0.07119
0.37162	0.10103	0.47892	-0.07204
0.39493	0.10134	0.45560	-0.07258
0.41815	0.10135	0.43204	-0.07279
0.44081	0.10106	0.40860	-0.07268
0.46355	0.10044	0.38502	-0.07223
0.48643	0.09951	0.35958	-0.07141
0.50849	0.09831	0.33280	-0.07031
0.52988	0.09679	0.30775	-0.06904
0.55071	0.09497	0.28325	-0.06747
0.57064	0.09284	0.25948	-0.06567
0.58993	0.09036	0.23626	-0.06357
0.60901	0.08746	0.21237	-0.06106
0.62824	0.08411	0.18963	-0.05841
0.64858	0.08010	0.16812	-0.05551
0.67122	0.07531	0.14673	-0.05223
0.69574	0.06980	0.12591	-0.04867
0.72299	0.06345	0.10626	-0.04487
0.75706	0.05528	0.08770	-0.04083
0.79126	0.04703	0.07039	-0.03653
0.82155	0.03985	0.05405	-0.03189
0.85009	0.03326	0.03936	-0.02700
0.87786	0.02706	0.02643	-0.02189
0.90703	0.02076	0.01543	-0.01656
0.94103	0.01358	0.00717	-0.01124
0.97871	0.00558	0.00179	-0.00540
1.00000	0.00096	0.	0.00099

AIRFOIL 32 COORDINATES

UPPER SURFACE		LOWER SURFACE	
X/C	Z/C	X/C	Z/C
0.	0.00099	1.00000	-0.00654
0.00071	0.00726	0.98563	-0.00472
0.00327	0.01588	0.97108	-0.00365
0.00783	0.02451	0.95534	-0.00322
0.01360	0.03192	0.93861	-0.00341
0.02124	0.03826	0.92065	-0.00418
0.03175	0.04535	0.90115	-0.00549
0.04324	0.05190	0.88082	-0.00728
0.05518	0.05746	0.86009	-0.00949
0.06904	0.06314	0.83915	-0.01209
0.08312	0.06798	0.81785	-0.01512
0.09842	0.07252	0.79582	-0.01860
0.11545	0.07692	0.77260	-0.02261
0.13310	0.08095	0.74713	-0.02728
0.15181	0.08470	0.71753	-0.03297
0.17129	0.08818	0.68314	-0.03969
0.19132	0.09132	0.65393	-0.04533
0.21204	0.09417	0.63169	-0.04941
0.23352	0.09675	0.61265	-0.05254
0.25515	0.09901	0.59445	-0.05504
0.27719	0.10094	0.57585	-0.05710
0.29978	0.10260	0.55625	-0.05880
0.32250	0.10394	0.53546	-0.06020
0.34531	0.10497	0.51348	-0.06130
0.36817	0.10568	0.48982	-0.06216
0.39114	0.10608	0.46453	-0.06281
0.41407	0.10617	0.43889	-0.06322
0.43657	0.10594	0.41333	-0.06337
0.45896	0.10538	0.38783	-0.06327
0.48142	0.10449	0.36256	-0.06292
0.50339	0.10330	0.33766	-0.06232
0.52467	0.10179	0.31319	-0.06146
0.54533	0.09996	0.28917	-0.06034
0.56523	0.09781	0.26551	-0.05895
0.58442	0.09531	0.24222	-0.05729
0.60330	0.09239	0.21946	-0.05536
0.62249	0.08896	0.19727	-0.05316
0.64266	0.08491	0.17532	-0.05064
0.66455	0.08014	0.15470	-0.04794
0.68881	0.07454	0.13393	-0.04483
0.71521	0.06817	0.11423	-0.04148
0.74661	0.06039	0.09723	-0.03823
0.78386	0.05103	0.08029	-0.03428
0.81638	0.04299	0.06335	-0.02989
0.84544	0.03595	0.04820	-0.02538
0.87298	0.02948	0.03363	-0.02030
0.90251	0.02278	0.02100	-0.01526
0.94276	0.01381	0.01150	-0.01048
0.97514	0.00661	0.00448	-0.00519
1.00000	0.00096	0.	0.00099

AIRFOIL 35 COORDINATES

UPPER SURFACE		LOWER SURFACE	
X/C	Z/C	X/C	Z/C
0.	0.00099	1.00000	-0.00467
0.00080	0.00771	0.98318	-0.00268
0.00352	0.01653	0.96843	-0.00175
0.00823	0.02519	0.95268	-0.00146
0.01420	0.03265	0.93590	-0.00176
0.02209	0.03912	0.91787	-0.00263
0.03286	0.04633	0.89867	-0.00402
0.04459	0.05300	0.87859	-0.00589
0.05676	0.05868	0.85795	-0.00819
0.07084	0.06447	0.83710	-0.01088
0.08546	0.06952	0.81584	-0.01398
0.10339	0.07504	0.79382	-0.01754
0.12339	0.08099	0.77055	-0.02162
0.14064	0.08550	0.74480	-0.02642
0.15881	0.08974	0.71346	-0.03247
0.17807	0.09373	0.67563	-0.03988
0.19768	0.09735	0.64824	-0.04513
0.21795	0.10066	0.62685	-0.04901
0.23856	0.10361	0.60797	-0.05205
0.25949	0.10621	0.58978	-0.05452
0.28082	0.10848	0.57114	-0.05655
0.30248	0.11040	0.55158	-0.05825
0.32433	0.11198	0.53096	-0.05963
0.34626	0.11321	0.50910	-0.06074
0.36830	0.11409	0.48593	-0.06159
0.39052	0.11462	0.46147	-0.06220
0.41262	0.11480	0.43657	-0.06258
0.43438	0.11462	0.41204	-0.06269
0.45607	0.11408	0.38733	-0.06253
0.47783	0.11317	0.36253	-0.06212
0.49935	0.11191	0.33816	-0.06146
0.52044	0.11030	0.31410	-0.06054
0.54100	0.10834	0.29028	-0.05935
0.56084	0.10604	0.26667	-0.05789
0.58015	0.10336	0.24343	-0.05617
0.59925	0.10024	0.22069	-0.05419
0.61854	0.09662	0.19834	-0.05193
0.63879	0.09237	0.17658	-0.04942
0.66069	0.08737	0.15543	-0.04664
0.68460	0.08160	0.13458	-0.04354
0.71097	0.07495	0.11489	-0.04026
0.74264	0.06673	0.09665	-0.03681
0.77850	0.05726	0.07914	-0.03300
0.81127	0.04871	0.06202	-0.02878
0.84133	0.04103	0.04651	-0.02441
0.87003	0.03389	0.03279	-0.01989
0.90050	0.02651	0.02080	-0.01513
0.93615	0.01808	0.01140	-0.01039
0.97678	0.00842	0.00446	-0.00517
1.00000	0.00284	0.	0.00099

AIRFOIL 37 COORDINATES

UPPER SURFACE		LOWER SURFACE	
X/C	Z/C	X/C	Z/C
0.	0.00099	1.00000	-0.00466
0.00082	0.00784	0.98655	-0.00284
0.00371	0.01700	0.97215	-0.00158
0.00874	0.02603	0.95710	-0.00094
0.01520	0.03376	0.94108	-0.00087
0.02390	0.04063	0.92390	-0.00132
0.03611	0.04863	0.90564	-0.00226
0.04950	0.05637	0.88646	-0.00365
0.06314	0.06313	0.86658	-0.00548
0.07872	0.07001	0.84639	-0.00767
0.09612	0.07687	0.82600	-0.01023
0.11589	0.08414	0.80500	-0.01320
0.13461	0.09054	0.78285	-0.01665
0.15317	0.09629	0.75903	-0.02065
0.17265	0.10177	0.73171	-0.02547
0.19272	0.10689	0.69701	-0.03177
0.21330	0.11166	0.66050	-0.03841
0.23416	0.11602	0.63746	-0.04243
0.25530	0.11997	0.61815	-0.04551
0.27670	0.12352	0.60013	-0.04798
0.29825	0.12666	0.58232	-0.05000
0.31996	0.12937	0.56393	-0.05162
0.34164	0.13165	0.54456	-0.05294
0.36330	0.13348	0.52409	-0.05395
0.38508	0.13489	0.50248	-0.05470
0.40665	0.13585	0.47964	-0.05519
0.42777	0.13634	0.45564	-0.05545
0.44869	0.13636	0.43147	-0.05548
0.46951	0.13590	0.40746	-0.05526
0.49012	0.13498	0.38284	-0.05479
0.51030	0.13358	0.35790	-0.05408
0.52987	0.13170	0.33313	-0.05315
0.54877	0.12936	0.30852	-0.05200
0.56702	0.12651	0.28380	-0.05060
0.58468	0.12313	0.25909	-0.04898
0.60225	0.11909	0.23462	-0.04714
0.62119	0.11405	0.21026	-0.04507
0.64348	0.10764	0.18588	-0.04276
0.66887	0.09998	0.16165	-0.04023
0.69691	0.09122	0.13708	-0.03741
0.73658	0.07858	0.11352	-0.03449
0.77361	0.06679	0.09017	-0.03134
0.80361	0.05741	0.07127	-0.02860
0.83125	0.04901	0.05569	-0.02584
0.85792	0.04118	0.04274	-0.02282
0.88499	0.03351	0.03135	-0.01939
0.91345	0.02573	0.02043	-0.01496
0.94478	0.01740	0.01127	-0.01030
0.97808	0.00863	0.00457	-0.00528
1.00000	0.00284	0.	0.00099

AIRFOIL 40 COORDINATES

UPPER SURFACE		LOWER SURFACE	
X/C	Z/C	X/C	Z/C
0.	0.00099	1.00000	-0.00466
0.00111	0.00823	0.98690	-0.00307
0.00445	0.01665	0.97246	-0.00194
0.00987	0.02458	0.95733	-0.00134
0.01676	0.03131	0.94124	-0.00126
0.02613	0.03752	0.92397	-0.00165
0.03912	0.04485	0.90561	-0.00248
0.05194	0.05115	0.88631	-0.00371
0.06649	0.05742	0.86631	-0.00532
0.08214	0.06337	0.84601	-0.00727
0.09993	0.06946	0.82548	-0.00955
0.11987	0.07593	0.80433	-0.01219
0.13827	0.08140	0.78211	-0.01525
0.15687	0.08641	0.75837	-0.01877
0.17642	0.09119	0.73060	-0.02309
0.19649	0.09565	0.69255	-0.02922
0.21704	0.09980	0.65932	-0.03452
0.23784	0.10358	0.63681	-0.03798
0.25891	0.10701	0.61722	-0.04072
0.28022	0.11008	0.59894	-0.04291
0.30167	0.11278	0.58101	-0.04467
0.32325	0.11512	0.56244	-0.04608
0.34480	0.11707	0.54288	-0.04722
0.36633	0.11863	0.52231	-0.04808
0.38797	0.11982	0.49905	-0.04875
0.40936	0.12062	0.47213	-0.04939
0.43031	0.12101	0.44855	-0.04971
0.45108	0.12098	0.42753	-0.04973
0.47175	0.12054	0.40434	-0.04952
0.49219	0.11968	0.37962	-0.04905
0.51220	0.11841	0.35499	-0.04837
0.53158	0.11674	0.33029	-0.04749
0.55032	0.11463	0.30628	-0.04641
0.56841	0.11209	0.28210	-0.04510
0.58595	0.10907	0.25768	-0.04357
0.60349	0.10547	0.23317	-0.04181
0.62250	0.10096	0.20850	-0.03983
0.64488	0.09524	0.18337	-0.03761
0.67033	0.08842	0.15960	-0.03527
0.69857	0.08061	0.13798	-0.03292
0.73852	0.06934	0.11797	-0.03046
0.77510	0.05903	0.09931	-0.02783
0.80476	0.05083	0.08165	-0.02496
0.83222	0.04345	0.06489	-0.02182
0.85877	0.03656	0.04903	-0.01841
0.88575	0.02980	0.03474	-0.01480
0.91414	0.02294	0.02216	-0.01122
0.94535	0.01559	0.01173	-0.00753
0.97836	0.00790	0.00466	-0.00364
1.00000	0.00284	0.	0.00099

NLF(1)-0414F DERIVATIVE COORDINATES

UPPER SURFACE		LOWER SURFACE	
X/C	Z/C	X/C	Z/C
0.	0.	1.00000	-0.03222
0.00186	0.01031	0.98227	-0.03142
0.00644	0.01855	0.95985	-0.03068
0.01382	0.02604	0.94339	-0.03029
0.02371	0.03288	0.92658	-0.03009
0.03634	0.03967	0.90728	-0.03022
0.05095	0.04618	0.88640	-0.03080
0.06691	0.05215	0.86809	-0.03177
0.08448	0.05780	0.84862	-0.03328
0.10364	0.06314	0.82854	-0.03534
0.12394	0.06812	0.80882	-0.03780
0.14609	0.07292	0.78996	-0.04062
0.16967	0.07758	0.77226	-0.04362
0.19357	0.08180	0.75418	-0.04734
0.21743	0.08558	0.73578	-0.05209
0.24141	0.08890	0.71808	-0.05603
0.26561	0.09177	0.70111	-0.05965
0.29042	0.09426	0.68390	-0.06239
0.31527	0.09635	0.66733	-0.06415
0.34004	0.09798	0.64795	-0.06598
0.36476	0.09915	0.62644	-0.06748
0.39045	0.09993	0.60372	-0.06868
0.41668	0.10035	0.58042	-0.06959
0.44265	0.10037	0.55679	-0.07019
0.46822	0.09998	0.53164	-0.07054
0.49341	0.09919	0.50558	-0.07058
0.51819	0.09798	0.47865	-0.07038
0.54275	0.09632	0.45169	-0.06996
0.56694	0.09424	0.42499	-0.06928
0.59078	0.09177	0.39861	-0.06835
0.61372	0.08888	0.37215	-0.06716
0.63603	0.08556	0.34551	-0.06571
0.65774	0.08184	0.31867	-0.06399
0.67794	0.07779	0.29161	-0.06201
0.69681	0.07326	0.26482	-0.05982
0.71399	0.06858	0.23856	-0.05741
0.73064	0.06307	0.21290	-0.05479
0.74944	0.05570	0.18797	-0.05199
0.77182	0.04635	0.16353	-0.04894
0.79837	0.03517	0.14062	-0.04579
0.82284	0.02521	0.11846	-0.04240
0.84388	0.01704	0.09732	-0.03877
0.86440	0.00976	0.07854	-0.03517
0.88642	0.00248	0.05997	-0.03114
0.90683	-0.00363	0.03953	-0.02589
0.92526	-0.00867	0.02610	-0.02172
0.94253	-0.01301	0.01506	-0.01735
0.95973	-0.01695	0.00685	-0.01280
0.97947	-0.02098	0.00177	-0.00752
1.00000	-0.02472	0.	0.

Nose Shape Parameters

L.E. Radius % of Chord		Δy (DATCOM) % of Chord	
MS(1) - 0317	2.9%	MS(1)-0317	4.4%
NACA 66 ₃ -418	2.0%	NLF-0416	3.9%
KU-26A	1.8%	KU-26A	3.9%
NLF-0416	1.4%	KU-32A	3.9%
Viken*	1.3%	KU-35B	3.9%
KU-32A	1.0%	KU-37A	3.9%
KU-35B	1.0%	NACA 66 ₃ -418	3.4%
KU-37A	1.0%	KU-40A	3.3%
Vought**	0.6%	Viken*	2.8%
KU-40	0.5%	Vought**	2.8%

* Near equal to NASA NLF(1)-0414F (Reference 16).

** See Section 2.4.